UNIVERSITY OF SUSSEX

DOCTORAL THESIS

The geometric influence of domain-size on the dynamics of reaction-diffusion systems with applications in pattern formation

---

Author:
Wakil SARFARAZ

Supervisor:
Prof. Anotida MADZVAMUSE

A thesis submitted in fulfillment of the requirements for the degree of Doctor of Philosophy in

Mathematical & Computational Biology
School of Mathematical and Physical Sciences

September 26, 2018

Declaration of Authorship

I, Wakil SARFARAZ, declare that this thesis titled, "The geometric influence of domain-size on the dynamics of reaction-diffusion systems with applications in pattern formation" and the work presented in it are my own. I confirm that:

- This work was done wholly or mainly while in candidature for a research degree at this University.
- Where any part of this thesis has previously been submitted for a degree or any other qualification at this University or any other institution, this has been clearly stated.
- Where I have consulted the published work of others, this is always clearly attributed.
- Where I have quoted from the work of others, the source is always given. With the exception of such quotations, this thesis is entirely my own work.
- I have acknowledged all main sources of help.
- Where the thesis is based on work done by myself jointly with others, I have made clear exactly what was done by others and what I have contributed myself.

Signed:

_____

Date:

_____

"Mathematical reasoning may be regarded rather schematically as the exercise of a combination of two facilities, which we may call intuition and ingenuity."

Alan Turing,

UNIVERSITY OF SUSSEX

Abstract

Department of Mathematics

School of Mathematical and Physical Sciences

Doctor of Philosophy

The geometric influence of domain-size on the dynamics of reaction-diffusion systems with applications in pattern formation

by Wakil SARFARAZ

This thesis presents through a number of applications a self-contained and robust methodology for exploring mathematical models of pattern formation from the perspective of a dynamical system. The contents of this work applies the methodology to investigate the influence of the domain-size and geometry on the evolution of the dynamics modelled by reaction-diffusion systems (RDSs). We start with deriving general RDSs on evolving domains and in turn explore Arbitrary Lagrangian Eulerian (ALE) formulation of these systems. We focus on a particular RDS of *activator-depleted* class and apply the detailed framework consisting of the application of linear stability theory, domain-dependent harmonic analysis and the numerical solution by the finite element method to predict and verify the theoretically proposed behaviour of pattern formation governed by the evolving dynamics. This is achieved by employing the results of domain-dependent harmonic analysis on three different types of two-dimensional convex and non-convex geometries consisting of a rectangle, a disc and a flat-ring.

Acknowledgements

First and foremost I wish to thank and honour Prof. Anotida Madzvamuse for the instructional guidance towards the quality and presentation of my research without which the completion of this thesis would be far from possible. Secondly, I would like to thank Dr. Chandrasekhar Venkataraman and Dr. Max Jensen for their partial supervision during the period of my PhD studies. I also thank each and every one of my family members for their ongoing support and encouragement in every possible shape or form, with the help of which I overcame all the difficulties associated to the duration of my Doctoral research. I would like to also formally thank the School of Mathematical and Physical Sciences for funding my Doctoral studies at the University of Sussex. I acknowledge to offer my gratitude to the staff of the Mathematics Department specially Richard Chambers, Oonagh Caunter, Felicity Thompson, Rebecca Foster and Lily King for facilitating a resourceful environment appropriately equipped with all the necessary professional research materials. I would like to also extend my thanks to all my great friends whose emotional and motivational support plays an important role in my achievements to date and so is hoped towards my achievements in the future.

Contents

List of Figures

List of Tables

List of Abbreviations

RDSs	**R**eaction-**D**iffusion **S**ystem**s**
ODEs	**O**rdinary **D**ifferential **E**quation**s**
PDEs	**P**artial **D**ifferential **E**quation**s**
ALE	**A**rbitrary **L**agrangian **E**ulerian
SS	**S**teady **S**tate
USS	**U**niform **S**teady **S**tate
Re	**R**eal **P**art **o**f
CPU	**C**entral **P**rocessing **U**nit
sup	**S**upremum
inf	**I**nfemum
MATLAB	**Mat**rix **Lab**oratory
ode45	Runge-Kutta(**4,5**) numerical package on MATLAB
lim	**L**imit
distmesh	**D**ist_**M**esh (An interactive triangulation algorithm)

Dedicated to Pasoon and Adania...

Chapter 1

Preliminaries

This chapter serves to establish the motivation for mathematical research of systems with self-organising dynamical behaviour and how reaction-diffusion theory can be used to explain the underlying dynamics leading to spatially periodic pattern in nature. A detailed literature review is therefore, presented in the scope of this chapter to acknowledge all the major aspects of the existing relevant research. The research questions are identified in the scope of introduction, which are tackled by the contents of this thesis. A brief overview of the methodology is presented to facilitate a starting point for those desiring to extend any aspect of the current research. Finally the thesis outline is explained to understand in brevity about the contents of all subsequent chapters.

1.1 Background and motivation

The emergence of spatial pattern in nature is a phenomena encountered in various biological processes such as the development of an embryo (Mullins et al., 1996), population dynamics (Schmitz et al., 2007; Yan et al., 2013; Ghorai and Poria, 2016) or animal skin pigmentation (Turing, 1952; Murray, 2001). It arises experimentally in other branches of natural science such as experimental chemistry, where chemical species evolve through diffusion and chemical reaction into a particular self-organised spatial pattern (Lengyel and Epstein, 1992; De Kepper, Boissonade, and Szalai, 2009). The natural emergence of self-organised pattern has become an attractive area of research

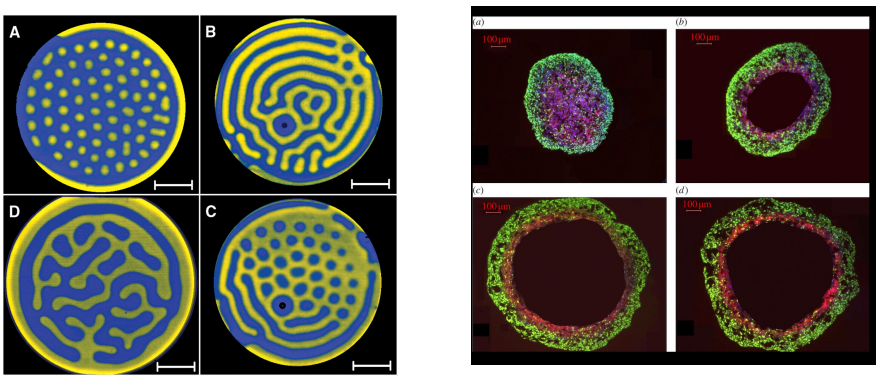

(a) (b)

FIGURE 1.1: In (a) the experimentally evolved spatial pattern achieved by chemical reaction and diffusion on a disc-shape domain is shown (De Kepper, Boissonade, and Szalai, 2009). In (b) the cross-section of a mature tumour at its hypoxic stage is shown (Grimes et al., 2014).

for scientists since 1952 when Alan Turing proposed a mathematical theory presenting an elegant and formal explanation for the phenomenon on the study of morphogenesis (Turing, 1952). The underlying theory of natural emergence of spatial pattern is modelled by a coupled system of reaction-diffusion equations, which usually consists of non-linear second order parabolic class of PDEs. An example of a self-organised spatial pattern from the evolution of chemical reaction of activator-depleted class is shown in Figure 1.1 (a), which is presented with great details in (De Kepper, Boissonade, and Szalai, 2009). Figure 1.1 (a) also motivates the importance of studying RDSs on circular geometries, on which a domain-dependent bifurcation analysis of RDSs is conducted in great details in Chapter 4. Turing models of reaction-diffusion equations are also used to explore the evolving interactions of immune cells on the surface of a tumour (Chaplain, Ganesh, and Graham, 2001), in particular when a tumour attains maturity in growth and it reaches a stage called hypoxia, which is shown in Figure 1.1 (b) with a detailed biological background presented in (Grimes et al., 2014). Figure 1.1 (b) sets up a premises to study RDSs on a two dimensional cross-section of a 3D hollow sphere (tumour), approximated by a flat two dimensional annular region, which is thoroughly investigated in the contents of Chapter 5. Figure 1.1 (b) shows four snapshot of the cross-section of a tumour indicating a transitional change in topology

from a convex domain (ball) to a non-convex domain (hollow sphere). The scope of the current thesis presents pattern formation analysis on a static disc-shape domain which can also be used as a model of the cross-section of a solid tumour at pre-hypoxic stage, however the contents of Chapter 5 investigate the same reaction-diffusion system on a flat-ring with potential applicability to model the cross-section of a solid tumour at or after reaching the hypoxic stage. Examples of the natural emergence of spatial pattern can be found in animal coats, such as spots of a cheetah, stripes of a zebra and spots of a stingray, which are respectively shown in Figure 1.2 (a), (b) and (c). It is entailed by the proposed theory of Alan Turing in (Turing, 1952) that the natural emergence of biological and chemical spatial pattern is triggered, when two or more chemical species undergo a process called *diffusion-driven instability* (Turing, 1952; Murray, 2001; Edelstein-Keshet, 1988). It is a process where a uniform and homogeneous stable (in the absence of diffusion) steady state of a dynamical system becomes unstable when the diffusion is added to the system. The physical effects of the diffusion operator is that of enhancing the homogeneity of concentration gradient, therefore, it is in its own right a stabilising phenomenon. It was mathematically formalised (Turing, 1952; Murray, 2001; Edelstein-Keshet, 1988; Korvasová et al., 2015; Madzvamuse, Gaffney, and Maini, 2010) that upon combining diffusion with reaction-kinetics near a uniform stable steady state, the diffusion can destabilise a stable steady state. Despite that Turing's original work in this discipline was concentrated on the study of morphogenesis (Turing, 1952), however, the scope and formalism associated to his work served as a generalised mathematical theory for the emergence of spatial pattern in nature. For example the theory behind the spatial variation of skin pigmentation on various vertebrates (Kondo and Miura, 2010), or the initiation of spatially periodic pattern in the development of embryo (Mullins et al., 1996) and so forth. From a scientific research perspective the theory of spatial pattern formation modelled by a system of reaction-diffusion equations is yet to be proven experimentally, however, a large number of experimental (De Kepper, Boissonade, and Szalai, 2009; Horváth, Szalai, and De Kepper, 2009) evidences show that the underlying mechanism in chemical reactions that

(a) (b) (c)

FIGURE 1.2: Spatial pattern of skin pigmentation on vertebrates

yield spatially periodic behaviour is that proposed by Turing (Turing, 1952). Similar evidence can be found in collaborative research by experimental biologists and applied mathematicians that provide strong indications and accurate predictions of the development of spatially periodic pattern by the numerical solutions of reaction-diffusion (Turing) systems (Venkataraman, 2011). It is due to the extensive diversity of the relevant applications of pattern formation in experimental chemistry and biology that Turing systems encapsulate, it becomes essential to concentrate on a particular aspect of these systems, because it is practically infeasible to cover all aspects of the subject by the contents of a single PhD thesis. Reaction-diffusion systems that model spatial pattern formation are sets of parabolic PDEs (usually) with non-linear reaction kinetics, whose solution can serve to predict the evolution of spatial pattern in nature. This approach sets up a premises to treat RDS as a dynamical system (Sarfaraz and Madzvamuse, 2017). Turing's original work was mostly concerned with the initiation of a static spatial pattern, whose structure and order is invariant in time (Perraud et al., 1992). In fact most researchers who study Turing systems in collaboration with experimental verification of reaction-diffusion system mainly focus to validate Turing mechanism for the emergence of spatial pattern (Hsia et al., 2012; Lee et al., 1994). If Turing systems are explored from the viewpoint of a dynamical system, then the scope of the research question naturally extends to investigate whether the temporal invariance of Turing pattern is related to the properties of RDSs, or is it that through a particular set of parameter values these systems can be capable of temporal pattern

formation in the same way as their numerical solutions exhibit spatial pattern. Examples of the temporal variation of a spatial pattern can be found in biological species, such as stingray's seasonal change in the order of spots (Barrio et al., 2009). Scholars who explore reaction-diffusion systems from a theoretical perspective also look into the possibility of a Turing system producing a temporal periodicity of a spatial pattern (Schnakenberg, 1979; Liu et al., 2013). The study of stability analysis and the evolution of a linear dynamical system of ordinary differential equations (ODEs) is a matured and sufficiently rich area of research (Perko, 2013). It is in this effect that an approach from the perspective of dynamical system is motivated to explore the behaviour of RDSs near a uniform steady state.

1.2 Introduction

The study of RDSs is a vast area of research in applied mathematics (Madzvamuse and Chung, 2016; Madzvamuse and Chung, 2014; Barreira, Elliott, and Madzvamuse, 2011; Zhang et al., 2014; Madzvamuse, 2008; Venkataraman, Lakkis, and Madzvamuse, 2012; Mackenzie and Madzvamuse, 2009), mathematical and computational biology (Murray, 2001; Edelstein-Keshet, 1988; Mullins et al., 1996; Chaplain, Ganesh, and Graham, 2001; Korvasová et al., 2015), chemical engineering (Lengyel and Epstein, 1992; De Kepper, Boissonade, and Szalai, 2009; Horváth, Szalai, and De Kepper, 2009) and so forth. Few of the popular reaction kinetics models studied in the context of RDSs are the *activator-depleted* (also known as the Schnakenberg) (Murray, 2001; Edelstein-Keshet, 1988; Schnakenberg, 1979), Meinhardt (Gierer and Meinhardt, 1972), Thomas (Thomas, Broun, and Sélégny, 1972) and Gray-scot (Muratov and Osipov, 2002; Doelman, Kaper, and Zegeling, 1997) reaction kinetic models. The study of RDSs is conducted through different types of approaches, one of which focuses on the local behaviour of the dynamics of the RDS near a uniform steady state, which in turn relates to the subject of stability analysis (Yan et al., 2013; Liu et al., 2013; Madzvamuse, 2008; Madzvamuse, Chung, and Venkataraman, 2015) of RDSs using

the stability matrix. Linear stability analysis offers a great deal of insight regarding the behaviour of RDSs in the neighbourhood of a uniform steady state. The other usual approach is numerical computation of the actual solution of RDSs using finite element, finite difference and other numerical methods (Madzvamuse, 2006; Thomée and Wahlbin, 1975; Lakkis, Madzvamuse, and Venkataraman, 2013; Estep, Larson, and Williams, 2000). Numerical solution of RDSs helps to visualise the evolution of the dynamics in time. Numerical approaches in their own right provide a partial insight to obtain an empirical understanding of the spatio-temporal behaviour of the dynamics governed by RDS, since it requires verified analysis and classification of the parameter spaces (Sarfaraz and Madzvamuse, 2017; Sarfaraz and Madzvamuse, 2018) from which the values of the relevant parameters of a particular RDS are to be chosen such that these parameter values are within the bifurcation region of a particular expected behaviour in the evolving dynamics. In order to better understand the behaviour of RDSs, it is necessary to have prior knowledge on the classification of the parameter values. In (Madzvamuse, Chung, and Venkataraman, 2015; Madzvamuse, Ndakwo, and Barreira, 2016) regions of parameter spaces are found, corresponding to diffusion-driven instability with and without cross-diffusion respectively using the well-known *activator-depleted* reaction kinetics. Their approach to finding unstable regions in the parameter space is restricted to Turing instability only. One of the few complementary contributions from the results of the current thesis is the application of a novel numerical technique (exclusive to this work) in order to obtain the full classification of parameter space. The numerical method is also employed to solve the equations for the implicit curves forming the partitioning of the classification within the parameter space. A detailed study in (Iron, Wei, and Winter, 2004) is conducted on the stability analysis of Turing patterns generated by *activator-depleted* reaction kinetics in one spatial dimension. Despite the presentation of rigorous and well-demonstrated proofs in (Iron, Wei, and Winter, 2004), their results are restricted to spatial patterns with focus on the emergence of the number of spatial peaks relative to the eigenvalues of the one-dimensional diffusion operator. The significance

of the current approach in contrast to (Iron, Wei, and Winter, 2004) is that the spectrum of Laplace operator is employed to derive the full classification of the parameter spaces, and relating the domain-size to the admissibility of different types of bifurcations in the dynamics, which is conducted through a transferable framework as a tool to explore general RDSs. A study on *activator-depleted* reaction-diffusion model is conducted in (Xu and Wei, 2012) again with restriction to one spatial dimension focusing mainly on Hopf bifurcation. The approach in (Xu and Wei, 2012) is not aimed to produce any results that relate the domain-size to the reaction-diffusion constants. Researchers also studied bifurcation analysis and spatio-temporal patterns of a diffusive predator-prey system in one space dimension in (Yi, Wei, and Shi, 2009). The results obtained in (Yi, Wei, and Shi, 2009) are mainly theoretical with limited numerical demonstration and in comparison with the current study, no attention is given to explore whether domain-size has any role to play in the bifurcation properties of the RDS in question. Reaction-diffusion system with *activator-depleted* reaction kinetics is investigated in (Gaffney, Yi, and Lee, 2016) with time delay in one-dimensional space and it is theoretically proven with limited numerical verifications that Hopf bifurcation can occur with given constraints on the parameter values of the system. In (Liu et al., 2013) it is attempted to find constraints on the parameters of RDSs with *activator-depleted* reaction kinetics that causes the system to exhibit Hopf and transcritical bifurcations. The proofs in (Liu et al., 2013) are focused on the existence of bifurcation points for some theoretical constraints of parametrised variables of the actual parameters, with no relation between the domain-size and reaction-diffusion rates. Comparing their work to the approach taken by the present thesis, our methodology is robust in the sense that we explicitly relate domain-size to the magnitude of reaction-diffusion constants through employing the results from domain-dependent harmonic analysis on the spectrum of the diffusion operator. Using this relationship, the parameter space is classified for different types of bifurcations on three distinct two-dimensional geometries, which consist of rectangular, circular and annular regions. Moreover, in the present thesis the parameter constraints are a consequence of

the relationship between the domain-size and the reaction-diffusion rates. An additional drawback in the analysis of (Liu et al., 2013) is that their results are produced on parametrised variables of the model and not on the actual parameters of the equations, which makes their results applicable to non-realistic possibilities (negative values). This drawback is effectively resolved in the methodology presented in this thesis as the analysis and numerical study are conducted on the actual two-dimensional positive real parameter space, which in addition to confirming the existence of different bifurcation regions, it offers concrete quantitative classification of the parameter space that guarantees the numerical solution of RDSs to exhibit the expected dynamics. The types of RDSs in the literature (Schnakenberg, 1979; Gierer and Meinhardt, 1972; Muratov and Osipov, 2002; Doelman, Kaper, and Zegeling, 1997) that exhibit spatial or temporal pattern, contain non-linear terms in their reaction kinetics, which makes the mathematical and numerical analysis of such systems extremely challenging. With no closed form analytical solutions, studies of the local behaviour of the systems are generally conducted through applying linear stability theory close to bifurcation points. Here, the behaviour of a system can be theoretically predicted in the neighbourhood of the uniform steady states. Despite that a robust investigation of RDS in the context of pattern formation requires a computational approach to visualise the evolution of the emerging pattern (Madzvamuse, Maini, and Wathen, 2005; Madzvamuse, Wathen, and Maini, 2003; Madzvamuse and Maini, 2007), However, it is essential that a computational approach is conducted in light of results from stability theory (Madzvamuse, Gaffney, and Maini, 2010; Liu et al., 2013; Madzvamuse, 2008) on the RDS, which in turn creates the necessity to perform bifurcation analysis on the parameter spaces. Linear stability analysis can help derive certain conditions on the reaction kinetics, which lead to causing instability in the dynamics of RDSs in the presence of diffusion. A routinely used approach related to stability analysis of RDSs (Yan et al., 2013; Liu et al., 2013; Madzvamuse, 2008; Madzvamuse, Chung, and Venkataraman, 2015) focuses on deriving linear stability conditions in terms of the characteristics of

the stability matrix for diffusion-driven instability, lacking to explore what the numerical application of these conditions induce on the admissible choice of the parameter space for a certain RDS. Diffusion-driven instability crucially depends on the values of diffusion and reaction constants of each reactant, however, more importantly it depends on the parameter choice of the reaction kinetics. The current thesis extends the existing knowledge on the conditions for diffusion-driven instability in the literature, through applying a series of analytical and numerical techniques (Sarfaraz and Madzvamuse, 2017), in order to obtain new insights on the combined effects of diffusion and reaction rates, and in turn relating these to domain-size on which the pattern evolves. The detailed and quantitative analysis on the relationship between the domain-size and diffusion-reaction rates in light of the parameter classification is an aspect that has not been studied in the literature. In order to observe instability caused by the diffusion, the usual methods employed by most researchers in selecting parameters for numerical computations of RDSs (Madzvamuse, 2006; Thomée and Wahlbin, 1975; Lakkis, Madzvamuse, and Venkataraman, 2013; Estep, Larson, and Williams, 2000) consist of trial and error approach on the choices of parameters from the behaviour of RDSs in the absence of diffusion or by using values from previously published work on the same model. Therefore, the absence of a robust methodology to fully classify the parameter space conditional to domain-size and reaction-diffusion constants, creates an arguable platform for the importance of the proposed framework.

The motivation of the approach in this thesis originates from the hypothesis of the spatial dependence of the eigenfunctions of the diffusion operator on the domain-size itself and extending this idea to rigorously investigate how such spatial dependence induces an influence on the linearised stability-matrix of a reaction-diffusion system through the spectral properties of the diffusion operator. Although a limited number of geometries are encapsulated in the current thesis with restriction on reaction kinetics to only *activator-depleted* class, the current thesis can however serve as a framework for developing a standard independent method that collectively employ all the major

and routinely used techniques of exploring the topic namely bifurcation analysis, parameter spaces and computational methods, that could be utilised for general reaction-diffusion systems. The lack of a self-contained, diverse and general framework that combines all the known distinct approaches of exploring this topic creates a credible argument for the development of a generally applicable approach, in which the routinely used methods of studying RDSs collectively serve as compartmental elements of a methodology that is applicable to general RDSs. Which means the methodology used in the scope of this thesis is an attempt to unify the known routines of studying RDSs into a single compartmental framework, whose applicability is not necessarily restricted to RDSs.

It is a commonly accepted hypothesis in the mathematical theory of biological pattern formation (Casten and Holland, 1977; Meier, 1990), that the emergence of spatially periodic pattern in the computational simulations of a reaction-diffusion system has some relevance to the structural properties of the associated eigenfunctions of the diffusion operator in the corresponding domain. On the other hand, the drawback associated with pure computational approaches in general (Madzvamuse, Maini, and Wathen, 2005; Madzvamuse, Wathen, and Maini, 2003; Madzvamuse and Maini, 2007; Lakkis, Madzvamuse, and Venkataraman, 2013; Estep, Larson, and Williams, 2000) is that it lacks to provide rigorous insight on the role that the eigenfunctions play in the emergence of spatial pattern, thus forming a natural platform to explore the evolution of spatial patterns from the perspective of dynamical systems. This is done through employing the analytical results of domain-dependent harmonic study of the Laplace operator into the stability matrix and in turn the combined geometric effect of domain-size and reaction-diffusion constants on the bifurcation properties of the system on the two-dimensional admissible parameter plane is explored. Efficient analytical as well as computational methods are employed to demonstrate the quantitative relationship between the domain-size and the magnitude of the diffusion and reaction constants for an *activator-depleted* RDS. Activator-depleted class of reaction kinetics are best explained through a thought experiment in the context of a phenomena known

as *diffusion-driven instability*. Suppose the reaction of two chemical species (activator and inhibitor) is governed by a a chemical interaction where the activator consumes the inhibitor through the process of reaction-based dispersion with a nonlinear rate of proportionality, the inhibitor however, despite having the nature of chemical inhibition against the invasion of the activator sacrifices a rate of its consumption (like a prey) purely as a consequence of mere physical exposure to the existence of the activating substance within the same domain. Activator-depleted reaction-kinetics are modelled by a set of nonlinear equations satisfying the chemical interaction between the activator and the inhibitor. Suppose that the equations of such reaction kinetics (Schnakenberg, 1979) in the absence of diffusion have a uniform stable steady state. Adding diffusion to this system of equations leads to a change in the expected dynamics. If the diffusion rate of the activator is assumed very large, then a uniform steady state is expected where the complete consumption of the inhibitor occurs upon which the activator reaches a constant steady state. A natural extension of this setup provides a scenario where if one chooses the diffusion rate of the activator smaller than that of the inhibitor, then the original stable steady state becomes unstable due to the presence of diffusion, where the spots of high concentration of the inhibitor succeed in resisting against the weak diffusion of the activator, so dynamically the system undergoes the aforementioned phenomena namely *diffusion-driven instability*, which facilitates for a spatially periodic pattern to emerge. This type of reaction kinetics are also known as *short-range activation with long-range inhibition*, which indicates the quantitative description of the dynamics in the sense that the process of producing spots or stripes (activation) is usually a much faster process than the process of reaching the spatially non-uniform equilibrium (the process of inhibition), leading to the emergence of a spatial pattern in the domain. The findings, which relate the domain-size of different geometries to the diffusion and reaction rates, are presented in the form of theorems with rigorous mathematical proofs and these theoretical results are supported computationally by the finite element numerical solutions corresponding to the *activator-depleted* RDS on stationary rectangular, circular and annular domains.

For each numerical demonstration the relative convergence plots of the discrete time derivatives of the numerical solutions in Euclidean norm for each successive time-step are presented to visualise the convergence of the numerical approximate solutions. The scope of the current thesis serves as a leap in generalising a self-contained methodology presented in (Sarfaraz and Madzvamuse, 2017; Sarfaraz and Madzvamuse, 2018) as a successful approach to the study of reaction-diffusion systems. The novelty and scientific contribution from this work substantially lies in the execution of a profound and diverse theoretical approach through a series of successful applications of the methodology by introducing techniques to analytically solve the spectrum of the diffusion operator on the geometry of a given domain. These analytical findings are then employed to derive bifurcation results through which the relationship between the domain-size and the reaction-diffusion rates is established.

1.3 Methodology outline

A conceptual outline for the methodology used in the contents of Chapters 3, 4 and 5 is presented with a brief indication to each of the major steps, this is to serve as a conceptual user-guide when it is desirable to reproduce the results of the current thesis or extend to apply the methodology to other geometries and models that arise from interdisciplinary research. The contents of Chapter 2 are excluded from the application of this methodology, due to the irrelevance of the research question that is dealt with therein. The issues discussed under the title “Possible research extensions" in Chapter 6 entail the directions of possible extension of the current methodology. This is in case the results of this thesis attract the interests of a reader whose wishes to contribute to mathematical and/or computational generalisation of the methodology. Although the steps of the methodology are presented in the context of a system of reaction-diffusion equations on a bounded domain with a set of prescribed boundary and initial conditions, the phraseology used for each step is easily extendable for applications in other systems of PDEs.

- Identify a uniform stable steady state of the system in the absence of diffusion.
- Linearise the system through the following two steps:
  - Taylor expand to linearise the reaction terms near the uniform steady state.
  - Acquire analytical (if possible) or numerical solutions for the spectrum of the Laplace operator satisfying the original set of boundary conditions prescribed for the model.
- Ansatz satisfying the general form of the system can be reconstructed from the spectrum of the Laplace operator and an admissible time-dependent function.
- Use the results of linearisation to obtain the stability matrix with entries given in terms of those parameters on which one wishes to conduct bifurcation analysis.
- Identify the corresponding discrete eigenvalue problem entailed by the stability matrix of the system.
- Obtain the characteristic polynomial in terms of trace and determinant of the stability matrix, where trace and determinant are now functions of the bifurcation parameters.
- Analyse the cases where the eigenvalues of the stability matrix are complex and real independent from each other and in both cases find the influence of the domain controlling parameter from the spectrum of the Laplace operator on the real part of the discrete eigenvalues.
- Establish the equations that partition the bifurcation plane and analyse the effect of discrete variation of domain-size, diffusion and reaction constants to understand the dynamical consequences that a large or small domain has on large and small values for reaction-diffusion constants.

- Summarise the empirical findings on how the domain-size is connected to reaction-diffusion constants to govern the admissibility of the dynamics through the presence of the corresponding parameters in the trace and determinant of the stability matrix.

- Use a desirable numerical scheme to simulate the original model in the domain and provide the system with initial conditions such that these are small perturbations near the uniform steady state, and using the conditions derived in the scope of bifurcation analysis, simulate the numerical approximate solutions to observe the predicted dynamics.

Identifying to establish the connection of domain-size through the expression for the eigenvalues of the Laplace operator and in turn through the trace and determinant of the stability matrix, leads to find the quantitative influence on the dynamical admissibility of the system. If the problem is posed on an irregular geometry the current methodology would suggest to find the domain-size dependence of the spectrum from the numerical solution of the eigenvalue problem posed on the aforementioned irregular domain. This is one possible extension to equip the current methodology with a numerical solver for eigenvalue problem on irregular domains. This in turn also expresses one of the limitations associated to this methodology that not always do we get in interdisciplinary research geometries that are analytically tractable in the context of harmonic analysis. Another limitation of the current methodology is that it substantially employs computational analysis to draw conclusions, for example the numerical solution of the partitioning curves on the bifurcation plane can be a computationally expensive process if the admissible parameter space is large.

1.4 Thesis outline

Despite that the main results pertained by the current thesis with entirety focus on exploring RDSs on stationary domains, however, due to the natural occurrence of the

relevant applications of RDSs arising from biological processes are found on continuously evolving domains, therefore, it is important that the derivation of RDSs from the first principle on time-dependent domains is presented for completeness purposes. It is in this effect that Chapter 2 contains the mathematical derivation of a general RDS on a continuously evolving domain. ALE (conservative and non-conservative) formulation of RDSs on a reference and evolving frame is derived. In the contents of Chapters 3, 4 and 5 the reaction kinetics are restricted to an *activator-depleted* class reaction-diffusion model on stationary domains. Chapter 3 explores the model on a rectangular compact geometry and relates the side-lengths of a rectangular geometry to the magnitude of reaction-diffusion constants, where the numerical verification through the formulation, implementation and the results of finite element is provided. Chapter 4 presents a detailed study of the model on circular two dimensional compact geometry, in which the radius of a disc-shape domain is related to the magnitude of reaction-diffusion parameters in the context of bifurcation analysis. Chapter 5 conducts a similar study on a non-compact domain that consists of annular region, in which the thickness of a two dimensional flat ring is used to explore the admissibility of different types of bifurcations subject to the choice of thickness of a shell with respect to the choice of reaction-diffusion parameters. Chapter 6 concludes the thesis with a brief direction of potential projects that can arise from possible extension of the study pertained by this thesis.

Chapter 2

Derivation and ALE formulation

This chapter recaps the mathematical derivation of RDSs on time-dependent domains using conservation of matter and Fick's law of diffusion (Muir, Lowry, and Balcom, 2011). We also present both conservative and non-conservative Arbitrary Lagrangian Eulerian (ALE) formulations (Bonito, Kyza, and Nochetto, 2013; Sarrate, Huerta, and Donea, 2001; Nobile and Formaggia, 1999) of RDSs on time-dependent domains. Due to the natural properties of most biological processes (Mullins et al., 1996; Grimes et al., 2014) concerning the analysis and computation of RDSs, which usually takes place on continuously evolving domains, it is considered to include for completeness purposes the ALE formulation. Including the domain growth in the analysis of RDSs requires to mathematically express the physical laws obeyed by such evolution, which initiates two possibilities. The first possibility is if the material velocity of the phenomenon expressed by the RDS is modelled to coincide with the velocity of domain evolution, which is a case dealt with by pure Lagrangian formulation (Venkataraman, 2011; Lakkis, Madzvamuse, and Venkataraman, 2013). The second possibility is when the domain evolution obeys a law that is different from that according to which the material within the domain move. The latter possibility is one in which a combination of Lagrangian and Eulerian approaches is required to compensate for the shortfall of each approach by continuous interaction through time-dependent mappings. Introduction to arbitrary frame through mappings treat a case for which both (pure

Lagrangian or pure Eulerian) formulations are subject to unreliably poor approximations. One example of such a case is when a domain is subject to a uniform deformation within which the material modelled by RDS is exposed to a non-uniform advection.

2.1 Derivation of RDSs on growing domains

Let $\Omega_t \subset \mathbb{R}^d$ and $\partial\Omega_t$ respectively denote a connected domain that is bounded and its boundary, which are both continuously evolving with time. We consider a closed bounded subset $M_t \subset \Omega_t$ and investigate the rate of change of the total amount of a particular quantity u_i. We take the following assumptions to hold in the evolution of Ω_t and its boundary $\partial\Omega_t$.

- For all $t \geq 0$, Ω_t remains closed and bounded.
- For all $t \geq 0$, the evolution does not change the topology of Ω_t .

We derive the equations for the evolution of u_i for $i = 1, ..., k$ denoting the dependent variables in the RDS under the assumption that each u_i diffuses with an independent rate and satisfies a specific reaction rate denoted by F_i. Every unknown u_i is a function of a time-dependent position vector $\boldsymbol{x}$, which consists of d spatial variables and a time variable t. Due to the evolution of the domain every point contained in Ω_t becomes a function of time also. Let $\boldsymbol{x}_0 = (x_1, x_2, ..., x_d)^T$ be a point contained in the initial state of Ω_t at $t = 0$, which we denote by Ω_0. With the deformation of Ω_t we note that the spatial coordinates also evolve with time, therefore for $t > 0$, $\boldsymbol{x}_0$ becomes $\boldsymbol{x}(t) = \Big(x_1(t), x_2(t), ..., x_d(t)\Big)^T$. We consider and formulate the diffusion and reaction of k unknowns denoted by $\boldsymbol{u} = (u_1, u_2, ..., u_k)^T$, which results in a coupled system of k reaction-diffusion equations. The concentration of the ith unknown in the evolving system defined on Ω_t at the point $\boldsymbol{x}$ and at time t can be written as

$$u_i(\boldsymbol{x}(t), t).$$

The total concentration of u_i in an arbitrary closed and bounded region of the domain namely $M_t \subset \Omega_t$ is given by

$$\int_{M_t} u_i(\boldsymbol{x}(t), t) dM_t. \tag{2.1}$$

If we are to investigate the rate of change over time of the total amount of concentration contained in the region M_t, one way is to explore its time derivative, which is

$$\frac{d}{dt} \int_{M_t} u_i(\boldsymbol{x}(t), t) dM_t. \tag{2.2}$$

Since we are unable to commute the operator $\frac{d}{dt}$ with the integral, due to the time-dependence of M_t, therefore we apply the Reynold's Transport theorem (Acheson, 1990; Madzvamuse, 2000; Venkataraman, 2011). Reynold's Transport theorem is a generalisation of Leibniz integral rule (Oldham and Spanier, 1974) which tackles differentiation under the integral sign when the limits of integration depend on the variable of differentiation. For a scalar valued function $g(\boldsymbol{x}(t), t)$ in a time-dependent domain M_t the Reynold's Transport theorem states

$$\frac{d}{dt} \int_{\Omega_t} g(\boldsymbol{x}(t), t) dM_t = \int_{\Omega_t} \frac{Dg}{Dt} + (\nabla \cdot \boldsymbol{v}) g dM_t, \tag{2.3}$$

where $\boldsymbol{v}$ denotes the velocity of the flow in the consequence of time-dependence of M_t and $\frac{Dg}{Dt}$ denotes the material derivative (Acheson, 1990) of g, which is defined by

$$\frac{Dg}{Dt} = \frac{\partial g}{\partial t} + \boldsymbol{v} \cdot \nabla g. \tag{2.4}$$

Applying (2.3) and (2.4) to (2.2) leads to write the total rate of change of the concentration u_i in the region M_t as

$$\frac{d}{dt} \int_{M_t} u_i(\boldsymbol{x}(t), t) dM_t = \int_{M_t} \left[\frac{\partial u_i}{\partial t} + \boldsymbol{v} \cdot \nabla u_i + (\nabla \cdot \boldsymbol{v}) u_i \right] dM_t. \tag{2.5}$$

We can write (2.5) in a compact form, which is

$$\frac{d}{dt}\int_{M_t} u_i(\boldsymbol{x}(t),t)dM_t = \int_{M_t}\Big[\frac{\partial u_i}{\partial t} + \nabla\cdot(\boldsymbol{v}u_i)\Big]dM_t. \tag{2.6}$$

Consider the total rate of change with respect to time of the concentration of the same quantity u_i, through the evolution of its net production within M_t. Note that the total rate of change of u_i can also be expressed to depend on the net flux through the boundary ∂M_t and on the net production of u_i inside M_t. Let $\boldsymbol{q}$ and $\boldsymbol{n}$ denote the net flux and the outward normal through ∂M_t respectively and $F_i(\boldsymbol{u})$ denoting the production rate of u_i in M_t then we can write the total rate of change with respect to time of $u_i(\boldsymbol{x}(t),t)$ as

$$\frac{d}{dt}\int_{M_t} u_i(\boldsymbol{x}(t),t)dM_t = \int_{\partial M_t}\boldsymbol{q}\cdot\boldsymbol{n}dS + \int_{M_t} F_i(\boldsymbol{u})dM_t. \tag{2.7}$$

For the term involving $\boldsymbol{q}$ and $\boldsymbol{n}$ we employ the divergence theorem (Acheson, 1990; Pfeffer, 1986) to write

$$\int_{\partial M_t}\boldsymbol{q}\cdot\boldsymbol{n}dS = -\int_{M_t}\nabla\cdot\boldsymbol{q}dM_t. \tag{2.8}$$

Now we are in a position to write the right hand side of (2.7) as a single integral in the form

$$\int_{\partial M_t}\boldsymbol{q}\cdot\boldsymbol{n}dS + \int_{M_t} F_i(\boldsymbol{u})dM_t = \int_{M_t}\Big[-\nabla\cdot\boldsymbol{q} + F_i(\boldsymbol{u})\Big]dM_t. \tag{2.9}$$

We use the relationship given by Fick's law (Muir, Lowry, and Balcom, 2011) of diffusion to determine the connection between the concentration gradient ∇u_i with the flux $\boldsymbol{q}$. The relationship is given by

$$\boldsymbol{q} = -D_i\nabla u_i, \tag{2.10}$$

where D_i is the diffusion coefficient, which we assume to be an independent positive constant for each unknown u_i. If we combine the relative expressions for the left and

the right hand-sides of (2.7) and substitute for $\boldsymbol{q}$ we obtain

$$\int_{M_t} \Big[\frac{\partial u_i}{\partial t} + \nabla \cdot (\boldsymbol{v} u_i)\Big] dM_t = \int_{M_t} \Big[\nabla \cdot (D_i \nabla u_i) + F_i(\boldsymbol{u})\Big] dM_t. \tag{2.11}$$

Rearranging (2.11), we can write

$$\int_{M_t} \Big[\frac{\partial u_i}{\partial t} + \nabla \cdot (\boldsymbol{v} u_i) - D_i \Delta u_i - F_i(\boldsymbol{u})\Big] dM_t = 0. \tag{2.12}$$

Since M_t is an arbitrary non-empty subset of Ω_t, therefore, it follows that the contents of the integrand must be identically zero everywhere in Ω_t, hence

$$\frac{\partial u_i}{\partial t} + \nabla \cdot (\boldsymbol{v} u_i) - D_i \Delta u_i - F_i(\boldsymbol{u}) = 0, \tag{2.13}$$

which is the reaction-diffusion equation for the quantity u_i. The usual type of boundary conditions for reaction-diffusion systems are the homogeneous Neumann type, which entails that there is a zero-flux condition on all the reacting and diffusing species through $\partial\Omega_t$. This is written in the form $\frac{\partial u_i}{\partial \boldsymbol{n}} = 0$, where $\boldsymbol{n}$ denotes the unit normal in the outward direction to $\partial\Omega_t$. The initial conditions for reaction-diffusion systems usually take the form of continuous bounded positive functions, which resembles the initial existence of some non-zero finite quantity of a particular concentration in the domain. This is written in the form $u_i(\boldsymbol{x}(0), 0) = u_i^0(\boldsymbol{x}_0)$, which completes the derivation of a k-component reaction-diffusion system.

2.2 ALE formulation

ALE formulation is one of the widely used (Madzvamuse, 2008; Mackenzie and Madzvamuse, 2009; Bonito, Kyza, and Nochetto, 2013; Sarrate, Huerta, and Donea, 2001; Nobile and Formaggia, 1999) approaches for solving the type of evolution problems, in which material satisfy a certain convection law and it is posed on a domain that is also time-dependent but not necessarily obeying the same law as the material evolution.

In some regions the material moves with the same rate as the domain deformation, which would be best suitable for a Lagrangian approach. In other regions the material move relatively faster than the domain deformation, which is clearly better treated by an Eulerian approach. The significant advantage of an arbitrary frame of reference is that it effectively deals with this problem, by the means that for regions where the relative velocity of material to the domain deformation is zero, the ALE behaves as if it was a Lagrangian formulation, on the other hand when the material velocity is significantly different from the domain deformation, then an Eulerian type of behaviour is expected and hence the name Arbitrary Lagrangian Eulerian formulation. This way the accuracy and contribution from both velocities and their combination is preserved and hence higher accuracy in the results of numerical methods. The decision of how to choose the arbitrary frame of reference is highly dependent on the nature of the problem posed and the behaviour of domain evolution. It also depends on what numerical method one has in mind for implementation. Moreover, it depends on the nature of the introduced mapping, the image of which defines the physically evolving frame. We derive the ALE formulation of the system using functions that are defined on Eulerian frame and present an equivalent derivation on Lagrangian coordinates. The idea of ALE formulation is to transform an RDS expressed on a time-dependent domain to a problem that is posed on an arbitrary frame of reference, that could contain regions which can adopt subject to necessity the Lagrangian properties of the formulation (where the material advection is the same as the velocity of the domain deformation) and where needed the formulation adopts the Eulerian properties (where the material advection is non-zero in a static domain). We aim to transform the problem given by (2.13) using ALE frame both for functions that are defined on a pure Lagrangian frame as well as for functions that are only defined on Eulerian frame. It should be noted that exclusive to the notational convention of this chapter, we denote functions that are defined on Lagrangian frame by $\hat{u}_i$ and those defined on Eulerian frame are denoted by u_i. The evolving frame is denoted by Ω_t and the corresponding coordinates are referred to by $\boldsymbol{x}$, where as the Lagrangian frame is denoted by Ω_L and the

associated coordinates are expressed by $\boldsymbol{\xi}$, which are written as $\boldsymbol{x} \in \Omega_t$ and $\boldsymbol{\xi} \in \Omega_L$. In order to choose an arbitrary framework we require a set of time-dependent mappings through which we establish a one to one correspondence between the coordinates $\boldsymbol{x}$ and $\boldsymbol{\xi}$. The mappings that are employed to compute the arbitrary frame of reference must be time-dependent in order to maintain one to one correspondence between every point from coordinates $\boldsymbol{x}$ to every point in coordinates $\boldsymbol{\xi}$. Let $\boldsymbol{\xi} = (\xi_1, ..., \xi_d)^T$ and $\boldsymbol{x} = (x_1, ..., x_d)^T$ both denote d dimensional Lagrangian and Eulerian spatial position vectors defined on Ω_L and Ω_t respectively. Time is assumed fixed and the same for both coordinates and is denoted by t. For ALE formulation of RDSs a set of notation is presented in Table 2.1, which is used exclusively in the contents of this chapter. It is

Notation	Description
$\boldsymbol{x}$	Eulerian coordinates
$\boldsymbol{\xi}$	Lagrangian coordinates
t	Time
$\boldsymbol{v}$	Material velocity
$\boldsymbol{n}$	Outward normal
$\boldsymbol{\mathcal{X}}(\boldsymbol{\xi}, t) = \boldsymbol{x}$	Mapping from coordinates $\boldsymbol{\xi}$ to $\boldsymbol{x}$
$\boldsymbol{\mathcal{Y}}(\boldsymbol{x}, t) = \boldsymbol{\xi}$	Mapping from coordinates $\boldsymbol{x}$ to $\boldsymbol{\xi}$
$\mathbb{X}$	Jacobian matrix of the mapping $\boldsymbol{\mathcal{X}}$
$\mathbb{Y}$	Jacobian matrix of the mapping $\boldsymbol{\mathcal{Y}}$
$\boldsymbol{J}$	Determinant of $\mathbb{X}$
$\boldsymbol{K}$	Determinant of $\mathbb{Y}$
Ω_t	Eulerian frame
Ω_L	Lagrangian frame
∇_δ	Gradient with respect to the variable δ
$\boldsymbol{a}$	Time derivative of $\boldsymbol{\mathcal{X}}$
$\boldsymbol{b}$	Time derivative of $\boldsymbol{\mathcal{Y}}$
$\dot{\boldsymbol{\partial}}_{\boldsymbol{a}}$	Material derivative with respect to the velocity $\boldsymbol{a}$

TABLE 2.1: Table showing the notations and their descriptions

assumed that Ω_t is subject to a continuous deformation for all $t \in [0, T]$, where T is the final time up to which we wish to observe or obtain the solution of the problem under consideration. For $\boldsymbol{\mathcal{X}}$ to be appropriate for ALE formulation, it must be a bijective diffeomorphism (Lakkis, Madzvamuse, and Venkataraman, 2013) with a smooth and differentiable inverse, where we define $\boldsymbol{\mathcal{Y}} = \boldsymbol{\mathcal{X}}^{-1}$. The relationship of $\boldsymbol{\mathcal{X}}$ and $\boldsymbol{\mathcal{Y}}$ is that of the forward and pull back mappings respectively between the coordinates $\boldsymbol{x}$ and $\boldsymbol{\xi}$. With the help of these mappings we are able to relate every point from Ω_t and Ω_L,

which means that for every point $\boldsymbol{x} \in \Omega_t$ we have a point $\boldsymbol{\xi} \in \Omega_L$ such that $\boldsymbol{\mathcal{X}}(\boldsymbol{\xi}, t) = \boldsymbol{x}$. Similarly, every point $\boldsymbol{\xi} \in \Omega_L$ maybe related to a point $\boldsymbol{x} \in \Omega_t$ by $\boldsymbol{\mathcal{Y}}(\boldsymbol{x}, t) = \boldsymbol{\xi}$. We may write these relations formally as

$$\boldsymbol{\mathcal{X}} : \Omega_L \subset \mathbb{R}^d \to \Omega_t \subset \mathbb{R}^d, \quad \boldsymbol{\mathcal{X}}(\boldsymbol{\xi}, t) = \boldsymbol{x},$$
$$\boldsymbol{\mathcal{Y}} : \Omega_t \subset \mathbb{R}^d \to \Omega_L \subset \mathbb{R}^d, \quad \boldsymbol{\mathcal{Y}}(\boldsymbol{x}, t) = \boldsymbol{\xi}.$$

We denote by $\mathbb{X}$, $\mathscr{X}_i$ and $\mathbb{Y}$, $\mathscr{Y}_i$ the Jacobian matrices and components of the mappings $\boldsymbol{\mathcal{X}}$ and $\boldsymbol{\mathcal{Y}}$ respectively, where the entries of $\mathbb{X}$ and $\mathbb{Y}$ are computed by the formulae

$$\mathbb{X}_{i,j} = \frac{\partial \mathscr{X}_i}{\partial \xi_j} \qquad \text{and} \qquad \mathbb{Y}_{i,j} = \frac{\partial \mathscr{Y}_i}{\partial x_j},$$

with i, j running from 1 to the number of spatial dimensions. Let $\boldsymbol{J}$ and $\boldsymbol{K}$ denote the determinants of $\mathbb{X}$ and $\mathbb{Y}$ respectively. We define the divergence for a vector valued function $\boldsymbol{g}(\boldsymbol{x}, t)$ by

$$\nabla \cdot \boldsymbol{g}(\boldsymbol{x}, t) = \sum_{i=1}^{d} \frac{\partial g_i}{\partial x_i}(\boldsymbol{x}, t),$$

however, if $g(\boldsymbol{x}, t)$ is a scalar valued function then we define the gradient and Laplacian of g by

$$\nabla_x g = \nabla_x g(\boldsymbol{x}, t) = \Big(\frac{\partial g}{\partial x_1}, ..., \frac{\partial g}{\partial x_d}\Big)^T,$$
$$\Delta g(\boldsymbol{x}, t) = \nabla_x \cdot \nabla_x g(\boldsymbol{x}, t) = \sum_{i=1}^{d} \frac{\partial^2 g}{\partial x_i^2}.$$

We denote by $\boldsymbol{a}$ and $\boldsymbol{b}$ the time derivatives of $\boldsymbol{\mathcal{X}}$ and $\boldsymbol{\mathcal{Y}}$ respectively, which we may write formally as

$$\boldsymbol{a}\big(\boldsymbol{\mathcal{X}}(\boldsymbol{\xi}, t)\big) = \Big(\frac{\partial \mathscr{X}_1}{\partial t}, ..., \frac{\mathscr{X}_d}{\partial t}\Big)^T \quad \text{and} \quad \boldsymbol{b}\big(\boldsymbol{\mathcal{Y}}(\boldsymbol{x}, t)\big) = \Big(\frac{\partial \mathscr{Y}_1}{\partial t}, ..., \frac{\mathscr{Y}_d}{\partial t}\Big)^T.$$

Finally we define the inner product of two vector valued functions g and f on a domain Ω by

$$\langle f, g \rangle = \sum_{i=1}^{d} \int_{\Omega} f_i g_i d\Omega.$$

Before embarking on the derivation of ALE formulation of RDS we derive the famous and important Euler's formula (Acheson, 1990), that relates the time derivative of the determinant of the Jacobian matrix to the time derivative of the mapping itself. This formula will prove useful to derive the conservative ALE formulation of RDSs. Our derivation of Euler's formula is for three spatial and one time dimension, however, the method of derivation is applicable to arbitrary number of dimensions. Also this derivation is presented only for the determinant of the Jacobian of the forward mapping $\mathcal{X}$ and the process is similar when it is desirable to derive the equivalent for $\mathcal{Y}$. We aim to derive the formula (Madzvamuse, 2008; Acheson, 1990)

$$\frac{d}{dt}\Big(J(\xi,t)\Big) = J\nabla \cdot a(\xi,t).$$

For three dimensional real space the mapping $\mathcal{X}(\xi,t)$ is a vector valued function with the Jacobian of the form

$$\mathbb{X}(\xi,t) = \begin{bmatrix} \frac{\partial \mathcal{X}_1}{\partial \xi_1}(\xi,t) & \frac{\partial \mathcal{X}_1}{\partial \xi_2}(\xi,t) & \frac{\partial \mathcal{X}_1}{\partial \xi_3}(\xi,t) \\ \frac{\partial \mathcal{X}_2}{\partial \xi_1}(\xi,t) & \frac{\partial \mathcal{X}_2}{\partial \xi_2}(\xi,t) & \frac{\partial \mathcal{X}_2}{\partial \xi_3}(\xi,t) \\ \frac{\partial \mathcal{X}_3}{\partial \xi_1}(\xi,t) & \frac{\partial \mathcal{X}_3}{\partial \xi_2}(\xi,t) & \frac{\partial \mathcal{X}_3}{\partial \xi_3}(\xi,t) \end{bmatrix},$$

for which the determinant is denoted by J and given by

$$\begin{aligned} J(\xi,t) =& \frac{\partial \mathcal{X}_1}{\partial \xi_1}\frac{\partial \mathcal{X}_2}{\partial \xi_2}\frac{\partial \mathcal{X}_3}{\partial \xi_3}(\xi,t) - \frac{\partial \mathcal{X}_1}{\partial \xi_1}\frac{\partial \mathcal{X}_2}{\partial \xi_3}\frac{\partial \mathcal{X}_3}{\partial \xi_2}(\xi,t) - \frac{\partial \mathcal{X}_1}{\partial \xi_2}\frac{\partial \mathcal{X}_2}{\partial \xi_1}\frac{\partial \mathcal{X}_3}{\partial \xi_3}(\xi,t) \\ &+ \frac{\partial \mathcal{X}_1}{\partial \xi_2}\frac{\partial \mathcal{X}_2}{\partial \xi_3}\frac{\partial \mathcal{X}_3}{\partial \xi_1}(\xi,t) + \frac{\partial \mathcal{X}_1}{\partial \xi_3}\frac{\partial \mathcal{X}_2}{\partial \xi_1}\frac{\partial \mathcal{X}_3}{\partial \xi_2}(\xi,t) - \frac{\partial \mathcal{X}_1}{\partial \xi_3}\frac{\partial \mathcal{X}_2}{\partial \xi_2}\frac{\partial \mathcal{X}_3}{\partial \xi_1}(\xi,t). \end{aligned} \tag{2.14}$$

We differentiate with respect to t the expression for $J(\xi,t)$ term by term, conducting the calculations on all of the six terms on the right hand-side of (2.14);

1.

$$\begin{aligned}\frac{d}{dt}\Big(\frac{\partial \mathscr{X}_1}{\partial \xi_1}\frac{\partial \mathscr{X}_2}{\partial \xi_2}\frac{\partial \mathscr{X}_3}{\partial \xi_3}(\boldsymbol{\xi},t)\Big) =&\Big(\frac{\partial \mathscr{X}_3}{\partial \xi_3}\frac{\partial \mathscr{X}_2}{\partial \xi_2}\frac{\partial}{\partial \xi_1}\Big)\Big(\frac{\partial \mathscr{X}_1}{\partial t}\Big)(\boldsymbol{\xi},t)\\ &+\Big(\frac{\partial \mathscr{X}_3}{\partial \xi_3}\frac{\partial \mathscr{X}_1}{\partial \xi_1}\frac{\partial}{\partial \xi_2}\Big)\Big(\frac{\partial \mathscr{X}_2}{\partial t}\Big)(\boldsymbol{\xi},t)\\ &+\Big(\frac{\partial \mathscr{X}_1}{\partial \xi_1}\frac{\partial \mathscr{X}_2}{\partial \xi_2}\frac{\partial}{\partial \xi_3}\Big)\Big(\frac{\partial \mathscr{X}_3}{\partial t}\Big)(\boldsymbol{\xi},t)\end{aligned}$$

2.

$$\begin{aligned}\frac{d}{dt}\Big(-\frac{\partial \mathscr{X}_1}{\partial \xi_1}\frac{\partial \mathscr{X}_2}{\partial \xi_3}\frac{\partial \mathscr{X}_3}{\partial \xi_2}(\boldsymbol{\xi},t)\Big) =&-\Big(\frac{\partial \mathscr{X}_2}{\partial \xi_3}\frac{\partial \mathscr{X}_3}{\partial \xi_2}\frac{\partial}{\partial \xi_1}\Big)\Big(\frac{\partial \mathscr{X}_1}{\partial t}\Big)(\boldsymbol{\xi},t)\\ &-\Big(\frac{\partial \mathscr{X}_1}{\partial \xi_1}\frac{\partial \mathscr{X}_3}{\partial \xi_2}\frac{\partial}{\partial \xi_3}\Big)\Big(\frac{\partial \mathscr{X}_2}{\partial t}\Big)(\boldsymbol{\xi},t)\\ &-\Big(\frac{\partial \mathscr{X}_1}{\partial \xi_1}\frac{\partial \mathscr{X}_2}{\partial \xi_3}\frac{\partial}{\partial \xi_2}\Big)\Big(\frac{\partial \mathscr{X}_3}{\partial t}\Big)(\boldsymbol{\xi},t)\end{aligned}$$

3.

$$\begin{aligned}\frac{d}{dt}\Big(-\frac{\partial \mathscr{X}_1}{\partial \xi_2}\frac{\partial \mathscr{X}_2}{\partial \xi_1}\frac{\partial \mathscr{X}_3}{\partial \xi_3}(\boldsymbol{\xi},t)\Big) =&-\Big(\frac{\partial \mathscr{X}_2}{\partial \xi_1}\frac{\partial \mathscr{X}_3}{\partial \xi_3}\frac{\partial}{\partial \xi_2}\Big)\Big(\frac{\partial \mathscr{X}_1}{\partial t}\Big)(\boldsymbol{\xi},t)\\ &-\Big(\frac{\partial \mathscr{X}_1}{\partial \xi_2}\frac{\partial \mathscr{X}_3}{\partial \xi_3}\frac{\partial}{\partial \xi_1}\Big)\Big(\frac{\partial \mathscr{X}_2}{\partial t}\Big)(\boldsymbol{\xi},t)\\ &-\Big(\frac{\partial \mathscr{X}_1}{\partial \xi_2}\frac{\partial \mathscr{X}_2}{\partial \xi_1}\frac{\partial}{\partial \xi_3}\Big)\Big(\frac{\partial \mathscr{X}_3}{\partial t}\Big)(\boldsymbol{\xi},t)\end{aligned}$$

4.

$$\begin{aligned}\frac{d}{dt}\Big(\frac{\partial \mathscr{X}_1}{\partial \xi_2}\frac{\partial \mathscr{X}_2}{\partial \xi_3}\frac{\partial \mathscr{X}_3}{\partial \xi_1}(\boldsymbol{\xi},t)\Big) =&\Big(\frac{\partial \mathscr{X}_2}{\partial \xi_3}\frac{\partial \mathscr{X}_3}{\partial \xi_1}\frac{\partial}{\partial \xi_2}\Big)\Big(\frac{\partial \mathscr{X}_1}{\partial t}\Big)(\boldsymbol{\xi},t)\\ &+\Big(\frac{\partial \mathscr{X}_1}{\partial \xi_2}\frac{\partial \mathscr{X}_3}{\partial \xi_1}\frac{\partial}{\partial \xi_3}\Big)\Big(\frac{\partial \mathscr{X}_2}{\partial t}\Big)(\boldsymbol{\xi},t)\\ &+\Big(\frac{\partial \mathscr{X}_1}{\partial \xi_2}\frac{\partial \mathscr{X}_2}{\partial \xi_3}\frac{\partial}{\partial \xi_1}\Big)\Big(\frac{\partial \mathscr{X}_3}{\partial t}\Big)(\boldsymbol{\xi},t)\end{aligned}$$

5.

$$\begin{aligned}\frac{d}{dt}\Big(\frac{\partial \mathscr{X}_1}{\partial \xi_3}\frac{\partial \mathscr{X}_2}{\partial \xi_1}\frac{\partial \mathscr{X}_3}{\partial \xi_2}(\boldsymbol{\xi},t)\Big) =&\Big(\frac{\partial \mathscr{X}_2}{\partial \xi_1}\frac{\partial \mathscr{X}_3}{\partial \xi_2}\frac{\partial}{\partial \xi_3}\Big)\Big(\frac{\partial \mathscr{X}_1}{\partial t}\Big)(\boldsymbol{\xi},t)\\ &+\Big(\frac{\partial \mathscr{X}_1}{\partial \xi_3}\frac{\partial \mathscr{X}_3}{\partial \xi_2}\frac{\partial}{\partial \xi_1}\Big)\Big(\frac{\partial \mathscr{X}_2}{\partial t}\Big)(\boldsymbol{\xi},t)\\ &+\Big(\frac{\partial \mathscr{X}_1}{\partial \xi_3}\frac{\partial \mathscr{X}_2}{\partial \xi_1}\frac{\partial}{\partial \xi_2}\Big)\Big(\frac{\partial \mathscr{X}_3}{\partial t}\Big)(\boldsymbol{\xi},t)\end{aligned}$$

6.

$$\begin{aligned}\frac{d}{dt}\Big(-\frac{\partial \mathscr{X}_1}{\partial \xi_3}\frac{\partial \mathscr{X}_2}{\partial \xi_2}\frac{\partial \mathscr{X}_3}{\partial \xi_1}(\boldsymbol{\xi},t)\Big) =&-\Big(\frac{\partial \mathscr{X}_2}{\partial \xi_2}\frac{\partial \mathscr{X}_3}{\partial \xi_1}\frac{\partial}{\partial \xi_3}\Big)\Big(\frac{\partial \mathscr{X}_1}{\partial t}\Big)(\boldsymbol{\xi},t)\\ &-\Big(\frac{\partial \mathscr{X}_1}{\partial \xi_3}\frac{\partial \mathscr{X}_3}{\partial \xi_1}\frac{\partial}{\partial \xi_2}\Big)\Big(\frac{\partial \mathscr{X}_2}{\partial t}\Big)(\boldsymbol{\xi},t)\\ &-\Big(\frac{\partial \mathscr{X}_1}{\partial \xi_3}\frac{\partial \mathscr{X}_2}{\partial \xi_2}\frac{\partial}{\partial \xi_1}\Big)\Big(\frac{\partial \mathscr{X}_3}{\partial t}\Big)(\boldsymbol{\xi},t)\end{aligned}$$

Collecting all the terms appropriately and factoring out $\frac{\partial}{\partial \xi_i}$ and $\frac{\partial \mathscr{X}_i}{\partial t}$ for $i = 1,2,3$ leads to write

$$\begin{aligned}\frac{d}{dt}\Big(J(\boldsymbol{\xi},t)\Big) = &\Bigg[\Big(\frac{\partial \mathscr{X}_3}{\partial \xi_3}\frac{\partial \mathscr{X}_2}{\partial \xi_2}-\frac{\partial \mathscr{X}_2}{\partial \xi_3}\frac{\partial \mathscr{X}_3}{\partial \xi_2}\Big)\Big(\frac{\partial}{\partial \xi_1}\Big)+\Big(\frac{\partial \mathscr{X}_2}{\partial \xi_3}\frac{\partial \mathscr{X}_3}{\partial \xi_1}-\frac{\partial \mathscr{X}_2}{\partial \xi_1}\frac{\partial \mathscr{X}_3}{\partial \xi_3}\Big)\Big(\frac{\partial}{\partial \xi_2}\Big)\\ &+\Big(\frac{\partial \mathscr{X}_2}{\partial \xi_1}\frac{\partial \mathscr{X}_3}{\partial \xi_2}-\frac{\partial \mathscr{X}_2}{\partial \xi_2}\frac{\partial \mathscr{X}_3}{\partial \xi_1}\Big)\Big(\frac{\partial}{\partial \xi_3}\Big)\Bigg]\frac{\partial \mathscr{X}_1}{\partial t}(\boldsymbol{\xi},t)\\ &+\Bigg[\Big(\frac{\partial \mathscr{X}_1}{\partial \xi_3}\frac{\partial \mathscr{X}_3}{\partial \xi_2}-\frac{\partial \mathscr{X}_1}{\partial \xi_2}\frac{\partial \mathscr{X}_3}{\partial \xi_3}\Big)\Big(\frac{\partial}{\partial \xi_1}\Big)+\Big(\frac{\partial \mathscr{X}_1}{\partial \xi_1}\frac{\partial \mathscr{X}_3}{\partial \xi_3}-\frac{\partial \mathscr{X}_1}{\partial \xi_3}\frac{\partial \mathscr{X}_3}{\partial \xi_1}\Big)\Big(\frac{\partial}{\partial \xi_2}\Big)\\ &+\Big(\frac{\partial \mathscr{X}_1}{\partial \xi_2}\frac{\partial \mathscr{X}_3}{\partial \xi_1}-\frac{\partial \mathscr{X}_1}{\partial \xi_1}\frac{\partial \mathscr{X}_3}{\partial \xi_2}\Big)\Big(\frac{\partial}{\partial \xi_3}\Big)\Bigg]\frac{\partial \mathscr{X}_2}{\partial t}(\boldsymbol{\xi},t)\\ &+\Bigg[\Big(\frac{\partial \mathscr{X}_1}{\partial \xi_2}\frac{\partial \mathscr{X}_2}{\partial \xi_3}-\frac{\partial \mathscr{X}_1}{\partial \xi_3}\frac{\partial \mathscr{X}_2}{\partial \xi_2}\Big)\Big(\frac{\partial}{\partial \xi_1}\Big)+\Big(\frac{\partial \mathscr{X}_1}{\partial \xi_3}\frac{\partial \mathscr{X}_2}{\partial \xi_1}-\frac{\partial \mathscr{X}_1}{\partial \xi_1}\frac{\partial \mathscr{X}_2}{\partial \xi_3}\Big)\Big(\frac{\partial}{\partial \xi_2}\Big)\\ &+\Big(\frac{\partial \mathscr{X}_1}{\partial \xi_1}\frac{\partial \mathscr{X}_2}{\partial \xi_2}-\frac{\partial \mathscr{X}_1}{\partial \xi_2}\frac{\partial \mathscr{X}_2}{\partial \xi_1}\Big)\Big(\frac{\partial}{\partial \xi_3}\Big)\Bigg]\frac{\partial \mathscr{X}_3}{\partial t}(\boldsymbol{\xi},t).\end{aligned}$$

Respecting the alternating sign property of computing the determinant we can write this expression using the determinants of the block matrices of $\boldsymbol{J}$

$$\begin{aligned}\frac{d}{dt}\Big(\boldsymbol{J}(\boldsymbol{\xi},t)\Big) =& \left(\begin{vmatrix} \frac{\partial \mathscr{X}_2}{\partial \xi_2} & \frac{\partial \mathscr{X}_2}{\partial \xi_3} \\ \frac{\partial \mathscr{X}_3}{\partial \xi_2} & \frac{\partial \mathscr{X}_3}{\partial \xi_3} \end{vmatrix} \frac{\partial}{\partial \xi_1} + \begin{vmatrix} \frac{\partial \mathscr{X}_2}{\partial \xi_1} & \frac{\partial \mathscr{X}_2}{\partial \xi_3} \\ \frac{\partial \mathscr{X}_3}{\partial \xi_1} & \frac{\partial \mathscr{X}_3}{\partial \xi_3} \end{vmatrix} \frac{\partial}{\partial \xi_2} + \begin{vmatrix} \frac{\partial \mathscr{X}_2}{\partial \xi_1} & \frac{\partial \mathscr{X}_2}{\partial \xi_2} \\ \frac{\partial \mathscr{X}_3}{\partial \xi_1} & \frac{\partial \mathscr{X}_3}{\partial \xi_2} \end{vmatrix} \frac{\partial}{\partial \xi_3} \right) \frac{\partial \mathscr{X}_1}{\partial t}(\boldsymbol{\xi},t) \\ &+ \left(\begin{vmatrix} \frac{\partial \mathscr{X}_1}{\partial \xi_2} & \frac{\partial \mathscr{X}_1}{\partial \xi_3} \\ \frac{\partial \mathscr{X}_3}{\partial \xi_2} & \frac{\partial \mathscr{X}_3}{\partial \xi_3} \end{vmatrix} \frac{\partial}{\partial \xi_1} + \begin{vmatrix} \frac{\partial \mathscr{X}_1}{\partial \xi_1} & \frac{\partial \mathscr{X}_1}{\partial \xi_3} \\ \frac{\partial \mathscr{X}_3}{\partial \xi_1} & \frac{\partial \mathscr{X}_3}{\partial \xi_3} \end{vmatrix} \frac{\partial}{\partial \xi_2} + \begin{vmatrix} \frac{\partial \mathscr{X}_1}{\partial \xi_1} & \frac{\partial \mathscr{X}_1}{\partial \xi_2} \\ \frac{\partial \mathscr{X}_3}{\partial \xi_1} & \frac{\partial \mathscr{X}_3}{\partial \xi_2} \end{vmatrix} \frac{\partial}{\partial \xi_3} \right) \frac{\partial \mathscr{X}_2}{\partial t}(\boldsymbol{\xi},t) \\ &+ \left(\begin{vmatrix} \frac{\partial \mathscr{X}_1}{\partial \xi_2} & \frac{\partial \mathscr{X}_1}{\partial \xi_3} \\ \frac{\partial \mathscr{X}_2}{\partial \xi_2} & \frac{\partial \mathscr{X}_2}{\partial \xi_3} \end{vmatrix} \frac{\partial}{\partial \xi_1} + \begin{vmatrix} \frac{\partial \mathscr{X}_1}{\partial \xi_1} & \frac{\partial \mathscr{X}_1}{\partial \xi_3} \\ \frac{\partial \mathscr{X}_2}{\partial \xi_1} & \frac{\partial \mathscr{X}_2}{\partial \xi_3} \end{vmatrix} \frac{\partial}{\partial \xi_2} + \begin{vmatrix} \frac{\partial \mathscr{X}_1}{\partial \xi_1} & \frac{\partial \mathscr{X}_1}{\partial \xi_2} \\ \frac{\partial \mathscr{X}_2}{\partial \xi_1} & \frac{\partial \mathscr{X}_2}{\partial \xi_2} \end{vmatrix} \frac{\partial}{\partial \xi_3} \right) \frac{\partial \mathscr{X}_3}{\partial t}(\boldsymbol{\xi},t). \end{aligned} \tag{2.15}$$

Let β_{ij} denote the determinant of the 2 block matrix that is multiplied by $\frac{\partial \mathscr{X}_i}{\partial t}$ and $\frac{\partial}{\partial \xi_j}$ then the right hand-side of (2.15) can be written as the product of the determinant $\boldsymbol{J}$, the gradient with respect to $\boldsymbol{\xi}$ and the time derivative of the mapping namely $\boldsymbol{a}(\boldsymbol{\mathscr{X}}(\boldsymbol{\xi},t),t)$, which leads to the desired formula that can also be written as the dot product of the following two vectors

$$\frac{d}{dt}\big(\boldsymbol{J}(\boldsymbol{\xi},t)\big) = \begin{pmatrix} \sum_{i=1}^3 \beta_{1i}\frac{\partial}{\partial \xi_i}, & \sum_{i=1}^3 \beta_{2i}\frac{\partial}{\partial \xi_i}, & \sum_{i=1}^3 \beta_{3i}\frac{\partial}{\partial \xi_i} \end{pmatrix} \cdot \begin{pmatrix} \frac{\partial \mathscr{X}_1}{\partial t} \\ \frac{\partial \mathscr{X}_2}{\partial t} \\ \frac{\partial \mathscr{X}_3}{\partial t} \end{pmatrix},$$

which is equivalent to writing

$$\frac{d}{dt}\big(\boldsymbol{J}(\boldsymbol{\xi},t)\big) = \boldsymbol{J}\nabla_{\boldsymbol{\xi}} \cdot \boldsymbol{a}(\boldsymbol{\mathscr{X}}(\boldsymbol{\xi},t),t).$$

The system we wish to analyse in the ALE frame contains $i = 1,...,k$ unknowns modelled by a k-component RDS, with positive bounded initial conditions and Neumann

type boundary in the form

$$\begin{cases} \frac{\partial u_i}{\partial t}(\boldsymbol{x},t) + \nabla_x \cdot (\boldsymbol{v}u_i)(\boldsymbol{x},t) - \nabla_x \cdot D_i \nabla_x u_i(\boldsymbol{x},t) - F_i(\boldsymbol{u}(\boldsymbol{x},t)) = 0, \quad \boldsymbol{x} \in \Omega_t, \quad t \in [0,T], \\ \begin{cases} (\boldsymbol{n} \cdot \nabla u_i)(\boldsymbol{x},t) = 0 \qquad \boldsymbol{x} \in \partial\Omega_t, \quad t \geq 0, \\ u_i(\boldsymbol{x},t) = u_i^0(\boldsymbol{x}) \qquad \boldsymbol{x} \in \Omega_t, \quad t = 0. \end{cases} \end{cases} \tag{2.16}$$

where $\boldsymbol{v}$ represents the material advection. The independent diffusion coefficient for every unknown u_i is denoted by D_i. This is a system of $i = 1, ..., k$ reaction-diffusion equations, each of which governs the evolution of u_i through independent diffusion and a specific reaction kinetic F_i for every equation. The function F_i measures the net production of the species u_i and is a function of at most k unknowns and in real world applications F_i usually quantifies chemical reaction kinetics, therefore it is highly likely to be a non-linear function. In principle we aim to analyse a reaction-diffusion system of k equations with k unknowns. The usual appropriate type of boundary conditions for these models are the zero-flux (Homogeneous Neumann) boundary conditions (Avnir and Kagan, 1984; Hoveyda, Evans, and Fu, 1993). The initial conditions of such systems are usually assuming the existence of a bounded non-zero positive quantity (Yan et al., 2013; Chaplain, Ganesh, and Graham, 2001) denoted by u_i^0 of each of the unknown in Ω_t at $t = 0$. We assume the boundary of Ω_L and Ω_t to be Lipschitz continuous (Lakkis, Madzvamuse, and Venkataraman, 2013). We note that every point in Ω_t is time-dependent, which is related to the computational frame Ω_L through employing the mappings $\boldsymbol{\mathcal{X}}$ and $\boldsymbol{\mathcal{Y}}$ to maintain correspondence between these two domains. For notational convenience functions defined on Ω_L and those defined on Ω_t are denoted by the same letter with and without hats respectively. Therefore, we may introduce for every $u : \Omega_t \to \mathbb{R}$, its corresponding counterpart $\hat{u} : \Omega_L \to \mathbb{R}$. The relationship of u and $\hat{u}$ can be explicitly given by noting that $\hat{u} : \Omega_L \to \mathbb{R}, \quad \hat{u}(\boldsymbol{\xi},t) = u(\boldsymbol{\mathcal{X}}(\boldsymbol{\xi},t),t)$ and $u : \Omega_t \to \mathbb{R}, \quad u(\boldsymbol{x},t) = \hat{u}(\boldsymbol{\mathcal{Y}}(\boldsymbol{x},t),t)$.

The time derivative of u and $\hat{u}$ using the ALE frame will take the form of material derivatives with respect to the velocities $\boldsymbol{a}$ and $\boldsymbol{b}$ that arise in the consequence of time

differentiation of $\boldsymbol{\mathcal{X}}$ and $\boldsymbol{\mathcal{Y}}$, so we have

$$\begin{aligned}\frac{\partial u}{\partial t}(\boldsymbol{x},t) = \frac{\partial u}{\partial_2 t}(\boldsymbol{\mathcal{X}}(\boldsymbol{\xi},t),t) = \dot{\boldsymbol{\partial}}_{\boldsymbol{a}}\hat{u}(\boldsymbol{\xi},t) - \left[\mathbb{K}^T\nabla_{\boldsymbol{\xi}}\hat{u}\cdot\boldsymbol{a}\right](\boldsymbol{\mathcal{X}}(\boldsymbol{\xi},t),t) \qquad (\boldsymbol{\xi},t)\in\Omega_L\times[0,T],\\ \frac{\partial \hat{u}}{\partial t}(\boldsymbol{\xi},t) = \frac{\partial \hat{u}}{\partial_2 t}(\boldsymbol{\mathcal{Y}}(\boldsymbol{x},t),t) = \dot{\boldsymbol{\partial}}_{\boldsymbol{b}}u(\boldsymbol{x},t) - \left[\mathbb{J}^T\nabla_x u\cdot\boldsymbol{b}\right](\boldsymbol{\mathcal{Y}}(\boldsymbol{x},t),t) \qquad \boldsymbol{x}\in\Omega_t \quad t\in[0,T],\end{aligned} \tag{2.17}$$

where ∂_2 means the derivative with respect to the second argument t only and $\dot{\boldsymbol{\partial}}_{\boldsymbol{a}}\hat{u}(\boldsymbol{\xi},t)$ denotes the material derivative with respect of the velocity $\boldsymbol{a}$. The term $\nabla_x\cdot(vu_i)(\boldsymbol{x},t)$ can be easily transformed to the ALE frame by simply decomposing the derivative of the product and applying the transformation to both terms separately, so we have

$$\nabla_x\cdot(vu_i)(\boldsymbol{x},t) = \left[\nabla_x\cdot\boldsymbol{v}\right]u(\boldsymbol{x},t) + \left[\nabla_x u\cdot\boldsymbol{v}\right](\boldsymbol{x},t). \tag{2.18}$$

Both terms on the right-hand side of (2.18) will produce a tensor factor upon transforming, which is the inverse matrix of the Jacobian of their respective mappings. The first term on right-hand side transforms as

$$\begin{aligned}\left[\nabla_{\boldsymbol{\mathcal{X}}}\cdot\boldsymbol{v}\right]u(\boldsymbol{\mathcal{X}}(\boldsymbol{\xi},t),t) &= \left[\mathbb{Y}^T\nabla_{\boldsymbol{\xi}}\cdot\boldsymbol{v}\right]\hat{u}(\boldsymbol{\xi},t) \qquad (\boldsymbol{\xi},t)\in\Omega_L,\\ \left[\nabla_{\boldsymbol{\mathcal{Y}}}\cdot\boldsymbol{v}\right]\hat{u}(\boldsymbol{\mathcal{Y}}(\boldsymbol{x}),t) &= \left[\mathbb{X}^T\nabla_x\cdot\boldsymbol{v}\right]u(\boldsymbol{x},t), \qquad \boldsymbol{x}\in\Omega_t, \quad t\in[0,T].\end{aligned} \tag{2.19}$$

The second term from the right-hand side of (2.18) also transforms as

$$\begin{aligned}\left[\nabla_{\boldsymbol{\mathcal{X}}}u\cdot\boldsymbol{v}\right](\boldsymbol{\mathcal{X}}(\boldsymbol{\xi},t),t) &= \left[\mathbb{Y}^T\nabla_{\boldsymbol{\xi}}\hat{u}\cdot\boldsymbol{v}\right](\boldsymbol{\xi},t) \qquad (\boldsymbol{\xi},t)\in\Omega_L,\\ \left[\nabla_{\boldsymbol{\mathcal{Y}}}\hat{u}\cdot\boldsymbol{v}\right](\boldsymbol{\mathcal{Y}}(\boldsymbol{x}),t) &= \left[\mathbb{X}^T\nabla_x u\cdot\boldsymbol{v}\right](\boldsymbol{x},t) \qquad \boldsymbol{x}\in\Omega_t, \quad t\in[0,T].\end{aligned} \tag{2.20}$$

The Laplace operator namely $\nabla_x\cdot\nabla_x u(\boldsymbol{x},t)$ transforms as

$$\begin{aligned}\nabla_{\boldsymbol{\mathcal{X}}}\cdot\nabla_{\boldsymbol{\mathcal{X}}}u(\boldsymbol{\mathcal{X}}(\boldsymbol{\xi},t),t) &= \nabla_{\boldsymbol{\xi}}\cdot\left[\mathbb{Y}\mathbb{Y}^T\nabla_{\boldsymbol{\xi}}\hat{u}\right](\boldsymbol{\xi},t),\\ \nabla_{\boldsymbol{\mathcal{Y}}}\cdot\nabla_{\boldsymbol{\mathcal{Y}}}\hat{u}(\boldsymbol{\mathcal{Y}}(\boldsymbol{x},t),t) &= \nabla_x\cdot\left[\mathbb{X}\mathbb{X}^T\nabla_x u\right](\boldsymbol{x},t).\end{aligned} \tag{2.21}$$

Note that $\mathbb{X}$ and $\mathbb{Y}$ are both $d\times d$ matrices, whose entries are time-dependent with

d the number of spatial dimensions. We also write the Euler's formula for the time derivative of the determinants of the Jacobians of $\boldsymbol{\mathcal{X}}$ and $\boldsymbol{\mathcal{Y}}$ as

$$\begin{aligned} \frac{d\boldsymbol{J}}{dt}(\boldsymbol{\xi},t) &= \boldsymbol{J}\nabla_{\boldsymbol{\xi}}\cdot\boldsymbol{a}(\boldsymbol{\mathcal{X}}(\boldsymbol{\xi},t),t), \\ \frac{d\boldsymbol{K}}{dt}(\boldsymbol{x},t) &= \boldsymbol{K}\nabla_{x}\cdot\boldsymbol{b}(\boldsymbol{\mathcal{Y}}(\boldsymbol{x}),t). \end{aligned} \tag{2.22}$$

Now we are in a position to present the system (2.16) in the ALE frame both for functions that are defined on Ω_t and those defined on Ω_L. Two types of formulation is presented on the coordinates, namely the *conservative* and the *non-conservative* ALE formulations.

2.2.1 Non-conservative ALE formulation on reference frame

The *non-conservative* ALE formulation of the system (2.16) can be written by replacing the time derivative of u_i by its equivalent ALE representation given by (2.17). Therefore the *non-conservative* ALE formulation of (2.16) for functions defined on the coordinates $\boldsymbol{\xi}$ is

$$\dot{\boldsymbol{\partial}}_{\boldsymbol{a}}\hat{u}_i - \left[\mathbb{Y}^T\nabla_{\boldsymbol{\xi}}\hat{u}_i\cdot\boldsymbol{a}\right] + \left[\mathbb{Y}^T\nabla_{\boldsymbol{\xi}}\cdot\boldsymbol{v}\right]\hat{u}_i + \left[\mathbb{Y}^T\nabla_{\boldsymbol{\xi}}\hat{u}_i\cdot\boldsymbol{v}\right] - D_i\nabla_{\boldsymbol{\xi}}\cdot\left[\mathbb{Y}\mathbb{Y}^T\nabla_{\boldsymbol{\xi}}\hat{u}_i\right] - F_i(\hat{\boldsymbol{u}}) = 0 \tag{2.23}$$

with $\hat{u}_i = \hat{u}_i(\boldsymbol{\xi},t)$ and $(\boldsymbol{\xi},t)\in\Omega_L\times[0,T]$, and Ω_L is defined as the image of the time-dependent mapping $\boldsymbol{\mathcal{Y}}$ such that

$$\boldsymbol{\mathcal{Y}}:\Omega_t\to\Omega_L,\quad \boldsymbol{\mathcal{Y}}(\boldsymbol{x},t)=\boldsymbol{\xi},\quad \boldsymbol{x}\in\Omega_t,\quad t\in[0,T].$$

Rearranging the terms in (2.23) we obtain the non-conservative ALE formulation on Ω_L

$$\begin{cases} \dot{\boldsymbol{\partial}}_{\boldsymbol{a}}\hat{u}_i + \mathbb{Y}^T\nabla_{\xi}\hat{u}_i \cdot (\boldsymbol{v}-\boldsymbol{a}) - D_i\nabla_{\xi}\cdot\left[\mathbb{Y}\mathbb{Y}^T\nabla_{\xi}\hat{u}_i\right] + \left[\mathbb{Y}^T\nabla_{\xi}\cdot\boldsymbol{v}\right]\hat{u}_i - F_i(\hat{\boldsymbol{u}}) = 0, \\ \text{on} \quad \Omega_L\times[0,T], \qquad t>0, \\ (\boldsymbol{n}\cdot\mathbb{Y}^T\nabla_{\xi}\hat{u}_i)(\boldsymbol{\xi},t) = 0 \qquad \boldsymbol{\xi}\in\partial\Omega_L, \quad t\geq 0, \\ \hat{u}_i(\boldsymbol{\xi},0) = u_i^0(\boldsymbol{\xi}) \qquad \boldsymbol{\xi}\in\Omega_L, \quad t=0. \end{cases} \tag{2.24}$$

Note that the term containing $(\boldsymbol{v}-\boldsymbol{a})$ serves to contribute for the difference of the velocities of material movement and the deformation of the domain. It can be observed, where $\boldsymbol{a}$ is zero, which means that the domain does not evolves with time, note that upon substituting $\boldsymbol{a}=0$, in (2.24) the formulation returns the system (2.13) exactly as it was defined. However, upon considering $\boldsymbol{a}=\boldsymbol{v}$, we obtain the case where the domain deformation exactly coincides with the convection of the material, therefore, upon canceling the term with the velocity difference, we obtain a pure Lagrangian formulation. Note also that if we substitute for $\boldsymbol{v}=\boldsymbol{a}=0$, in the formulation (2.24), it returns a reaction-diffusion system on a stationary domain.

2.2.2 Non-conservative ALE formulation on evolving frame

We use similar substitution of the transformed terms to obtain the *non-conservative* formulation of the system (2.13) for functions that are defined on Ω_t. We write

$$\dot{\boldsymbol{\partial}}_{\boldsymbol{b}}u_i - \left[\mathbb{X}^T\nabla_x u_i\cdot\boldsymbol{b}\right] + \left[\mathbb{X}^T\nabla_x\cdot\boldsymbol{v}\right]u_i + \left[\mathbb{X}^T\nabla_x u_i\cdot\boldsymbol{v}\right] - D_i\nabla_x\cdot\left[\mathbb{X}\mathbb{X}^T\nabla_x u_i\right] - F_i(\boldsymbol{u}) = 0, \tag{2.25}$$

with $u_i = u_i(\boldsymbol{x},t)$ where $\boldsymbol{x}\in\Omega_t$ and $t\in[0,T]$. The domain of this formulation is the physically evolving frame, which we reconstruct through the introduction of the time-dependentmappings from Ω_L. Therefore, the evolving domain Ω_t is defined as

the image of the time-dependentset of mappings $\boldsymbol{\mathcal{X}}$ such that

$$\boldsymbol{\mathcal{X}} : \Omega_L \to \Omega_t, \qquad \boldsymbol{\mathcal{X}}(\boldsymbol{\xi}, t) = \boldsymbol{x}, \qquad \boldsymbol{\xi} \in \Omega_L, \quad t \in [0, T]$$

Rearranging (2.25) leads to obtain the *non-conservative* ALE formulation of the system (2.13) for functions defined on Ω_t as

$$\begin{cases} \dot{\boldsymbol{\partial}}_{\boldsymbol{b}} u_i + \mathbb{X}^T \nabla_x u_i \cdot (\boldsymbol{v} - \boldsymbol{b}) - D_i \nabla_x \cdot [\mathbb{X}\mathbb{X}^T \nabla_x u_i] + [\mathbb{X}^T \nabla_x \cdot \boldsymbol{v}] u_i - F_i(\boldsymbol{u}) = \quad 0, \text{ on } \Omega_t, \\ \begin{cases} (\boldsymbol{n} \cdot \mathbb{X}^T \nabla_x u_i)(\boldsymbol{x}, t) = 0 \qquad \boldsymbol{x} \in \Omega_t, \qquad t \in [0, T], \\ u_i(\boldsymbol{x}, 0) = u_i^0(\boldsymbol{x}) \qquad \boldsymbol{x} \in \Omega_t, \qquad t = 0. \end{cases} \end{cases} \tag{2.26}$$

2.2.3 Conservative ALE formulation on reference frame

For *conservative* ALE formulation note that due to the importance of conservation properties of u_i or $\hat{u}_i$ we have to take the Jacobians of the mappings into account when we write the transformed representation. Taking the conservation properties of u_i (Sarrate, Huerta, and Donea, 2001; Nobile and Formaggia, 1999) during transformation from Ω_t to Ω_L is written as

$$\int_{\Omega_t} u(\boldsymbol{x}, t) d\Omega_t = \int_{\Omega_L} \hat{u}(\boldsymbol{\mathcal{Y}}(\boldsymbol{x}, t), t) \boldsymbol{K} d\Omega_L = \int_{\Omega_L} \hat{u}(\boldsymbol{\xi}, t) \boldsymbol{K} d\Omega_L. \tag{2.27}$$

Taking the time derivative of (2.27) yields

$$\frac{d}{dt} \int_{\Omega_t} u(\boldsymbol{x}, t) d\Omega_t = \int_{\Omega_L} \frac{\partial}{\partial t} \left(\hat{u}\boldsymbol{K}\right)(\boldsymbol{\xi}, t) d\Omega_L. \tag{2.28}$$

Applying the product rule to differentiate the right-hand side of (2.28) results in

$$\int_{\Omega_L} \frac{\partial}{\partial t} \left(\hat{u}\boldsymbol{K}\right)(\boldsymbol{\xi}, t) d\Omega_L = \int_{\Omega_L} \left[\boldsymbol{K} \frac{\partial \hat{u}}{\partial t}(\boldsymbol{\xi}, t) + \hat{u} \frac{\partial \boldsymbol{K}}{\partial t}(\boldsymbol{\xi}, t)\right](\boldsymbol{\xi}, t) d\Omega_L. \tag{2.29}$$

Substituting (2.22) in (2.29) we obtain

$$\int_{\Omega_L} \frac{\partial}{\partial t}(\hat{u}\boldsymbol{K})(\boldsymbol{\xi},t)d\Omega_L = \int_{\Omega_L} \boldsymbol{K}\Big[\frac{\partial \hat{u}}{\partial t}(\boldsymbol{\xi},t) + \hat{u}\mathbb{Y}^T\nabla_{\xi}\cdot\boldsymbol{b}\Big](\boldsymbol{\xi},t)d\Omega_L. \tag{2.30}$$

Therefore, we can write

$$\frac{\partial \hat{u}}{\partial t}(\boldsymbol{\xi},t) = \frac{1}{\boldsymbol{K}}\frac{\partial}{\partial t}(\hat{u}\boldsymbol{K})(\boldsymbol{\xi},t) - \hat{u}\mathbb{Y}^T\nabla_{\xi}\cdot\boldsymbol{b}(\boldsymbol{\xi},t) \tag{2.31}$$

Substituting the conservative description in (2.13), replacing by the appropriate transformed terms and rearranging we obtain the *conservative* ALE formulation defined on Ω_L as

$$\begin{cases} \frac{1}{K}\frac{\partial}{\partial t}(\hat{u}_i\boldsymbol{K}) + \mathbb{Y}^T\nabla_{\xi}\cdot\Big[(\boldsymbol{v}-\boldsymbol{b})\hat{u}_i - D_i\mathbb{Y}^T\nabla_{\xi}\hat{u}_i\Big] - F_i(\hat{\boldsymbol{u}}) = 0, \quad \text{on } \Omega_L\times[0,T], \\ \begin{cases} (\boldsymbol{n}\cdot\mathbb{Y}^T\nabla_{\xi}\hat{u}_i)(\boldsymbol{\xi},t) = 0, \quad \boldsymbol{\xi}\in\Omega_L, \quad t\geq 0, \\ \hat{u}_i(\boldsymbol{\xi},0) = \hat{u}_i^0(\boldsymbol{\xi}), \qquad \boldsymbol{\xi}\in\Omega_L, \quad t=0. \end{cases} \end{cases} \tag{2.32}$$

2.2.4 Conservative ALE formulation on evolving frame

Using a similar approach we may derive the ALE conservative formulation also for functions defined on Ω_t in the form of

$$\begin{cases} \frac{1}{J}\frac{\partial}{\partial t}(u_i\boldsymbol{J}) + \mathbb{X}^T\nabla_x\cdot\Big[(\boldsymbol{v}-\boldsymbol{a})u_i - D_i\mathbb{X}^T\nabla_x u_i\Big] - F_i(\boldsymbol{u}) = 0, \text{ on } \Omega_t \\ \begin{cases} (\boldsymbol{n}\cdot\mathbb{X}^T u_i)(\boldsymbol{x},t) = 0, \qquad \boldsymbol{x}\in\partial\Omega_t, \quad t\geq 0, \\ u_i(\boldsymbol{x},t) = u_i^0(\boldsymbol{x}), \quad \boldsymbol{x}\in\Omega_t \quad \text{at } t=0. \end{cases} \end{cases} \tag{2.33}$$

2.3 Conclusion

Using conservation of mass and Fick's law of diffusion a mathematical derivation of RDSs from the first principle on a continuously evolving domain is presented. ALE transformation of convection-dominated RDSs on time-dependent domains helps to

efficiently deal with the type of velocities where, pure Lagrangian formulation or pure Eulerian formulation result in a relatively poor approximation of the contribution from the domain or material movement. Pure Lagrangian approach is usually subject to a drawback when the material advection is substantially different from the velocity of domain deformation. Therefore, a pure Lagrangian approach does not suffice to include the contribution due to the difference of material velocity and that of the domain deformation. Similarly in the case of a purely Eulerian approach the assumption to fix the domain and only consider the deformation of the material within a static frame, which offers no consideration to contribution caused by the domain movement with respect to the material velocity. Both approaches maybe subject to significant drawbacks when considered alone for a domain that evolves with time as well as the material changing position within the domain. The ALE formulation of RDSs on evolving domains is provided as a computational frame to be able to solve a system of RDSs on a reference frame and yet be able to analyse and explore the behaviour of it on growing domains through employing the time-dependent mappings. The computational challenges associated to the numerical implementation of schemes on evolving domains is much more laborious and complicated (Baines, 1994; Larson and Bengzon, 2013; Huang and Russell, 2010) compared to exploring the same system on a reference frame through a set of continuous time-dependent mappings that sustain a one to one correspondence between the computational frame and the physically evolving frame. Since the remaining chapters of the thesis are motivated to explore the dynamical behaviour and the bifurcation analysis with influence from domain-size, therefore, for the remaining of the chapters we focus to explore RDSs from the perspective of a dynamical system on stationary regular geometries on which closed-form harmonic analysis is tractable. Next chapter is devoted to a detailed study of bifurcation analysis and parameter classification of a particular RDS of *activator-depleted* class on a standard rectangular domain.

Chapter 3

Analysis on rectangular geometries

This chapter explores bifurcation analysis and the classification of parameter spaces for reaction-diffusion systems of two chemical species on stationary rectangular domains. The contents of this chapter with its full entirety is contained in (Sarfaraz and Madzvamuse, 2017), which is already published at the time of writing this thesis. The dynamics of the system are explored both in the absence and presence of diffusion. The parameter space is fully classified in terms of the types and stability of the uniform steady state. In the absence of diffusion the results on the classification of parameter space are supported by simulations of the corresponding vector-field and some trajectories of the phase-plane around the uniform steady state. In the presence of diffusion, the main findings are the quantitative analysis relating the domain-size with the reaction and diffusion rates and their corresponding influence on the dynamics of the reaction-diffusion system when perturbed in the neighbourhood of the uniform steady state. Theoretical predictions are supported by numerical simulations both in the presence as well as in the absence of diffusion. Conditions on the domain-size with respect to the diffusion and reaction rates are related to the types of diffusion-driven instabilities namely Turing, Hopf and Transcritical types of bifurcations. The first condition is a lower bound on the area of a rectangular domain in terms of the diffusion and reaction rates, which is necessary for Hopf and Transcritical bifurcation to occur. The second condition is an upper bound on the area of domain in terms of reaction-diffusion rates that restricts the diffusion-driven instability to Turing type

behavior, whilst forbidding the existence of Hopf and Transcritical bifurcation. Theoretical findings are verified by the finite element solution of the coupled system on a two dimensional rectangular domain.

3.1 Model equations and absence of diffusion case

The dynamics of two chemical species u and v in a coupled system of non-linear parabolic equations is considered. Both species diffuse with independent rates and satisfy the well-known *activator-depleted* reaction-diffusion system in a closed two-dimensional rectangular domain denoted by $\Omega = [0, L_x] \times [0, L_y] \subset \mathbb{R}^2$ with area $L_x \times L_y$, where L_x and L_y are the corresponding side lengths in the direction of x and y axes respectively. The domain Ω is considered static (which implies $\boldsymbol{a} = 0$ in Chapter 2 derivation) and species are assumed to move purely due to reaction and diffusion, therefore, the model is formulated with no material convection (this implies $\boldsymbol{v} = 0$ in Chapter 2 derivation). The reaction-diffusion system satisfying the *activator-depleted* model for u and v in its non-dimensional form (Schnakenberg, 1979; Murray, 2001) reads as

$$\begin{cases} \frac{\partial u}{\partial t} = & \Delta u + \gamma(\alpha - u + u^2 v), \\ \frac{\partial v}{\partial t} = & d\Delta v + \gamma(\beta - u^2 v), \end{cases} \tag{3.1}$$

where d, γ, α and β are non-dimensional positive constants. In (3.1) the non-dimensional parameter d denotes the quantity $\frac{D_v}{D_u}$, where D_u is the diffusion rate of the variable u and D_v is the diffusion rate of the variable v. The non-dimensional parameter γ denotes the reaction rate, which is also known as the scaling parameter for the reaction kinetics. The boundary $\partial\Omega$ is subject to zero flux condition, which means on $\partial\Omega$ the chemical species u and v satisfy homogeneous Neumann boundary conditions in the form

$$\frac{\partial u}{\partial \boldsymbol{n}} = \frac{\partial v}{\partial \boldsymbol{n}} = 0, \qquad \text{on} \quad (x, y) \in \partial\Omega, \quad t \geq 0, \tag{3.2}$$

where $\boldsymbol{n}$ denotes the outward normal through $\partial\Omega$. For initial conditions the existence of some strictly positive quantity from each of these chemical concentrations is assumed present, which is written as

$$u(x,y,0) = u_0(x,y), \qquad v(x,y,0) = v_0(x,y), \qquad (x,y) \in \Omega, \quad t = 0. \tag{3.3}$$

3.1.1 Remark

Despite the fact that all the results obtained in this paper hold for general rectangular geometries of Ω i.e. with possibilities $L_x \neq L_y$, however for simplicity in the analysis Ω is considered as a square, which means $L_x = L_y$. The results can be readily extended to a rectangular case by taking the area of Ω as L^2, where $L = \max\{L_x, L_y\}$.

3.1.2 Stability analysis in the absence of diffusion

In the absence of diffusion system (3.1) takes the form of a set of ordinary differential equations of the form

$$\begin{cases} \frac{du}{dt} = & \gamma(\alpha - u + u^2 v) = \gamma f(u,v), \\ \frac{dv}{dt} = & \gamma(\beta - u^2 v) = \gamma g(u,v). \end{cases} \tag{3.4}$$

To analyse the stability of system (3.4), it is necessary to compute its uniform steady state solution. Let (u_s, v_s) denote the uniform steady state solution of the system (3.4), then (u_s, v_s) must simultaneously satisfy the system of non-linear algebraic equations in the form

$$f(u_s,v_s) = \alpha - u_s + u_s^2 v_s = 0, \qquad g(u_s,v_s) = \beta - u_s^2 v_s = 0. \tag{3.5}$$

The non-linear algebraic system (3.5) admits a unique solution in the form $(u_s, v_s) = \left(\alpha + \beta, \frac{\beta}{(\alpha+\beta)^2}\right)$, which enforces a restriction on the parameters of the system such

that $\alpha + \beta \neq 0$. Since both of these parameters resemble physical quantities, therefore, strictly positive, an appropriate interpretation of this restriction is that they both simultaneously cannot become zero. The stability of system (3.4) is analysed by computing the Jacobian matrix (Murray, 2001) of (3.5) and conducting the stability analysis using the uniform steady state solution (u_s, v_s), hence

$$\boldsymbol{J}|_{(u_s,v_s)} = \gamma \begin{bmatrix} \frac{\partial f}{\partial u} & \frac{\partial f}{\partial v} \\ \frac{\partial g}{\partial u} & \frac{\partial g}{\partial v} \end{bmatrix}_{(u_s,v_s)} = \gamma \begin{bmatrix} 2uv - 1 & u^2 \\ -2uv & -u^2 \end{bmatrix}_{(u_s,v_s)}.$$

Substituting the expressions in terms of α and β for (u_s, v_s) in $\boldsymbol{J}$ the matrix becomes

$$\boldsymbol{J}|_{(u_s,v_s)} = \gamma \begin{bmatrix} \frac{\beta-\alpha}{\alpha+\beta} & (\beta+\alpha)^2 \\ -\frac{2\beta}{\beta+\alpha} & -(\beta+\alpha)^2 \end{bmatrix},$$

which is called the stability matrix (Murray, 2001; Edelstein-Keshet, 1988; Perko, 2013) for system (3.5). Let

$$T(\alpha,\beta) = \gamma\Big(\frac{\beta - \alpha - (\beta+\alpha)^3}{\beta+\alpha}\Big) \quad \text{and} \quad D(\alpha,\beta) = \gamma^2(\alpha+\beta)^2.$$

denote the trace and determinant of $\boldsymbol{J}$ respectively, then the characteristic polynomial for the eigenvalues $\lambda_{1,2}$ of $\boldsymbol{J}$ in terms of $T(\alpha,\beta)$ and $D(\alpha,\beta)$ takes the form

$$\lambda^2 - T(\alpha,\beta)\lambda + D(\alpha,\beta) = 0.$$

Hence, the two roots of this characteristic polynomial in terms of $T(\alpha,\beta)$ and $D(\alpha,\beta)$ are given by

$$\lambda_{1,2} = \frac{1}{2}T(\alpha,\beta) \pm \frac{1}{2}\sqrt{T^2(\alpha,\beta) - 4D(\alpha,\beta)}. \tag{3.6}$$

Expression (3.6) for the eigenvalues is studied through investigating the domain of T and D, which is the positive real cartesian plane $(\alpha,\beta) \in \mathbb{R}^2_+$. The classification that would cause the uniform steady state (u_s, v_s) to change stability and type due to the

selection of the choice of the parameter values (α, β) is explored by examining the sign of the real part (Murray, 2001; Edelstein-Keshet, 1988; Iron, Wei, and Winter, 2004) of $\lambda_{1,2}$. For example the parameter space that makes the uniform steady state (u_s, v_s) stable, is the simultaneous combined choice of $\alpha, \beta \in \mathbb{R}_+$ that ensures the real part of the eigenvalues to be negative, which in turn is related to the discriminant of the roots expressed by (3.6). The full parameter space is investigated, so that all the possible types of influences due to the choice of parameters α and β on the stability and types of the uniform steady state (u_s, v_s) are encapsulated. The classification is conducted based on $\lambda_{1,2}$ to be a complex conjugate in the first case, then in the second case the parameter space is analysed when $\lambda_{1,2}$ are real roots. In each case, the space is further classified into stable and unstable regions. In addition to this the partitioning curves, on which the steady state (u_s, v_s) changes its type, are studied using a numerical technique that is employed exclusively and for the first time in the context of the present topic.

3.1.3 Analysis for the case of complex eigenvalues

It is clear that the eigenvalues are a complex conjugate pair if and only if the discriminant is negative, which means the parameters (α, β) must satisfy the inequality

$$T^2(\alpha, \beta) - 4D(\alpha, \beta) = \gamma^2 \Big(\frac{\beta - \alpha - (\beta + \alpha)^3}{\beta + \alpha} \Big)^2 - 4\gamma^2 (\beta + \alpha)^2 < 0. \tag{3.7}$$

In order to find what region is satisfied by (3.7), we must find the critical curves on which the expression on the left of (3.7) is equal to zero, which means that the discriminant changes sign by moving accross these curves in the plane $(\alpha, \beta) \in \mathbb{R}^2_+$. These curves can be found by solving the equation $T^2(\alpha, \beta) - 4D(\alpha, \beta) = 0$ if and only if

$$\gamma^2 \Big(\frac{\beta - \alpha - (\beta + \alpha)^3}{\beta + \alpha} \Big)^2 - 4\gamma^2 (\beta + \alpha)^2 = 0. \tag{3.8}$$

Solving (3.8) implies finding the implicit curves that represent the critical region on the $(\alpha, \beta) \in \mathbb{R}_+$ plane, for which the discriminant in the expression for $\lambda_{1,2}$ is zero. The solution to (3.8) provides the boundaries, for the region of the plane that results in $\lambda_{1,2}$ to be a complex conjugate pair. The choice of (α, β) on the curves satisfying (3.8) enforces the eigenvalues of the system to be repeated real values, therefore, on these curves the steady state (u_s, v_s) becomes a star node, whose stability will be analysed in the Section 3.1.5 with real eigenvalues. The left hand-side of (3.8) can be factorised in the form $\phi(\alpha, \beta)\psi(\alpha, \beta)$, which provides the equations of the two implicit curves $\phi(\alpha, \beta) = 0$ and $\psi(\alpha, \beta) = 0$ that determine the boundaries of the region corresponding to complex eigenvalues $\lambda_{1,2}$, where ϕ and ψ are respectively given by

$$\begin{cases} \phi(\alpha, \beta) = \beta - \alpha - (\beta + \alpha)^3 - 2(\beta + \alpha)^2, \\ \psi(\alpha, \beta) = \beta - \alpha - (\beta + \alpha)^3 + 2(\beta + \alpha)^2. \end{cases} \tag{3.9}$$

A mesh is constructed on a square domain $D = [0, \alpha_{max}] \times [0, \beta_{max}]$, which is discretised by N points in both directions of α and β, where N is a positive integer. This constructs a square mesh of $(N-1) \times (N-1)$ cells, each of size $\frac{\alpha_{max}}{N-1} \times \frac{\beta_{max}}{N-1}$, with N^2 points in D. To find the implicit solution for (3.9), at every mesh point in the direction α, the roots of the cubic polynomial in β namely $\phi(\alpha_i, \beta) = 0$, denoted by $\phi_i(\beta) = 0$ are computed using the Matlab command '*roots*'. It is worth noting that for every fixed α_i, one obtains $\phi_i(\beta)$, to be a cubic polynomial (of degree 3) in β of the form

$$\phi_i(\beta) = C_0^i + C_1^i\beta + C_2^i\beta^2 + C_3^i\beta^3,$$

where the coefficients are given by $C_0^i = -\alpha_i - \alpha_i^3 - 2\alpha_i^2$, $C_1^i = 1 - 4\alpha_i - 3\alpha_i^2$, $C_2^i = -3\alpha_i - 2$, and $C_3^i = -1$. Similarly for each i in the direction of α, there are N cubic polynomials in β satisfying $\psi_i(\beta) = 0$, with ψ_i of the form

$$\psi_i(\beta) = C_0^i + C_1^i\beta + C_2^i\beta^2 + C_3^i\beta^3,$$

where $C_0^i = -\alpha_i - \alpha_i^3 + 2\alpha_i^2$, $C_1^i = 1 + 4\alpha_i - 3\alpha_i^2$, $C_2^i = -3\alpha_i + 2$, and $C_3^i = -1$. Each of the equations $\phi_i(\beta) = 0$ and $\psi_i(\beta) = 0$ have at most three roots (Milewski, 2001) namely $(\beta_1, \beta_2, \beta_3)$ for every fixed α_i, which means for every fixed α_i the three points namely (α_i, β_j) for $j = 1, 2, 3$ are the three points that lie on the implicit curve given by (3.9). Since (α, β) are positive real parameters in the system, therefore, at every fixed α_i, only the positive real roots β_j are considered and any root that is either real negative or complex is ignored.

Solving (3.8) alone serves to determine the boundaries of the complex region, but does not tell us, which side of these implicit curves correspond to real eigenvalues and which side corresponds to complex eigenvalues. This can be decided, by finding another curve on which the eigenvalues are purely imaginary with zero real parts. Since the real part of the eigenvalues is given by $\frac{1}{2}T(\alpha, \beta)$ and the determinant $D(\alpha, \beta) = (\alpha + \beta)^2$ is strictly positive, therefore, the choice of (α, β) that solves the equation

$$T(\alpha, \beta) = 0 \qquad \Longleftrightarrow \qquad \frac{\beta - \alpha - (\beta + \alpha)^3}{\beta + \alpha} = 0, \tag{3.10}$$

will ensure that the eigenvalues of the system are purely imaginary. Solving (3.10) is equivalent to finding the set of $(\alpha, \beta) \in \mathbb{R}_+$ such that the equation $h(\alpha, \beta) = 0$ is true, where h is given by

$$h_i(\beta) = C_0^i + C_2^i\beta + C_2^i\beta^2 + C_3^i\beta^3,$$

with coefficients $C_0^i = -\alpha_i - \alpha_i^3$, $C_1^i = 1 - \alpha_i^2$, $C_2^i = -3\alpha_i$, and $C_3^i = -1$. The curve satisfying equation (3.10) forms the boundary for the positive and negative real parts of the eigenvalues $\lambda_{1,2}$ when they are complex conjugate pair, because on $h_i(\beta) = 0$ the real part of the eigenvalues are zero and hence changes the sign by moving across it. The positive real combination of (α, β) that satisfies (3.10) is given by the red $c2$ curve in Figure 3.1. The location of the $c2$ curve also indicates that the region between the curves $c1$ and $c3$ results in that $\lambda_{1,2}$ are complex numbers. If (α, β) are chosen from values on curves $c1$ and $c3$, then the eigenvalues will be repeated real roots, since on these curves the discriminant is zero. However if (α, β) are chosen

from the values on the curve $c3$ then the eigenvalues are purely imaginary of the form $\lambda_{1,2} = \pm i\sqrt{4D(\alpha,\beta)} = \pm i2(\alpha+\beta)$. This implies that the steady state (u_s, v_s) is a centre with the system exhibiting periodic oscillations around the uniform steady state. It is worth noting that $h_i(\beta) = 0$ is a sufficient condition for (u_s, v_s) to be a centre, due to the strictly positive expression for $D(\alpha,\beta) = (\alpha+\beta)^2$ in the discriminant. Figure 3.1, was simulated for $\alpha_{max} = \beta_{max} = 5$ and $N = 5000$, which means the curve $c1$, $c2$ and $c3$ are respectively formed from the positive real roots of 5000 cubic polynomials of $\psi_i(\beta) = 0$, $h_i(\beta) = 0$ and $\phi_i(\beta) = 0$ for $i = 1, ..., 5000$. The curves $c1$ and $c3$ in Figure 3.1 (a) are the critical boundaries, at which the type of the steady state (u_s, v_s) changes from node to a spiral or vice versa, depending on whether one enters or exists the region between $c1$ and $c3$. The real part of $\lambda_{1,2}$ is studied to find the stability classification of the parameter space, when $\lambda_{1,2}$ are complex conjugate pair. Knowing that the region bounded by $c1$ and $c3$ curves in Figure 3.1 (a) results in $\lambda_{1,2}$ to be complex, the next step is to find which part of this region corresponds to positive real part of the complex numbers $\lambda_{1,2}$, and which part of this region corresponds to negative real part of $\lambda_{1,2}$. In order to determine their stability we must analyse the real part of $\lambda_{1,2}$, simultaneously with the assumption that the roots are a pair of complex conjugate numbers, which is given by

$$T(\alpha,\beta) = \frac{\beta - \alpha - (\beta+\alpha)^3}{\beta+\alpha}. \tag{3.11}$$

If the sign of (3.11) is negative in the region between the curves $c1$ and $c3$ in Figure 3.1 (a), then (u_s, v_s) is a stable spiral, if it is positive then it is an unstable spiral. This means that the steady state (u_s, v_s) is a stable spiral if (α,β) simultaneously satisfy (3.7) and the inequality $\beta - \alpha < (\alpha+\beta)^3$ holds, which corresponds to the green region A shown in Figure 3.1 (b). Similarly, the steady state (u_s, v_s) is an unstable spiral if parameters (α,β) simultaneously satisfy (3.7) and the inequality $\beta - \alpha > (\alpha+\beta)^3$, which is the yellow region B shown in Figure 3.1 (b). It is worth noting that the trace $T(\alpha,\beta)$ for positive values of α and β is bounded by the value of 1 (Sarfaraz and Madzvamuse,

2017), which means $\frac{\beta-\alpha-(\alpha+\beta)^3}{\beta+\alpha} \leq 1$ for all $\alpha, \beta \in \mathbb{R}_+$.

3.1.4 Numerical demonstration of complex eigenvalues

The numerical package for ordinary differential equations *ode45* in MATLAB was employed to simulate and visualise the local behaviour of the system (3.4) near the uniform steady state (u_s, v_s). Each simulation was run up to a final time $T = 5$, starting at the initial time $T = 0$, with time step $\tau = 5 \times 10^{-2}$. Parameter values were chosen from the regions A, B and on the curve $c2$ from Figure 3.1 (b) and plotted with 8 trajectories around the uniform steady state (u_s, v_s). Figure 3.2 shows that the behaviour of the trajectories around the uniform steady state in each case is in agreement with the theoretically predicted type of (u_s, v_s). The summary of the chosen numerical values for these simulations are all summarised in Table 3.1 on Page 50 and these are also indicated in the relevant captions for each figure. The eigenvalues of the stability matrix for each choice of the parameters and at the corresponding uniform steady state are presented in the corresponding captions. In each simulation the vertical axis corresponds to the variable v and the horizontal axis corresponds to the variable u. The red trajectories show the interactive behaviour of u and v in relation to the corresponding steady state. The physical interpretation of this classification is that, whenever the choice of α and β is taken from region B in Figure 3.1 then the dynamics of the perturbed system near the constant steady state (u_s, v_s) will spirally move away as time grows, which resembles the shape of an outward spreading spiral. This behaviour is shown in Figure 3.2 (b). However if the parameter values are chosen from region A then the dynamics of the perturbed system will spirally move in towards the constant stable steady state (u_s, v_s), therefore, any trajectory near the steady state forms the shape of spiral that is uniformly moving towards its centre, which is the constant steady state namely the point (u_s, v_s). This behaviour is shown in Figure 3.2 (a). If the values of the parameters are chosen from those on the curve c_2, then the dynamics of the system behaves in such a way that it neither goes away from the steady state, and nor does it reach the steady state, instead the trajectories of the system move on fixed

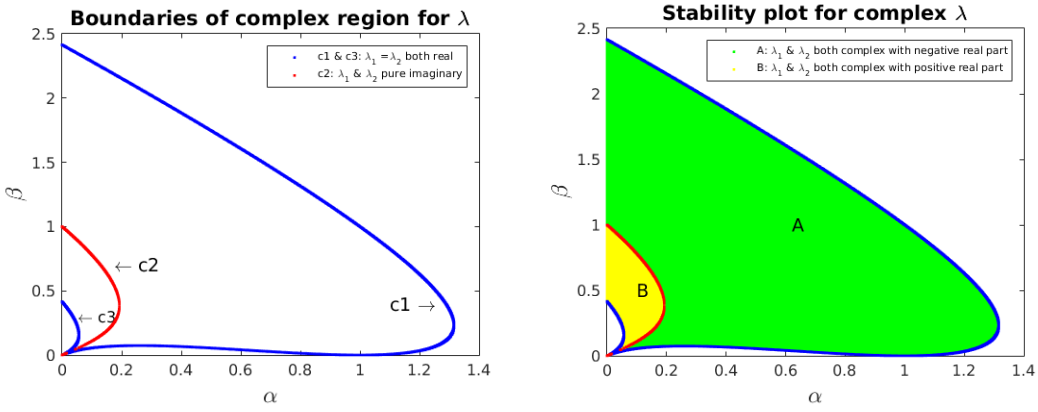

(a) (b)

FIGURE 3.1: In (a) the choice for α and β on curves $c1$ and $c3$ makes (u_s, v_s) to be star node, whereas α and β on the curve $c2$ make (u_s, v_s) to be a centre with periodic oscillations. In (b) the choice for α and β in the green region A results in (u_s, v_s) to be a stable spiral, whereas α and β from the yellow region B results in (u_s, v_s) being an unstable spiral.

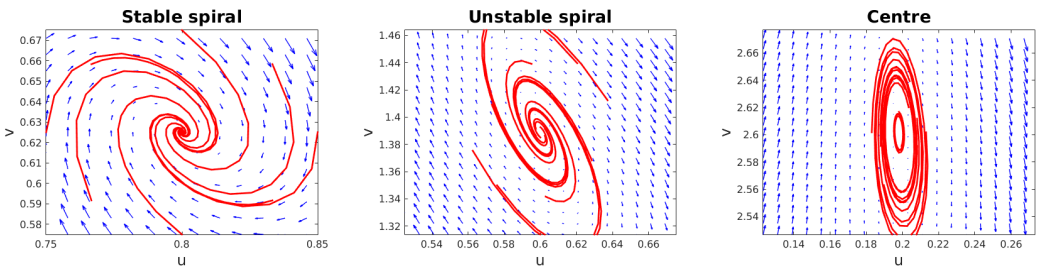

(a) (b) (c)

FIGURE 3.2: In (a) parameters $(\alpha, \beta) = (0.4, 0.4)$, resulting in the uniform steady state $(u_s, v_s) = (0.8, 0.625)$ and eigenvalues $\lambda_{1,2} = -0.32 \pm 0.73i$. In (b) parameters $(\alpha, \beta) = (0.1, 0.5)$, resulting in the uniform steady state $(u_s, v_s) = (0.6, 1.39)$ and eigenvalues $\lambda_{1,2} = 0.15 \pm 0.58i$. In (c) parameters $(\alpha, \beta) = (0.096, 0.102)$, resulting in the uniform steady state $(u_s, v_s) = (0.198, 2.6)$ and eigenvalues $\lambda_{1,2} = \pm 0.20i$ with $i = \sqrt{-1}$.

orbits around the uniform steady state (u_s, v_s), forming either circles or ellipse. This behaviour of u and v is shown in Figure 3.2 (c).

3.1.5 Analysis for the case of real eigenvalues

When both eigenvalues of the system are real numbers at the steady state (u_s, v_s) then the uniform steady state becomes a node. If $\lambda_{1,2}$ is a positive repeated root, then the steady state is an unstable star node. If $\lambda_{1,2}$ is a negative repeated root, then the steady state is a stable star node. Parameter space resulting in (u_s, v_s) to be a node can be analysed through studying the sign of $\lambda_{1,2}$, when both eigenvalues are real. This consequently means that the discriminant has to satisfy the inequality

$$T^2(\alpha,\beta) - 4D(\alpha,\beta) = \left(\frac{\beta-\alpha-(\beta+\alpha)^3}{\beta+\alpha}\right)^2 - 4(\beta+\alpha)^2 \geq 0. \tag{3.12}$$

Similarly, to the previous section, treating the equal case of (3.12) first will provide the boundaries between the real and complex regions for $\lambda_{1,2}$. These are $c1$ and $c3$ curves in Figure 3.1 from the previous section. On $c1$ and $c3$ it was concluded that $\lambda_{1,2}$ are repeated real roots, which are precisely $\lambda_{1,2} = \frac{1}{2}\left(\frac{\beta-\alpha-(\beta+\alpha)^3}{\beta+\alpha}\right)$. In order to determine the stability of (u_s, v_s), when (α, β) are on $c1$ and $c3$ blue curves in Figure 3.1, it is required to find the classification of this curve on which the sign of the repeated eigenvalue $\lambda_{1,2}$ is positive or negative. The steady state (u_s, v_s) is a star, if $\lambda_{1,2}$ is repeated real values, which means that the discriminant must be zero

$$T^2(\alpha,\beta) - 4D(\alpha,\beta) = \left(\frac{\beta-\alpha-(\beta+\alpha)^3}{\beta+\alpha}\right)^2 - 4(\beta+\alpha)^2 = 0. \tag{3.13}$$

The steady state (u_s, v_s) is a stable star if the choice of parameters (α, β) simultaneously satisfy (3.13) and the inequality $\beta - \alpha < (\alpha+\beta)^3$, which is the $c1$ curve in Figure 3.3 (a) in blue colour. The steady state (u_s, v_s) is unstable star if the choice of parameters (α, β) simultaneously satisfy (3.13) and the inequality $\beta - \alpha > (\alpha+\beta)^3$, which is the $c2$ curve in Figure 3.3 (a) in red colour.

The remaining region outside $c1$ and $c2$ curves in Figure 3.3 (a) can be classified into two parts, one where (α, β) satisfy (3.12) and yet both $\lambda_{1,2}$ are distinct negative real values. This means that (α, β) must satisfy the inequality

$$\lambda_{1,2} = \frac{1}{2}\frac{\beta - \alpha - (\beta + \alpha)^3}{\beta + \alpha} \pm \sqrt{\Big(\frac{\beta - \alpha - (\beta + \alpha)^3}{\beta + \alpha}\Big)^2 - 4(\beta + \alpha)^2} < 0,$$

such that both eigenvalues are negative real. This is true if (α, β) satisfy the inequality

$$\frac{1}{2}\frac{\beta - \alpha - (\beta + \alpha)^3}{\beta + \alpha} + \sqrt{\Big(\frac{\beta - \alpha - (\beta + \alpha)^3}{\beta + \alpha}\Big)^2 - 4(\beta + \alpha)^2} < 0. \tag{3.14}$$

The region in the $(\alpha, \beta) \in \mathbb{R}_+$ plane satisfying (3.14) is denoted by A in Figure 3.3 (b) shaded in green colour. The remaining region to analyse is the region outside the $c2$ curve in Figure 3.3 (a). Any combination of (α, β) from this region corresponds to the remaining 2 cases, in which either one of λ_1 or λ_2 is positive, causing (u_s, v_s) to be a saddle point which is unstable by definition. The other case is if $\lambda_{1,2}$ are both positive real values, which makes (u_s, v_s) to be an unstable node. The region satisfying the criteria for a saddle point or unstable node is indicated by B in Figure 3.3 (b) in yellow colour. It is worth noting that the steady state (u_s, v_s) with either one or both positive real eigenvalues is by definition a saddle point or an unstable node, respectively. Under the current classification these both types fall under one category namely unstable node. The fact that one of the eigenvalues is real positive, hence as time grows very large, the behaviour of the solution is similar to that of an unstable node.

3.1.6 Numerical demonstration for the case of real eigenvalues

The system (3.4) is numerically simulated using *ode45* package in MATLAB to visualise the behaviour of trajectories in the neighbourhood of (u_s, v_s), when $\lambda_{1,2}$ are real values. The final time and time steps are chosen exactly the same as for complex eigenvalues case in the previous section. Each simulation is tested on phase plane diagram, to observe the trajectories of solution. In each case the steady state (u_s, v_s) is computed

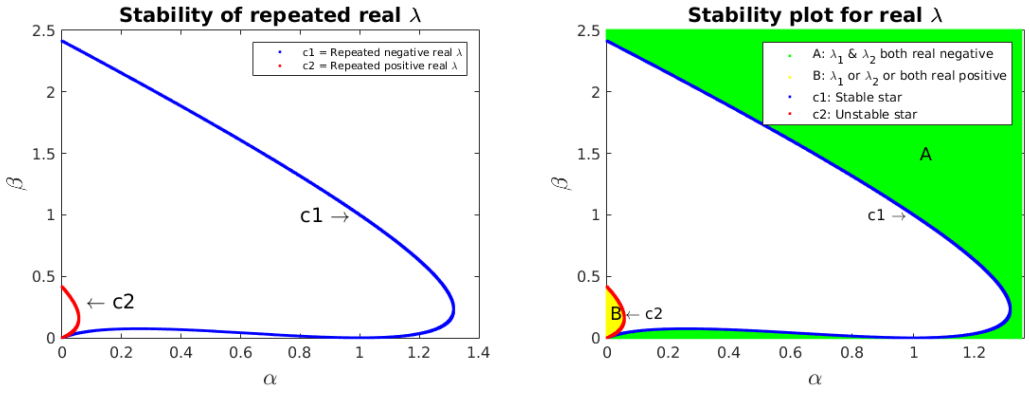

(a) (b)

FIGURE 3.3: In (a) the combination of (α, β) from $c1$, $c2$ (blue and red curves) results in (u_s, v_s) being an unstable star and a stable star respectively, which are both of type node. In (b) the combination of (α, β) from the yellow B and green A regions results in (u_s, v_s) being an unstable and a stable node respectively.

and 8 trajectories around the steady state whose behaviour is governed by the relevant vector-field are plotted. If the values of α and β are selected from those on the curves c_1 or c_3 then the dynamics of the perturbed system will either radially move away or towards the point of the constant steady state (u_s, v_s), forming the shape of a star. If parameters are selected from the curve c_1 in Figure 3.3 (b), then the eigenvalues are positive real repeated roots. The dynamics of the perturbed system near the constant steady steady state will radially move outward (see Figure 3.4 (d)). If the values of α and β are chosen from those lying on the c_3 curve in Figure 3.3 (b), then the local dynamics of the system near the constant steady state radially move inward towards the point (u_s, v_s) (see Figure 3.4 (c)). Similarly, if α and β are chosen from region A in Figure 3.3 (b), it will result in $\lambda_{1,2}$ to be a pair of distinct negative real roots. This means for the dynamics of the system to move towards the stable constant steady state. The trajectories near by the steady state in this case move towards a single point namely (u_s, v_s). If parameters are however chosen from region B in Figure 3.3 (b), this results in the constant steady state to be an unstable node, it means the behaviour of trajectories near the steady state are expected to behaviour similarly to those corresponding to the curve c_2 (see Figure 3.4 (a)).

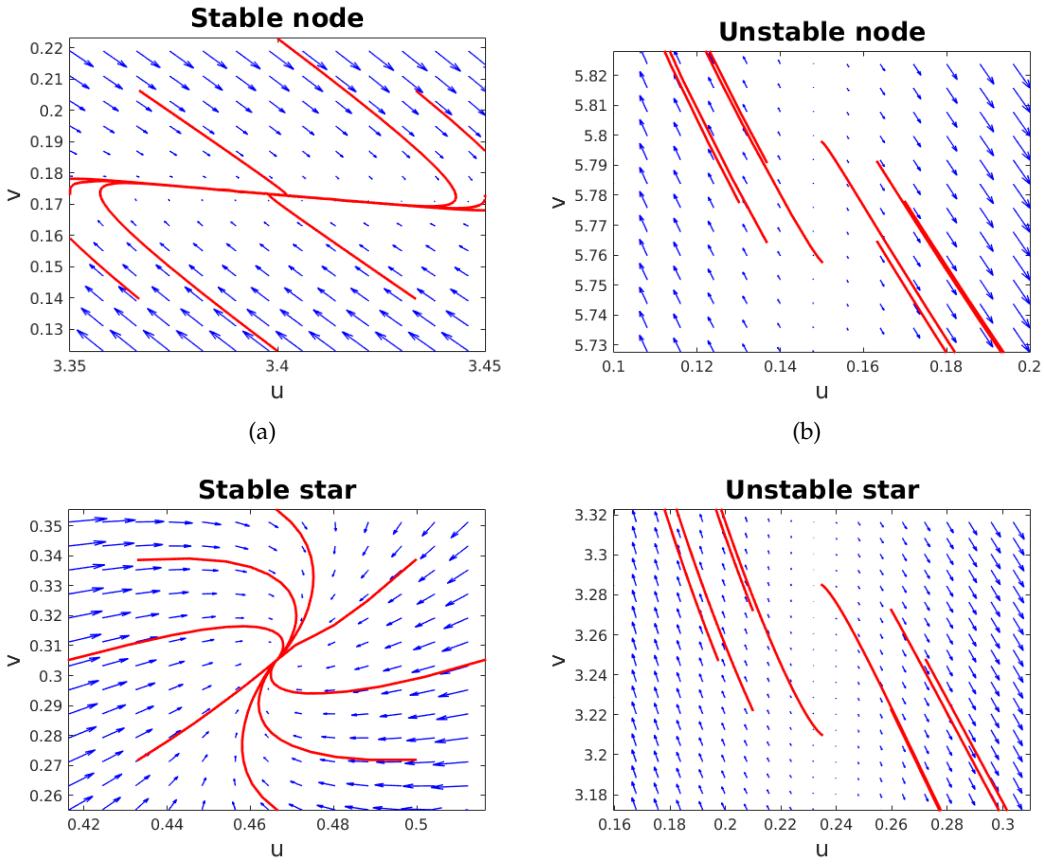

FIGURE 3.4: In (a) parameters $(\alpha, \beta) = (1.4, 2.0)$, resulting in the uniform steady state $(u_s, v_s) = (3.4, 0.173)$ and eigenvalues $\lambda_{1,2} = (-10.26, -1.13)$. In (b) parameters $(\alpha, \beta) = (0.02, 0.13)$, resulting in the uniform steady state $(u_s, v_s) = (0.15, 5.78)$ and eigenvalues $\lambda_{1,2} = (0.03, 0.68)$. In (c) parameters $(\alpha, \beta) = (0.40, 0.066)$, resulting in the uniform steady state $(u_s, v_s) = (0.8, 0.625)$ and eigenvalues$\lambda_{1,2} = (-0.47, -0.47)$. In (d) parameters $(\alpha, \beta) = (0.06, 0.18)$, resulting in the uniform steady state $(u_s, v_s) = (0.23, 3.25)$ and eigenvalues $\lambda_{1,2} = (0.20, 0.20)$.

3.1.7 Summary of parameter classification in the absence of diffusion

In general, the parameter space that influences the nature of the uniform steady state (u_s, v_s) can be categorised into four different regions, which are separated by three curves. This classification is in principle equivalent to that presented in Murray, 2001, however the distinction with the current work is that for the specific system given by (3.4) the full parameter plane is classified subject to the proposed theory given in Murray, 2001. Each region is characterised and the behavior of the uniform steady state is established by choosing parameters α and β from the region. Figure 3.5 (a) summarises the full classification of the parameter space in the absence of diffusion for the uniform steady state (u_s, v_s). It can be noted that in terms of stability only and irrespective of the type of the steady state, the full parameter space namely the $(\alpha, \beta) \in \mathbb{R}_+$ plane can be classified into two regions namely stable or unstable, this is the partition established by the location of the yellow curve in Figure 3.5 (a). Stability classification irrespective of the type of steady state is explicitly presented in Figure 3.5 (b). The purpose of stability partition will prove beneficial in the next section when the diffusion-driven instability is explored. Because diffusion-driven instability as the name suggests, is to explore how a stable steady state becomes unstable for the same choice of parameters (α, β), when diffusion is added to the system. Therefore, with the help of stability partition, one is able to observe the change in the location of the yellow curve in Figure 3.5 (b). Table 3.1 shows the values of the parameters (α, β) and the values of the unique steady state (u_s, v_s) with the relative eigenvalues that corresponds to the summary of full classification of parameter space presented in Figure 3.5 (a), and these parameter values are used in the numerical simulations.

3.2 Stability analysis in the presence of diffusion

It is intuitive to understand that normally diffusion serves to enhance spatial homogeneity of concentration gradients (Murray, 2001; Madzvamuse and Chung, 2014), however, in the case of reaction-diffusion systems, it has the opposite effect in that the

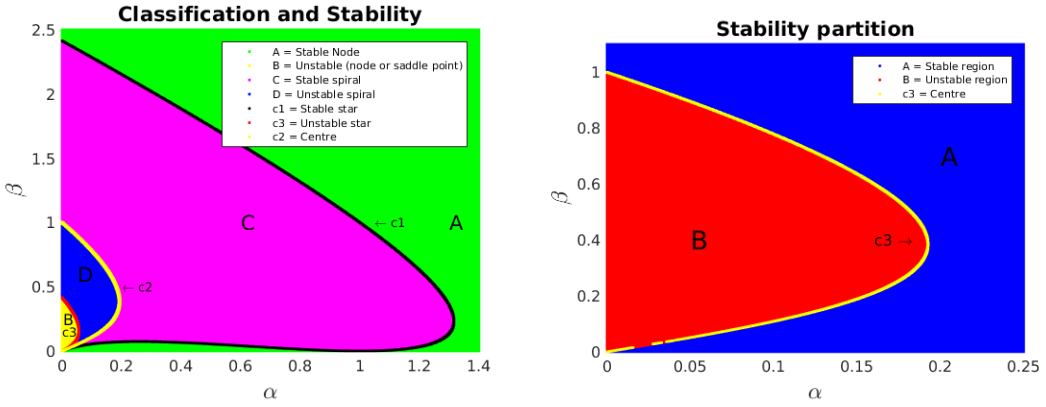

(a) (b)

FIGURE 3.5: In (a) parameter space classification that results in the steady state (u_s, v_s) to be of different types, and their corresponding stability as indicated in the legend. In (b) parameters from red region make (u_s, v_s) unstable, whereas any combination of (α, β) from the blue region make (u_s, v_s) stable, and parameters lying on the yellow curve results in (u_s, v_s) being a centre.

Name (SS)	(α, β)	(u_s, v_s)	$\lambda_{1,2}$	Fig 3.5(a)	Phaseplane
Stable node	$(1.400, 2.000)$	$(3.400, 0.173)$	(-10.26, -1.13)	Region A	Fig 3.4 (a)
Unstable node	$(0.020, 0.130)$	$(0.150, 5.780)$	(0.03, 0.68)	Region B	Fig 3.4 (b)
Stable spiral	$(0.400, 0.400)$	$(0.800, 0.625)$	$-0.32 \pm 0.73i$	Region C	Fig 3.2 (a)
Unstable spiral	$(0.100, 0.500)$	$(0.600, 1.390)$	$0.15 \pm 0.58i$	Region D	Fig 3.2 (b)
Stable star	$(0.400, 0.066)$	$(0.470, 0.310)$	(-0.47, -0.47)	Curve $c1$	Fig 3.4 (c)
Unstable star	$(0.060, 0.180)$	$(0.230, 3.250)$	(0.20, 0.20)	Curve $c3$	Fig 3.4 (d)
Centre	$(0.096, 0.102)$	$(0.198, 2.600)$	$\pm 0.20i$	Curve $c2$	Fig 3.2 (c)

TABLE 3.1: Table showing the summary of all types of steady states and their corresponding phase plane diagrams with reference to the parameter space on $(\alpha, \beta) \in \mathbb{R}_+$ plane.

uniform steady state which was stable in the absence of diffusion becomes unstable in its presence (Venkataraman, 2011; Madzvamuse, 2000; Murray, 2001; Madzvamuse and Chung, 2014). In this work, the mathematical rigour of how reaction and diffusion together can give rise to instability is investigated, which is responsible for diffusion-driven pattern formation. One of the explicit aims of the current work is to investigate the consequences of the conditions of diffusion-driven instability on the classification of the parameter space in the presence of diffusion. Furthermore, we want to explore quantitative relationship between the domain-size and the types of diffusion-driven

instability. The uniform steady state (u_s, v_s) as previously mentioned satisfies the system with diffusion (3.1) and the zero-flux boundary conditions (3.2), therefore, without loss of generality, (u_s, v_s) is considered a steady state of the system in presence of diffusion as well. System (3.1) is first linearised by introducing new variables namely $\bar{u}$ and $\bar{v}$ in such a way that they are perturbed slightly from the steady state (u_s, v_s), so that their relationships to u and v are $(\bar{u}, \bar{v}) = (u - u_s, v - v_s)$. For u and v, the perturbed variables $\bar{u} + u_s$ and $\bar{v} + v_s$ are substituted in (3.1) and expanded using Taylor expansion for functions of two variables to obtain a linearised system which can be written in matrix form as

$$\frac{\partial}{\partial t}\begin{bmatrix} \bar{u} \\ \bar{v} \end{bmatrix} = \begin{bmatrix} 1 & 0 \\ 0 & d \end{bmatrix}\begin{bmatrix} \Delta\bar{u} \\ \Delta\bar{v} \end{bmatrix} + \begin{bmatrix} \frac{\partial f}{\partial u}(u_s, v_s) & \frac{\partial f}{\partial v}(u_s, v_s) \\ \frac{\partial g}{\partial u}(u_s, v_s) & \frac{\partial g}{\partial u}(u_s, v_s) \end{bmatrix}\begin{bmatrix} \bar{u} \\ \bar{v} \end{bmatrix}. \tag{3.15}$$

We state the definitions of the concepts such as *Turing instability*, *Hopf bifurcation* and *limit-cycle behaviour* to express the adoption of these terminologies in the context of reaction-diffusion theory.

Definition 1 (Turing instability) *(Murray, 2001) A system of differential equations undergoes Turing instability if a uniform stable fixed point in the absence of diffusion destabilises in the consequence of adding diffusion to the system.*

Definition 2 (Hopf bifurcation) *(Marsden, 1978) A dynamical system of differential equations undergoes Hopf bifurcation if the real part of complex eigenvalues of the corresponding stability matrix passes through the imaginary axis in the consequences of a parameter variation.*

Definition 3 (Limit-cycle behaviour) *(Marsden, 1978; Schnakenberg, 1979) A dynamical system of differential equations undergoes a limit-cycle behaviour if in the process of a parameter variation a fixed point of the system switches stability as the real part of the eigenvalues of the system changes sign.*

In order to complete the linearisation in the presence of diffusion, it is necessary to find the eigenfunctions of the Laplace operator, that satisfies the homogeneous Neumann

boundary conditions. Eigenfunctions of the Laplace operator on planar domains are well-studied in the literature (Benedetto, 1996; Madzvamuse, 2000). It is presumed that $\bar{u}$ and $\bar{v}$ both satisfy ansatz of a similar form. The eigenfunctions for the Laplace operator are found by solving the relevant eigenvalue problems, that satisfy the given boundary conditions of problem (3.1). Such an eigenvalue problem is of the form

$$\begin{cases} \frac{\partial^2 \bar{u}}{\partial x^2} + \frac{\partial^2 \bar{u}}{\partial y^2} = \eta \bar{u}, & \eta \in \mathbb{R}, \\ \frac{\partial \bar{u}}{\partial x}(0,y) = 0, & \frac{\partial \bar{u}}{\partial x}(L,y) = 0, & 0 \leq y \leq L, \\ \frac{\partial \bar{u}}{\partial y}(x,0) = 0, & \frac{\partial \bar{u}}{\partial y}(x,L) = 0, & 0 \leq x \leq L. \end{cases} \tag{3.16}$$

The method of separation of variables is used to find the solution to problem (3.16) by presuming that the solution is in the form of a product of two functions namely $X(x)$ and $Y(y)$, so $\bar{u}$ has the form $\bar{u}(x,y) = X(x)Y(y)$. This form of solution is substituted in equation (3.16) to obtain two one-dimensional eigenvalue problems, which are individually solved and the resulting set of eigenfunctions solving (3.16) are given by $\bar{u}_{n,m}(x,y) = C_{n,m} \cos\left(\frac{n\pi x}{L}\right) \cos\left(\frac{m\pi y}{L}\right)$, where $C_{n,m}$ are the coefficients depending on the mode of the eigenfunctions. The solution to problem (3.15) can be, therefore, written as the sum of infinite expansion in the form of the product of $T(t)$, and the eigenfunctions for the two dimensional Laplace operator, so we have

$$\begin{aligned} \bar{u}(x,y,t) &= \sum_{n=0}^{\infty} \sum_{m=0}^{\infty} U_{n,m} \exp(\lambda_{n,m} t) \cos\left(\frac{n\pi x}{L}\right) \cos\left(\frac{m\pi y}{L}\right), \\ \bar{v}(x,y,t) &= \sum_{n=0}^{\infty} \sum_{m=0}^{\infty} V_{n,m} \exp(\lambda_{n,m} t) \cos\left(\frac{n\pi x}{L}\right) \cos\left(\frac{m\pi y}{L}\right), \end{aligned}$$

where $U_{n,m}$ and $V_{n,m}$ are the coefficients of the infinite expansion. Substituting this form of solution in (3.15), the problem can be written as a two-dimensional discrete set of algebraic equations in the form, with $\lambda = \lambda_{n,m}$

$$\lambda \begin{bmatrix} \bar{u} \\ \bar{v} \end{bmatrix} = -\frac{(n^2+m^2)\pi^2}{L^2} \begin{bmatrix} 1 & 0 \\ 0 & d \end{bmatrix} \begin{bmatrix} \bar{u} \\ \bar{v} \end{bmatrix} + \gamma \begin{bmatrix} \frac{\beta-\alpha}{\beta+\alpha} & (\beta+\alpha)^2 \\ -\frac{2\beta}{\beta+\alpha} & -(\beta+\alpha)^2 \end{bmatrix} \begin{bmatrix} \bar{u} \\ \bar{v} \end{bmatrix}, \tag{3.17}$$

which can also be written as a two-dimensional discrete eigenvalue problem

$$\begin{bmatrix} \gamma\frac{\beta-\alpha}{\beta+\alpha} - \frac{(n^2+m^2)\pi^2}{L^2} & \gamma(\beta+\alpha)^2 \\ -\gamma\frac{2\beta}{\beta+\alpha} & -\gamma(\beta+\alpha)^2 - d\frac{(n^2+m^2)\pi^2}{L^2} \end{bmatrix} \begin{bmatrix} \bar{u} \\ \bar{v} \end{bmatrix} = \lambda \begin{bmatrix} \bar{u} \\ \bar{v} \end{bmatrix}. \tag{3.18}$$

For the stability of the steady state (u_s, v_s) in the presence of diffusion, the eigenvalues of problem (3.18) are analysed. The characteristic polynomial for (3.18) is given by

$$\begin{vmatrix} \gamma\frac{\beta-\alpha}{\beta+\alpha} - \frac{(n^2+m^2)\pi^2}{L^2} - \lambda & \gamma(\beta+\alpha)^2 \\ -\gamma\frac{2\beta}{\beta+\alpha} & -\gamma(\beta+\alpha)^2 - d\frac{(n^2+m^2)\pi^2}{L^2} - \lambda \end{vmatrix} = 0, \tag{3.19}$$

which is a quadratic polynomial in λ. Let $\mathcal{T}$ and $\mathcal{D}$ denote the trace and determinant of the stability matrix (3.18) then the pair of eigenvalues $\lambda_{1,2}$ of system (3.18) satisfy the quadratic polynomial in terms of the trace and determinant in the form

$$\lambda^2 - \mathcal{T}(\alpha,\beta)\lambda + \mathcal{D}(\alpha,\beta) = 0, \tag{3.20}$$

where $\mathcal{T}(\alpha,\beta)$ and $\mathcal{D}(\alpha,\beta)$ are given by

$$\begin{aligned} \mathcal{T}(\alpha,\beta) =& \gamma\frac{\beta-\alpha-(\beta+\alpha)^3}{\beta+\alpha} - (d+1)\frac{(n^2+m^2)\pi^2}{L^2}, \\ \mathcal{D}(\alpha,\beta) =& \Big(\gamma\frac{\beta-\alpha}{\beta+\alpha} - \frac{(n^2+m^2)\pi^2}{L^2}\Big)\Big(-\gamma(\beta+\alpha)^2 - (d+1)\frac{(n^2+m^2)\pi^2}{L^2}\Big) + 2\gamma^2\beta(\beta+\alpha). \end{aligned}$$

The roots of (3.20) are $\lambda_{1,2} = \frac{1}{2}\mathcal{T}(\alpha,\beta) \pm \frac{1}{2}\sqrt{\mathcal{T}^2(\alpha,\beta) - 4\mathcal{D}(\alpha,\beta)}$. We note that, in comparison to the case when no diffusion is present, the trace $\mathcal{T}(\alpha,\beta)$ of the Jacobian matrix becomes more negative when diffusion is introduced since a positive quantity is being subtracted, thereby enhancing the stability of the system. This is equivalent to the default intuition that diffusion may only promote stability, due to its natural property of homogenising concentration gradient. However, the modification to determinant part $\mathcal{D}(\alpha,\beta)$ in the form of an additional positive term $(d+1)\pi^4\frac{(n^2+m^2)^2}{L^4}$ is intuitively expected to dominate the strictly positive term which is subtracted from

$\mathcal{T}(\alpha,\beta)$, namely $(d+1)\frac{(n^2+m^2)\pi^2}{L^2}$. These modifications to the trace and the determinant of the stability matrix due to the presence of diffusion to the system are investigated thoroughly to derive possible quantitative relationships between domain-size, reaction and diffusion rates in the context of the parameter classification. We also attempt to quantitatively understand how this modification of both $\mathcal{T}(\alpha,\beta)$ and $\mathcal{D}(\alpha,\beta)$ contributes to creating instability. The regions of the parameter space for all types of steady states and their stability is analysed. Once the regions for different types of steady states are classified, then subject to this classification the influence of the domain-size Ω is explored on the types and existence of diffusion-driven instabilities.

3.2.1 Analysis for the case of complex eigenvalues

To determine the types of steady state (u_s, v_s), with corresponding parameter space, it is important to realise that despite the dependence on α and β, the type of steady state also depends on the additional parameters namely γ, d and L. The variation of the additional parameters are investigated for fixed n and m to explore how the parameter space varies for different values of d, for example. Another important relationship to investigate is between the area of the domain L^2 and the reaction rate γ and how these influence the process of diffusion-driven instability. First, we analyse the case of complex eigenvalues. The eigenvalues $\lambda_{1,2}$ are complex values if (α,β) are chosen such that the discriminant of (3.20) is negative. It means that (α,β) must satisfy

$$\frac{1}{4}\mathcal{T}^2(\alpha,\beta) < \mathcal{D}(\alpha,\beta). \tag{3.21}$$

One immediate consequence of this inequality is that $\mathcal{D}(\alpha,\beta)$ must be positive, because if $\mathcal{D}(\alpha,\beta)$ is negative, then for no choice of (α,β) do the eigenvalues $\lambda_{1,2}$ become complex. This immediate observation is automatically in agreement with the conditions for diffusion-driven instability presented in (Liu et al., 2013; Madzvamuse, Chung, and Venkataraman, 2015). Furthermore, this condition on one hand will determine the region of the $(\alpha,\beta) \in \mathbb{R}_+$ plane on which $\lambda_{1,2}$ are a complex conjugate

pair. On the other hand it serves to indicate the equations for the partitioning implicit curves on which the eigenvalues change type from real to complex. Bearing in mind, that inequality (3.21) is a sufficient condition for $\lambda_{1,2}$ to have imaginary parts, therefore, it suffices to study (3.21) for (u_s, v_s) to be a spiral. Before numerical treatment of the critical curve for the complex region, the stability of (u_s, v_s) is studied analytically given that $\lambda_{1,2}$ have imaginary parts. Stability of (u_s, v_s) is determined by the sign of the real part of $\lambda_{1,2}$ when it is a pair of complex conjugate values. Given that this is the case then the real part of $\lambda_{1,2}$ is given by

$$\mathrm{Re}(\lambda_{1,2}) = \frac{1}{2}\Big(\gamma\frac{\beta-\alpha-(\beta+\alpha)^3}{\beta+\alpha} - (d+1)\frac{(n^2+m^2)\pi^2}{L^2}\Big).$$

If we wish to find the parameter space for which (u_s, v_s) is a stable spiral then we require the real part of both eigenvalues to be negative, which means in addition to the condition (3.21) we want $\mathcal{T}(\alpha,\beta)$ to be negative or equivalently (α,β) must satisfy

$$\gamma\frac{\beta-\alpha-(\beta+\alpha)^3}{\beta+\alpha} < (d+1)\frac{(n^2+m^2)\pi^2}{L^2}. \tag{3.22}$$

In comparison to the absence of diffusion, the condition for stability of (u_s, v_s) when $\lambda_{1,2}$ are complex eigenvalues is similar to (3.22) except that the right-hand side of inequality is a strictly positive real quantity. The quantity on the right hand-side of (3.22) has L^2 in the denominator. The maximum value that $T(\alpha,\beta)$ in the absence of diffusion could attain on $(\alpha,\beta) \in \mathbb{R}_+$ is 1 [see Theorem 3.3.2 on Page 64]. The expression for $\mathcal{T}(\alpha,\beta)$ in the presence of diffusion is the same as $T(\alpha,\beta)$ in the absence of diffusion except it is reduced by a strictly positive constant and multiplied by γ. This relationship indicates that the stability of (u_s, v_s) when $\lambda_{1,2}$ are complex, depends on the extra parameters L, d and γ. The maximum of the left-hand side of (3.22) is the non-zero positive constant γ [see Theorem 3.3.1 on Page 60], which suggests that the real part of $\lambda_{1,2}$ is negative if the term on the right-hand side of (3.22) satisfies

$$(d+1)\frac{(n^2+m^2)\pi^2}{L^2} > \gamma \qquad \Longleftrightarrow \qquad L^2 < \pi^2\frac{(d+1)(m^2+n^2)}{\gamma}. \tag{3.23}$$

In the presence of diffusion, if $\lambda_{1,2}$ is a pair of complex conjugate eigenvalues then the real part of $\lambda_{1,2}$ is always negative given that the area L^2 of Ω satisfies (3.23), otherwise no choice of $\alpha > 0$, $\beta > 0$ and $d > 0$ can change the sign of $\mathrm{Re}(\lambda_{1,2})$ to positive. This claim is formally proven in Theorem 3.3.1 as well as numerically demonstrated that no choice of α, β and d can invalidate inequality (3.22), given that L satisfies (3.23). For the first eigenvalue of the Laplace operator, which corresponds to $m = n = 0$, inequality (3.21) takes exactly the same form as the inequality that was necessary for (u_s, v_s) to be a spiral in the absence of diffusion, namely inequality (3.7). Therefore, to avoid repetition the stability analysis of the steady state (u_s, v_s) with $m = n = 0$ is skipped and the non-trivial case is studied, i.e. $m, n \geq 1$. In the absence of diffusion, in the region where (u_s, v_s) is a spiral, there are sub-regions that correspond to a stable spiral as well as sub-regions that correspond to an unstable spiral. One immediate consequence of including diffusion, into the model, is that it puts the condition (3.23) on the domain-size L^2 for the real part of $\lambda_{1,2}$ to remain negative. Similarly the real part of $\lambda_{1,2}$ becomes positive if condition (3.23) is violated. This means, diffusion-driven instability only serves to destabilise a spiral type of uniform steady state (u_s, v_s) if the parameter L violates inequality (3.23), which means

$$L^2 > \pi^2 \frac{(d+1)(m^2+n^2)}{\gamma}. \tag{3.24}$$

Conditions (3.23) and (3.24) both have consequences in terms of the stability of the original system. The first consequence is that if $\lambda_{1,2}$ have imaginary parts, then condition (3.23) guarantees that the real part of $\lambda_{1,2}$ is negative for all choices of α and β, allowing the eigenvalues to be positive if and only if they are both real repeated or real distinct (with at least one of them positive). Hence, restricting the system from undergoing *Hopf* bifurcation. Similarly, if $\lambda_{1,2}$ have imaginary parts, then condition (3.23) must be violated (condition (3.24) must be satisfied) in order for the real part of $\lambda_{1,2}$ to become positive whilst the eigenvalues are still complex conjugate pair. It means that for the original system to undergo *Hopf* bifurcation, the necessary condition on

the domain-size is (3.24). Both of these statements are formally proven in the form of theorems in the Section 3.3. If the real part of the complex eigenvalues becomes zero, then the roots become purely imaginary, indicating that the system undergoes a time-periodic oscillations whilst experiencing spatial stability. This type of instability is referred to as *Transcritical bifurcation* and this entails that the real part of $\lambda_{1,2}$ must become zero, which means

$$\gamma\frac{\beta-\alpha-(\beta+\alpha)^3}{\beta+\alpha}-(d+1)\frac{(n^2+m^2)\pi^2}{L^2}=0. \tag{3.25}$$

Rearranging (3.25) and solving for L^2, the necessary condition for transcritical bifurcation is obtained in the form

$$L^2=\frac{(\beta+\alpha)(d+1)(n^2+m^2)\pi^2}{\gamma\big(\beta-\alpha-(\alpha+\beta)^3\big)}. \tag{3.26}$$

If the parameter L satisfies condition (3.24) simultaneously with condition (3.26) and $\mathcal{D}(\alpha,\beta)>0$, then the system exhibits a temporal periodicity in the dynamics (Marsden, 1978).

3.2.2 Interpretation of the dynamics for the case of complex eigenvalues

For a domain-size satisfying (3.23) the dynamics of the system with diffusion is expected to undergo spatial patterning only. If the diffusion rate d is increased, yet satisfying (3.23), instability is still expected to invade stable regions in the parameter plane, however the only type of instability one may expect is spatial and not temporal. This type of instability is referred to as *Turing Instability* (Murray, 2001; Liu et al., 2013; Madzvamuse, Chung, and Venkataraman, 2015), where a certain region in the parameter space is stable in the absence of diffusion and yet becomes spatially unstable upon adding diffusion to the system. Findings of the current study suggest that, if the relationship between L, γ and d is maintained as given by (3.23), the type of diffusion-driven instability is always restricted to *Turing Instability*. It means that the only pattern one can achieve with (3.23) is spatially periodic pattern, with no temporal

periodicity. However, if L, γ and d are given to satisfy condition (3.24) then the system may undergo both temporal and/or spatial periodicity. Upon increasing the value of d, yet maintaining condition (3.24) the system is expected to become temporally unstable. This type of instability is referred to as *Hopf Bifurcation* (Marsden, 1978), where the real part of the eigenvalues of the stability changes sign. In this case one may expect the system to undergo temporal periodicity (pattern along the *time-axis*).

3.2.3 Analysis for the case of real eigenvalues

The eigenvalues $\lambda_{1,2}$ are both real if the discriminant of the roots is either zero or positive, which in turn means that both eigenvalues are real values if the relationship between $\mathcal{T}(\alpha,\beta)$ and $\mathcal{D}(\alpha,\beta)$ is such that

$$\mathcal{T}^2(\alpha,\beta) \geq 4\mathcal{D}(\alpha,\beta). \tag{3.27}$$

The equal case of (3.27) is looked at first, where we have

$$\mathcal{T}^2(\alpha,\beta) = 4\mathcal{D}(\alpha,\beta), \tag{3.28}$$

which means that the discriminant is zero, hence the roots are repeated real values of the form $\lambda_1 = \lambda_2 \in \mathbb{R}$, given by

$$\lambda_1 = \lambda_2 = \frac{1}{2}\Big(\gamma\frac{\beta-\alpha-(\beta+\alpha)^3}{\beta+\alpha} - (d+1)\frac{(n^2+m^2)\pi^2}{L^2}\Big). \tag{3.29}$$

When α and β satisfy condition (3.28), the stability of the steady state is determined by the sign of the root itself. The expression given by (3.29) can be easily shown to be negative if the area L^2 of the domain satisfies the inequality

$$L^2 < \pi^2\frac{(\beta+\alpha)(d+1)(n^2+m^2)}{\gamma\big(\beta-\alpha-(\beta+\alpha)^3\big)}. \tag{3.30}$$

Otherwise, the repeated root is positive provided that L satisfies

$$L^2 > \pi^2 \frac{(\beta+\alpha)(d+1)(n^2+m^2)}{\gamma\left(\beta-\alpha-(\beta+\alpha)^3\right)}. \tag{3.31}$$

Analysing (3.30) and (3.31) carefully, it can be observed that the only terms that can possibly invalidate the inequalities are in the denominator of the right hand-side, namely the expression $\beta-\alpha-(\beta+\alpha)^3$. Therefore, a restriction is required to be stated on this term to ensure that the area of Ω is not compared against a negative quantity, such a restriction is

$$\beta > \alpha + (\beta+\alpha)^3. \tag{3.32}$$

It must be noted that (3.32) is the same restriction on the parameter choice obtained for the case of repeated real eigenvalues in the absence of diffusion. The region where the eigenvalues are real repeated roots are implicit curves in the parameter space satisfying (3.27), these curves are computed numerically in the last part of Section 4. These curves form the boundary between the regions of complex and real eigenvalues. Varying the diffusion rate d causes a shift to the location of the curves indicating clearly regions that are subject to diffusion-driven instability. The remaining case to look at is when both eigenvalues are real distinct. This happens if α and β are chosen such that the strict inequality case of (3.27) is satisfied. This case corresponds to the diffusion-driven instability *Turing type* only, because both eigenvalues are real and distinct.

3.2.4 Interpretation of the dynamics for the case of real eigenvalues

If both eigenvalues are negative distinct real values, then the system is spatially as well as temporally stable, the dynamics will achieve no patterns, hence the system returns to the uniform constant steady state (u_s, v_s) as time grows, [see Section 5 Figure 3.12] with no effect from diffusion. If the eigenvalues are both real with different signs, then the type of instability caused by diffusion is spatially periodic or oscillatory in space, because this case corresponds to the steady state becoming a saddle point. If both

eigenvalues are positive real distinct values, then the dynamics are expected to exhibit a spatially periodic pattern, in the form of stripes or spots.

3.3 Bifurcation results and numerical experiments

This section contains the main results relating the domain-size to the admissibility of certain types of dynamical behaviour that system (3.1). The analytical findings are formally presented in the form of two theorems with proofs. Each of which indicates the relationship between the domain-size with the diffusion coefficient d and reaction rate γ. The numerical technique for computing the critical boundary curves is also briefly explained and results of parameter space classification are numerically computed. Numerical verification of both theorems is carried out in this section, where the reaction-diffusion system is numerically solved using the finite element method on a unit square domain. The relationship between domain length and parameters d and γ is shown to be in agreement with theoretical predictions presented.

Theorem 3.3.1 (Turing type diffusion-driven instability) *Let u and v satisfy the non-dimensional reaction-diffusion system with activator-depleted reaction kinetics* (3.1)-(3.2) *on a square domain $\Omega \subset \mathbb{R}^2$ with area L^2 and positive parameters $\gamma > 0$, $d > 0$, $\alpha > 0$ and $\beta > 0$. Given that the area of the square domain $\Omega \subset \mathbb{R}^2$ satisfies the inequality* (3.23) *where $m, n \in \mathbb{N}$ then for all $\alpha, \beta \in \mathbb{R}_+$ in the neighbourhood of the unique steady state $(u_s, v_s) = \left(\alpha + \beta, \frac{\beta}{(\alpha+\beta)^2}\right)$ the diffusion driven instability is restricted to Turing type only, forbidding the existence of Hopf and transcritical bifurcation.*

Proof

The strategy of this proof is through detailed analysis of the real part of the eigenvalues of the linearised system, when the eigenvalues are a complex conjugate pair. This can be done through studying the surface $\mathcal{T}(\alpha, \beta)$, and finding that it has a unique extremum point at $(0, 0)$. The method of second derivative test and Hessian matrix is

used to determine the type of this extremum. Upon finding its type, then the monotonicity of $\mathcal{T}(\alpha,\beta)$ is analysed in the neighbourhood of the extremum point in both directions α and β. The monotonicity analysis and the type of the extremum leads to proving the claim of the theorem.

The eigenvalues $\lambda_{1,2}$ in the presence of diffusion, in terms of trace $\mathcal{T}(\alpha,\beta)$ and determinant $\mathcal{D}(\alpha,\beta)$ are given by $\lambda_{1,2} = \frac{1}{2}\mathcal{T}(\alpha,\beta) \pm \frac{1}{2}\sqrt{\mathcal{T}^2(\alpha,\beta) - 4\mathcal{D}(\alpha,\beta)}$, where

$$\begin{aligned}\mathcal{T}(\alpha,\beta) =& \gamma\frac{\beta-\alpha-(\beta+\alpha)^3}{\beta+\alpha} - (d+1)\frac{(n^2+m^2)\pi^2}{L^2},\\ \mathcal{D}(\alpha,\beta) =& \Big(\gamma\frac{\beta-\alpha}{\beta+\alpha} - \frac{(n^2+m^2)\pi^2}{L^2}\Big)\Big(-\gamma(\beta+\alpha)^2 - d\frac{(n^2+m^2)\pi^2}{L^2}\Big) + 2\gamma^2\beta(\beta+\alpha).\end{aligned}$$

It can be immediately observed that in the neighbourhood of (u_s, v_s) for the system to exhibit Hopf or transcritical bifurcation the discriminant of the characteristic polynomial must satisfy the inequality $\mathcal{T}^2(\alpha,\beta) - 4\mathcal{D}(\alpha,\beta) < 0$. Therefore, the stability and type of the steady state (u_s, v_s) in this case is determined by the sign of the real part of $\lambda_{1,2}$. The aim is to investigate $\mathcal{T}(\alpha,\beta)$ and derive from it condition (3.23) on L^2 as a requirement for $\mathcal{T}(\alpha,\beta)$ to be negative for all strictly positive choices of γ, α, β and $d > 0$. First derivative test is used on $\mathcal{T}(\alpha,\beta)$ to find all stationary points of $\mathcal{T}(\alpha,\beta)$ on the domain $[0,\infty)\times[0,\infty)$. All stationary points of $\mathcal{T}(\alpha,\beta)$ must satisfy $\frac{\partial\mathcal{T}}{\partial\alpha} = -\gamma\frac{2(\alpha+\beta)^3+2\beta}{(\alpha+\beta)^2} = 0$, which is true if and only if

$$(\alpha+\beta)^3 + \beta = 0. \tag{3.33}$$

Similarly all stationary points of $\mathcal{T}(\alpha,\beta)$ must also satisfy $\frac{\partial\mathcal{T}}{\partial\beta} = -\gamma\frac{2(\alpha+\beta)^3-2\alpha}{(\alpha+\beta)^2} = 0$, which implies

$$(\alpha+\beta)^3 - \alpha = 0. \tag{3.34}$$

The system of non-linear algebraic equations obtained from (3.33) and (3.34) has a unique solution namely $\alpha = 0$ and $\beta = 0$ [see Remark 3.3.1]. Therefore, $\mathcal{T}(\alpha,\beta)$ has a unique stationary point at the origin. The type of this stationary point is determined

by the second derivative test for which the Hessian matrix $H(\mathcal{T}(\alpha,\beta))$ must be computed and evaluated at the point $(0,0)$.

$$H(\mathcal{T}(\alpha,\beta))|_{(0,0)} = \begin{bmatrix} \frac{\partial^2\mathcal{T}}{\partial\alpha^2} & \frac{\partial^2\mathcal{T}}{\partial\beta\partial\alpha} \\ \frac{\partial^2\mathcal{T}}{\partial\alpha\partial\beta} & \frac{\partial^2\mathcal{T}}{\partial\beta^2} \end{bmatrix}_{(0,0)} = \begin{bmatrix} -\gamma\frac{4\beta-2(\alpha+\beta)^3}{(\alpha+\beta)^3} & -\gamma\frac{2(\alpha+\beta)^3+2(\alpha-\beta)}{(\alpha+\beta)^3} \\ -\gamma\frac{2(\alpha+\beta)^3+2(\alpha-\beta)}{(\alpha+\beta)^3} & -\gamma\frac{2(\alpha+\beta)^3+4\alpha}{(\alpha+\beta)^3} \end{bmatrix}_{(0,0)}.$$

It is clear that the entries of H upon direct evaluation at the point $(0,0)$ are undefined. This is treated by using L'Hopital's rule. L'Hopital's rule sometimes does not work for functions of two variables defined on cartesian coordinates, therefore a transformation of the entries to polar coordinates might be applied. We will exploit this technique to express the Hessian matrix in polar coordinates and differentiate accordingly. The entries of H are transformed to polar coordinates using $\alpha = r\cos(\theta)$ and $\beta = r\sin(\theta)$, so the rule can be applied by taking the $\lim_{r\to 0} H$. Using (r,θ) coordinates the entries of H take the following form

$$H(\mathcal{T}(r,\theta))|_{r=0} = -\gamma \begin{bmatrix} \frac{4r\sin\theta-2r^3(\cos\theta+\sin\theta)^3}{r^3(\cos\theta+\sin\theta)^3} & \frac{2r^3(\cos\theta+\sin\theta)^3+2r(\cos\theta-\sin\theta)}{r^3(\cos\theta+\sin\theta)^3} \\ \frac{2r^3(\cos\theta+\sin\theta)^3+2r(\cos\theta-\sin\theta)}{r^3(\cos\theta+\sin\theta)^3} & \frac{4r\cos\theta+2r^3(\cos\theta+\sin\theta)^3}{r^3(\cos\theta+\sin\theta)^3} \end{bmatrix}_{r=0}. \tag{3.35}$$

L'Hopital's rule is applied to each entry of H separately and the $\lim_{r\to 0} H_{ij}(\mathcal{T}(r,\theta))$ is computed for $i,j = 1,2$. Starting with the entry H_{11} and cancelling r, the expression takes the form

$$\lim_{r\to 0} H_{11} = \lim_{r\to 0} \frac{4\sin\theta - 2r^2(\cos\theta+\sin\theta)^3}{r^2(\cos\theta+\sin\theta)^3}.$$

Let $\mathcal{T}_1(r,\theta)$ and $\mathcal{T}_2(r,\theta)$ respectively denote the numerator and the denominator of the expression for H_{11}, then the application of L'Hopital's rule suggests that

$$\lim_{r\to 0} H_{11}(\mathcal{T}(r,\theta)) = \lim_{r\to 0} \frac{\mathcal{T}_1(r,\theta)}{\mathcal{T}_2(r,\theta)} = \frac{\lim_{r\to 0}\frac{d\mathcal{T}_1}{dr}(r,\theta)}{\lim_{r\to 0}\frac{d\mathcal{T}_2}{dr}(r,\theta)} = \lim_{r\to 0} \frac{-4r(\cos\theta+\sin\theta)^3}{2r(\cos\theta+\sin\theta)^3} = -2.$$

Applying the same procedure for H_{12}, H_{21} and H_{22}, all the entries of H are computed and given by

$$H(\mathcal{T}(\alpha,\beta))|_{(0,0)} = -\gamma \begin{bmatrix} -2 & 2 \\ 2 & 2 \end{bmatrix}. \tag{3.36}$$

Since the $\det(H) = -8\gamma^2 < 0$, therefore, the second derivative test suggests that $(0,0)$ is a saddle point of $\mathcal{T}(\alpha,\beta)$. Since it was previously shown that $\mathcal{T}(\alpha,\beta)$ attains a unique stationary point in the domain $[0,\infty) \times [0,\infty)$, i.e. by solving the equations (3.33) and (3.34), therefore, if $(0,0)$ was a maximum and $\mathcal{T}(0,0) < 0$, this would suggest that, whenever $\lambda_{1,2}$ has a non-zero imaginary part then $Re(\lambda_{1,2}) < 0$ regardless of the choice of d, γ and L^2, however due to fact that $(0,0)$ is a saddle point, it remains to show that $\mathcal{T}(\alpha,\beta)$ is negative at $(0,0)$ and its first derivatives in the neighbourhood of $(0,0)$ of $\mathcal{T}(\alpha,0)$ and $\mathcal{T}(0,\beta)$ for positive values of α and β in both directions are negative and do not change sign. Let $\mathcal{T}_0(\alpha)$ and $\mathcal{T}_0(\beta)$ denote the curves for constants $\beta = 0$ and $\alpha = 0$ respectively on the plane $\mathcal{T}(\alpha,\beta)$, then

$$\mathcal{T}_0(\alpha) = \lim_{\beta\to 0} \mathcal{T}(\alpha,\beta) = -\gamma(1+\alpha^2) - (d+1)\frac{(m^2+n^2)\pi^2}{L^2},$$
$$\mathcal{T}_0(\beta) = \lim_{\alpha\to 0} \mathcal{T}(\alpha,\beta) = \gamma(1-\beta^2) - (d+1)\frac{(m^2+n^2)\pi^2}{L^2}.$$

The expression for $\mathcal{T}_0(\alpha)$ clearly satisfy that it is negative at $\alpha = 0$ and its first derivative in the direction of α is $\frac{d\mathcal{T}_0(\alpha)}{d\alpha} = -2\gamma\alpha < 0$ for all $\gamma, \alpha \in [0,\infty)$. The expression for $\mathcal{T}_0(\beta)$ however is not trivially negative for all values, since the sign of the constant γ in the expression is positive, which if computed at $\beta = 0$, leads to the desired condition

$$\mathcal{T}_0(\beta)\big|_{\beta=0} = \gamma - (d+1)\frac{(m^2+n^2)\pi^2}{L^2} < 0 \qquad \Longleftrightarrow \qquad L^2 < \pi^2\frac{(d+1)(m^2+n^2)}{\gamma}.$$

It has been shown that the condition (3.23) is necessary for $\mathcal{T}(\alpha,\beta)$ to be negative at the unique stationary point namely $(0,0)$, it remains to show that the first derivative of $\frac{d\mathcal{T}_0}{d\beta}(\beta) < 0$, $\frac{d\mathcal{T}_0}{d\beta} = -2\gamma\beta < 0$ for all $\gamma\beta \in [0,\infty)$ which completes the proof.□

3.3.1 Remark

The parameters $(\alpha, \beta) = (0, 0)$ are not the admissible choices for the original system, because this choice of parameters leads to the trivial steady state $(u_s, v_s) = (0, 0)$, which is globally and unconditionally stable and has no physical relevance. However, the surface defined by $\mathcal{T}(\alpha, \beta)$, which determines the sign of the real part of $\lambda_{1,2} \in \mathbb{C}\backslash\mathbb{R}$ attains a unique extremum at $(0, 0)$, which makes the analysis of the neighbourhood of this point important for studying the sign of $\mathcal{T}(\alpha, \beta)$. It is reasonable to argue that the point $(\alpha, \beta) = (0, 0)$ is not permissible to use as the platform of the proof of Theorem 3.3.1, in that case, proving the results become a step closer by only showing that $\mathcal{T}(\alpha, \beta)$ is a strictly monotonically decreasing function (with no extrema in $(\alpha, \beta) \in \mathbb{R}^2_+$) and it can only attain bounded positive values in the neighbourhood of $(0, 0)$ if and only if the condition (3.23) on the domain-size L^2 is violated. Therefore, given that L^2 maintains to satisfy (3.23), the sign of the real part i.e. $\mathcal{T}(\alpha, \beta)$ of $\lambda_{1,2} \in \mathbb{C}\backslash\mathbb{R}$ is guaranteed to be negative, which is a step shorter to reach the claim of Theorem 3.3.1. Therefore, it is brought to the attention of the reader that the use of the point $(\alpha, \beta) = (0, 0)$ as an extremum of $\mathcal{T}(\alpha, \beta)$ is more of complementary factor to the proof rather than an essential one.

Theorem 3.3.2 (Hopf or transcritical bifurcation) *Let u and v satisfy the non-dimensional reaction-diffusion system with activator-depleted reaction kinetics* (3.1)-(3.2) *on a square domain $\Omega \subset \mathbb{R}^2$ with length L and positive parameters γ, $d > 0$, $\alpha > 0$ and $\beta > 0$. For the system to exhibit Hopf or transcritical bifurcation in the neighbourhood of the unique steady state $(u_s, v_s) = \left(\alpha + \beta, \frac{\beta}{(\alpha+\beta)^2}\right)$, the necessary condition on the area L^2 of the square domain $\Omega \subset \mathbb{R}^2$ is* (3.24) *where m and n are any integers.*

Proof

The strategy to this proof is some what different from that of Theorem 3.3.1, because in Theorem 3.3.1 the aim was to show that condition (3.23) must be satisfied by L^2 for $\mathcal{T}(\alpha, \beta)$ to be negative and to maintain negative sign throughout the (α, β) plane. For

this proof the only important step is to derive the condition for $\mathcal{T}(\alpha,\beta)$ to be positive, because when $\lambda_{1,2}$ are complex eigenvalues then the sign of $\mathcal{T}(\alpha,\beta)$ is precisely what determines the stability of (u_s, v_s). The system undergoes Hopf or transcritical bifurcation in the neighbourhood of (u_s, v_s), if the sign $\mathcal{T}(\alpha,\beta)$ is positive. Therefore for diffusion-driven instability to influence (u_s, v_s) when $\lambda_{1,2}$ are complex conjugate pair it is necessary that

$$\mathcal{T}(\alpha,\beta) = \gamma\frac{\beta-\alpha-(\beta+\alpha)^3}{\beta+\alpha} - (d+1)\frac{(n^2+m^2)\pi^2}{L^2} \geq 0, \tag{3.37}$$

which can equivalently be written as

$$\gamma\frac{\beta-\alpha-(\beta+\alpha)^3}{\beta+\alpha} \geq (d+1)\frac{(n^2+m^2)\pi^2}{L^2}. \tag{3.38}$$

The expression on the left hand-side of (3.38) is explored in particular to find its upper bound, it can be written it in the form of difference between two rational functions as

$$\gamma\frac{\beta-\alpha-(\beta+\alpha)^3}{\beta+\alpha} = \gamma\Big(f_1(\alpha,\beta) - f_2(\alpha,\beta)\Big), \tag{3.39}$$

where $f_1(\alpha,\beta) = \frac{\beta}{\beta+\alpha}$ and $f_2(\alpha,\beta) = \frac{\alpha+(\beta+\alpha)^3}{\beta+\alpha}$. The range for $f_1(\alpha,\beta)$ and $f_2(\alpha,\beta)$ are independently analysed to find the supremum of the expression on the left of (3.39). Starting with $f_1(\alpha,\beta)$, which is bounded below and above in the domain $(\alpha,\beta) \in [0,\infty)\times[0,\infty)$, we have $\sup_{\alpha,\beta\in\mathbb{R}_+} f_1(\alpha,\beta) = 1$, and the $\inf_{\alpha,\beta\in\mathbb{R}_+} f_1(\alpha,\beta) = 0$ for all $\alpha,\beta \in \mathbb{R}_+$. Similarly considering the expression for $f_2(\alpha,\beta)$, we have $\sup_{\alpha,\beta\in\mathbb{R}_+} f_2(\alpha,\beta) = \infty$, and the $\inf_{\alpha,\beta\in\mathbb{R}_+} f_2(\alpha,\beta) = 0$, for all $\alpha,\beta \in \mathbb{R}_+$. Since the ranges of both $f_1(\alpha,\beta)$ and $f_2(\alpha,\beta)$ are non-negative within their respective domains, therefore the supremum of their difference is bounded by the supremum of the function with positive sign, which

is $\sup_{\alpha,\beta\in\mathbb{R}_+} f_1(\alpha,\beta) = 1$. Therefore, inequality (3.37) can be written as

$$\begin{aligned}(d+1)\frac{(n^2+m^2)\pi^2}{L^2} &\leq \gamma\frac{\beta-\alpha-(\beta+\alpha)^3}{\beta+\alpha}\\ &\leq \gamma \sup_{\alpha,\beta\in\mathbb{R}_+}\big(f_1(\alpha,\beta)-f_2(\alpha,\beta)\big) = \gamma \sup_{\alpha,\beta\in\mathbb{R}_+} f_1(\alpha,\beta) = \gamma,\end{aligned}$$

which by rearranging leads to the desired condition (3.24).□

3.3.2 Equations of the implicit partitioning curves

A similar method to that used in the case of the absence of diffusion is applied to solve for the partitioning curves in the parameter plane. The partitioning curve for the complex region, on the plane $(\alpha,\beta)\in\mathbb{R}_+$ must satisfy

$$\mathcal{T}^2(\alpha,\beta) - 4\mathcal{D}(\alpha,\beta) = 0, \tag{3.40}$$

since this is the curve on which the discriminant of the expression for eigenvalues change sign. It means the curve satisfying (3.40) determines the boundary on one side of which $\lambda_{1,2}$ are both real and on the other side of it, $\lambda_{1,2}$ are both complex conjugate eigenvalues. Equation (3.40) is solved by a similar method to that used for solving (3.9) on a square domain and for each fixed mesh point in the direction of α it is found that its solution is equivalent to finding the positive real roots of the polynomial of degree 6 in β for fixed values of α_i in the form

$$\begin{aligned}\psi(\alpha_i,\beta) = C_0(\alpha_i) + C_1(\alpha_i)\beta + C_2(\alpha_i)\beta^2 + C_3(\alpha_i)\beta^3\\ + C_4(\alpha_i)\beta^4 + C_5(\alpha_i)\beta^5 + C_6(\alpha_i)\beta^6,\end{aligned} \tag{3.41}$$

where for each α_i the coefficients are given by

$$\begin{aligned}
C_0(\alpha_i) =& L^4\gamma^2{\alpha_i}^6 + \big(4\,L^4\pi^2m^2 + 4\,L^4\pi^2n^2 + 2\,L^2\gamma\pi^2dm^2 + 2\,L^2\gamma\pi^2dn^2 + 4\,L^6 \\
&+ 2\,L^2\gamma\pi^2m^2 + 2\,L^2\gamma\pi^2n^2 + 2\,L^4\gamma^2\big){\alpha_i}^4 + \big(-4\,L^2\pi^4dm^4 - 8\,L^2\pi^4dm^2n^2 \\
&- 4\,L^2\pi^4dn^4 - 4\,L^2\pi^4m^4 - 8\,L^2\pi^4m^2n^2 - 4\,L^2\pi^4n^4 - 4\,L^4\pi^2dm^2 \\
&- 4\,L^4\pi^2dn^2 - 4\,L^4\pi^2m^2 - 4\,L^4\pi^2n^2\big){\alpha_i}^3 + \big(\pi^4d^2m^4 + 2\,\pi^4d^2m^2n^2 \\
&+ \pi^4d^2n^4 + 2\,\pi^4dm^4 + 4\,\pi^4dm^2n^2 + 2\,\pi^4dn^4 + \pi^4m^4 + 2\,\pi^4m^2n^2 \\
&+ \pi^4n^4 + 2\,L^2\gamma\pi^2dm^2 + 2\,L^2\gamma\pi^2dn^2 + 2\,L^2\gamma\pi^2m^2 + 2\,L^2\gamma\pi^2n^2 + L^4\gamma^2\big){\alpha_i}^2,
\end{aligned}$$

$$\begin{aligned}
C_1(\alpha_i) =& 6\,L^4\gamma^2{\alpha_i}^5 - 8\,L^4{\alpha_i}^4 + \big(8\,L^4\pi^2m^2 + 8\,L^4\pi^2n^2 + 8\,L^2\gamma\pi^2dm^2 + 8\,L^2\gamma\pi^2dn^2 \\
&+ 8\,L^2\gamma\pi^2m^2 + 8\,L^2\gamma\pi^2n^2 + 4\,L^4\gamma^2\big){\alpha_i}^3 + \big(-12\,L^2\pi^4dm^4 - 24\,L^2\pi^4dm^2n^2 \\
&- 12\,L^2\pi^4dn^4 - 12\,L^2\pi^4m^4 - 24\,L^2\pi^4m^2n^2 - 12\,L^2\pi^4n^4 - 4\,L^4\pi^2dm^2 \\
&- 4\,L^4\pi^2dn^2 - 4\,L^4\pi^2m^2 - 4\,L^4\pi^2n^2\big){\alpha_i}^2 + \big(2\,\pi^4d^2m^4 + 4\,\pi^4d^2m^2n^2 \\
&+ 2\,\pi^4d^2n^4 + 4\,\pi^4dm^4 + 8\,\pi^4dm^2n^2 + 4\,\pi^4dn^4 + 2\,\pi^4m^4 + 4\,\pi^4m^2n^2 \\
&+ 2\,\pi^4n^4 - 2\,L^4\gamma^2\big)\alpha_i,
\end{aligned}$$

$$\begin{aligned}
C_2(\alpha_i) =& 15\,L^4\gamma^2{\alpha_i}^4 - 32\,L^4{\alpha_i}^3 + \big(12\,L^2\gamma\pi^2dm^2 + 12\,L^2\gamma\pi^2dn^2 - 8\,L^6 + 12\,L^2\gamma\pi^2m^2 \\
&+ 12\,L^2\gamma\pi^2n^2\big){\alpha_i}^2 + \big(-12\,L^2\pi^4dm^4 - 24\,L^2\pi^4dm^2n^2 - 12\,L^2\pi^4dn^4 \\
&- 12\,L^2\pi^4m^4 - 24\,L^2\pi^4m^2n^2 - 12\,L^2\pi^4n^4 + 4\,L^4\pi^2dm^2 + 4\,L^4\pi^2dn^2 \\
&+ 4\,L^4\pi^2m^2 + 4\,L^4\pi^2n^2\big)\alpha_i + \pi^4d^2m^4 + 2\,\pi^4d^2m^2n^2 + \pi^4d^2n^4 + 2\,\pi^4dm^4 \\
&+ 4\,\pi^4dm^2n^2 + 2\,\pi^4dn^4 + \pi^4m^4 + 2\,\pi^4n^2m^2 + \pi^4n^4 - 2\,L^2\gamma\pi^2dm^2 \\
&- 2\,L^2\gamma\pi^2dn^2 - 2\,L^2\gamma\pi^2m^2 - 2\,L^2\gamma^2\pi^2n^2 + L^4\gamma^2,
\end{aligned}$$

$$\begin{aligned}
C_3(\alpha_i) =& 20\,L^4\gamma^2{\alpha_i}^3 - 48\,L^4{\alpha_i}^2 + \big(-8\,L^4\pi^2m^2 - 8\,L^4\pi^2n^2 + 8\,L^2\gamma\pi^2dm^2 \\
&+ 8\,L^2\gamma\pi^2dn^2 + 8\,L^2\gamma\pi^2m^2 + 8\,L^2\gamma\pi^2n^2 - 4\,L^4\gamma\big)\alpha_i - 4\,L^2\pi^4dm^4 \\
&- 8\,L^2\pi^4dm^2n^2 - 4\,L^2\pi^4dn^4 - 4\,L^2\pi^4m^4 - 8\,L^2\pi^4m^2n^2 - 4\,L^2\pi^4n^4 \\
&+ 4\,L^4\pi^2dm^2 + 4\,L^4\pi^2dn^2 + 4\,L^4\pi^2m^2 + 4\,L^4\pi^2n^2,
\end{aligned}$$

$$C_4(\alpha_i) = 15\,L^4\gamma^2{\alpha_i}^2 - 32\,L^4\alpha_i - 4\,L^4\pi^2m^2 - 4\,L^4\pi^2n^2 + 2\,L^2\gamma\pi^2dm^2 + 2\,L^2\gamma\pi^2dn^2 + 4\,L^6 + 2\,L^2\gamma\pi^2m^2 + 2\,L^2\gamma\pi^2n^2 - 2\,L^4\gamma^2,$$

$$C_5(\alpha_i) = 6\,L^4\gamma^2\alpha_i - 8\,L^4, \quad \text{and} \quad C_6(\alpha_i) = \gamma^2L^4.$$

The implicit curve satisfying (3.41) indicates the choices of (α, β) for which the eigenvalues are repeated real roots, since this is the curve on which the discriminant is zero. Therefore it forms the boundary region in the plane corresponding to complex eigenvalues. The polynomial $\psi_i(\beta)$ of degree 6, given by (3.41) is solved for 5000 fixed α_i on a domain with $\alpha_{max} = \beta_{max} = 3$. For each α_i the positive real roots of $\psi_i(\beta)$ are extracted and plotted on the $(\alpha, \beta) \in \mathbb{R}_+$ plane. The algorithm is run for five different values of the non-dimensional parameter d, associated to both cases, where the area L^2 of Ω satisfies condition (3.23) of Theorem 3.3.1 as well as condition (3.24) of Theorem 3.3.2. The equation for the second curve that partitions the region corresponding to complex eigenvalues of the parameter plane is the curve on which the real parts of the complex roots are zero, hence satisfying the equation

$$\mathcal{T}(\alpha, \beta) = \gamma\frac{\beta - \alpha - (\alpha + \beta)^3}{\beta + \alpha} - \frac{(d+1)(m^2+n^2)\pi^2}{L^2} = 0. \tag{3.42}$$

The solution of (3.42) by algebraic manipulation can be found to be equivalent to finding the positive real roots of the cubic polynomial $\phi(\alpha_i, \beta) = 0$ for fixed α_i, where ϕ is given by

$$\phi(\alpha_i, \beta) = C_0(\alpha_i) + C_1(\alpha_i)\beta + C_2(\alpha_i)\beta^2 + C_3(\alpha_i)\beta^3, \tag{3.43}$$

with $C_0(\alpha_i) = -\left(L^2\gamma + (d+1)(n^2+m^2)\pi^2\right) - L^2\gamma\alpha_i^3$, $C_1(\alpha_i) = L^2\gamma - (d+1)(n^2 + m^2)\pi^2 - 3L^2\gamma\alpha_i^2$, $C_2(\alpha_i) = -3L^2\gamma\alpha_i$, and $C_3(\alpha_i) = -L^2\gamma$. Variations of the parameter d are investigated, whilst the area L^2 remains to satisfy condition (3.23) and as expected it is found that in the region of the parameter plane corresponding to complex eigenvalues, there is no sub-region that corresponds to $\lambda_{1,2}$ to have positive real parts. For each value of d the region corresponding to complex eigenvalues is tested by looking for a critical curve on which $\lambda_{1,2}$ is purely imaginary, i.e. satisfying (3.43). If such

a curve exists, it would correspond to the system undergoing periodic oscillations around (u_s, v_s), thus the system exhibiting transcritical bifurcation, which also implies the existence of a region in the parameter space that corresponds to real parts of $\lambda_{1,2}$ to be positive. Upon investigating this region, it is found that such a curve under condition (3.23) does not exists, and all roots corresponding to the cubic polynomial given by (3.43) are either complex eigenvalues or they are negative real values, therefore cannot be the choice of admissible parameters of the system. Another observation is that as d increases the area of the region corresponding to complex eigenvalues in the (α, β) plane gradually decreases. The domain-size of length $L = 5$ satisfying the condition of Theorem 3.3.1 is tested for stability analysis of (u_s, v_s) when $\lambda_{1,2}$ are complex eigenvalues. The results are shown for different values of d by a distinct colour in Figure 3.4 (a). Finding the solutions of these curves does not however indicate, which side of them correspond to complex $\lambda_{1,2}$ and which side to real $\lambda_{1,2}$. This is decided by some numerical trial and error by evaluating $\lambda_{1,2}$ using few values from both sides of each curve. Trial and error indicates that the regions under these curves correspond to $\lambda_{1,2}$ to be a complex conjugate pair and hence any combination of (α, β) from this region ensures that the eigenvalues $\lambda_{1,2}$ contain a non-zero imaginary part. When the area L^2 of Ω satisfies condition (3.23), the absence of a region satisfying (3.43) verifies the statement of Theorem 3.3.1, therefore the region corresponding to complex eigenvalues for the choice of L^2 satisfying (3.23) has no sub-partitions, because everywhere in this region the real part of the eigenvalues is negative, hence no choice of parameters could result in the system to exhibit Hopf or transcritical bifurcation. The eigenvalues only become positive when they are both real values, therefore condition (3.23) restricts the diffusion-driven instability to Turing type only. Figure 3.6 (a) shows how the partitioning curve changes location, as the value of d is varied. The region under those curves corresponds to the complex eigenvalues. Similarly Figure 3.6 (b) indicates the regions corresponding to complex eigenvalues for the corresponding values of d. Each stripe in Figure 3.6 (b) is denoted by a letter that represents the set of all points corresponding to a distinct colour stripe. Similarly, the regions where the

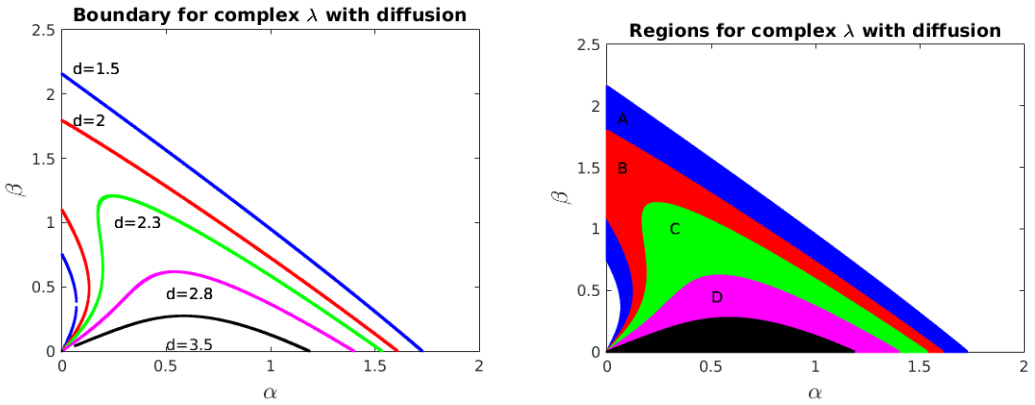

(a) (b)

FIGURE 3.6: In (a) boundary curves for complex $\lambda_{1,2}$ with corresponding values of d and the condition $L^2 = 25 < \pi^2\frac{(d+1)(m^2+n^2)}{\gamma}$. In (b) regions corresponding to complex eigenvalues associated to values of d indicated in (a) and condition (3.23).

eigenvalues $\lambda_{1,2}$ are negative real roots are presented by Figure 3.7 (a), corresponding to the same values of the parameter d. Figure 3.7 (b) shows regions where at least one or both eigenvalues are positive real roots. The summary of Figures 3.6 and 3.7 is presented in Table 3.2. The algorithm is also run for the case when L^2 is chosen such

Plot index	Figure 3.7 (a)	Figure 3.7 (b)	Figure 3.6 (b)	Figure 3.6 (b)	Figure 3.6 (b)
Eigenvalues	$0 > \lambda_{1,2} \in \mathbb{R}$	$0 < \lambda_{1,2} \in \mathbb{R}$	$\lambda \in \mathbb{C}, Re(\lambda_{1,2}) < 0$	$\lambda \in \mathbb{C}, Re(\lambda_{1,2}) > 0$	$\lambda \in \mathbb{C}, Re(\lambda) = 0$
Type of (SS) / Value of d	Stable node	Turing type instability	Stable spiral	Hopf bifurcation	Transcritical bifurcation
1.5	A	E	$A \cup B \cup C \cup D \cup E$	$\emptyset$	$\emptyset$
2	$A \cup B$	$E \cup D$	$B \cup C \cup D \cup E$	$\emptyset$	$\emptyset$
2.3	$A \cup B \cup C$	$E \cup D \cup C$	$C \cup D \cup E$	$\emptyset$	$\emptyset$
2.8	$A \cup B \cup C \cup D$	$E \cup D \cup C \cup B$	$D \cup E$	$\emptyset$	$\emptyset$
3.5	$A \cup B \cup C \cup D \cup E$	$E \cup D \cup C \cup B \cup A$	E	$\emptyset$	$\emptyset$

TABLE 3.2: Table showing regions corresponding to domain-size $L^2 < \frac{\pi^2(d+1)(m^2+n^2)}{\gamma}$, which satisfies (3.23) of Theorem 3.3.1.

that it satisfies (3.24) and we find that the region corresponding to complex eigenvalues is further partitioned by the curve satisfying (3.42). This is the curve on which the eigenvalues are purely imaginary. This curve also indicates that within the region corresponding to complex eigenvalues there is a sub-region in which the eigenvalues are complex with positive real part, which corresponds to the system exhibiting Hopf bifurcation. For choices of parameter values on the curve the system is expected to undergo transcritical bifurcation. The area of the domain Ω is taken as $L^2 = 225$ in

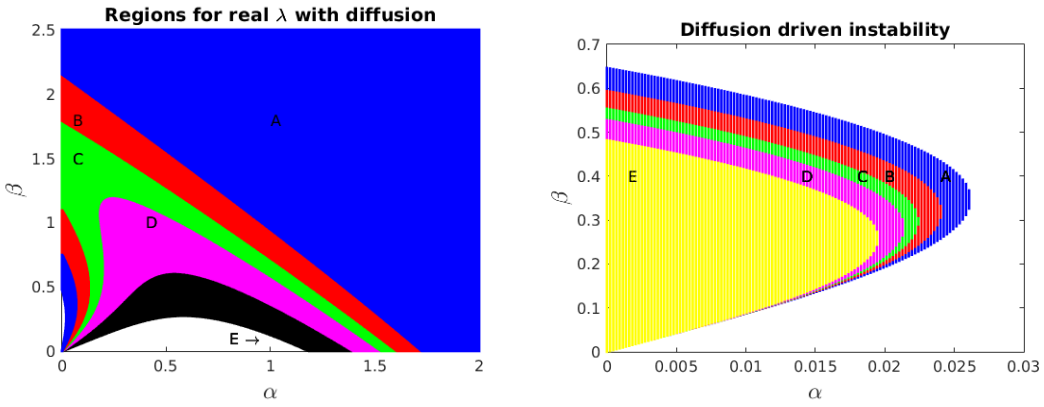

(a) (b)

FIGURE 3.7: In (a) regions where $\lambda_{1,2}$ are both real and negative. In (b) regions where both eigenvalues are real and at least one of λ_1 or λ_2 are positive.

order to satisfy the condition given by Theorem 3.3.2 with respect to d and γ, so that there is enough space for varying d and yet maintaining condition (3.24). It can be easily observed from the parameter space classification that there is a relatively small region in each case corresponding to diffusion-driven instability. This indicates the importance of making sure to choose parameter choices wisely, in order to expect the dynamics of the system to evolve to certain types of patterns or maybe no patterns at all. Table 3.3 presents the summary for how the regions of the parameter space change with varying the parameter d. It would be reasonable to use the same variation of the parameter d in both cases of the domain-sizes, however, in the first case where the domain-size satisfies (3.23) the span of varying parameter d is relatively small, yet causing significant observable change in the parameter space. However, when the domain-size is chosen according to condition (3.24), small variations in the diffusion coefficient makes insignificant changes to the parameter spaces, therefore, in order to pictorially observe the consequential change in the parameter plane (α, β) the span of variations for d have to be significantly large as seen in Table 3.2. In the case when L^2 satisfies Theorem 3.3.1, it can be observed that the type of diffusion-driven instability that can occur is restricted to Turing type only, which is increased as the

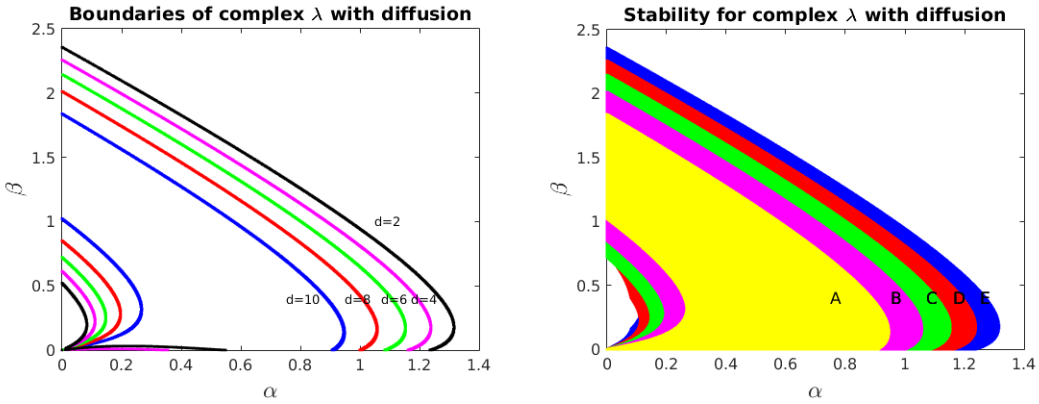

(a) (b)

FIGURE 3.8: In (a) boundary curves for complex $\lambda_{1,2}$ with corresponding values of d and the condition $L^2 = 225 > \pi^2 \frac{(d+1)(m^2+n^2)}{\gamma}$. In (b) regions corresponding to complex eigenvalues associated to values of d indicated in Figure (a) and condition (3.24).

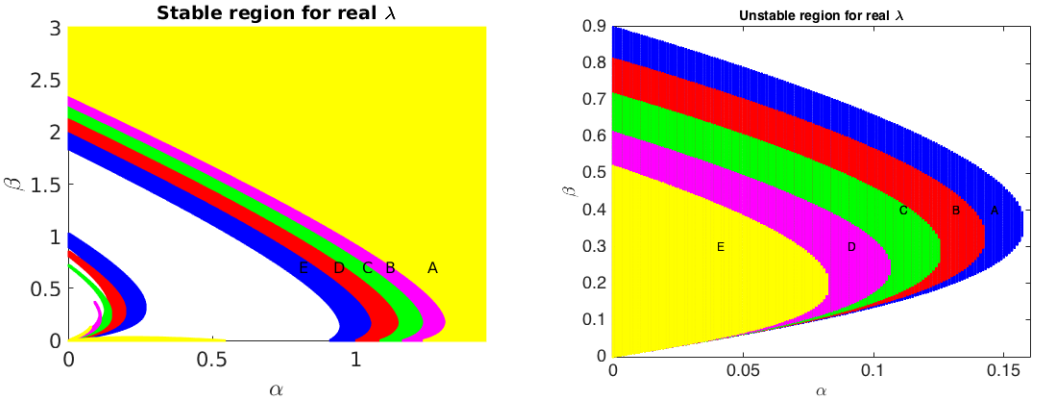

(a) (b)

FIGURE 3.9: In (a) the region correspond to real $\lambda_{1,2}$ with distinct and both negative values. In (b) the regions are shown where $\lambda_{1,2}$ are real distinct and at least one of them positive.

Plot index	Figure 3.9 (a)	Figure 3.9 (b)	Figure 3.8 (b)	Figure 3.10 (a)	Figure 3.10 (b)
Eigenvalues	$0 > \lambda_{1,2} \in \mathbb{R}$	$0 < \lambda_{1,2} \in \mathbb{R}$	$\lambda \in \mathbb{C}, Re(\lambda_{1,2}) < 0$	$\lambda \in \mathbb{C}, Re(\lambda_{1,2}) > 0$	$\lambda \in \mathbb{C}, Re(\lambda) = 0$
Type of (SS) / Value of d	Stable node	Turing type instability	Stable spiral	Hopf bifurcation	Transcritical bifurcation
2	A	E	$A \cup B \cup C \cup D \cup E$	$A \cup B \cup C \cup D \cup E$	c_5
4	$A \cup B$	$E \cup D$	$B \cup C \cup D \cup E$	$B \cup C \cup D \cup E$	c_4
6	$A \cup B \cup C$	$E \cup D \cup C$	$C \cup D \cup E$	$C \cup D \cup E$	c_3
8	$A \cup B \cup C \cup D$	$E \cup D \cup C \cup B$	$D \cup E$	$D \cup E$	c_2
10	$A \cup B \cup C \cup D \cup E$	$E \cup D \cup C \cup B \cup A$	E	E	c_1

TABLE 3.3: Table showing regions corresponding to the domain-size $L^2 = 225 \geq \frac{\pi^2(d+1)(m^2+n^2)}{\gamma}$, which satisfies (3.24) of Theorem 3.3.2.

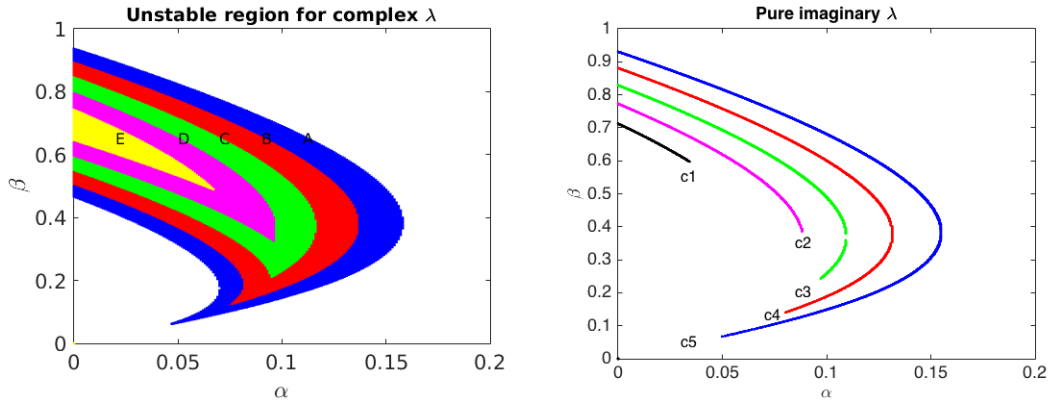

(a) (b)

FIGURE 3.10: In (a) region for complex $\lambda_{1,2}$ and positive real part with corresponding values of d and the condition $L^2 = 225 > \pi^2 \frac{(d+1)(m^2+n^2)}{\gamma}$. In (b) regions corresponding to complex eigenvalues associated to values of d indicated in Figure (a) and condition (3.24).

non-dimensional diffusion coefficient d was increased. Turing diffusion-driven instability also occurs for the case when L^2 satisfies condition (3.24) and it also increases with increased value of d as shown in Figure 3.9 (b). The interpretation is that regions in the parameter space exist, which result in the system to be stable in the absence of diffusion, but when diffusion is added to the system, the choice of the parameters from these particular regions result in the system exhibiting instability. This type of instability is restricted to space and hence leads to spatial patterning only, because the eigenvalues are both real. However, if L^2 satisfies (3.24), then in addition to the existence of regions of the parameter space corresponding to Hopf and transcritical bifurcations, it can also be observed that with increased values of parameter d, unlike Turing instability, the regions for Hopf and transcritical bifurcations reduce as shown in Figure 3.10 (a) and (b). The mathematical intuition for this inverse relation is the direct proportionality of d on the lower bound for the domain-size i.e. the right-hand side of (3.24). Therefore, as d grows, one gets closer to the violation of the necessary condition (3.24) for Hopf and transcritical bifurcations as proposed by Theorem 3.3.2. However, the region for Hopf and transcritical bifurcations remains to exist as long

as L^2 satisfies (3.24), which ultimately means that for the system to exhibit temporal periodicity (patterning in time) the domain-size has to be sufficiently large satisfying (3.24).

3.3.3 Remark

The eigenfunction modes used for the current simulations corresponds to the first non-trivial (non-zero) eigenvalues, namely the case where $m = n = 1$. The results can be readily obtained for any positive integer values of m and n. Despite the fact that using larger integer values for m and n will shift or scale the classification for the parameter space, the conditions given by Theorem 3.3.1 and Theorem 3.3.2 will remain intact irrespective of the values of m and n, so long as they are positive integers.

3.3.4 Finite element formulation and simulation

To validate the proposed classification of parameter space, the reaction-diffusion system (3.1)-(3.3) is numerically solved using the finite element method (Smith, Griffiths, and Margetts, 2013; Becker, 1998) on a unit square domain with a uniform triangular mesh. The solution and test spaces for the weak formulation (Wang, 2003) are respectively given by

$$\begin{aligned} H^1_E(\Omega) =& \{w : w \in H^1(\Omega) : w \text{ satisfies Neumann boundary conditions on } \Omega\} \\ H^1_{E^0}(\Omega) =& \{w : w \in H^1(\Omega) : \frac{\partial w}{\partial \boldsymbol{n}} = 0, \forall x, y \text{ on } \partial\Omega\}, \end{aligned}$$

where $\boldsymbol{n}$ is the outward normal to $\partial\Omega$. Before writing the weak formulation we write the system (3.1)-(3.3) in the form

$$\begin{cases} \frac{\partial u}{\partial t} - \Delta u = & \gamma(\alpha - u + u^2 v) \\ \frac{\partial v}{\partial t} - d\Delta v = & \gamma(\beta - u^2 v). \end{cases} \tag{3.44}$$

To obtain the weak formulation, we multiply both sides of (3.44) by a test function $w \in H^1_{E^0}(\Omega)$ and integrate the system over Ω to obtain

$$\begin{aligned}\int_\Omega \Big(\frac{\partial u}{\partial t} - \Delta u\Big) w d\Omega &= \gamma \int_\Omega \Big(\alpha - u + u^2 v\Big) w d\Omega \\ \int_\Omega \Big(\frac{\partial v}{\partial t} - d\Delta v\Big) w d\Omega &= \gamma \int_\Omega \Big(\beta - u^2 v\Big) w d\Omega.\end{aligned}$$

Integration by parts and application of Green's formula to the diffusion terms in both equations yields

$$\begin{aligned}\int_\Omega \Big(\frac{\partial u}{\partial t} w + \nabla u \cdot \nabla w\Big) d\Omega - \int_{\partial\Omega} \frac{\partial w}{\partial \boldsymbol{n}} u dS &= \gamma \int_\Omega \Big(\alpha - u + u^2 v\Big) w d\Omega \\ \int_\Omega \Big(\frac{\partial v}{\partial t} w + d\nabla v \cdot \nabla w\Big) d\Omega - \int_{\partial\Omega} \frac{\partial w}{\partial \boldsymbol{n}} v dS &= \gamma \int_\Omega \Big(\beta - u^2 v\Big) w d\Omega.\end{aligned}$$

Since w is chosen from the test space, therefore is it defined to satisfy zero flux boundary conditions on Ω, which suggests to vanish the boundary terms in both equations. This leads to the weak formulation of (3.44), which is to find $u, v \in H^1_E(\Omega)$ such that

$$\begin{aligned}\int_\Omega \Big(\frac{\partial u}{\partial t} w + \nabla u \cdot \nabla w\Big) d\Omega &= \gamma \int_\Omega \Big(\alpha - u + u^2 v\Big) w d\Omega \\ \int_\Omega \Big(\frac{\partial v}{\partial t} w + d\nabla v \cdot \nabla w\Big) d\Omega &= \gamma \int_\Omega \Big(\beta - u^2 v\Big) w d\Omega,\end{aligned} \tag{3.45}$$

for all $w \in H^1_{E^0}(\Omega)$. Let $V^h_E(\Omega)$ and $V^h_{E^0}(\Omega)$ be finite dimensional subspaces of $H^1_E(\Omega)$ and $H^1_{E^0}(\Omega)$ respectively, then the finite element formulation for (3.45) is to find $u_h, v_h \in V^h_E(\Omega)$ such that

$$\begin{aligned}\int_\Omega \Big(\frac{\partial u_h}{\partial t} w_h + \nabla u_h \cdot \nabla w_h\Big) d\Omega &= \gamma \int_\Omega \Big(\alpha - u_h + u_h^2 v_h\Big) w_h d\Omega \\ \int_\Omega \Big(\frac{\partial v_h}{\partial t} w_h + d\nabla v_h \cdot \nabla w_h\Big) d\Omega &= \gamma \int_\Omega \Big(\beta - u_h^2 v_h\Big) w_h d\Omega,\end{aligned} \tag{3.46}$$

for all $w_h \in V^h_{E^0}(\Omega)$. Functions u_h and v_h can be expanded in terms of its finite dimensional basis functions in the form

$$u_h = \sum_{i=1}^{N} U_i(t)\phi_i(x,y), \qquad \text{and} \qquad v_h = \sum_{i=1}^{N} V_i(t)\phi_i(x,y),$$

where $U_i(t)$ and $V_i(t)$ are the values of u_h and v_h at node i and $\phi_i(x,y)$ is the basis function, which collectively spans the finite dimensional subspace $V_E^h(\Omega)$. Substituting the expressions for u_h and v_h turns (3.46) into a system of ordinary differential equations in the form

$$\begin{aligned} M\boldsymbol{U}'(t) + S\boldsymbol{U}(t) =& \gamma\alpha\boldsymbol{A} - \gamma M\boldsymbol{U}(t) + \gamma C(\boldsymbol{U},\boldsymbol{V})\boldsymbol{U}(t) \\ M\boldsymbol{V}'(t) + dS\boldsymbol{V}(t) =& \gamma\beta\boldsymbol{A} - \gamma D(\boldsymbol{U})\boldsymbol{V}(t), \end{aligned} \tag{3.47}$$

where $\boldsymbol{U}$ and $\boldsymbol{V}$ are N dimensional vectors, whose entries upon solving the linear system (3.47) will contain the discrete solution values of the system (3.1)-(3.3). Let $\mathcal{T}$ denote the uniform triangulation of Ω, consisting of triangles. The algorithm is programmed to compute locally on each triangle $K \in \mathcal{T}$, the entries of all the matrices M, S, C and D and vector $\boldsymbol{A}$. The local contribution of the N dimensional vector $\boldsymbol{A}$ in (3.47) are 3 dimensional vectors for each triangle K, whose entries are given by

$$A_j = \sum_{K\in\mathcal{T}} \int_K \phi_j(x,y)dxdy. \tag{3.48}$$

Mass and stiffness matrices are denoted by M and S in (3.47) respectively. The contributions from M and S are locally 3×3 matrices for each triangle K whose entries are denoted by M_{ij} and S_{ij} respectively and given by

$$\begin{aligned} M_{ij} &= \sum_{K\in\mathcal{T}} \int_K \phi_i(x,y)\phi_j(x,y)dxdy \\ S_{ij} &= \sum_{K\in\mathcal{T}} \int_K \nabla\phi_i(x,y)\cdot\nabla\phi_j(x,y)dxdy. \end{aligned} \tag{3.49}$$

Matrices associated to the non-linear terms of system (3.1)-(3.3) are denoted by $C(\boldsymbol{U},\boldsymbol{V})$ and $D(\boldsymbol{U})$, whose entries for triangle $K \in \mathcal{T}$ are respectively given by

$$\begin{aligned} C_{ij}(U,V) &= \sum_{K\in\mathcal{T}} \int_K \Big(\sum_{k=1}^{3} U_k(t)\phi_k(x,y)\Big)\Big(\sum_{l=1}^{3} V_l(t)\phi_l(x,y)\Big)\phi_i(x,y)\phi_j(x,y)dxdy \\ D_{ij}(U) &= \sum_{K\in\mathcal{T}} \int_K \Big(\sum_{k=1}^{3} U_k(t)\phi_k(x,y)\Big)^2\phi_i(x,y)\phi_j(x,y)dxdy. \end{aligned} \tag{3.50}$$

System (3.47) of differential equations is solved in time using semi-implicit Euler scheme. It must be noted, that fully implicit scheme is not trivially applicable to the system due to the existence of unknowns in the coefficient matrices namely in $C(\boldsymbol{U}, \boldsymbol{V})$ and in $D(\boldsymbol{U})$. Subject to this constraint we use semi-implicit method, in which the values of the unknowns in the system matrices are treated explicitly and for all other terms in the equations the values of the unknowns are treated implicitly. We discretise time $[0, T]$ by finite number of intervals in the form $(0, T_1, T_2, ..., T_f)$ with uniform step size Δt, where $T_f = T$. Let $\boldsymbol{U}^m$ and $\boldsymbol{V}^m$ denote the solution vectors of the equations for u and v at mth time step. The linear system (3.47) with semi-implicit discrete time stepping takes the form

$$\begin{aligned} M\frac{\boldsymbol{U}^{m+1}-\boldsymbol{U}^m}{\Delta t} + S\boldsymbol{U}^{m+1} =& \gamma\alpha\boldsymbol{A} - \gamma M\boldsymbol{U}^{m+1} + \gamma C(\boldsymbol{U}^m, \boldsymbol{V}^m)\boldsymbol{U}^{m+1}, \\ M\frac{\boldsymbol{V}^{m+1}-\boldsymbol{V}^m}{\Delta t} + dS\boldsymbol{V}^{m+1} =& \gamma\beta\boldsymbol{A} - \gamma D(\boldsymbol{U}^m)\boldsymbol{V}^{m+1}, \end{aligned} \tag{3.51}$$

which proposes that the discrete solution of system (3.1)-(3.3) is given by the set of algebraic equations for each time step in the form

$$\begin{aligned} A_1\boldsymbol{U}^{m+1} =& \boldsymbol{B}_1(\boldsymbol{U}^m), \\ A_2\boldsymbol{V}^{m+1} =& \boldsymbol{B}_2(\boldsymbol{U}^m), \end{aligned} \tag{3.52}$$

where the matrices A_1 and A_2 are expressed by

$$\begin{aligned} A_1 =& M + \Delta tS + \Delta t\gamma M - \Delta t\gamma C(\boldsymbol{U}^m, \boldsymbol{V}^m), \\ A_2 =& M + d\Delta tS + \Delta t\gamma D(\boldsymbol{U}^m). \end{aligned} \tag{3.53}$$

The right hand-side vectors $\boldsymbol{B}_1$ and $\boldsymbol{B}_2$ are given by

$$\begin{aligned} \boldsymbol{B}_1(\boldsymbol{U}^m) =& M\boldsymbol{U}^m + \gamma\alpha\Delta t\boldsymbol{A}, \\ \boldsymbol{B}_2(\boldsymbol{U}^m) =& M\boldsymbol{V}^m + \gamma\beta\Delta t\boldsymbol{A}. \end{aligned} \tag{3.54}$$

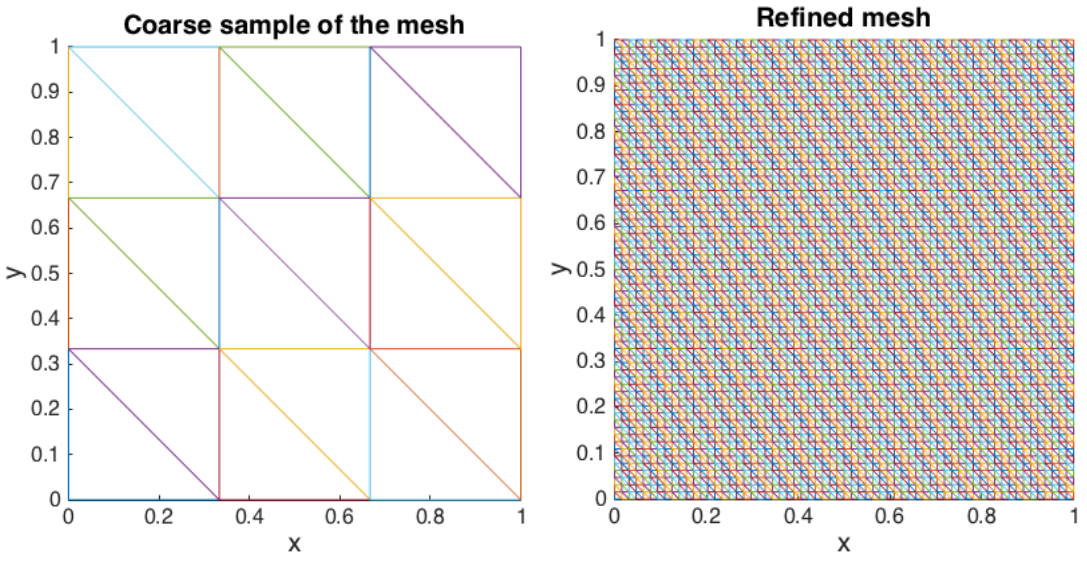

(a) (b)

FIGURE 3.11: In (a) the coarse geometry of the triangulation set-up is shown. In (b) the fully refined mesh is shown.

Simulations are all computed on a unit square domain, with uniform triangular mesh. Unit square is discretised by 64 points in both directions x and y, leading to create 4225 nodes and 4096 quadrilateral cells. These quadrilateral cells are further triangulated by diagonal lines of slope negative one connecting all nodes that lie on the straight line, which leads to a discretised Ω_h, consisting of 8192 triangles. Figure 3.11 (a) and (b) respectively show a coarse geometry of the mesh and the actual refinement of the triangulation used for simulations. For the current simulations the choice of finite elements used are piecewise linear polynomials, which is a reasonable choice for this demonstration. Although the improvement in accuracy associated with using higher order polynomials is known to researchers, however due to the significant amount of computational weight it adds to the task, makes it not a desirable trade for the purpose of this work. Numerical simulations are performed for various choices of parameter values α and β, chosen from the appropriate parameter spaces to demonstrate and validate our theoretical findings. In all our simulations, we vary the parameters d and γ and keep fixed the domain length size L and this allows us to keep constant the well refined number of degrees of freedom for the mesh. The initial conditions for each

simulation are taken as small random perturbations around the neighbourhood of the steady state of the form (Madzvamuse, Gaffney, and Maini, 2010; Madzvamuse, 2008)

$$\begin{cases} u_0(x,y) = \alpha + \beta + 0.0016\cos(2\pi(x+y)) + 0.01\sum_{i=1}^{8}\cos(i\pi x), \\ v_0(x,y) = \frac{\beta}{(\alpha+\beta)^2} + 0.0016\cos(2\pi(x+y)) + 0.01\sum_{i=1}^{8}\cos(i\pi x). \end{cases} \tag{3.55}$$

The final time T is chosen to ensure that beyond T the convergence of solutions in successive time-step differences decay to a threshold of 10^{-5} for all the simulations. Therefore, in the case where the area L^2 of the domain-size satisfies condition (3.23) proven in Theorem 3.3.1, when temporal instability is forbidden by the condition on the domain-size, the final time of numerical simulations is relatively shorter compared to that used for other cases. For numerical simulations on the domain-size L^2 satisfying condition (3.24) proven in Theorem 3.3.2, the final time is experimented for longer periods to capture possible existence of temporal periodicity in the dynamics. Simulations with domain-size satisfying (3.24) are captured at different times, which varies with cases, for which details are included in Table 3.4. In all our numerical results, we only exhibit numerical solutions corresponding to the $u(x,y,t)$ component, those of $v(x,y,t)$ are known to be 180-degrees out of phase to those of u. Figure 3.12 presents the case where the parameters $\alpha = 2$ and $\beta = 2$ are chosen from stable node region of Table 3.2, with final time $T = 2$. It can be observed that the evolved profile of the concentration u uniformly converges to the steady state value forming neither spatial nor temporal patterns (Figure 3.12 (a)). As predicted in Theorem 3.3.1, no choice of parameters α and β can influence the dynamics to exhibit temporal periodicity, therefore any choice of the parameters outside Turing space, given that the domain-size satisfies (3.23) will uniformly converge to the stable steady state $(u_s, v_s) = (\alpha+\beta, \frac{\beta}{(\alpha+\beta)^2}) \approx (4, 0.125)$ as seen in Figure 3.12 (a). Figure 3.12 (b) shows the uniform convergence of the discrete L_2-norm difference between solutions at successive time-steps to the constant steady state (u_s, v_s), where there is no sign of instability occurring, when parameters are outside the Turing space. Finite element nu-

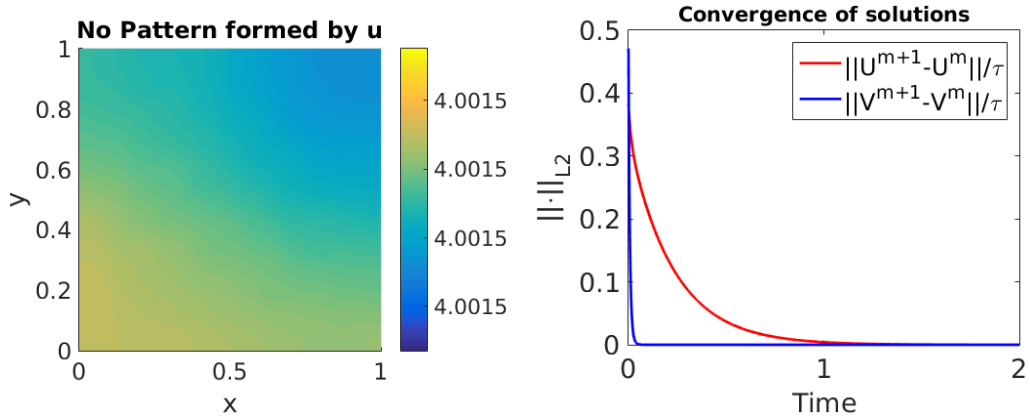

(a) (b)

FIGURE 3.12: In (a) the evolved discrete solution U at the final time step $T = 2$ is shown. In (b) the convergence of the discrete time derivative of the numerical solutions U and V for successive time steps is shown.

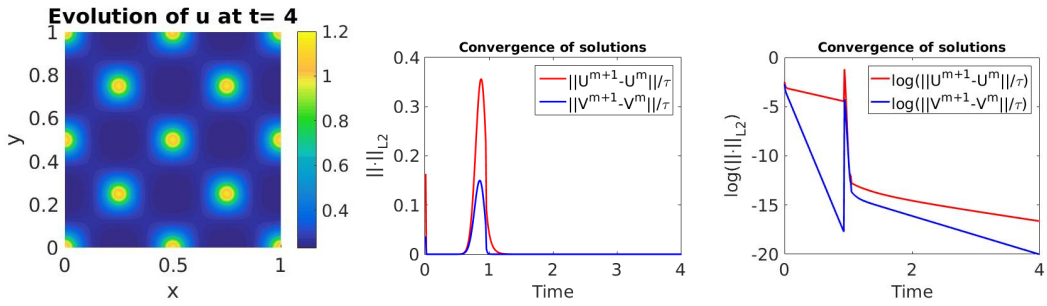

(a) (b) (c)

FIGURE 3.13: In (a) the evolved discrete solution U at the final time step $T = 4$ is shown. In (b) the convergence in the L_2 norm of the discrete time derivative of the solutions U and V. In (c) the logarithmic convergence in the L_2 norm of the discrete time derivative of the solutions U and V is shown.

merical simulations corresponding to the u of the model system (3.1) with parameter values α and β selected from the Turing space (see Table 3.4 for values) and domain-size satisfying (3.23). We observe the formation of spot patterns, again in agreement with the theoretical predictions. Figure 3.14 shows the simulation for the choice of parameters from the Turing space presented in Table 3.3 for the domain-size satisfying (3.24). In this case as predicted in Theorem 3.3.2, regions of parameter space exist for which the dynamic can exhibit Hopf type bifurcation, therefore, the possibility of temporal periodicity in the dynamics. Figure 3.15 presents such periodicity in time for spatial patterns. The relative discrete L_2-norm of the difference in the solutions for successive time-steps is therefore showing time periodicity as illustrated in Figure 3.15 (d), which indicates the transition of the solution from the initially achieved spatial pattern to a different spatial pattern.

Plot index	Figure 3.12	Figure 3.13	Figure 3.14	Figure 3.15
Instability / Parameters	No instability No pattern	Turing type instability Spatial pattern	Turing type instability Spatial pattern	Hopf bifurcation Spatial and temporal pattern
(α, β)	$(2, 2)$	$(0.025, 0.4)$	$(0.1, 0.6)$	$(0.05, 0.8)$
(d, γ)	$(10, 210)$	$(10, 210)$	$(10, 300)$	$(10, 350)$
Condition on Ω	(3.23)	(3.23)	(3.24)	(3.24)
Simulation time	2	4	4	6
CPU time (sec)	77.14	149.60	149.55	215.02

TABLE 3.4: Showing the choice of parameters (α, β) for each simulation and the choice of (d, γ) subject to the relevant condition referred to in third row. Each simulation was run with time-step of 1×10^{-3}.

3.4 Conclusion

In this chapter the full parameter spaces for a reaction-diffusion system with *activator-depleted* reaction kinetics was classified through the use of linear stability theory and in each region of the parameter space the dynamics of the reaction-diffusion system were verified to exhibit the predicted type of behaviour. In the absence of diffusion, theoretical results on the dynamics of the system were supported by use of the phase-plane analysis, where in each case the numerical solution of the system was observed to be in agreement with the theoretically predicted behaviour. In the presence of diffusion, for a two-component reaction-diffusion system, two conditions relating the

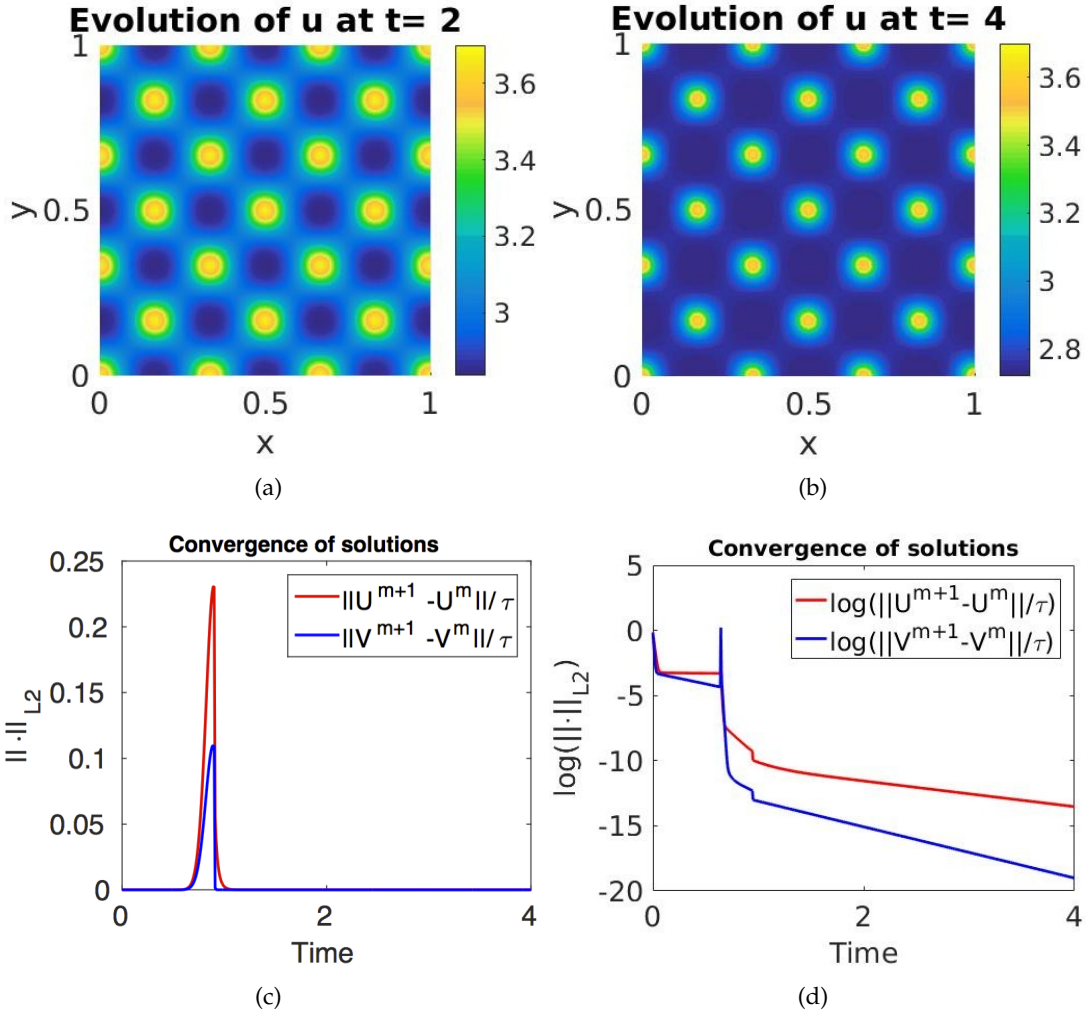

FIGURE 3.14: In (a) the evolving discrete solution U captured at time step $t = 2$ is shown. In (b) the evolved discrete solution U captured at final time step $t = 4$ is shown. In (c) the convergence in the L_2 norm of the discrete time derivative of the solutions U and V. In (d) the logarithmic convergence in the L_2 norm of the discrete time derivative of the solutions U and V is shown.

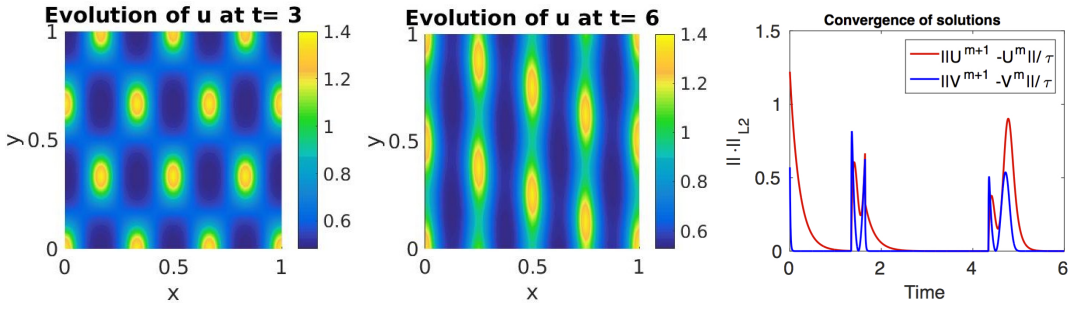

(a) (b) (c)

FIGURE 3.15: In (a) the evolving discrete solution U captured at time step $t = 0.4$ is shown. In (b) the evolving discrete solution U captured at time step $t = 3$ is shown. In (c) convergence of the difference of the discrete solution U and V for successive time steps is shown.

domain-size to the diffusion and reaction rates were derived. The proofs of these conditions were presented in Theorems 3.3.2 and 3.3.1, respectively. For full classification of the parameter space, a numerical method was used to compute the solutions of the implicit curves in the parameter space forming the partitions of classification. In particular, using condition (3.23) the numerical method for solving the partitioning curves showed the non-existence of a region in parameter space that (if existed) would lead to Hopf bifurcation or limit-cycle behaviour. Similarly, applying the numerical method to compute the partitioning curves under condition (3.24), it was shown that regions in parameter space exist for both Hopf and transcritical bifurcation. Parameters from Hopf bifurcation region as well as from Turing regions under both conditions on the domain-size were shown to be in agreement with the theoretical prediction, when the system was numerically solved by using the finite element method. For each simulation the discrete L_2-norm of the successive time-step difference of the solutions is also given to visualise the temporal dynamics of the behaviour of the solutions during the convergence process. This work sets the premises to study more complex systems of non-autonomous reaction-diffusion equations during growth development whereby the parameter spaces are continuously evolving due to domain growth. It will be revealing to study how the Turing diffusion-driven parameter space, the Hopf and Transcritical regions evolve with time and how the dynamics of the model system evolve.

The motivation for such extension is to find whether the conditions (3.23) and (3.24) for the domain-size with reaction and diffusion rates continue to hold or whether a threshold for the domain-size exists, beyond which, these conditions can be invalidated. Another direction of further investigation is to try and find similar relationships for different geometries such as spherical, elliptical and cylindrical domains. It may be noted that the eigenvalues and eigenfunctions of the Laplace operator change significantly depending on the boundary conditions and the geometry of the domain, therefore, application of the present method suggests, that finding similar conditions for other geometries require a careful step-by-step procedure to find analogous conditions to those given by (3.23) and (3.24). It is in this effect that the next chapter is devoted to the application of this framework employing appropriate analytical and numerical techniques to a two dimensional disc-shape geometry in which the influence of the size of the radius of such geometry is explored in the context of bifurcation analysis.

Chapter 4

Analysis on circular geometries

In this chapter the *activator-depleted* reaction-diffusion system is investigated on polar coordinates with the aim of exploring the relationship and the corresponding influence of domain-size on the types of possible diffusion-driven instabilities. This chapter consists of the contents of (Sarfaraz and Madzvamuse, 2018), which is accepted and is in press for publication at the time of writing this thesis. Quantitative relationships are found in the form of necessary conditions on the area of a disc-shape domain with respect to the diffusion and reaction rates for certain types of diffusion-driven instabilities to occur. Robust analytical methods are applied to find explicit expressions for the eigenvalues and eigenfunctions of the diffusion operator on a disc-shape domain with homogeneous Neumann boundary conditions in polar coordinates. Spectral method is applied using Chebyshev non-periodic grid for the radial variable and Fourier periodic grid on the angular variable to verify the nodal lines and eigen-surfaces subject to the proposed analytical findings. The full classification of the parameter space in light of the bifurcation analysis is obtained and numerically verified by finding the solutions of the partitioning curves inducing such a classification. Furthermore, analytical results are found relating the area of a flat (disc-shape) domain with reaction-diffusion rates in the form of necessary conditions for the different types of bifurcations. These results are on one hand presented in the form of mathematical theorems with proofs, and, on the other hand using finite element method on a non-uniform mesh, each

claim of the corresponding theorems are verified by obtaining the theoretically predicted behaviour of the dynamics in the numerical simulations. Spatio-temporal periodic behaviour is demonstrated in the numerical solutions of the system for a proposed choice of parameters and a mathematical proof of the existence of infinitely many such points in the parameter plane is presented under a restriction on the area of the domain, with a lower bound in terms of reaction-diffusion rates.

4.1 Model equations

Two chemical species u and v are modelled by the well-known *activator-depleted* reaction-diffusion system. The RDS is considered on a two dimensional circular domain denoted by $\Omega \in \mathbb{R}^2$, where Ω is defined by

$$\Omega = \{(x, y) \in \mathbb{R}^2 : x^2 + y^2 < \rho^2\}.$$

This forms a two dimensional disc-shape domain with a circle forming its boundary denoted by $\partial\Omega$, which contains the points given by

$$\partial\Omega = \{(x, y) \in \mathbb{R}^2 : x^2 + y^2 = \rho^2\}.$$

The RDS with *activator-depleted* reaction kinetics in its non-dimensional form on cartesian coordinates has the form

$$\begin{cases} \frac{\partial u}{\partial t} = & \Delta u + \gamma(\alpha - u + u^2 v), \qquad (x, y) \in \Omega, \quad t > 0, \\ \frac{\partial v}{\partial t} = & d\Delta v + \gamma(\beta - u^2 v), \end{cases} \tag{4.1}$$

where α, β, γ and d are strictly positive real constants. In system (4.1) the positive parameter d denotes the non-dimensional ratio of diffusion rates given by $d = \frac{D_v}{D_u}$, where D_v and D_u are the independent diffusion rates of v and u respectively. The non-dimensional parameter γ is known as the scaling parameter of (4.1), which quantifies the reaction rate. The boundary of Ω under the current study assumes zero flux

conditions, which means that the chemical species u and v can neither escape nor enter through $\partial\Omega$. This type of boundary conditions are referred to as homogeneous Neumann boundary conditions, which are written as

$$\frac{\partial u}{\partial \boldsymbol{n}} = \frac{\partial v}{\partial \boldsymbol{n}} = 0, \qquad \text{on} \quad (x,y) \in \partial\Omega, \quad t \geq 0, \tag{4.2}$$

where $\boldsymbol{n}$ denotes the normal to $\partial\Omega$ in the outward direction. Initial conditions for (4.1) are prescribed such that initially some strictly positive quantity is present from each concentration at the starting instant of the dynamics, which is written as

$$u(x,y,0) = u_0(x,y), \qquad v(x,y,0) = v_0(x,y), \qquad (x,y) \in \Omega, \quad t = 0, \tag{4.3}$$

where $u_0(x,y)$ and $v_0(x,y)$ are positive bounded continuous functions.

4.1.1 Transformation of the coordinates

In order to set out appropriate framework for the analysis of (4.1) and due to the geometric nature of Ω, it becomes essential to transform (4.1)-(4.3) to polar coordinates. Using the transformation $x = r\cos\theta$ and $y = r\sin\theta$ all the operators and relevant boundary and initial conditions are transformed from the usual cartesian coordinates of the form (x,y,t) to polar coordinates of the form (r,θ,t). First of all note that the transformation is purely spatial, hence it precludes any relevance with the independent variable t, therefore, the time derivative of each variable remains the same in both sets of coordinates, which means we may write

$$\frac{\partial u}{\partial t}(x,y,t) = \frac{\partial u}{\partial t}(r,\theta,t), \qquad \frac{\partial v}{\partial t}(x,y,t) = \frac{\partial v}{\partial t}(r,\theta,t). \tag{4.4}$$

The transformation of the diffusion operator to polar coordinates is a well-studied process in the literature (Hobson, 1944; Arfken and Weber, 1999), however for the purpose of completion, it is briefly explained. The usual method for computing the diffusion operator in polar coordinates is the forward application of chain rule and

direct transformation of each term in the operator, which is a laborious process, thus for the present purpose a reverse-like method is approached, which significantly reduces the length and complexity of the computation. We start by stating clearly the expressions for the first derivatives of cartesian variables (x, y) with respect to polar variables (r, θ), which are given by

$$\frac{\partial x}{\partial r} = \cos\theta, \qquad \frac{\partial x}{\partial \theta} = -r\sin\theta, \qquad \frac{\partial y}{\partial r} = \sin\theta, \qquad \frac{\partial y}{\partial \theta} = r\cos\theta. \tag{4.5}$$

Using (4.5), the first and second derivatives of the dependent variable u are computed with respect to the polar variables r and θ respectively. Application of chain rule and using (4.5) leads to the expression for $\frac{\partial u}{\partial r}$, in the form

$$\frac{\partial u}{\partial r} = \cos\theta\frac{\partial u}{\partial x} + \sin\theta\frac{\partial u}{\partial y} \tag{4.6}$$

Repeating the process yields the expression for $\frac{\partial^2 u}{\partial r^2}$ in the form

$$\frac{\partial^2 u}{\partial r^2} = \cos^2\theta\frac{\partial^2 u}{\partial x^2} + 2\sin\theta\cos\theta\frac{\partial^2 u}{\partial x\partial y} + \sin^2\theta\frac{\partial^2 u}{\partial y^2}. \tag{4.7}$$

Applying the same process leads to the expressions for $\frac{\partial u}{\partial \theta}$ and $\frac{\partial^2 u}{\partial \theta^2}$, which are respectively given by

$$\frac{\partial u}{\partial \theta} = -r\sin\theta\frac{\partial u}{\partial x} + r\cos\theta\frac{\partial u}{\partial y}. \tag{4.8}$$

and

$$\frac{\partial^2 u}{\partial \theta^2} = -r\Big(\cos\theta\frac{\partial u}{\partial x} + \sin\theta\frac{\partial u}{\partial y}\Big) + r^2\Big(\sin^2\theta\frac{\partial^2 u}{\partial x^2} - 2\cos\theta\sin\theta\frac{\partial^2 u}{\partial x\partial y} + \cos^2\theta\frac{\partial^2 u}{\partial y^2}\Big). \tag{4.9}$$

Direct substitution of (4.6) in (4.9) and dividing both sides of (4.9) by r^2, one obtains

$$\frac{1}{r^2}\frac{\partial^2 u}{\partial \theta^2} = -\frac{1}{r}\frac{\partial u}{\partial r} + \sin^2\theta\frac{\partial^2 u}{\partial x^2} - 2\cos\theta\sin\theta\frac{\partial^2 u}{\partial x\partial y} + \cos^2\theta\frac{\partial^2 u}{\partial y^2}. \tag{4.10}$$

Adding (4.7) to (4.10) and using the property $\sin^2\theta + \cos^2\theta = 1$ leads to the final expression for the diffusion operator in polar coordinates which is given by

$$\frac{\partial^2 u}{\partial r^2} + \frac{1}{r}\frac{\partial u}{\partial r} + \frac{1}{r^2}\frac{\partial^2 u}{\partial \theta^2} = \frac{\partial^2 u}{\partial x^2} + \frac{\partial^2 u}{\partial y^2}. \tag{4.11}$$

Let the diffusion operator in polar coordinates be denoted by Δ_p, then the expression on the left of (4.11) is often found in literature in the following compact form

$$\Delta_p u(r,\theta) = \frac{1}{r}\frac{\partial}{\partial r}\left(r\frac{\partial u}{\partial r}\right) + \frac{1}{r^2}\frac{\partial^2 u}{\partial \theta^2}. \tag{4.12}$$

Using the statement given by (4.4) and the notation defined by (4.12), one may rewrite system (4.1) in a form defined in polar coordinates, which is

$$\begin{cases} \frac{\partial u}{\partial t} = & \Delta_p u + \gamma f(u,v), \\ \frac{\partial v}{\partial t} = & d\Delta_p v + \gamma g(u,v), \end{cases} \tag{4.13}$$

where u and v depend on coordinates (r,θ) and the functions f and g are defined by $f(u,v) = \alpha - u + u^2 v$ and $g(u,v) = \beta - u^2 v$. In (4.13) the strictly positive constants namely α, β, d and γ remain to satisfy exactly the same definitions as in (4.1). The boundary conditions may also be transformed to polar coordinates by noting that due to the circular geometry of the boundary $\partial\Omega$, the outward normal $\boldsymbol{n}$ at any point (ρ,θ) will always be found perpendicular to the tangent vector at that point. It means that the equivalent to zero flux boundary conditions in polar coordinates will take the form

$$\left.\frac{\partial u}{\partial r}\right|_{r=\rho} = \left.\frac{\partial v}{\partial r}\right|_{r=\rho} = 0, \qquad (r,\theta) \in \partial\Omega, \quad t \geq 0. \tag{4.14}$$

Finally the initial conditions can also be written in polar coordinates, which are by definition spatial strictly positive bounded functions of the form

$$u(r,\theta,0) = u_0(r,\theta), \qquad v(r,\theta,0) = v_0(r,\theta), \qquad (r,\theta) \in \Omega, \quad t = 0. \tag{4.15}$$

4.1.2 A note on the absence of diffusion case

Comparing system (4.1)-(4.3) in cartesian coordinates to system (4.13)-(4.15) in polar coordinates, they are exactly the same in formulation, except the significant difference in the expression for the diffusion operator. Therefore, omitting the diffusion operator from the transformed system (4.13)-(4.15) leads to take exactly the same as form as the original system given by (4.1)-(4.3). This means that stability analysis of system (4.1)-(4.3) in the absence of diffusion suffices to provide every insight about stability analysis in the absence of diffusion for system (4.13)-(4.15). Omitting the diffusion terms from system (4.13)-(4.15) yields a system of ordinary differential equations, therefore the analysis become independent of spatial geometry (Estep, Larson, and Williams, 2000). Hence, all the existing results on stability analysis and parameter classification of *activator-depleted* reaction kinetics in the absence of diffusion hold true independent of the choice of geometry for the domain. A detailed study in (Sarfaraz and Madzvamuse, 2017) on the classification of parameter spaces in light of stability analysis for *activator-depleted* reaction kinetics in the absence of diffusion, which holds true if the diffusion terms are excluded from system (4.13)-(4.15). Therefore, to avoid repetition of the same effort for known results, the investigation is directly focused on the presence of diffusion case in this chapter.

4.2 Linearisation and the eigenfunctions

Let u_s and v_s denote the uniform steady state solution of the *activator-depleted* reaction kinetics in the absence of diffusion. Then the unique pair of solution satisfying (4.1) in the absence of diffusion is of the form $(u_s, v_s) = (\alpha + \beta, \frac{\beta}{(\alpha+\beta)^2})$ (Murray, 2001; Edelstein-Keshet, 1988; Lakkis, Madzvamuse, and Venkataraman, 2013), which also satisfies the system (4.13)-(4.15) in the presence of diffusion. This is because the uniform steady state is a constant solution of the system, which vanishes on the application of the diffusion and the prescribed boundary conditions given by (4.14), therefore it is reasonable to consider this as the uniform steady state solution of the system

(4.13) also in the presence of diffusion. For linear stability analysis, system (4.13) is perturbed in the neighbourhood of the uniform steady state (u_s, v_s) and the dynamics of the perturbed system are explored. Let $\bar{u}$ and $\bar{v}$ denote the concentrations u and v after the system is perturbed in the neighbourhood of (u_s, v_s). The new variables $(\bar{u}, \bar{v})$ are chosen, so that their relationship with the original variables is of the form $(u, v) = (\bar{u} + u_s, \bar{v} + v_s)$, where u and v are assumed small. In system (4.13) the variables u and v are substituted by the expression in terms of $(\bar{u}, \bar{v})$ and (u_s, v_s) and expanded using Taylor expansion for functions of two variables up to and including the linear terms with the higher order terms discarded. This leads to the linearised version of system (4.13) written in matrix form as

$$\frac{\partial}{\partial t}\begin{bmatrix} \bar{u} \\ \bar{v} \end{bmatrix} = \begin{bmatrix} 1 & 0 \\ 0 & d \end{bmatrix}\begin{bmatrix} \Delta_p \bar{u} \\ \Delta_p \bar{v} \end{bmatrix} + \begin{bmatrix} \frac{\partial f}{\partial u}(u_s, v_s) & \frac{\partial f}{\partial v}(u_s, v_s) \\ \frac{\partial g}{\partial u}(u_s, v_s) & \frac{\partial g}{\partial u}(u_s, v_s) \end{bmatrix}\begin{bmatrix} \bar{u} \\ \bar{v} \end{bmatrix}. \tag{4.16}$$

The next step to complete the linearisation of system (4.13) is to compute the eigenfunctions of the diffusion operator namely Δ_p, which will require to find the solution to an elliptic 2 dimensional eigenvalue problem on a disc that satisfies the homogeneous Neumann boundary conditions prescribed for system (4.13).

4.2.1 Derivation of the eigenfunctions

The solution of eigenvalue problems on spherical domains is a relatively focused topic (Arfken and Weber, 1999; Benedetto, 1996; Li, 2007), with the majority of focus on problems with boundary-free manifolds such as circle, torus and/or sphere. Considering the restriction imposed from the boundary conditions prescribed for the current problem, entails that the case requires explicit detailed treatment to rigorously find the eigenfunctions satisfying these boundary conditions. Therefore, it is important to present a step-by-step demonstration of the process, starting with writing out the relevant eigenvalue problem all the way through to finding the closed form solution in the form of an infinite set of eigenfunctions satisfying such eigenvalue problem. The

eigenvalue problem we want to solve is of the form

$$\begin{cases} \Delta_p w = -\eta^2 w, & \eta \in \mathbb{R}, \\ \frac{\partial w}{\partial r}\big|_{r=\rho} = 0, & \rho \in \mathbb{R}_+ \backslash \{0\}, \end{cases} \tag{4.17}$$

where Δ_p is the diffusion operator in polar coordinates defined by (4.12), on a disc with radius ρ. Application of separation of variables to problem (4.17) requires a solution of the form $w(r,\theta) = R(r)\Theta(\theta)$, which is substituted in problem (4.17) to obtain

$$\frac{d^2R}{dr^2}\Theta + \frac{1}{r}\frac{dR}{dr}\Theta + \frac{1}{r^2}R\frac{d^2\Theta}{d\theta^2} = -\eta^2 R\Theta. \tag{4.18}$$

Dividing both sides of (4.18) by $R\Theta$, multiplying it by r^2 and rearranging, yields

$$r^2\frac{1}{R}\frac{d^2R}{dr^2} + r\frac{1}{R}\frac{dR}{dr} + \eta^2 r^2 = -\frac{1}{\Theta}\frac{d^2\Theta}{d\theta^2}. \tag{4.19}$$

Due to the periodic nature of $\Theta(\theta)$ the admissible solution is of the form $\Theta(\theta) = \exp(in\theta)$, where $i = \sqrt{-1}$ and $n \in \mathbb{R}$. This solution is substituted in (4.19) to obtain a second order ordinary differential equation with variable coefficients for $R(r)$ in the form

$$\frac{d^2R}{dr^2} + \frac{1}{r}\frac{dR}{dr} + (\eta^2 - \frac{n^2}{r^2})R = 0. \tag{4.20}$$

Applying a change of variable to (4.20), using linear transformation for the variable r in the form $x = \eta r$, will transform equation (4.20) to the exact form of Bessel's equation, written as

$$x^2\frac{d^2R}{dx^2} + x\frac{dR}{dx} + (x^2 - n^2)R = 0. \tag{4.21}$$

Equation (4.21) is referred to as Bessel's equation of order n, for which we seek the solution through Frobenius method. It is worth noting that equation (4.21) has different forms of solutions depending on the nature of its order namely the value of n. Even though the solution of Bessel's equation and Frobenius method are well-studied topics, however, due to the fact that our solution is expected to satisfy the boundary

conditions prescribed by (4.17), therefore, a step by step derivation of the solution is a reasonable approach. Equation (4.19) is first written in what is called a standard form, which offers the advantage of making singular points (if any exists) clear to observe. Dividing equation (4.21) by x^2 and simplifying, provides the standard form, which is written as

$$\frac{d^2R}{dx^2} + \frac{1}{x}\frac{dR}{dx} + \left(1 - \frac{n^2}{x^2}\right)R = 0. \tag{4.22}$$

It is clear from (4.22) that it has only one removable singular point at $x = 0$, which is the reason why Frobenius method is sufficient to find series solution of equation (4.22). We seek a solution in the form of an infinite sum of Frobenius series, which means we may write $R(x)$, $\frac{dR}{dx}$ and $\frac{d^2R}{dx^2}$ in the form

$$R(x) = \sum_{k=0}^{\infty} C_k x^{s+k}, \quad \frac{dR}{dx} = \sum_{k=0}^{\infty} C_k(s+k)x^{s+k-1}, \quad \frac{d^2R}{dx^2} = \sum_{k=0}^{\infty} C_k(s+k)(s+k-1)x^{s+k-2}. \tag{4.23}$$

Substituting (4.23) in (4.22) and following the usual steps required for Frobenius method (Boas, 2006; Lebedev, 1965) and comparing coefficients, one arrives at the indicial equation of the from $C_0\big(s(s-1)+s-n^2\big) = 0$, which holds true under the usual assumption that $C_0 \neq 0$ if and only if $s = \pm n$. This information is obtained from exploring the series solution up to and including the $(s-2)$ powers of x. In order to obtain a complete set of solutions, it is required to further investigate the expressions for the coefficients that correspond to higher powers of x in the series solutions, since a complete set of solution is expected to be in the form of an infinite series. The infinite series that corresponds to each term in the equation (4.22) can be written as a single sum using a shift of indices, in the form

$$\sum_{k=2}^{\infty}\Big(\big[(s+k)(s+k-1)+(s+k)-n^2\big]C_k + C_{k-2}\Big)x^{s+k-2} = 0, \tag{4.24}$$

which contains all the terms of the solution that are associated to powers beyond $(s-2)$ of x. The coefficients in (4.24) must be equated to zero for it to satisfy (4.22), which

leads to a recursive relation for the coefficients in the form

$$C_k = \frac{-C_{k-2}}{(s+k)^2 - n^2}, \tag{4.25}$$

where the solution of the indicial equation namely $s = n$ is substituted in the recursive relation (4.25) to obtain

$$C_k = \frac{-C_{k-2}}{k(2n+k)}. \tag{4.26}$$

Relation (4.26) can be readily used to verify that all the coefficients corresponding to odd integers of the form $C_k = C_{2j+1}, j \in \mathbb{N}$ must be zero. This leaves to further explore the coefficients corresponding to even integers, which can be studied through replacing C_k by $C_{2j}, j \in \mathbb{N}$ and finding the pattern that relates C_{2j} for any $j \in \mathbb{N}$ to the first non-zero coefficient of the series, which is by definition C_0. Such a relation can easily be found in the form

$$C_{2j} = \frac{(-1)^j C_0}{4^j \times j! \times (n+j) \times (n+j-1) \times \cdots \times (n+1)}. \tag{4.27}$$

Using relation (4.27), under the assumption that the value of n is neither a full nor is it a half integer, one may write the full solution to equation (4.22) as the sum of two linearly independent infinite series solutions in the form $R(x) = R^1(x) + R^2(x)$, where $R^1(x)$ and $R^2(x)$ are respectively given by

$$R^1(x) = x^n \sum_{j=0}^{\infty} \frac{(-1)^j C_0 x^{2j}}{4^j \times j! \times (n+j) \times (n+j-1) \times \cdots \times (n+1)} \tag{4.28}$$

and

$$R^2(x) = x^{-n} \sum_{j=0}^{\infty} \frac{(-1)^j C_0 x^{2j}}{4^j \times j! \times (-n+j) \times (-n+j-1) \times \cdots \times (-n+1)}. \tag{4.29}$$

Series solutions (4.28) and (4.29) are referred to as Bessel functions of the first kind (Benedetto, 1996; Spanier and Oldham, 1987). Before writing the general solution to problem (4.17), it must be noted that we require R to be a function of r and not that

of x, bearing in mind that r is related to x under the linear transformation given by $x = \eta r$. Therefore, the general solution to problem (4.17) can be written in the form

$$w(r,\theta) = R(x(r))\Theta(\theta), \tag{4.30}$$

where $R(x(r)) = R_1(x(r)) + R_2(x(r))$ and $\Theta(\theta) = \exp(in\theta)$, with R_1 and R_2 defined by (4.28) and (4.29) respectively. The homogeneous Neumann boundary conditions are imposed on the set of eigenfunctions (4.30), and noting that the flux is independent of the variable θ, which means that

$$\frac{\partial w}{\partial r}\Big|_{r=\rho} = 0 \qquad \Longrightarrow \qquad \frac{dR}{dr}\Big|_{r=\rho} = 0. \tag{4.31}$$

A straightforward application of chain rule yields $\frac{dR}{dr} = \eta \frac{dR}{dx}$, which may be written as

$$\frac{dR}{dr}\Big|_{r=\rho} = \eta \frac{dR}{dx}\Big|_{x=\eta\rho}. \tag{4.32}$$

Let a_j and b_j denote the coefficients corresponding the jth term in the infinite series for $R_1(x)$ and $R_2(x)$ respectively, then for every $j \in \mathbb{N}$ the expression for a_j and b_j takes the form

$$a_j = \frac{(-1)^j C_0}{4^j \times j! \times (n+j) \times (n+j-1) \times \cdots \times (n+1)}, \tag{4.33}$$

$$b_j = \frac{(-1)^j C_0}{4^j \times j! \times (-n+j) \times (-n+j-1) \times \cdots \times (-n+1)}, \tag{4.34}$$

which means that $R(x)$ can be written in the form

$$R(x) = \sum_{j=0}^{\infty} \left(a_j x^{n+2j} + b_j x^{-n+2j}\right). \tag{4.35}$$

Differentiating $R(x)$ with respect to x as written in (4.35) and equating it to zero with the substitution $x = \eta\rho$ and using the relation (4.32) one obtains the equation

$$\begin{aligned} 0 = \frac{dR}{dr}\Big|_{r=\rho} =& \eta \sum_{j=0}^{\infty} \left[a_j(n+2j)x^{n+2j-1} + b_j(-n+2j)x^{-n+2j-1}\right]\Big|_{x=\eta\rho} \\ =& \eta \sum_{j=0}^{\infty} \left[a_j(n+2j)(\eta\rho)^{n+2j-1} + b_j(-n+2j)(\eta\rho)^{-n+2j-1}\right] \\ =& \eta \Big[(\eta\rho)^n \sum_{j=0}^{\infty} a_j(n+2j)(\eta\rho)^{2j-1} + (\eta\rho)^{-n} \sum_{j=0}^{\infty} b_j(-n+2j)(\eta\rho)^{2j-1}\Big], \end{aligned} \tag{4.36}$$

which can only hold true if both of the summations are independently zero. Investigating the first summation and expanding it for a few successive terms, it can be shown that the successive terms carry alternating signs (due to the expression for a_j), therefore, the only way the infinite series can become zero is if each of the successive terms cancel one another. Let F_j and S_j denote the jth terms of the first summation and second summation in (4.36) respectively, then for (4.36) to hold true, $F_j + F_{j+1} = 0$ and $S_j + S_{j+1} = 0$ must be true for all $j \in \mathbb{N}$. The full expressions for F_j and F_{j+1} can be written as

$$F_j = \frac{(\eta\rho)^n(-1)^j C_0(n+2j)(\eta\rho)^{2j-1}}{4^j \times j! \times (n+j) \times (n+j-1) \times \cdots \times (n+1)} \tag{4.37}$$

and

$$F_{j+1} = \frac{(\eta\rho)^n(-1)^{j+1} C_0(n+2j+2)(\eta\rho)^{2j+1}}{4^{j+1} \times (j+1)! \times (n+j+1) \times (n+j) \times \cdots \times (n+1)} \tag{4.38}$$

For the first $(j = 0, j = 1)$, second $(j = 2, j = 3)$ and third $(j = 4, j = 5)$ successive pairs, independently equating the sum of the expressions (4.37) and (4.38) to zero yields a relation between η and ρ in the form

$$\eta_0^2 = \frac{4 \times 1 \times (n+1)}{\rho^2(n+2)}, \quad \eta_1^2 = \frac{4 \times 3 \times (n+3) \times (n+4)}{\rho^2 \times (n+6)}, \quad \eta_2^2 = \frac{4 \times 5 \times (n+5) \times (n+8)}{\rho^2 \times (n+10)}, \tag{4.39}$$

respectively, which follows a pattern that for the pair corresponding with an even integer j, such that $j = 2k$, then the kth eigenvalue must be related to the radius of Ω through the following equation

$$\eta_{n,k}^2 = \frac{4(2k+1)(n+2k+1)(n+4k)}{\rho^2(n+4k+2)}. \tag{4.40}$$

Similarly it can be shown that for the three successive pairs namely $(j = 0, j = 1)$, $(j = 2, j = 3)$ and $(j = 4, j = 5)$ upon imposing the requirement $S_j + S_{j+1} = 0$, one can find respective relations of η_0, η_1 and η_2 with ρ in a form exactly the same as given by (4.39). This completes the solution to problem (4.17), which is summarised by the statement in Theorem 1.

Theorem 4.2.1 *Let $w(r,\theta)$ satisfy problem (4.17) with homogeneous Neumann boundary conditions. Given that the order n of the associated Bessel's function belongs to the set $\mathbb{R}\backslash\frac{1}{2}\mathbb{Z}$, [see Remark 4.2.3] then the full set of eigenfunctions of the diffusion operator Δ_p as defined in (4.12) is given by*

$$w_{n,k} = \left[R_{n,k}^1(r) + R_{n,k}^2(r)\right]\Theta_n(\theta) \tag{4.41}$$

with the explicit expressions for $R_{n,k}^1(r)$, $R_{n,k}^2(r)$ and $\Theta_n(\theta)$ as

$$R_{n,k}^1(r) = \sum_{j=0}^{\infty} \frac{(-1)^j C_0(\eta_k r)^{2j+n}}{4^j j!(n+j)(n+j-1)\cdots(n+1)}, \tag{4.42}$$

$$R_{n,k}^2(r) = \sum_{j=0}^{\infty} \frac{(-1)^j C_0(\eta_k r)^{2j-n}}{4^j j!(-n+j)(-n+j-1)\cdots(-n+1)} \tag{4.43}$$

and

$$\Theta_n(\theta) = \exp(in\theta), \tag{4.44}$$

where for the kth successive pair $\eta_{n,k}$ satisfies (4.40), whenever $j = 2k$.

Proof

The proof consists of all the steps from (4.18) to (4.40).□

It is worth noting that for a set containing $j = 2k$ terms from the series solutions defining the eigenfunctions (4.41), one only obtains k eigenvalues that satisfies problem (4.17). Therefore, it is important to realize this fundamental point that unlike the eigenfunctions of a diffusion operator (Sarfaraz and Madzvamuse, 2017) on a rectangular geometry, here only pairwise terms can qualify in the series solutions to be claimed as the eigenfunction satisfying problem (4.17) and not individual terms associated discretely to the summation index j.

4.2.2 Numerical experiments using spectral method

Let $R_{n,k}(r)$ denote the expression $R^1_{n,k}(r) + R^2_{n,k}(r)$, then the full set of eigenfunctions to problem (4.17), can be written as $w(r,\theta) = \sum_{k=0}^{\infty} R_{n,k}(r)\Theta_n(\theta)$. For numerical demonstration of the statement in Theorem 4.2.1, spectral method (Trefethen, 2000) is employed on a unit disc centred at the origin of the x, y coordinates. A spectral mesh in polar coordinates is constructed on a unit disc $\Omega = \{(r,\theta) \in \mathbb{R}^2 : r \in [0,1], \theta \in [0, 2\pi]\}$, where a periodic Fourier grid is applied to the angular axis θ and a non-periodic Chebyshev grid is applied to the radial axis r (Trefethen, 2000). In order to tackle the singularity at $r = 0$, Chebyshev discretisation is applied to the whole of the diameter of Ω, which means that $-1 \leq r \leq 1$ is used instead of $0 \leq r \leq 1$. The interval $[-1, 1]$ is discretised in the form $r_i = \cos(\frac{i\pi}{N})$, for $i = 0, 1, 2, ..., N$, where $N = 2j + 1, j \in \mathbb{N}$ is a positive odd integer. Odd number of points on Chebyshev grid in this particular case serves to preclude complications that could rise from the singular point at $r = 0$ by locating it radially in the middle of two successive Chebyshev grid points. The second coordinate θ is discretised using $\theta_i = \frac{2i\pi}{M}$, for $i = 0, 1, 2, ..., M$, where $M = 2j, j \in \mathbb{N}$ is a positive even integer. For the full details on the implementation of spectral method in polar coordinates the reader is referred to (Trefethen, 2000). Figures 4.1 (a) shows a coarse structure of mesh on a unit disc using $N = 25$ and $M = 30$, with angular step-size of 12°. Similarly Figure 4.1 (b) shows the actual refined mesh using $N = 95$ and $M = 90$ with angular step-size of 4°, on which all the simulations for eigenfunctions $w(r,\theta)$ are performed to visualise the corresponding

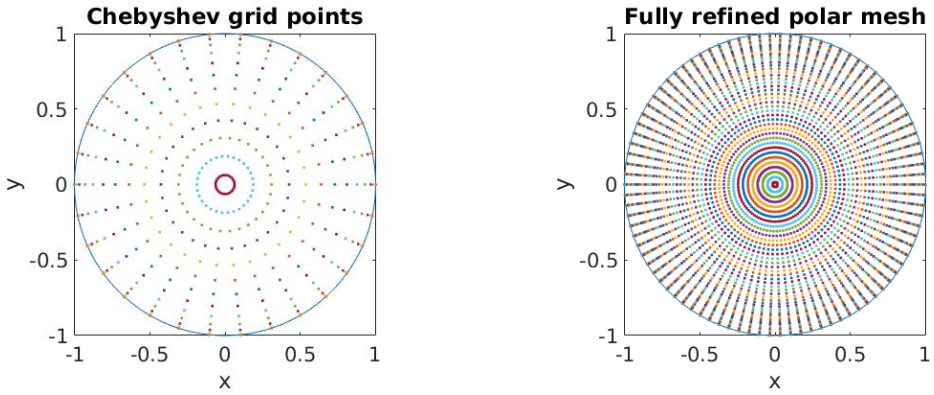

(a) (b)

FIGURE 4.1: In (a) the coarse structure of Chebyshev radial grid with $N = 25$ and periodic Fourier grid with $M = 30$ are shown, leading to an angular step-size of 12°. In (b) the fully refined polar mesh with $N = 95$ Chebyshev grid-points and $M = 90$ Fourier periodic grid-points, with angular step-size of 4°.

nodal lines and surfaces. Colour encoded plots, corresponding to nine different modes $k = \{1, 2, 3, 5, 6, 7, 9, 12, 15\}$ are simulated on the mesh given in Figure 4.1 (b) using a technique presented in (Steele, 2001). Due to the fact that eigenfunctions $w(r, \theta)$ are complex valued functions, therefore, trivial methods of visualising a real valued function of two variables do not suffice to give a meaningful representation to a complex valued function. Note that in the expression for eigenfunctions $w(r, \theta) = R(r)\Theta(\theta)$, only the function $\Theta(\theta)$ contains the non-zero imaginary part, therefore, the variable θ is encoded by a polar colour scheme (Hue, Saturation Value) and displayed directly on Ω. For full details on the implementation of this process the reader is referred to (Steele, 2001; Qian and Wegert, 2013). Figure 4.2 shows a colour encoded representation of nine different modes, each of which corresponds to one of the nine nodal line depictions of $w_{n,k}(r, \theta)$ in Figure 4.3. Nodal lines are the lines connecting nodes corresponding to stationary harmonics in the domain. Note that in Figure 4.3 different modes namely mode 2 and 3 result in the same eigenvalues that correspond to a different orientation of the nodal line depiction for $k = 2$ and $k = 3$. Similarly one may find that there are a lot of such pairs of positive integers k and $k + 1$, that correspond

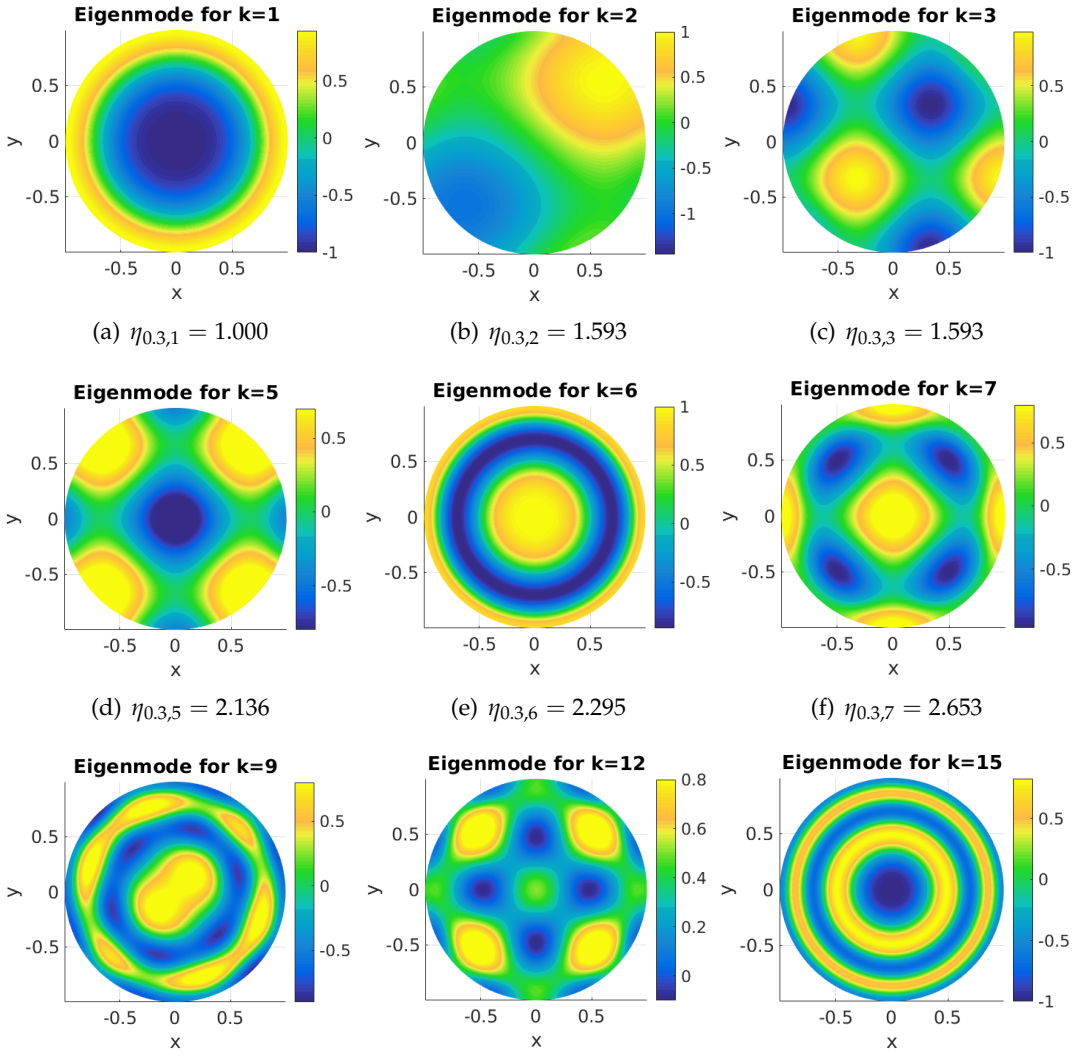

(a) $\eta_{0.3,1} = 1.000$ (b) $\eta_{0.3,2} = 1.593$ (c) $\eta_{0.3,3} = 1.593$

(d) $\eta_{0.3,5} = 2.136$ (e) $\eta_{0.3,6} = 2.295$ (f) $\eta_{0.3,7} = 2.653$

(g) $\eta_{0.3,9} = 2.917$ (h) $\eta_{0.3,12} = 3.155$ (i) $\eta_{0.3,15} = 3.598$

FIGURE 4.2: Colour encoded phase plots of $w(r, \theta)$ for different values of k indicated in each subtitle.

to different orientation of the same nodal line depiction. This occurs, when the multiplicity of an eigenvalue $\eta_{n,k}$ is 2, and in fact there are numerous such pairs of $w_{n,k}(r,\theta)$ and $w_{n,k+1}(r,\theta)$, that correspond to the same $\eta_{n,k}$, but for different orientation of eigenstates. However applying the colour encoded representation using the (HSV) colour scheme indicates a distinction between the plots corresponding to each integer value for k, shown in Figure 4.2.

4.2.3 Remark

The restriction on the order of the corresponding Bessel's equation namely $n \in \frac{1}{2}\mathbb{Z}$ in Theorem 4.2.1 can be relaxed by employing Bessel's function of the second kind and imposing on it the homogeneous Neumann boundary conditions. Therefore, for the purpose of the current study the order of the corresponding Bessel's equation is precluded from becoming a full or a half integer. Therefore, acquiring the solutions admitting the order of Bessel's equation to be a half or a full integer can be an extension of this work to obtain the full set of all possible harmonics for $n \in \mathbb{R}$ that can intern contribute to a generalisation of this work.

4.2.4 Stability matrix and characteristic polynomial

The solution to system (4.13) using separation of variables method, can be written (with bars omitted from $\bar{u}$ and $\bar{v}$) as the product of the eigenfunctions of the diffusion operator Δ_p and $T(t)$ in the form

$$u(r,\theta,t) = \sum_{k=0}^{\infty} U_{n,k} \exp(\sigma_{n,k} t) R_{n,k}(r) \Theta_n(\theta),$$
$$u(r,\theta,t) = \sum_{k=0}^{\infty} V_{n,k} \exp(\sigma_{n,k} t) R_{n,k}(r) \Theta_n(\theta),$$

where $U_{n,k}$ and $V_{n,k}$ are the coefficients associated to the mode of eigenfunctions in the infinite expansion. Substituting this form of solution in (4.16) and the steady state values in terms of the parameters α and β for (u_s, v_s), one obtains the fully linearised

form of (4.13) as a system of two algebraic equations of the form

$$\sigma \begin{bmatrix} u \\ v \end{bmatrix} = -\eta_{n,k}^2 \begin{bmatrix} 1 & 0 \\ 0 & d \end{bmatrix} \begin{bmatrix} u \\ v \end{bmatrix} + \gamma \begin{bmatrix} \frac{\beta-\alpha}{\beta+\alpha} & (\beta+\alpha)^2 \\ -\frac{2\beta}{\beta+\alpha} & -(\beta+\alpha)^2 \end{bmatrix} \begin{bmatrix} u \\ v \end{bmatrix}, \tag{4.45}$$

where $\sigma_{n,k} = \sigma$, which can in turn be written as a two dimensional discrete eigenvalue problem

$$\begin{bmatrix} \gamma\frac{\beta-\alpha}{\beta+\alpha} - \eta_{n,k}^2 & \gamma(\beta+\alpha)^2 \\ -\gamma\frac{2\beta}{\beta+\alpha} & -\gamma(\beta+\alpha)^2 - d\eta_{n,k}^2 \end{bmatrix} \begin{bmatrix} u \\ v \end{bmatrix} = \sigma \begin{bmatrix} u \\ v \end{bmatrix}. \tag{4.46}$$

The matrix in (4.46) is referred to as the stability matrix for system (4.13), with $\eta_{n,k}^2$ given by (4.40). In order to investigate the stability of the uniform steady state (u_s, v_s), it is required to analyse the eigenvalues satisfying (4.46), for which the characteristic polynomial takes the form of a quadratic equation in σ, written as

$$\begin{vmatrix} \gamma\frac{\beta-\alpha}{\beta+\alpha} - \eta_{n,k}^2 - \sigma & \gamma(\beta+\alpha)^2 \\ -\gamma\frac{2\beta}{\beta+\alpha} & -\gamma(\beta+\alpha)^2 - d\eta_{n,k}^2 - \sigma \end{vmatrix} = 0. \tag{4.47}$$

Let $\mathcal{T}(\alpha,\beta)$ and $\mathcal{D}(\alpha,\beta)$ respectively denote the trace and determinant of stability matrix given by (4.46), then the quadratic polynomial (4.47) can be written in terms of $\mathcal{T}$ and $\mathcal{D}$ as

$$\sigma^2 - \mathcal{T}(\alpha,\beta)\sigma + \mathcal{D}(\alpha,\beta) = 0, \tag{4.48}$$

with $\mathcal{T}(\alpha,\beta)$ and $\mathcal{D}(\alpha,\beta)$ expressed by

$$\begin{aligned} \mathcal{T}(\alpha,\beta) =& \gamma\frac{\beta-\alpha-(\beta+\alpha)^3}{\beta+\alpha} - (d+1)\eta_{n,k}^2, \\ \mathcal{D}(\alpha,\beta) =& \big(\gamma\frac{\beta-\alpha}{\beta+\alpha} - \eta_{n,k}^2\big)\big(-\gamma(\beta+\alpha)^2 - (d+1)\eta_{n,k}^2\big) + 2\gamma^2\beta(\beta+\alpha). \end{aligned} \tag{4.49}$$

The roots of equation (4.48) in terms of $\mathcal{T}$ and $\mathcal{D}$ are $\sigma_{1,2} = \frac{\mathcal{T}\pm\sqrt{\mathcal{T}^2-4\mathcal{D}}}{2}$. Stability of the uniform steady state (u_s, v_s) is decided by the signs of the two roots namely $\sigma_{1,2}$ if they are real valued. However, if $\sigma_{1,2}$ is a complex conjugate pair (with non-zero imaginary parts), then the sign of the real part is sufficient to predict the stability of

the uniform steady state (u_s, v_s). Since there are always exactly two roots on a complex plane for a quadratic equation, therefore, it is impossible with the same choice of parameters α, β, d, γ and $\eta_{n,k}^2$ for σ_1 to be real and σ_2 to be complex or vice versa. Therefore, a reasonable approach to encapsulate all the possibilities for the stability and types of the uniform steady state (u_s, v_s) in light of parameters α and β is to consider the cases when $\sigma_{1,2} \in \mathbb{C}\backslash\mathbb{R}$ independent from that where $\sigma_{1,2} \in \mathbb{R}$. In each case the parameter space is rigorously analysed and the classification of the parameter plane $(\alpha, \beta) \in \mathbb{R}_+^2$ with the effect from increasing the diffusion parameter d is studied. In light of such classification, the analysis is further extended to explore the effects of domain-size on the existence of regions in parameter space that corresponds to spatial and/or temporal bifurcations.

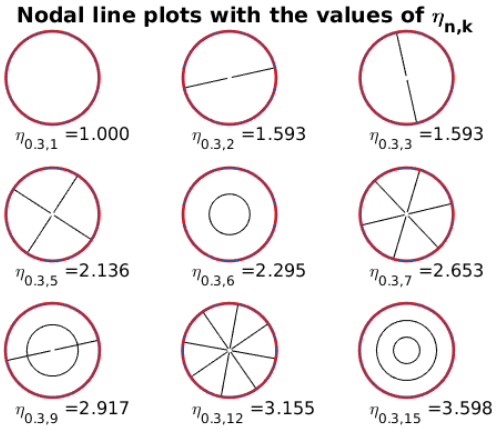

FIGURE 4.3: Nodal lines and eigenvalues.

4.3 Parameter spaces and bifurcation analysis

Bifurcation analysis of system (4.13) is better conducted when the parameter plane $(\alpha, \beta) \in \mathbb{R}_+^2$ is appropriately partitioned for both of the cases when $\sigma_{1,2} \in \mathbb{C}\backslash\mathbb{R}$ as well as when $\sigma_{1,2} \in \mathbb{R}$. To obtain such a partition on the parameter plane, it is required to find the equations of the partitioning curves and these can be found through a detailed analysis of the expression for $\sigma_{1,2}$, which in turn requires to explore the domains of $\mathcal{T}$ and $\mathcal{D}$.

4.3.1 Equations of the partitioning curves

Starting with the curve on the parameter plane $(\alpha, \beta) \in \mathbb{R}_+^2$ that forms a boundary for the region that corresponds to eigenvalues $\sigma_{1,2}$ containing non-zero imaginary part. It

must be noted that the only possibility through which $\sigma_{1,2}$ can have a non-zero imaginary part is if the inequality $\mathcal{T}^2 - 4\mathcal{D} < 0$ is true. It means that those parameter values α and β satisfying the equation $\mathcal{T}^2(\alpha, \beta) = 4\mathcal{D}(\alpha, \beta)$ must be lying on a partitioning curve that determines the boundary between the region on the parameter plane that corresponds to eigenvalues with non-zero imaginary part and that which corresponds to a pair of real eigenvalues. We therefore, state that the set of points on the parameter plane $(\alpha, \beta) \in \mathbb{R}^2_+$ satisfying the implicit equation

$$\begin{aligned}\Big(\gamma\frac{\beta-\alpha-(\beta+\alpha)^3}{\beta+\alpha} - (d+1)\eta_{n,k}^2\Big)^2 =& 4\Big(\big(\gamma\frac{\beta-\alpha}{\beta+\alpha} - \eta_{n,k}^2\big)\big(-\gamma(\beta+\alpha)^2 \\ & - (d+1)\eta_{n,k}^2\big) + 2\gamma^2\beta(\beta+\alpha)\Big),\end{aligned} \tag{4.50}$$

forms the partitioning curve between the region that corresponds to a real pair of $\sigma_{1,2}$ from that corresponding to a complex conjugate pair of $\sigma_{1,2}$. For the solution of (4.50) refer to Section 4.4, where the numerical technique presented in Chapter 3 is employed to find $\alpha, \beta \in \mathbb{R}_+$ on the plane $(\alpha, \beta) \in \mathbb{R}^2_+$ satisfying (4.50). It is worth noting that a combination of α and β satisfying (4.50), results the expression for $\sigma_{1,2}$ to yield a repeated real root of the form $\sigma_1 = \sigma_2 = \frac{1}{2}\mathcal{T}$, whose sign will require to be explored in Section 4.4 with real eigenvalues. Another important point to be made about the curve satisfying (4.50) is that it also partitions the parameter space for regions of spatial and temporal bifurcations. Because on one side of curve (4.50), both of the eigenvalues $\sigma_{1,2}$ are always real, which is irrelevant to spiral type behaviour i.e. the excitement of temporal periodicity in the dynamics near (u_s, v_s), where as on the other side, the eigenvalues $\sigma_{1,2}$ are always a complex conjugate pair, which can excite temporal periodicity in the dynamics. Therefore, on the side where $\sigma_{1,2}$ are a pair of real values, any instability that occurs in the dynamics of system (4.13) will be strictly relevant to spatial variation, hence any pattern that system (4.13) can evolve is strictly spatial (spots or stripes) with 'globally' stable and invariant structure in time. However, on the side where $\sigma_{1,2}$ have non-zero imaginary part, every possible instability in the dynamics of

system (4.13) will be strictly concerned with temporal periodicity, therefore any pattern that emerges from the dynamics of system (4.13) is expected to be periodic along the time axis. This analysis raises the interesting question that is it possible for the dynamics of (4.13) to cause a spatially periodic pattern to undergo an unstable temporal periodicity as well? To answer this question, on the first sight it sounds absurd to claim on one hand that a specific choice of admissible (α, β) can either cause spatial or temporal instability, and not both at the same time, which is an intuitive claim to make. Because, any admissible choice of (α, β) either yields a pair of real $\sigma_{1,2}$ or a complex conjugate pair of $\sigma_{1,2}$, therefore, a fixed choice of (α, β) is not expected to yield a real σ_1 and a complex σ_2 or vice versa. Therefore, it is intuitive to presume that system (4.13) should not admit the evolution of such dynamics, in which a combination of spatial and temporal instabilities can occur. However, the current study finds that this counter-intuitive behaviour is possible for system (4.13) to exhibit, which is related to the existence and shift in the location of the partitioning curve on which the real part of $\sigma_{1,2} \in \mathbb{C}\backslash\mathbb{R}$ becomes zero during the course of evolution. Such a curve is referred to as the *transcritical curve*, for which the implicit equation $\mathcal{T}(\alpha, \beta) = 0$ in terms of admissible α and β can be written in the form

$$\gamma \frac{\beta - \alpha - (\beta + \alpha)^3}{\beta + \alpha} = (d + 1)\eta_{n,k}^2, \tag{4.51}$$

under the assumption that $\mathcal{D}(\alpha, \beta) > 0$. It must be noted, that equations (4.50) and (4.51) are the only two equations that fully partition the parameter plane $(\alpha, \beta) \in \mathbb{R}_+^2$. However, one may expect the number of partitions subject to the types and stability of the uniform steady state (u_s, v_s), on the parameter plane $(\alpha, \beta) \in \mathbb{R}_+^2$ to be four regions separated by three curves. These regions are obtained by the sub partition of the region corresponding to a pair of real $\sigma_{1,2}$, into two sub-regions where $\sigma_{1,2}$ is a pair of real negative values and another where at least σ_1 or σ_2 is positive. The region on the parameter plane $(\alpha, \beta) \in \mathbb{R}_+^2$, that corresponds to complex eigenvalues can also be sub-divided into two regions, one where $\sigma_{1,2}$ is a complex conjugate pair

with negative real part, and the other where $\sigma_{1,2}$ is a complex conjugate pair, but with a positive real part. The numerical solution of equation (4.50) will reveal that the region corresponding to complex eigenvalues is in fact bounded by two curves in the parameter plane $(\alpha, \beta) \in \mathbb{R}^2_+$, each of which satisfies (4.50). Therefore, (4.50) is implicitly the equation of two partitioning curves instead of one, which including (4.51) makes a total of three curves dividing the admissible parameter space in to four different regions. It is worth bearing in mind, that subject to the types and stability of the uniform steady state, one obtains at most four regions separated by three curves, with the possibility that parameters such as γ, d and $\eta^2_{n,k}$ may induce equations (4.50) and (4.51) in such a way that the number of partitioning curves may become less than three in total. Consequently this entails that a region corresponding to a certain type of bifurcation may completely disappear from the admissible parameter space. This kind of influence on the location and existence of the partitioning curves is quantitatively investigated, in particular, the effect of ρ embedded in the expression for $\eta^2_{n,k}$ in (4.40) is explored to analyse its influence on the bifurcation of the uniform steady state.

4.3.2 Analysis for the case of complex eigenvalues

Before determining the region with complex eigenvalues on the admissible parameter plane $(\alpha, \beta) \in \mathbb{R}^2_+$ using a numerical treatment of (4.50), the real part of $\sigma_{1,2}$ is investigated analytically, when it is a complex conjugate pair. It can be noted that $\sigma_{1,2}$ can only become a pair of complex roots, if (α, β) satisfy the inequality

$$\mathcal{T}^2(\alpha, \beta) - 4\mathcal{D}(\alpha, \beta) < 0. \tag{4.52}$$

Given that (4.52) is satisfied, then the stability of the uniform steady steady state (u_s, v_s) is decided purely by the sign of the real part of $\sigma_{1,2}$, which is the expression

$$\mathrm{Re}(\sigma_{1,2}) = \frac{1}{2}\Big(\gamma\frac{\beta - \alpha - (\beta + \alpha)^3}{\beta + \alpha} - (d+1)\eta^2_{n,k}\Big). \tag{4.53}$$

If the sign of the expression give by (4.53) is negative, simultaneously with assumption (4.52) satisfied, then it can be predicted that no choice of parameters can excite temporal periodicity in the dynamics of system (4.13). Therefore, under the assumption (4.52), if the dynamics of system (4.13) do exhibit diffusion-driven instability, it will be restricted to spatially periodic behaviour only, which uniformly converges to a temporal steady state, consequently one obtains spatial pattern that is invariant in time. The sign of the expression given in (4.53) is further investigated to derive from it, relations between the parameter ρ controlling the domain-size and reaction-diffusion rates denoted by γ and d respectively. Given that assumption (4.52) is satisfied then the sign of expression (4.53) is negative if parameters α, β, γ and d satisfy the inequality

$$\frac{\beta - \alpha - (\beta + \alpha)^3}{\beta + \alpha} < \frac{(d+1)\eta_{n,k}^2}{\gamma}, \tag{4.54}$$

with $\eta_{n,k}^2$ defined by (4.40). Note that the expression on the left hand-side of (4.54) is a bounded quantity by the constant value of 1 (Sarfaraz and Madzvamuse, 2017), for all the admissible choices of $(\alpha, \beta) \in \mathbb{R}_+$, therefore, substituting for $\eta_{n,k}^2$ the expression in (4.40) and rearranging, it can be obtained that for inequality (4.54) to remain true, it induces a restriction on the value of ρ^2, which is of the form

$$\rho^2 < \frac{4(d+1)(2k+1)(n+2k+1)(n+4k)}{\gamma(n+4k+2)}. \tag{4.55}$$

Inequality (4.55) conversely implies that so long as the radius ρ of the disc-shape domain Ω satisfies (4.55), then the dynamics of system (4.13) is guaranteed for all n, k to exhibit global temporal stability, which also means that any possible instability in the dynamics must be restricted to spatial periodicity or spatial pattern. The formal proof of this claim is presented in Theorem 4.3.1. The type of instability concerning space and not time is referred to as *Turing instability*. On the other hand assuming that (4.52) is satisfied and using the upper bound of the quantity on the left hand-side of (4.54) with $\eta_{n,k}^2$ as defined in (4.40), it can be shown that a necessary condition for the sign of

the expression (4.53) to become positive is for ρ to satisfy the inequality

$$\rho^2 \geq \frac{4(d+1)(2k+1)(n+2k+1)(n+4k)}{\gamma(n+4k+2)}. \tag{4.56}$$

Conditions (4.55) and (4.56) both have quantitative influence on the location and topology of the partitioning curves obtained from the numerical solutions of (4.50) and (4.51) in the admissible parameter plane, namely $(\alpha, \beta) \in \mathbb{R}^2_+$. System (4.13) is restricted from any type of temporal bifurcation if the radius ρ of the disc-shape domain Ω is related to the reaction-diffusion parameters γ and d, through inequality (4.55). It also means that on a disc-shape domain Ω with radius ρ satisfying (4.55), the dynamics of system (4.13), either exhibit spatially periodic pattern or no pattern at all, both of which are globally stable in time. If the dynamics of a system become unstable along the time axis and exhibits temporal periodicity, then the system is said to undergo *Hopf bifurcation*. If the real part of a pair of complex eigenvalues become zero, then the system is expected to exhibit oscillations with temporal periodicity. This behaviour is known as *limit-cycle* behaviour. The consequences of the restriction on ρ in the present context means that, whenever the radius ρ of a disc-shape domain is bounded by (4.55) in terms of γ and d, then the dynamics of system (4.13) is guaranteed to forbid *Hopf* bifurcation and *limit-cycle* behaviour, only allowing for *Turing instability* to occur. If system (4.13) allows only Turing type instability to occur under condition (4.55), it indicates that the eigenvalues $\sigma_{1,2}$ only become positive, when they are a pair of real values with zero imaginary parts. Therefore, it is also an indication that diffusion-driven instability is still possible, but it just becomes strictly spatial with (4.55) satisfied. If the values of parameters γ and d are chosen such that inequality (4.56) is satisfied, then the possibility of all three types of diffusion-driven instabilities exist on the admissible parameter plane $(\alpha, \beta) \in \mathbb{R}^2_+$, namely Turing, Hopf and transcritical types of bifurcations. The influence from the area of Ω through the relationship (4.56) of ρ with the reaction-diffusion rates namely γ and d is summarised in Theorem 4.3.1 with a detailed sketch of proof.

Theorem 4.3.1 (Hopf or transcritical bifurcation) *Let u and v satisfy the non-dimensional reaction-diffusion system with activator-depleted reaction kinetics (4.13)-(4.15) on a disc-shape domain $\Omega \subset \mathbb{R}^2$ with radius ρ and positive real parameters $\gamma > 0$, $d > 0$, $\alpha > 0$ and $\beta > 0$. For the system to exhibit Hopf or transcritical bifurcation in the neighbourhood of the unique steady state $(u_s, v_s) = \left(\alpha + \beta, \frac{\beta}{(\alpha+\beta)^2}\right)$, the necessary condition on the radius ρ of the disc-shape domain $\Omega \subset \mathbb{R}^2$ is that it must be sufficiently large satisfying*

$$\rho \geq 2\sqrt{\frac{(d+1)(2k+1)(n+2k+1)(n+4k)}{\gamma(n+4k+2)}}, \tag{4.57}$$

where $n \in \mathbb{R}\backslash\frac{1}{2}\mathbb{Z}$ is the associated order of the Bessel's equations and k is any positive integer.

Proof

For system (4.13) to exhibit *Hopf* or *transcritical* bifurcations the eigenvalues of the stability matrix (4.46) must have non-zero imaginary part with non-negative real part. Consider the real part of $\sigma_{1,2}$, which is precisely given by $\frac{1}{2}\mathcal{T}(\alpha, \beta)$ under the assumption that the admissible choice of parameters $\alpha, \beta \in \mathbb{R}_+$ satisfies (4.52). Since the constant $\frac{1}{2}$ is positive, therefore, when $\sigma_{1,2} \in \mathbb{C}\backslash\mathbb{R}$, then the stability of the uniform steady state $(u_s, v_s) = \left(\alpha + \beta, \frac{\beta}{(\alpha+\beta)^2}\right)$ is precisely determined by the sign of $\mathcal{T}(\alpha, \beta)$, which is given by

$$\mathcal{T}(\alpha, \beta) = \gamma\frac{\beta - \alpha - (\beta + \alpha)^3}{\beta + \alpha} - (d+1)\eta_{n,k}^2. \tag{4.58}$$

System (4.13) undergoes Hopf or transcritical bifurcation if $\mathcal{T}(\alpha, \beta) \geq 0$, given that the strict inequality (4.52) is satisfied, which can only hold true if $\mathcal{D}(\alpha, \beta) > 0$. In (4.58) $\eta_{n,k}^2$ is given by

$$\eta_{n,k}^2 = \frac{4(2k+1)(n+2k+1)(n+4k)}{\rho^2(n+4k+2)}, \tag{4.59}$$

where $n \in \mathbb{R}\backslash\frac{1}{2}\mathbb{Z}$ is the order of the associated Bessel's equation and $k \in \mathbb{N}$ is any positive integer. To show the condition on ρ for Hopf or transcritical bifurcation, one

may substitute (4.59) in (4.58) and requiring the resulting quantity to be non-negative, which yields the inequality

$$\gamma\frac{\beta-\alpha-(\beta+\alpha)^3}{\beta+\alpha}\geq\frac{4(d+1)(2k+1)(n+2k+1)(n+4k)}{\rho^2(n+4k+2)}. \tag{4.60}$$

Noting that the left hand-side of (4.60) can be written as the difference between two non-negative functions $f_1(\alpha,\beta)$ and $f_2(\alpha,\beta)$ in the form $\gamma\big(f_1(\alpha,\beta)-f_2(\alpha,\beta)\big)$, where f_1 and f_2 are given by

$$f_1(\alpha,\beta)=\frac{\beta}{\alpha+\beta},\qquad f_2(\alpha,\beta)=\frac{\alpha+(\alpha+\beta)^3}{\alpha+\beta}. \tag{4.61}$$

Note also that ρ^2 resides in the denominator of the right hand-side of (4.60) and parameter γ is multiplied by the expression on the left hand-side. In order to find what this inequality induces on the relationship between parameters γ, d and ρ, it is essential to analyse the supremum and infemum of $f_1(\alpha,\beta)$ and $f_2(\alpha,\beta)$ within their respective domains which is $(\alpha,\beta)\in[0,\infty)\times[0,\infty)$. The range for $f_1(\alpha,\beta)$ and $f_2(\alpha,\beta)$ are independently analysed to find the supremum of the expression on the left of (4.60). Starting with $f_1(\alpha,\beta)$, which is bounded below and above in the domain $(\alpha,\beta)\in[0,\infty)\times[0,\infty)$, we have $\sup_{\alpha,\beta\in\mathbb{R}_+}f_1(\alpha,\beta)=1$, and the $\inf_{\alpha,\beta\in\mathbb{R}_+}f_1(\alpha,\beta)=0$ for all $\alpha,\beta\in\mathbb{R}_+$. Similarly considering the expression for $f_2(\alpha,\beta)$, we have $\sup_{\alpha,\beta\in\mathbb{R}_+}f_2(\alpha,\beta)=\infty$, and the $\inf_{\alpha,\beta\in\mathbb{R}_+}f_2(\alpha,\beta)=0$, for all $\alpha,\beta\in\mathbb{R}_+$. Since the ranges of both $f_1(\alpha,\beta)$ and $f_2(\alpha,\beta)$ are non-negative within their respective domains, therefore the supremum of their difference is bounded by the supremum of the function with positive sign, which is $\sup_{\alpha,\beta\in\mathbb{R}_+}f_1(\alpha,\beta)=1$. Therefore, inequality (4.60) takes the form

$$\begin{aligned}\frac{4(d+1)(2k+1)(n+2k+1)(n+4k)}{\rho^2(n+4k+2)}&\leq\gamma\frac{\beta-\alpha-(\beta+\alpha)^3}{\beta+\alpha}\\&\leq\gamma\sup_{\alpha,\beta\in\mathbb{R}_+}\big(f_1(\alpha,\beta)-f_2(\alpha,\beta)\big)\\&\leq\gamma\sup_{\alpha,\beta\in\mathbb{R}_+}f_1(\alpha,\beta)=\gamma,\end{aligned}$$

which by rearranging and writing the inequality for ρ in terms of everything else, yields the desired statement of Theorem 4.3.1, which is condition (4.57).□

Remark

Although the claim of Theorem 4.3.1 remains satisfied for all choices of $n \in \mathbb{R}\backslash\frac{1}{2}\mathbb{Z}$ and $k \in \mathbb{N}$, however, for the purpose of simulating diffusion-driven instability one must acquire excitable values for n and k, which is done through a method known as mode isolation and is used for extracting the excitable wave-numbers for spatial pattern to emerge as the solution of RDSs. Therefore, in order to explore the influence of higher modes on the governing dynamics of pattern formation, the values of n, k must satisfy the criteria for excitable wave-number. Using admissible large values of n and k enforces a change of domain-size to reproduce the expected behaviour in the dynamics. Employing the results of Theorem 4.3.1, the domain-size in turn can remain constant by altering the values of reaction-diffusion constants to compensate the enforcement of a change in domain-size i.e. using the expression (4.57). The method of mode isolation for excitable wave-number is explained in great details in (Madzvamuse, 2000). The claim of Theorem 4.3.1, is also numerically verified by showing that a region in the admissible parameter plane that corresponds to Hopf or transcritical bifurcations emerges only if radius ρ of a disc-shape domain Ω is sufficiently large satisfying the inequality (4.57). Otherwise, no choice of parameters exist in the admissible parameter plane $(\alpha, \beta) \in \mathbb{R}^2_+$, allowing the dynamics of (4.13) to exhibit Hopf or transcritical bifurcation.

4.3.3 Analysis for the case with real eigenvalues

The eigenvalues $\sigma_{1,2}$ are both real if the discriminant of the roots is either zero or positive, which in turn means that both eigenvalues are real values if the relationship between $\mathcal{T}(\alpha, \beta)$ and $\mathcal{D}(\alpha, \beta)$ is such that

$$\mathcal{T}^2(\alpha, \beta) \geq 4\mathcal{D}(\alpha, \beta). \tag{4.62}$$

The equal case of (4.62) is looked at first, where we have

$$\mathcal{T}^2(\alpha,\beta) = 4\mathcal{D}(\alpha,\beta), \tag{4.63}$$

which means that the discriminant is zero, hence the roots are repeated real values of the form $\sigma_1 = \sigma_2 \in \mathbb{R}$, given by

$$\sigma_1 = \sigma_2 = \frac{1}{2}\Big(\gamma\frac{\beta-\alpha-(\beta+\alpha)^3}{\beta+\alpha} - \frac{4(d+1)(2k+1)(n+2k+1)(n+4k)}{\rho^2(n+4k+2)}\Big). \tag{4.64}$$

When α and β satisfy condition (4.63), the stability of the steady state is determined by the sign of the root itself. The expression given by (4.64) can be easily shown to be negative if the radius ρ of the disc-shape domain Ω satisfies the inequality

$$\rho < 2\sqrt{\frac{(\alpha+\beta)(d+1)(2k+1)(n+2k+1)(n+4k)}{\gamma(\beta-\alpha-(\alpha+\beta)^3)(n+4k+2)}}. \tag{4.65}$$

Otherwise, the repeated root is positive provided that L satisfies

$$\rho > 2\sqrt{\frac{(\alpha+\beta)(d+1)(2k+1)(n+2k+1)(n+4k)}{\gamma(\beta-\alpha-(\alpha+\beta)^3)(n+4k+2)}}. \tag{4.66}$$

Analysing (4.65) and (4.66) carefully, it can be observed that the only terms that can possibly invalidate the inequalities are in the denominator of the right hand-side, namely the expression $\beta-\alpha-(\beta+\alpha)^3$. Therefore, a restriction is required to be stated on this term to ensure that the radius ρ of Ω is not compared against an imaginary number, such a restriction is

$$\beta > \alpha + (\beta+\alpha)^3. \tag{4.67}$$

It must be noted that (4.67) is the same restriction on the parameter choice obtained for the case of repeated real eigenvalues in the absence of diffusion (Sarfaraz and Madzvamuse, 2017). By further comparison of (4.66), it can be noted that it is very similar to condition (4.57) of Theorem 4.3.1, except that (4.57) is free from any dependence of the parameters α and β, which makes (4.57) a sharper version of (4.66) in the sense,

that the curve satisfying (4.63) subject to condition (4.66) must be the one forming the boundary of the region on the admissible parameter plane, that corresponds to complex eigenvalues $\sigma_{1,2}$ with positive real parts, which is the region for Hopf bifurcation. Therefore, the region of the admissible parameter plane that corresponds to Hopf bifurcation is on one side bounded by curve (4.63) and on the other side it is bounded by curve satisfying (4.51) under their respective assumptions. In Section 4.4 it is verified to be the case by the numerical computation of the partitioning curve (4.50), which is the same curve (4.63). This analysis motivates to explore the possibility of similar comparison between the conditions (4.65) and (4.55). A reasonable intuition behind this comparison is that the sub-region on the admissible parameter plane that corresponds to complex eigenvalues with negative real parts must be bounded by curve (4.63) subject to condition (4.65), outside of which every possible choice of parameters α and β will guarantee the eigenvalues $\sigma_{1,2}$ to be a pair of distinct real values, which promotes the necessity to state and prove Theorem 4.3.2.

Theorem 4.3.2 (Turing type diffusion-driven instability) *Let u and v satisfy the non-dimensional reaction-diffusion system with activator-depleted reaction kinetics (4.13)-(4.15) on a disc-shape domain $\Omega \subset \mathbb{R}^2$ with radius ρ and positive parameters $\gamma > 0$, $d > 0$, $\alpha > 0$ and $\beta > 0$. Given that the radius ρ of domain $\Omega \subset \mathbb{R}^2$ satisfies the inequality*

$$\rho < 2\sqrt{\frac{(d+1)(2k+1)(n+2k+1)(n+4k)}{\gamma(n+4k+2)}}, \tag{4.68}$$

where $n \in \mathbb{R}\backslash\frac{1}{2}\mathbb{Z}$ is the associated order of the Bessel's equations and k is any positive integer, then for all $\alpha, \beta \in \mathbb{R}_+$ in the neighbourhood of the unique steady state $(u_s, v_s) = \left(\alpha+\beta, \frac{\beta}{(\alpha+\beta)^2}\right)$ the diffusion driven instability is restricted to Turing type only, forbidding the existence of Hopf and transcritical bifurcation.

Proof

The strategy of this proof is through detailed analysis of the real part of the eigenvalues of the linearised system, when the eigenvalues are a complex conjugate pair. This

can be done through studying the surface $\mathcal{T}(\alpha,\beta)$, and finding that it has a unique extremum point at $(0,0)$. The method of second derivative test and Hessian matrix is used to determine the type of this extremum. Upon finding its type, then the monotonicity of $\mathcal{T}(\alpha,\beta)$ is analysed in the neighbourhood of the extremum point in both directions α and β. The monotonicity analysis and the type of the extrema leads to proving the claim of the theorem.

The eigenvalues $\sigma_{1,2}$, in terms of trace $\mathcal{T}(\alpha,\beta)$ and determinant $\mathcal{D}(\alpha,\beta)$ are given by $\sigma_{1,2} = \frac{1}{2}\mathcal{T}(\alpha,\beta) \pm \frac{1}{2}\sqrt{\mathcal{T}^2(\alpha,\beta) - 4\mathcal{D}(\alpha,\beta)}$, where

$$\begin{aligned}\mathcal{T}(\alpha,\beta) =& \gamma\frac{\beta-\alpha-(\beta+\alpha)^3}{\beta+\alpha} - (d+1)\eta_{n,k}^2,\\ \mathcal{D}(\alpha,\beta) =& \Big(\gamma\frac{\beta-\alpha}{\beta+\alpha} - \eta_{n,k}^2\Big)\Big(-\gamma(\beta+\alpha)^2 - d\eta_{n,k}^2\Big) + 2\gamma^2\beta(\beta+\alpha),\end{aligned}$$

with $\eta_{n,k}^2$ as given by (4.40). It can be immediately observed that in the neighbourhood of (u_s,v_s) for the system to exhibit Hopf or transcritical bifurcation the discriminant of the characteristic polynomial must satisfy the inequality $\mathcal{T}^2(\alpha,\beta) - 4\mathcal{D}(\alpha,\beta) < 0$. Therefore, the stability and type of the steady state (u_s,v_s) in this case is determined by the sign of the real part of $\sigma_{1,2}$. The aim is to investigate $\mathcal{T}(\alpha,\beta)$ and derive from it condition (4.68) on ρ as a requirement for $\mathcal{T}(\alpha,\beta)$ to be negative for all strictly positive choices of γ, α, β and d. First derivative test is used on $\mathcal{T}(\alpha,\beta)$ to find the stationary points of $\mathcal{T}(\alpha,\beta)$ on the domain $[0,\infty)\times[0,\infty)$. All stationary points of $\mathcal{T}(\alpha,\beta)$ must satisfy $\frac{\partial\mathcal{T}}{\partial\alpha} = -\gamma\frac{2(\alpha+\beta)^3+2\beta}{(\alpha+\beta)^2} = 0$, which is true if and only if

$$(\alpha+\beta)^3 + \beta = 0. \tag{4.69}$$

Similarly all stationary points of $\mathcal{T}(\alpha,\beta)$ must also satisfy $\frac{\partial\mathcal{T}}{\partial\beta} = -\gamma\frac{2(\alpha+\beta)^3-2\alpha}{(\alpha+\beta)^2} = 0$, which implies

$$(\alpha+\beta)^3 - \alpha = 0. \tag{4.70}$$

The system of non-linear algebraic equations obtained from (4.69) and (4.70) has a unique solution namely $\alpha = 0$ and $\beta = 0$ [see Remark 4.3.2]. Therefore, $\mathcal{T}(\alpha,\beta)$ has a

unique stationary point at the origin. The type of this stationary point is determined by the second derivative test for which the Hessian matrix $H(\mathcal{T}(\alpha,\beta))$ must be computed and evaluated at the point $(0,0)$.

$$H(\mathcal{T}(\alpha,\beta))|_{(0,0)} = \begin{bmatrix} \frac{\partial^2\mathcal{T}}{\partial\alpha^2} & \frac{\partial^2\mathcal{T}}{\partial\beta\partial\alpha} \\ \frac{\partial^2\mathcal{T}}{\partial\alpha\partial\beta} & \frac{\partial^2\mathcal{T}}{\partial\beta^2} \end{bmatrix}_{(0,0)} = \begin{bmatrix} -\gamma\frac{4\beta-2(\alpha+\beta)^3}{(\alpha+\beta)^3} & -\gamma\frac{2(\alpha+\beta)^3+2(\alpha-\beta)}{(\alpha+\beta)^3} \\ -\gamma\frac{2(\alpha+\beta)^3+2(\alpha-\beta)}{(\alpha+\beta)^3} & -\gamma\frac{2(\alpha+\beta)^3+4\alpha}{(\alpha+\beta)^3} \end{bmatrix}_{(0,0)}.$$

It is clear that the entries of H upon direct evaluation at the point $(0,0)$ are undefined. This is treated by using L'Hopital's rule. L'Hopital's rule sometimes does not work for functions of two variables defined on cartesian coordinates, therefore a transformation of the entries to polar coordinates is applied. We will exploit this technique to express the Hessian matrix in polar coordinates and differentiate accordingly. The entries of H are transformed to polar coordinates using $\alpha = \hat{r}\cos(\hat{\theta})$ and $\beta = \hat{r}\sin(\hat{\theta})$, so the rule can be applied by taking the $\lim_{r\to 0} H$. Using $(\hat{r},\hat{\theta})$ coordinates the entries of H take the following form

$$H(\mathcal{T}(\hat{r},\hat{\theta}))|_{\hat{r}=0} = -\gamma \begin{bmatrix} \frac{4\hat{r}\sin\hat{\theta}-2r^3(\cos\hat{\theta}+\sin\hat{\theta})^3}{r^3(\cos\hat{\theta}+\sin\hat{\theta})^3} & \frac{2\hat{r}^3(\cos\hat{\theta}+\sin\hat{\theta})^3+2\hat{r}(\cos\hat{\theta}-\sin\hat{\theta})}{\hat{r}^3(\cos\hat{\theta}+\sin\hat{\theta})^3} \\ \frac{2\hat{r}^3(\cos\hat{\theta}+\sin\hat{\theta})^3+2\hat{r}(\cos\hat{\theta}-\sin\hat{\theta})}{\hat{r}^3(\cos\hat{\theta}+\sin\hat{\theta})^3} & \frac{4\hat{r}\cos\hat{\theta}+2\hat{r}^3(\cos\hat{\theta}+\sin\hat{\theta})^3}{\hat{r}^3(\cos\hat{\theta}+\sin\hat{\theta})^3} \end{bmatrix}_{\hat{r}=0}. \tag{4.71}$$

L'Hopital's rule is applied to each entry of H separately and the $\lim_{\hat{r}\to 0} H_{ij}(\mathcal{T}(\hat{r},\hat{\theta}))$ is computed for $i,j = 1,2$. Starting with the entry H_{11} and cancelling $\hat{r}$, the expression takes the form

$$\lim_{\hat{r}\to 0} H_{11} = \lim_{\hat{r}\to 0} \frac{4\sin\hat{\theta} - 2\hat{r}^2(\cos\hat{\theta}+\sin\hat{\theta})^3}{\hat{r}^2(\cos\hat{\theta}+\sin\hat{\theta})^3}.$$

Let $\mathcal{T}_1(\hat{r},\hat{\theta})$ and $\mathcal{T}_2(\hat{r},\hat{\theta})$ respectively denote the numerator and the denominator of the expression for H_{11}, then the application of L'Hopital's rule suggests that

$$\lim_{r\to 0} H_{11}(\mathcal{T}(\hat{r},\hat{\theta})) = \lim_{\hat{r}\to 0} \frac{\mathcal{T}_1(\hat{r},\theta)}{\mathcal{T}_2(\hat{r},\theta)} = \frac{\lim_{\hat{r}\to 0}\frac{d\mathcal{T}_1}{d\hat{r}}(\hat{r},\hat{\theta})}{\lim_{\hat{r}\to 0}\frac{d\mathcal{T}_2}{d\hat{r}}(\hat{r},\hat{\theta})} = \lim_{\hat{r}\to 0}\frac{-4\hat{r}(\cos\hat{\theta}+\sin\hat{\theta})^3}{2\hat{r}(\cos\hat{\theta}+\sin\hat{\theta})^3} = -2.$$

Applying the same procedure for H_{12}, H_{21} and H_{22}, all the entries of H are computed and given by

$$H(\mathcal{T}(\alpha,\beta))|_{(0,0)} = -\gamma \begin{bmatrix} -2 & 2 \\ 2 & 2 \end{bmatrix}. \tag{4.72}$$

Since the $\det(H) = -8\gamma^2 < 0$, therefore, the second derivative test suggests that $(0,0)$ is a saddle point of $\mathcal{T}(\alpha,\beta)$. Since it was previously shown that $\mathcal{T}(\alpha,\beta)$ attains a unique stationary point in the domain $[0,\infty) \times [0,\infty)$, i.e. by solving the equations (4.69) and (4.70), therefore, if $(0,0)$ was a maximum and $\mathcal{T}(0,0) < 0$, this would suggest that, whenever $\lambda_{1,2}$ has a non-zero imaginary part then $Re(\lambda_{1,2}) < 0$ regardless of the choice of d, γ and L^2, however due to fact that $(0,0)$ is a saddle point, it remains to show that $\mathcal{T}(\alpha,\beta)$ is negative at $(0,0)$ and its first derivatives in the neighbourhood of $(0,0)$ of $\mathcal{T}(\alpha,0)$ and $\mathcal{T}(0,\beta)$ for positive values of α and β in both directions are negative and do not change sign. Let $\mathcal{T}_0(\alpha)$ and $\mathcal{H}_0(\beta)$ denote the curves for constants $\beta = 0$ and $\alpha = 0$ respectively on the surface defined by $\mathcal{T}(\alpha,\beta)$, then

$$\mathcal{T}_0(\alpha) = \lim_{\beta\to 0} \mathcal{T}(\alpha,\beta) = -\gamma(1+\alpha^2) - (d+1)\eta_{n,k}^2,$$
$$\mathcal{H}_0(\beta) = \lim_{\alpha\to 0} \mathcal{T}(\alpha,\beta) = \gamma(1-\beta^2) - (d+1)\eta_{n,k}^2.$$

The expression for $\mathcal{T}_0(\alpha)$ clearly satisfy that it is negative at $\alpha = 0$ and its first derivative in the direction of α is $\frac{d\mathcal{T}_0(\alpha)}{d\alpha} = -2\gamma\alpha < 0$ for all $\gamma, \alpha \in [0,\infty)$. The expression for $\mathcal{H}_0(\beta)$ however is not trivially negative for all values, since the sign of the constant γ in the expression is positive, which if computed at $\beta = 0$, with substituting (4.40) for $\eta_{n,k}^2$ leads to the desired condition (4.68)

$$\mathcal{H}_0(\beta)\big|_{\beta=0} = \gamma - (d+1)\eta_{n,k}^2 < 0 \qquad \Longrightarrow \qquad \rho < 2\sqrt{\frac{(d+1)(2k+1)(n+2k+1)(n+4k)}{\gamma(n+4k+2)}}. \tag{4.73}$$

It has been shown that the condition (4.68) is necessary for $\mathcal{T}(\alpha,\beta)$ to be negative at the unique stationary point namely $(0,0)$, it remains to show that the first derivative of $\frac{d\mathcal{H}_0}{d\beta} = -2\gamma\beta < 0$ is negative for all $\gamma, \beta \in [0,\infty)$ which completes the proof.□

The region where the eigenvalues are real repeated roots are implicit curves in the parameter space satisfying (4.63), these curves are computed numerically in Section 4.4. These curves form the boundary between the regions of complex and real eigenvalues. Varying the diffusion rate d causes a shift in the location of the curves indicating clearly regions that are subject to diffusion-driven instability. The remaining case to look at is when both eigenvalues are real distinct. This happens if α and β are chosen such that the strict inequality case of (4.62) is satisfied. This case corresponds to the diffusion-driven instability *Turing type* only, because both eigenvalues are real and distinct.

4.3.4 Remark

The choice of $(\alpha, \beta) = (0, 0)$ is not permissible, because it leads to the trivial stable steady state namely $(u_s, v_s) = (0, 0)$. The sign of the real part of $\sigma_{1,2}$ is determined by the sign of $\mathcal{T}(\alpha, \beta)$, when $\sigma_{1,2} \in \mathbb{C}\backslash\mathbb{R}$, which has a unique stationary point at $(0, 0)$. Due to the strict monotonicity of $\mathcal{T}(\alpha, \beta)$ in the admissible parameter plane, the relevant region that could invalidate the required condition (4.68) for stability of (u_s, v_s) is the neighbourhood of the point $(\alpha, \beta) = (0, 0)$. It is reasonable to argue that the point $(\alpha, \beta) = (0, 0)$ should not be used as the platform of the proof of Theorem 4.3.2, which entails that proving the statement of Theorem 4.3.2 become a step closer by only showing that $\mathcal{T}(\alpha, \beta)$ is a strictly monotonically decreasing function (with no extrema in $(\alpha, \beta) \in \mathbb{R}^2_+$) and it can only attain bounded positive values in the neighbourhood of $(0, 0)$ if and only if the condition (4.68) on a disc-shape domain with radius ρ is violated. Therefore, given that ρ maintains to satisfy (4.68), the sign of the real part of $\sigma_{1,2} \in \mathbb{C}\backslash\mathbb{R}$ i.e. the sign of $\mathcal{T}(\alpha, \beta)$ is guaranteed to be negative. It consequently means that the use of the point $(\alpha, \beta) = (0, 0)$ as an extremum of the surface $\mathcal{T}(\alpha, \beta)$ is not essential to the validity of the proof of Theorem 4.3.2, but it is rather a complementary factor.

4.3.5 Interpretation of the dynamics for the case of real eigenvalues

If both eigenvalues are negative distinct real values, then the system is spatially as well as temporally stable, the dynamics will achieve no patterns, hence the system returns to the uniform constant steady state (u_s, v_s) as time grows, [see Section 4.4 Figure 1] with no effect from diffusion. If the eigenvalues are both real with different signs, then the type of instability caused by diffusion is spatially periodic or oscillatory in space, because this case corresponds to the steady state becoming a saddle point. If both eigenvalues are positive real distinct values, then the dynamics are expected to exhibit a spatially periodic pattern, in the form of stripes or spots.

4.4 Solution of partitioning curves and numerical verification

This section mainly focuses on simulating the numerical solutions of (4.50) and (4.51), furthermore, a pictorial representation of the implicit curves satisfying (4.50) and (4.51) on the admissible parameter plane $(\alpha, \beta) \in \mathbb{R}^2_+$ is obtained in light of which the full classification of the admissible parameter plane is presented. Numerical solutions of the implicit partitioning curves satisfying (4.50) and (4.51) are computed subject to both conditions respectively given by (4.57) and (4.68) on the radius ρ of Ω in terms of parameters d and γ. Furthermore, the numerical verifications of Theorems 4.3.1 and 4.3.2 are carried out in this section, where the reaction-diffusion system is numerically solved using the finite element method on a unit disc-shape domain. The relationship between radius ρ of the domain and parameters d and γ is shown to be in agreement with theoretical predictions presented.

4.4.1 Numerical solution of partitioning curves

Using algebraic manipulation, expanding the brackets and rearranging one can easily show that equation (4.50) can be written as a six degree implicit polynomial in the variable β, where the coefficients of such polynomial depend on all the remaining parameters namely α, d, γ and the eigenvalues $\eta^2_{n,k}$ of the diffusion operator Δ_p. Let

$\psi(\alpha, \beta)$ denote the six degree polynomial obtained from manipulating and rearranging (4.50), then finding the implicit solution satisfying equation (4.50) is equivalent to finding all the roots of the six degree polynomial equation $\psi(\alpha, \beta) = 0$, which according to the fundamental theorem of algebra there exist at most six distinct roots (Milewski, 2001).

Solutions of the implicit curves satisfying (4.50) is obtained by constructing a two-dimensional quadrilateral mesh on a rectangular domain $P = [0, \alpha_{max}] \times [0, \beta_{max}]$, where α_{max} and β_{max} are the maximum positive real values in the respective directions of α and β beyond which in the admissible parameter space, the uniform steady state (u_s, v_s) neither changes type nor does it change stability. Domain P is discretised by N points in both directions of α and β, where N is a positive integer, which leads to a rectangular mesh of $(N-1) \times (N-1)$ cells, each of size $\frac{\alpha_{max}}{N-1} \times \frac{\beta_{max}}{N-1}$, with N^2 points in P. To obtain the implicit solutions for (4.50), at every mesh point α_i in the direction the parameter-coordinate α, the roots of the six degree polynomial in β namely $\psi(\alpha_i, \beta) = 0$, denoted by $\psi_i(\beta) = 0$ are computed using the Matlab command '*roots*'. For every fixed mesh point α_i and fixed parameters d, γ and eigenvalue $\eta_{n,k}$ one obtains $\psi_i(\beta)$, in the form

$$\psi_i(\beta) = C_0(\alpha_i) + C_1(\alpha_i)\beta + C_2(\alpha_i)\beta^2 + C_3(\alpha_i)\beta^3 + C_4(\alpha_i)\beta^4 + C_5(\alpha_i)\beta^5 + C_6(\alpha_i)\beta^6, \tag{4.74}$$

where the expressions for the coefficients are given by

$$\begin{aligned} C_0(\alpha_i) =& \alpha_i^2\gamma - 2\alpha_i^2\gamma\eta_{n,k}^2 + 2\alpha_i^4\gamma + \alpha_i^2\eta_{n,k}^4 - 2\alpha_i^2 d\gamma\eta_{n,k}^2 - 4\alpha_i^4\gamma^2 + 2\alpha_i^2 d\eta_{n,k}^4 - 4\alpha_i^3\eta_{n,k}^4 \\ &+ 2\alpha_i^4\gamma\eta_{n,k}^2 + \alpha_i^6\gamma + \alpha_i^2 d^2\eta_{n,k}^4 + 2\alpha_i^4 d\eta_{n,k}^2 - 4\alpha_i^5\gamma\eta_{n,k}^2, \end{aligned}$$

$$\begin{aligned} C_1(\alpha_i) =& 8\alpha_i^3\gamma d\eta_{n,k}^2 - 20\alpha_i^4\gamma\eta_{n,k}^2 - 12\alpha_i^2 d\eta_{n,k}^4 + 2\alpha_i^2 d\eta_{n,k}^4 + 6\alpha_i^5\gamma + 8\alpha_i^3\gamma\eta_{n,k}^2 - 12\alpha_i^2\eta_{n,k}^4 \\ &+ 4\alpha_i d\eta_{n,k}^4 + 2\alpha_i\eta_{n,k}^4 + 4\alpha_i^3\gamma - 2\alpha\gamma, \end{aligned}$$

$$\begin{aligned} C_2(\alpha_i) =& \gamma + 2\gamma\eta_{n,k}^2 + \gamma\eta_{n,k}^2 + \eta_{n,k}^4 + 2d\gamma\eta_{n,k}^2 + 24\alpha_i^2\gamma^2 + 2d\eta_{n,k}^4 - 12\alpha_i\eta_{n,k}^4 + 12\alpha_i^2\gamma\eta_{n,k}^2 \\ &+ 15\alpha_i^4\gamma + d^2\eta_{n,k}^4 - 12\alpha d\eta_{n,k}^4 + 12\alpha_i^2 d\gamma\eta_{n,k}^2 - 40\alpha_i^3\gamma\eta_{n,k}^2, \end{aligned}$$

$$C_3(\alpha_i) = 32\alpha_i\gamma^2 - 4\alpha_i\gamma - 4\eta_{n,k}^4 + 8\alpha_i\gamma\eta_{n,k}^2 + 20\alpha_i^3\gamma - 4d\eta_{n,k}^4 + 8\alpha_i d\gamma\eta_{n,k}^2 - 40\alpha_i^2\gamma\eta_{n,k}^2,$$

$$C_4(\alpha_i) = 12\alpha_i^2 - 2\gamma + 2\gamma\eta_{n,k}^2 + 15\gamma\alpha_i^2 + 2d\gamma\eta_{n,k}^2 - 20\alpha_i\gamma\eta_{n,k}^2,$$

$$C_5(\alpha_i) = 6\alpha_i\gamma - 4\gamma\eta_{n,k}^2, \quad \text{and} \quad C_6(\alpha_i) = \gamma.$$

In the expressions for the coefficients of (4.74), the values of $\eta_{n,k}$ are used as given by (4.40). Each of N polynomial equations in the direction of α has at most six roots for every fixed α_i. Let β_j for $j \in \{1,2,3,4,5,6\}$ denote all the six roots of $\psi_i(\beta) = 0$, then the point (α_i, β_j) obtained by pairing each index $i = 1,2,3,...,N$ with each root β_j lies on the curve satisfying (4.50). Similar procedure is applied to obtain the solutions of the second partitioning curve satisfying (4.51), that corresponds to a curve in the admissible parameter space on which the real part of $\sigma_{1,2} \in \mathbb{C}\backslash\mathbb{R}$ is zero and it corresponds to the uniform steady state (u_s, v_s) undergoing transcritical bifurcation. Using a similar notation as for $\psi_i(\beta) = 0$, the solutions to (4.51) is equivalent to finding all the roots of an implicit cubic polynomial in β of the form $\phi_i(\beta) = 0$, where $\phi_i(\beta)$ is given by

$$\phi_i(\beta) = C_0(\alpha_i) + C_1(\alpha_i)\beta + C_2(\alpha_i)\beta^2 + C_3(\alpha_i)\beta^3, \tag{4.75}$$

with expressions for the coefficients of (4.75), taking the forms $C_0(\alpha_i) = -\alpha_i^3\gamma - \alpha_i d\eta_{n,k}^2 - \alpha_i\eta_{n,k}^2 - \alpha_i\gamma$, $C_1(\alpha_i) = \gamma - \eta_{n,k}^2 - d\eta_{n,k}^2 - 3\alpha_i^2\gamma$, $C_2(\alpha_i) = -3\alpha_i\gamma$, $C_3(\alpha_i) = -\gamma$ and $\eta_{n,k}$ as given by (4.40). Parameters α and β are strictly positive real values in system (4.13), therefore, upon computing all the roots of polynomials (4.74) and (4.75), the algorithm is instructed to record only roots satisfying $\beta_j \in \mathbb{R}_+$, and any root that is either negative real or has non-zero imaginary part, is discarded. It is due to this constraint on the algorithm that gives all the admissible solutions satisfying (4.50) on the parameter space. In Figure 4.4 the number of intersections of a vertical straight line in the direction of β for a fixed value of α, indicates the number of positive real roots of polynomial (4.74). This algorithm is executed for five different values of d to obtain the solutions of (4.50) and (4.51) under both of the conditions (4.57) and (4.68) on the radius ρ. The shift and existence of both of the partitioning curves satisfying

(4.50) and (4.51) is analysed subject the variation of parameter d. It is worth noting that under the current analysis the variation of d suffices to disclose every desirable insight, one wishes to obtain about the variation of the parameter γ. This is due to their reciprocal locations in the expression on the right hand-sides of conditions (4.57) and (4.68). In other words, increasing parameter d is equivalent to decreasing parameter γ and vice versa. Therefore for fixed value of γ it suffices to study the variation of d. Using condition (4.57) of Theorem 4.3.1, the variation of the diffusion coefficient is analysed for five different values of d and Figure 4.4 (a) shows the shift of the solution of (4.50). It was shown that the solution (4.50) determines a partition for the region in the parameter space that corresponds to $\sigma_{1,2}$ to be a pair of complex values and it can be seen that under condition (4.57), as the value of the parameter d increases the region that corresponds to complex eigenvalues gradually decrease, however so long as condition (4.57) remains satisfied, the vertical axis β continues to have at least two distinct intercepts of the curves satisfying (4.50) for the same value of d. It is this behaviour of the real-complex eigenvalues partitioning curve that either preserves or vanishes the existence of a sub-partition for positive and negative real parts of a complex pair of roots. The five values of parameter d are clearly indicated on the curves in Figure 4.4. It would be reasonable to use exactly the same range for the variational values of d under both conditions (4.57) and (4.68), however, it was noted that, when domain-size is restricted by (4.68) then the same values used for varying d in Figure 4.4 (a) invalidates the inequality (4.68), therefore, the range of variational values for parameter d under condition (4.68) is significantly smaller. Using such range despite that a significant observable shift is emerged in the location of the solution curves, it does not invalidate the inequality (4.68) for ρ. Figure 4.4 (b) shows the variation of parameter d using the values indicated on each curve. It can be noted that as d increases significantly, the number of intercepts on β axis reduces from two to one and eventually to zero. The fact that condition (4.68) on the domain-size forbids the existence of a region in the admissible parameter space that corresponds to complex conjugate pair of $\sigma_{1,2}$ with positive real part, is related to the behaviour of the curve satisfying (4.74).

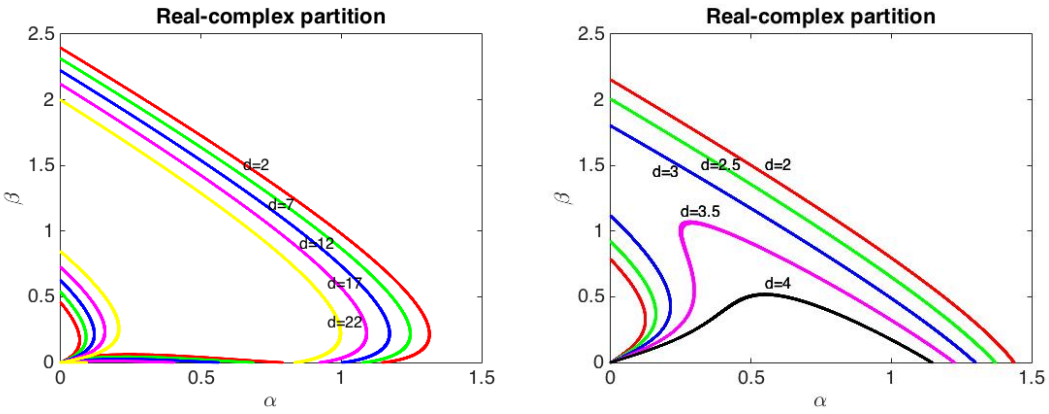

(a) (b)

FIGURE 4.4: In (a) partitioning curves satisfying (4.50) and condition (4.57) of Theorem 4.3.1 are shown, that partitions the region that corresponds to real $\sigma_{1,2}$ from that, which corresponds to complex conjugate pair of $\sigma_{1,2}$. In (b) the partitioning curves satisfying (4.50) and condition (4.68) of Theorem 4.3.2 are shown, that partitions the region corresponding to real pair of $\sigma_{1,2}$ from that, which corresponds to complex conjugate pair of $\sigma_{1,2}$.

It is the location of the curve associated to the solution of (4.74), that either admits or restricts the curve satisfying (4.75) on the admissible parameter space. This relation is a direct agreement and a numerical demonstration of conditions for diffusion driven instability presented in (Murray, 2001; Edelstein-Keshet, 1988; Madzvamuse, Chung, and Venkataraman, 2015). Trial and error method is used to identify which side of the partitioning curves in Figure 4.4, corresponds to complex $\sigma_{1,2}$, where the shift of such regions in the parameter space subject to the same respective variation of d is presented in Figure 4.5. Investigating the regions corresponding to complex values for $\sigma_{1,2}$ in Figure 4.5, using the solution of (4.75), it was found that a sub-partition only exists if the value of ρ satisfies condition (4.57), with respect to the values of d and γ. This is a numerical verification of the statement of Theorem 4.3.1. If the values of d and/or γ are changed such that ρ no longer satisfies condition (4.57), it causes to vanish the existence of a sub-partition, within the region corresponding to complex eigenvalues $\sigma_{1,2}$, which is in agreement with the prediction claimed by the statement of Theorem 4.3.2. Under such choices of d and γ, the region of the parameter spaces corresponding to complex $\sigma_{1,2}$ has no stability partition, therefore, every where on this

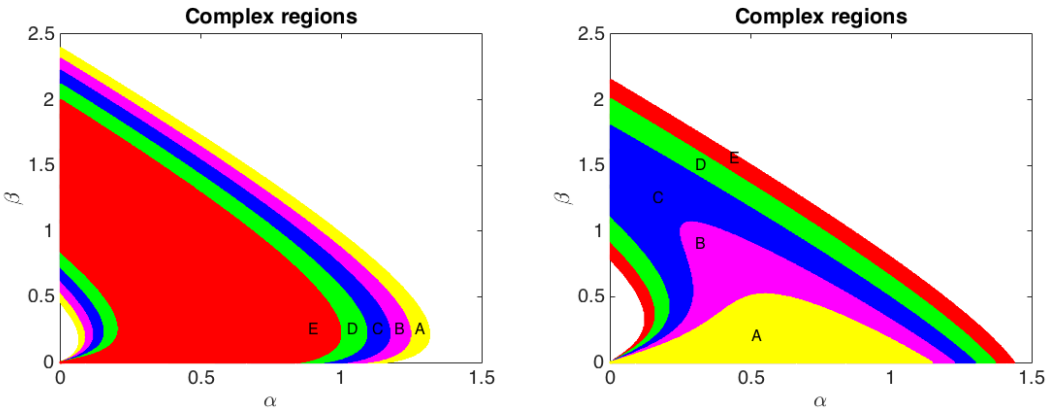

(a) (b)

FIGURE 4.5: In (a) the shift of regions is shown corresponding to complex $\sigma_{1,2}$ and subject to condition (4.57) of Theorem 4.3.1. In (b) the shift of regions corresponding to complex $\sigma_{1,2}$ and subject to condition (4.68) of Theorem 4.3.2 is shown.

region the real part of $\sigma_{1,2}$ is negative. If parameters α and β are fed into system (4.13), then the dynamics are expected to exhibit global temporal stability. Figure 4.6 shows the region on the admissible parameter spaces corresponding to complex $\sigma_{1,2} \in \mathbb{C}\backslash\mathbb{R}$ with negative real part. It can be noted that Figure 4.6 (b) portrays exactly the same spaces as shown in Figure 4.5 (b), which is a further verification of the claim made my the statement of Theorem 4.3.2, namely, when ρ satisfies condition (4.68), then for no choice of $\alpha, \beta \in \mathbb{R}_+$ the complex eigenvalue $\sigma_{1,2}$ can have positive real part. It further means that if ρ is chosen such that it satisfies condition (4.68), then system (4.13) is guaranteed to exhibit global temporal stability in the dynamics, with the only possibility of spatial periodic behaviour. The consequence of this relationship is to state that if the value of ρ is bounded above by the right hand-side of condition (4.68), then the diffusion-driven instability will remain restricted to Turing type only, hence any pattern obtained under condition (4.68) on ρ is expected to be spatially periodic pattern, with a global temporally stable behaviour. In this case we can only obtain a pattern of spots or stripes, with spatial periodicity. If a condition on ρ is set so that it is large enough to exceed the value on the right hand-side of condition (4.68), i.e. ρ satisfying (4.57), only then a sub-partition can emerge with in the admissible parameter space

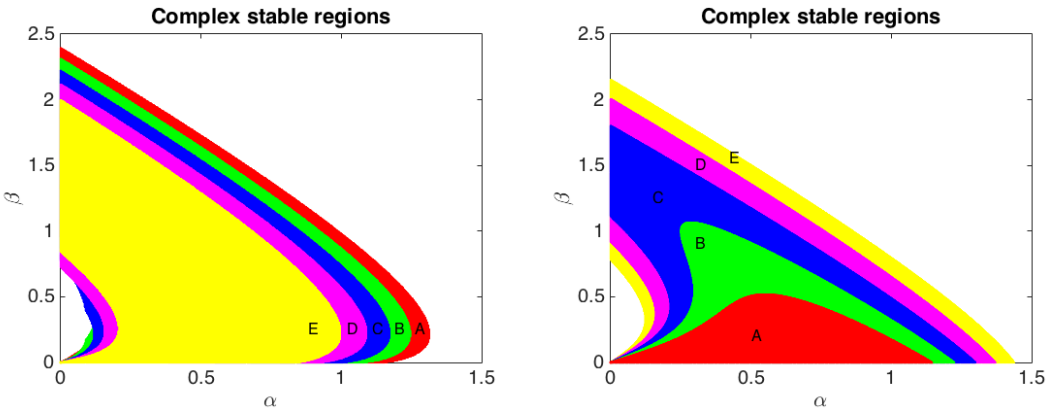

(a) (b)

FIGURE 4.6: In (a) the shift of regions corresponding to complex $\sigma_{1,2}$ with negative real part and subject to condition (4.57) of Theorem 4.3.1 is shown. In (b) the shift is shown of regions corresponding to complex $\sigma_{1,2}$ with negative real parts and subject to condition (4.68) of Theorem 4.3.2 is shown.

corresponding to complex pair of $\sigma_{1,2}$. This can be observed by comparing Figure 4.6 (a) with Figure 4.5 (a), in particular the a deficiency of regions is clearly visible on the inner stripes of the shifted spaces near the origin in Figure 4.6 (a). Figure 4.7 (b) shows the emergence of these curves that partitions the region corresponding to complex $\sigma_{1,2}$. Recalling that if a sub-partition in the regions indicated by Figure 4.5 exist then the corresponding partitioning curves must satisfy (4.51), which resemble the values of the parameter space, which causes the real part of $\sigma_{1,2}$ to become zero, when it is a pair of complex conjugate values. Therefore, on these curves the uniform steady state (u_s, v_s) undergoes transcritical bifurcation. These are also the curves on which the real part of $\sigma_{1,2} \in \mathbb{C}\backslash\mathbb{R}$ changes sign, which means to one side of these curves a region in the admissible parameter space exist, that corresponds to $\sigma_{1,2}$ to be complex conjugate pair, but with positive real part. Parameter values of such kind results in the uniform steady state (u_s, v_s) to become periodic in time, which means that the values of α and β from this region causes system (4.13) to exhibit Hopf bifurcation. Figure 4.7 (a) shows a shift in the region of the parameter spaces that corresponds to Hopf bifurcation for the same variation in the value of d as used in Figure 4.5. It is also worth noting that with increasing the value of d the parameter spaces corresponding to Hopf bifurcation

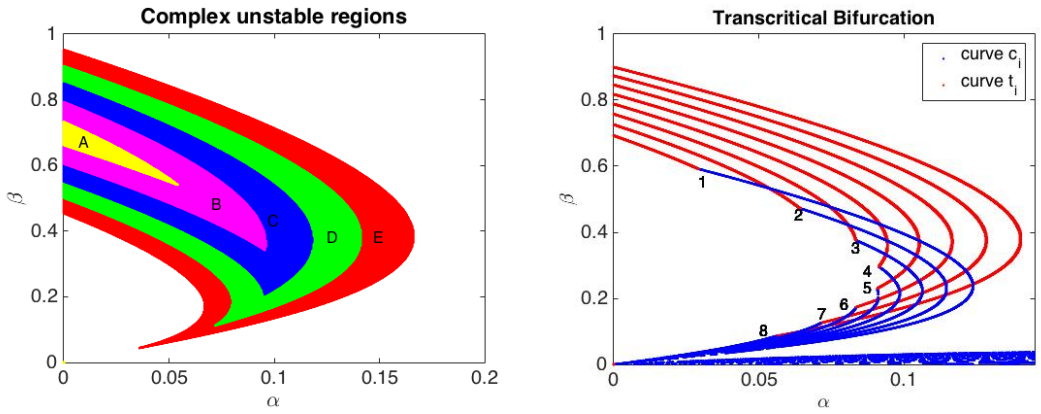

(a) (b)

FIGURE 4.7: In (a) the shift of regions corresponding to complex $\sigma_{1,2}$ with positive real part and ρ restricted to condition (4.57) of Theorem 4.3.1. In (b) the shift in the location of red curves t_i for eight different values of d, on which the values of $\sigma_{1,2}$ are pure imaginary, and ρ is restricted to condition (4.57) of Theorem 4.3.1.

gradually decreases, which is in agreement with the mathematical reasoning behind the statement of Theorem 4.3.1, because as the value of d is increased one get closer to the violation of the necessary condition (4.57) for the existence of regions for Hopf bifurcation. Figure 4.7 (b) shows a more gradual extinction of the sub-partitioning curves within the region corresponding to complex $\sigma_{1,2}$. For eight different values of d, with ρ still satisfying (4.57), the solution of (4.74) and (4.75) was plotted near the origin to closely observe the interaction and a shift of the location, where they intersect each other, it was found that for small values of d, the intersection between the curves (4.74) and (4.75) occurs such that a significant part of the curve satisfying (4.75) forms a sub-partition within the region of the admissible parameter space that corresponds to complex eigenvalues. However, as the value of d is gradually increased, so did the location of the intersection moved, reducing the sub-partition formed by the solution of (4.75). Curves c_i for $i \in \{1,2,3,4,5,6,7,8\}$ (blue colour) in Figure 4.7 (b) denote the solution satisfying (4.74). On curves c_i the eigenvalues $\sigma_{1,2}$ are repeated positive real roots, therefore, parameter values on these curves correspond to Turing type instability. Where as curves t_i (in red colour) indicate the sub-partition formed by the solution of (4.75) with in the region corresponding to complex eigenvalues $\sigma_{1,2}$.

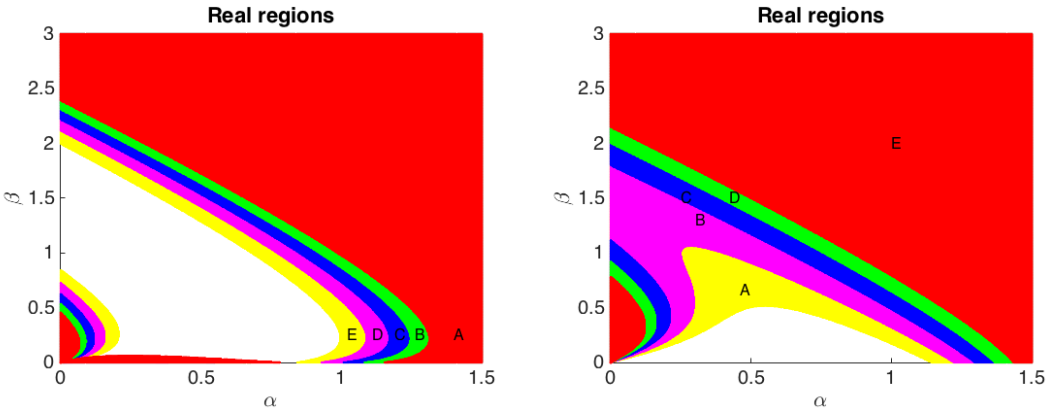

(a) (b)

FIGURE 4.8: In (a) the shift of regions corresponding to real $\sigma_{1,2}$ and subject to condition (4.57) of Theorem 4.3.1 is shown. In (b) the shift of regions corresponding to real $\sigma_{1,2}$ and subject to condition (4.68) of Theorem 4.3.2.

On curves t_i the uniform steady state (u_s, v_s) is expected to undergo transcritical bifurcation. In Figure 4.7 (b) curves t_i and c_i for $i = 8$ correspond to the smallest value of $d = 2$, which is gradually increased reaching a maximum value of $d = 22$ that corresponds to curves c_1 and t_1. The union of the spaces presented in Figure 4.5 and those corresponding to eigenvalues that are real $\sigma_{1,2} \in \mathbb{R}$ the whole of the admissible parameter plane, namely the top right quadrant of $\mathbb{R}^2_+$ plane. Figure 4.8 shows under both conditions (4.57) and (4.68) on ρ the shift of parameter spaces that corresponds to real eigenvalues for different values of d. The outer partitioning curves of the regions corresponding to complex eigenvalues in Figure 4.4, indicate the choice of α and β for which the eigenvalues $\sigma_{1,2}$ is a pair of real repeated negative values, therefore, parameter spaces bounded by these curves corresponds to a pair of distinct negative real values. Parameter choice from these regions corresponds to a global spatio-temporally stable behaviour of the dynamic of system (4.13). Figure 4.9 shows the shift of these spatio-temporal stable regions on the admissible parameter space. Any choice of α and β from these regions will result in the dynamics of system (4.13) to exhibit global stability in space as well as in time, which means that if system (4.13) is perturbed in

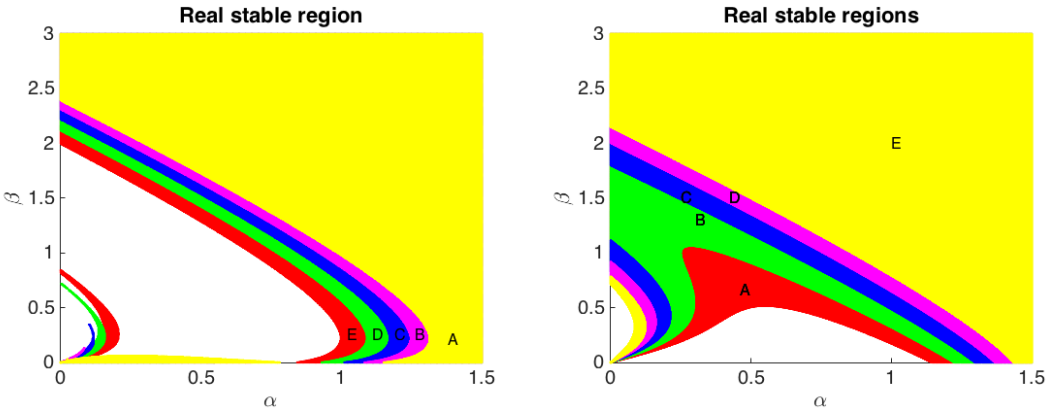

(a) (b)

FIGURE 4.9: In (a) the shift of regions corresponding to a pair of negative distinct real $\sigma_{1,2}$ and subject to condition (4.57) of Theorem 4.3.1 is shown. In (b) the Shift of regions corresponding to a pair of negative distinct real $\sigma_{1,2}$ and subject to condition (4.68) of Theorem 4.3.2.

the neighbourhood of the uniform steady state (u_s, v_s) using parameters from these regions, the dynamics will guarantee to return back to the uniform steady state (u_s, v_s). It can be clearly observed that under both conditions (4.57) and (4.68) on ρ, regions corresponding to a pair of real negative eigenvalues form a proper subset of those spaces that corresponds to a pair of real values irrespective of sign. Figure 4.9 shows under both conditions (4.57) and (4.68) on ρ the shift in the spaces that correspond to global spatio-temporally stable behaviour of the dynamics of system (4.13). Comparing Figure 4.8 and Figure 4.9 it can be clearly observed that under both conditions on ρ the regions of spaces corresponding to negative real values are deformed versions of those that corresponds to arbitrary real values. The remaining spaces to analyse are those corresponding to diffusion-driven instability of Turing type under conditions (4.57) and (4.68) on ρ. When $\sigma_{1,2}$ are a pair of real values with at least one of them positive. This region corresponds to Turing type instability and under both conditions on ρ these regions exist. It can be noted that near the origin of the admissible parameter space in Figure 4.4, for each value of d the small curves starting at the origin $(\alpha, \beta) = (0, 0)$ and curving back to intercept the β axis, are the curves on which the eigenvalues $\sigma_{1,2}$ are repeated positive real roots, therefore these curves correspond to

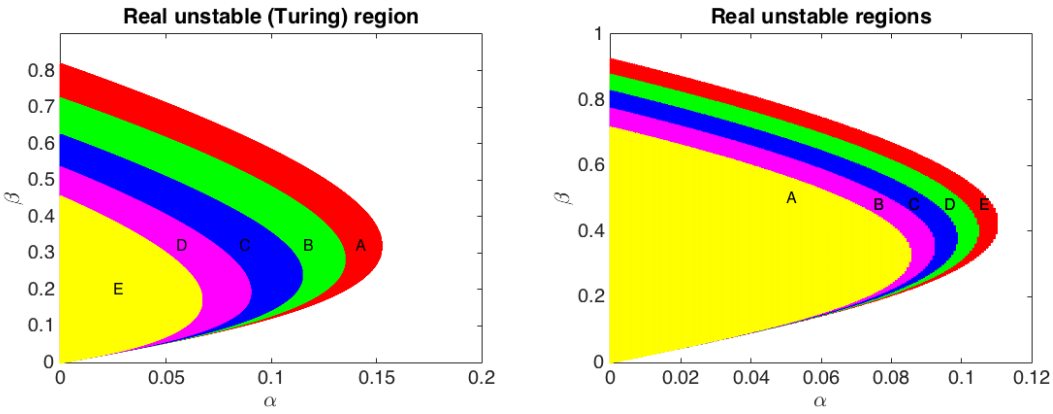

(a) (b)

FIGURE 4.10: In (a) the Shift of regions corresponding to Turing instability where at least one eigenvalue $\sigma_{1,2}$ is real positive and subject to condition (4.57) of Theorem 4.3.1 is shown. In (b) the shift of regions corresponding to Turing instability where at least one eigenvalue $\sigma_{1,2}$ is real positive and subject to condition (4.68) of Theorem 4.3.2 is shown.

diffusion-driven instability of Turing type. We know that the diffusion-driven instability can also happen, when either σ_1 or σ_2 are positive real. Figure 4.10 shows the shift of those regions corresponding to Turing type instability and it can be observed that as the value of parameter d increases, so does the region in the parameter space enlarges. It can be noted from Figures 4.6 and 4.10, that all the points specific to a certain colour on the parameter plane are denoted by an alphabetic letter. This is for the purpose to be able to cross reference using set notation to a specific region when summarising the results in Table 4.1. In each of Figures 4.6 to 4.10 the set of points on the parameter plane that correspond to a certain value of d specified by certain colour, are associated to the corresponding claims of Theorems 4.3.1 and 4.3.2 as well as the associated stability and types of the uniform steady state (u_s, v_s) is summarised in Table 4.1.

4.4.2 Remark

The first non-trivial mode $k = 1$ corresponding to the pair $(j = 1, j = 2)$ in the infinite series of the eigenfunctions is used for all the computations of the partitioning curves and the corresponding parameter spaces. It is worth noting that higher modes

Stability of USS (u_s, v_s)			Stable regions		Unstable regions		
Types of USS (u_s, v_s)			Node	Spiral	Turing-instability	Hopf bifurcation	Transcritical bifurcation
Figure index			Figure 4.9 (a)	Figure 4.6 (a)	Figure 4.10 (a)	Figure 4.7 (a)	Figure 4.7 (b)
Theorem 4.3.1	ρ satisfying (4.57)	$\sigma_{1,2}$ / (d,γ,ρ,n)	$0 > \sigma_{1,2} \in \mathbb{R}$	$\sigma_{1,2} \in \mathbb{C}\backslash\mathbb{R}$	$0 < \sigma_1 \in \mathbb{R}$ or $0 < \sigma_2 \in \mathbb{R}$	$\sigma_{1,2} \in \mathbb{C}\backslash\mathbb{R}$, $\mathrm{Re}(\sigma_{1,2}) > 0$	$\sigma_{1,2} \in \mathbb{C}\backslash\mathbb{R}$, $\mathrm{Re}(\sigma_{1,2}) = 0$
		(2.0, 1, 35, 1.7)	A	$A \cup B \cup C \cup D \cup E$	E	$A \cup B \cup C \cup D \cup E$	t_8
		(7.0, 1, 35, 1.7)	$A \cup B$	$B \cup C \cup D \cup E$	$E \cup D$	$A \cup B \cup C \cup D$	t_6
		(12, 1, 35, 1.7)	$A \cup B \cup C$	$C \cup D \cup E$	$E \cup D \cup C$	$A \cup B \cup C$	t_3
		(17, 1, 35, 1.7)	$A \cup B \cup C \cup D$	$D \cup E$	$E \cup D \cup C \cup B$	$A \cup B$	t_2
		(22, 1, 35, 1.7)	$A \cup B \cup C \cup D \cup E$	E	$E \cup D \cup C \cup B \cup A$	A	t_1
Figure index			Figure 4.9 (b)	Figure 4.6 (b)	Figure 4.10 (b)	Figure 4.7 (b)	Figure 4.6 (b)
Theorem 4.3.2	ρ satisfying (4.68)	$\sigma_{1,2}$ / (d,γ,ρ,n)	$0 > \sigma_{1,2} \in \mathbb{R}$	$\sigma_{1,2} \in \mathbb{C}\backslash\mathbb{R}$	$0 < \sigma_1 \in \mathbb{R}$ or $0 < \sigma_2 \in \mathbb{R}$	$\sigma_{1,2} \in \mathbb{C}\backslash\mathbb{R}$, $\mathrm{Re}(\sigma_{1,2}) > 0$	$\sigma_{1,2} \in \mathbb{C}\backslash\mathbb{R}$, $\mathrm{Re}(\sigma_{1,2}) = 0$
		(2.0, 1, 10, 1.7)	E	$A \cup B \cup C \cup D \cup E$	A	$\emptyset$	$\emptyset$
		(2.5, 1, 10, 1.7)	$E \cup D$	$A \cup B \cup C \cup D$	$A \cup B$	$\emptyset$	$\emptyset$
		(3.0, 1, 10, 1.7)	$E \cup D \cup C$	$A \cup B \cup C$	$A \cup B \cup C$	$\emptyset$	$\emptyset$
		(3.5, 1, 10, 1.7)	$E \cup D \cup C \cup B$	$A \cup B$	$A \cup B \cup C \cup D$	$\emptyset$	$\emptyset$
		(4.0, 1, 10, 1.7)	$E \cup D \cup C \cup B \cup A$	A	$A \cup B \cup C \cup D \cup E$	$\emptyset$	$\emptyset$

TABLE 4.1: The summary of the full classification of parameter spaces for system (4.13) is presented with the associated numerical verification of the predictions made by Theorems 4.3.1 and 4.3.2. Furthermore, it is shown how a certain type of bifurcation space shifts according to the variation of parameter d.

such as $k = 2, 3, ...$ for the expressions of the eigenvalues $\eta_{n,k}$ will only cause a scaled shift in the location of the partitioning curves, whilst keeping the validity of conditions (4.57) and (4.68) intact. This is because the choice of higher modes k enforces a corresponding change in the value of radius ρ in order for the inequalities corresponding to conditions (4.57) and (4.68) to hold. In other words, given that conditions (4.57) and (4.68) are satisfied the dynamics are guaranteed to exhibit the proposed behaviour independent of the choice of the mode k and the order of the corresponding Bessel's equation $n \in \frac{1}{2}\mathbb{Z}$.

4.5 Finite element solutions of RDS

To verify numerically the classification of parameter spaces proposed by Theorems 4.3.1 and 4.3.2, the reaction-diffusion system (4.13)-(4.15) is simulated using finite element method (Smith, Griffiths, and Margetts, 2013; Becker, 1998) on a unit disc Ω. Due to the curved boundary of Ω, the triangulation is obtained through an application of iterative algorithm using a technique called *distmesh* (Persson and Strang, 2004; Schnepf and Leitner, 2009; Lee and Schachter, 1980).

4.5.1 Overview of *distmesh* triangulation

The algorithm for *distmesh* was originally developed by collaboration of Prof PerOlof Persson and Prof Gilbert Strang (Persson and Strang, 2004). The algorithm is coded in MATLAB for generating uniform and non-uniform refined meshes on two and three dimensional geometries. The algorithm of *distmesh* uses signed-distance function $d(x, y)$, which is negative inside the discretised domain Ω and it is positive outside the $\partial\Omega$. The construction of distmesh triangulation is an iterative process using a set of two interactive algorithms, one of which controls the displacement of nodes within the domain and the other ensures that the consequences of node displacement does not violate the properties of Delaunay triangulation (Lee and Schachter, 1980). Node-moving algorithm controls and keeps track of the displacement and coordinates of all nodes after each iteration. The movement of each node depends on the forces of truss acting normal of the boundary $\partial\Omega$ and the algorithm seeks an equilibrium solution subject to the input parameters from the user. For topological consistency a second algorithm is called within the code, that controls the edges of each triangle according to the restriction of Delaunay triangulation (Lee and Schachter, 1980). A reaction force with large enough magnitude acts normal to the boundary preventing nodes from exiting the domain. The code continues to iterate until an equilibrium solution is reached upon which the x, y coordinates of all nodes are collected and recorded in an array of size $N \times 2$ of the form $\boldsymbol{p} = [\boldsymbol{x}, \boldsymbol{y}]$, where N is the number of nodes in the domain. A vector valued function $\boldsymbol{F}(\boldsymbol{p})$ determines the required displacement of $\boldsymbol{p}$ in the process of reaching equilibrium. The resultant force from the horizontal and vertical components of $\boldsymbol{F}$ is applied in each iteration to displace the location of each node one step closer to the equilibrium solution. Upon reaching the equilibrium solution the algorithm further assigns a connectivity array of size $M \times 3$ to the output of the final iteration on $\boldsymbol{F}(\boldsymbol{p})$, where M is the number of triangles forming the discretised domain Ω. In order to ensure convergence to an equilibrium, it is necessary to choose the input parameters sensibly so that equilibrium is reached within a realistic time limit.

4.5.2 Finite element simulations

Using *distmesh* algorithm a unit disc Ω was discretised to obtain a uniform triangulation. Each simulation in this section is performed on a unit disc centred at the origin of Cartesian plane, which is discretised by 6327 triangles consisting of 3257 nodes. The initial conditions for each simulation are taken to be small random perturbations in the neighbourhood of the steady state (u_s, v_s) of the form (Madzvamuse, Gaffney, and Maini, 2010; Madzvamuse, 2008)

$$\begin{cases} u_0(x,y) = \alpha + \beta + 0.0016\cos(2\pi(x+y)) + 0.01\sum_{i=1}^{8}\cos(i\pi x), \\ v_0(x,y) = \frac{\beta}{(\alpha+\beta)^2} + 0.0016\cos(2\pi(x+y)) + 0.01\sum_{i=1}^{8}\cos(i\pi x). \end{cases} \tag{4.76}$$

Choices of parameters α and β are verified from each of the four regions where the dynamics of system (4.13)-(4.15) exhibit diffusion-driven instability. In all our simulations, the parameters d and γ are varied, whilst keeping the value of radius $\rho = 1$ fixed, which allows us to keep constant the well refined number of degrees of freedom for the mesh. It proves computationally expensive to vary ρ, therefore in order to satisfy conditions (4.57) and (4.68), it suffices to change the values of d and γ to ensure that a particular condition on the domain-size in terms of reaction-diffusion rates is satisfied. The actual numerical values for each simulation are presented in Table 4.2. Before demonstrating diffusion-driven instability a pair of parameter values α, β from spatio-temporally stable region indicated in Table 4.1 is used to demonstrate in Figure 4.11 (a), how the dynamics over come small perturbations and reach the uniform steady state (u_s, v_s) without evolving any pattern. The uniform convergence to the constant steady state (u_s, v_s) is shown in Figure 4.11 (b), through the convergence of the discrete L_2 norm of the difference in the solutions u and v for the successive time steps. Figure 4.12 (a) shows the evolution of spatial pattern as a consequence of choosing (α, β) from Turing region under condition (4.68) indicated in Figure 4.10 (b). The only unstable region in the admissible parameter space $(\alpha, \beta) \in \mathbb{R}^2_+$ when ρ satisfies condition (4.68) is the region presented in Figure 4.10 (b), which causes the dynamics

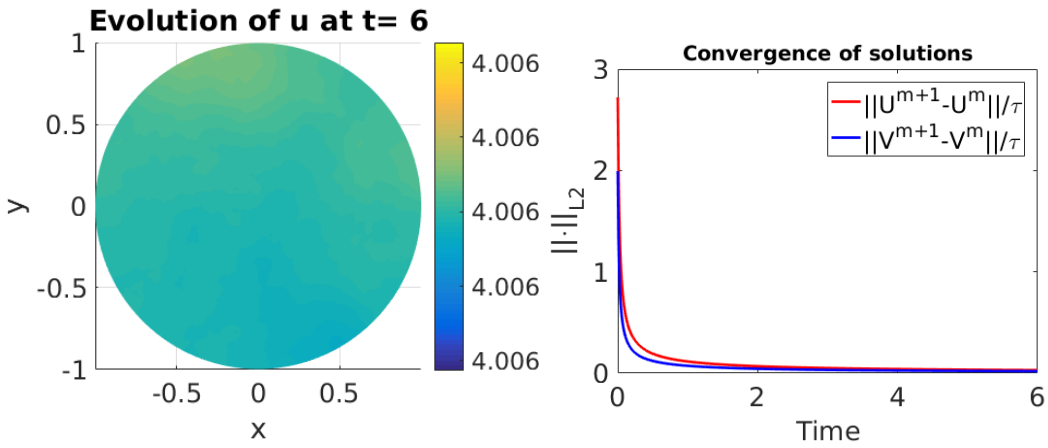

FIGURE 4.11: In (a) no pattern is evolved when parameters α and β are chosen outside Turing space under condition (4.68) on the radius ρ. In (b) uniform convergence of the discrete L_2 norm of the successive time-step difference of the solutions u and v is shown.

of system (4.13)-(4.15) to evolve spatially periodic pattern as presented in Figure 4.12. Depending on the initial conditions and the mode of the eigenfunctions, the spatially periodic pattern provided by parameter spaces in Figure 4.10 (b) is expected to be a combination of radial and angular stripes or spots. Once the initial pattern is formed by the evolution of the dynamics, then the system is expected to uniformly converge to a Turing-type steady state, which means the initially evolved spatial pattern becomes temporally invariant as time grows. The simulation of Figure 4.12 was executed with a threshold of the successive time-step difference in the L_2 norm to be less than 5×10^{-4}. Figure 4.12 (b) demonstrates the behaviour of the discrete L_2 norm of the difference of the solutions u and v for the successive time-steps. It is observed that after the initial Turing-type instability, the evolution of the system uniformly converges to a spatially patterned steady state. Figure 4.13 presents a series of three snapshots to show how the spatially periodic pattern is evolved to a Turing type steady state, when parameters α and β are chosen from Turing region and ρ satisfying condition (4.57), with respect to d and γ. For simulations in Figure 4.13, parameters α and β are chosen from regions presented in Figure 4.10 (a), therefore the dynamics corresponds to these regions also evolve spatial pattern with global temporal stability. It can be noted from

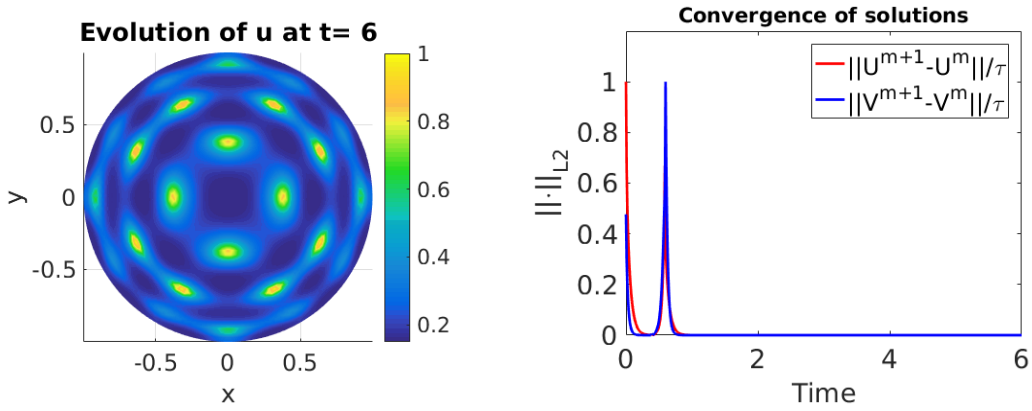

(a) (b)

FIGURE 4.12: In (a) the evolution of pattern is restricted to spatial periodicity for α and β in Turing space under condition (4.68) on the radius ρ. In (b) the instability of the discrete L_2 norm of the successive time-step difference of the solutions u and v.

Figure 4.13 (d), that after the initial pattern is formed, the system is uniformly converging to the spatially periodic steady state, without admitting any deformation to occur to the initial pattern. This verifies, that Turing instability is a domain independent phenomena, which only depends on the choice of parameters and the initial conditions. At $t = 6$ the required threshold of 5×10^{-4} on the discrete L_2 norm of the difference in the solutions between successive time-steps is reached, which can be observed in Figure 4.13 (d). The remaining two unstable regions in the admissible parameter space presented in Figure 4.7 correspond to spatio-temporal periodicity. Regions presented in Figure 4.7 (a) are those corresponding to a complex conjugate pair of eigenvalues with non-zero positive real part. These regions emerge in the admissible parameter space under condition (4.57) on ρ. Choosing parameters from regions in Figure 4.7 (a) admits temporal periodic behaviour in the dynamics of system (4.13)-(4.15), which are presented in Figure 4.14. The initial pattern in Figure 4.14 (a) is in fact achieved earlier than than at $t = 1$, therefore, the temporal gap between the initial and second pattern in Figure 4.14 (b) is relatively smaller than those temporal gaps that exist between the second, third and fourth temporal periods.It is worth noting that the temporal period between the successive transitional temporal instabilities from one type

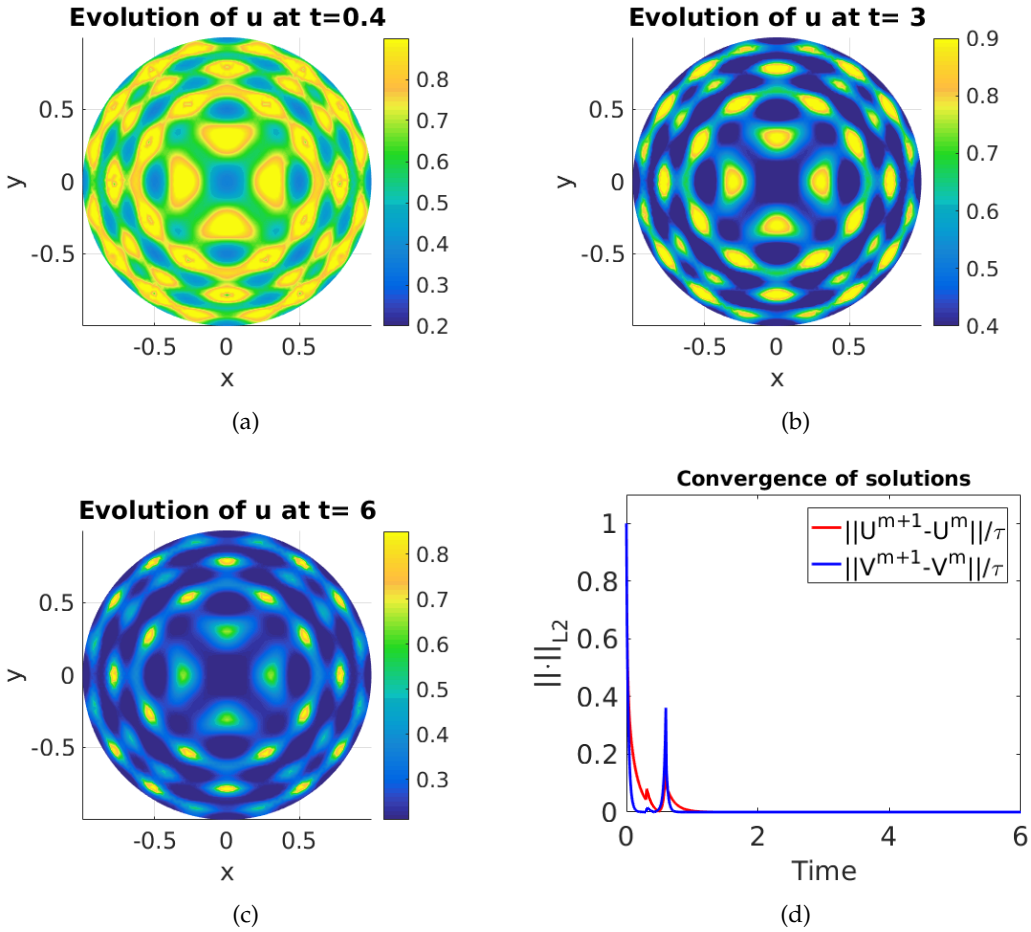

FIGURE 4.13: In (a) the initial stage of evolving spatially periodic pattern when, α and β are chosen from Turing space under condition (4.57) on the radius ρ. In (b) the spatially periodic pattern at $t = 3$ is as expected converging to the Turing type steady state without allowing the structure of the initial pattern to be deformed. In (c) Turing type steady state is reached at $t = 6$, with a successive time-step difference in the solutions decaying to 5×10^{-4} in the discrete L_2 norm. In (d) the instability and convergence is shown through the behaviour of the discrete L_2 norm of the successive time-step difference of the solutions u and v.

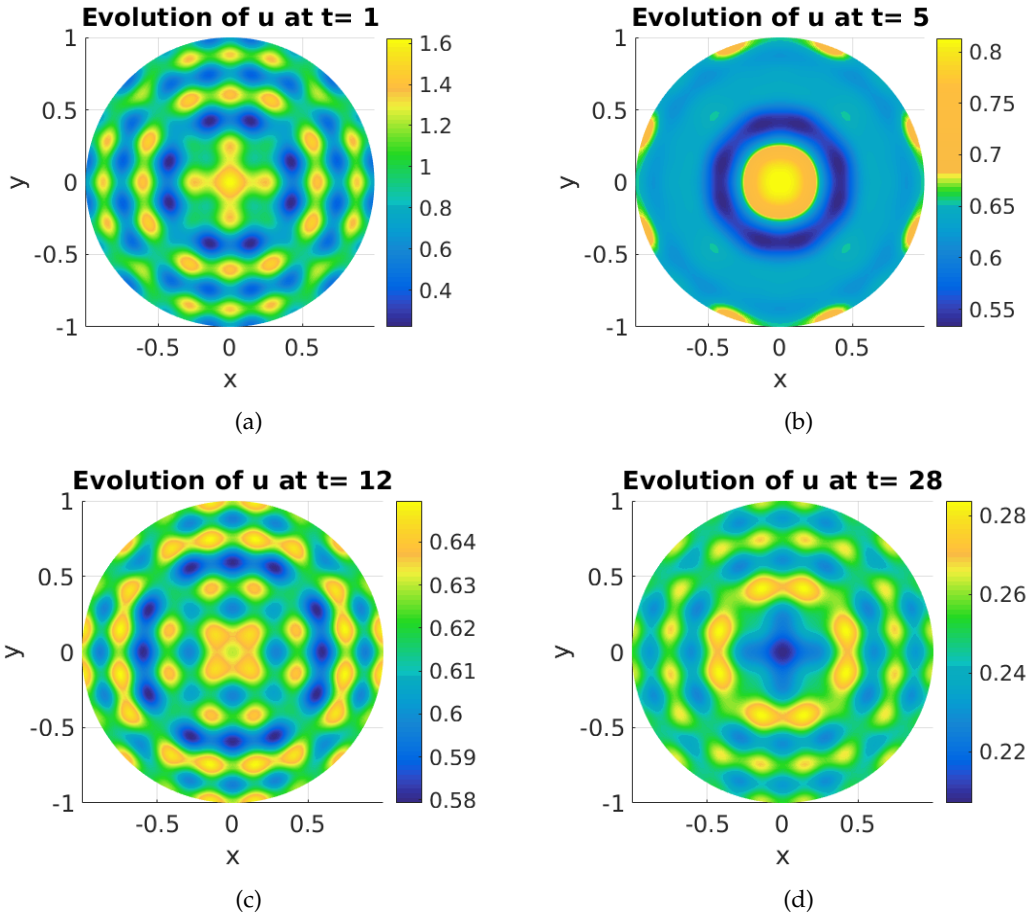

FIGURE 4.14: In (a) the first temporal period evolving to the initial spatially periodic pattern at $t = 1$ is shown. In (b) the spatial pattern during the second temporal period at $t = 5$ is shown. In (c) the spatial pattern during the third temporal period at $t = 12$ is shown. In (d) the spatial pattern during the fourth temporal period obtained at $t = 28$ is shown.

of spatial pattern to another grows larger with time. The initial pattern is obtained at around $t = 1$, which becomes unstable during the transition to the second temporal period at $t = 5$ in Figure 4.14 (b). At $t \approx 8$ the system undergoes third period of instability and reaches a different spatial pattern at $t = 12$ shown in Figure 4.14 (c). The fourth period of temporal instability is reached at $t \approx 20$, which converges to the fourth local spatial steady state at $t = 28$ presented in Figure 4.14 (d). It indicates that when parameters are chosen from Hopf bifurcation region then the temporal gaps in the dynamics of system (4.13)-(4.15) between successive transitional instabilities from one spatial pattern to another is approximately doubled as time grows.

It is speculated that the temporal period-doubling behaviour is connected to the analogy of unstable spiral behaviour in the theory of ordinary differential equations (Perko, 2013). If the eigenvalues of a dynamical system modelled by a set of ordinary differential equations is a complex number with positive real part, then the cycles of the corresponding unstable spiral grow larger as time grows. The long-term evolution of temporal instability depends on the magnitude of the real part of $\sigma_{1,2}$. If parameters (α, β) are chosen such that the trace of the stability matrix (4.46) is large and yet the discriminant is negative, then the dynamics exhibit long-term temporal periodicity, which means that the frequency of temporal periods will become smaller. A decaying frequency in temporal periods means that locally on the time axis, the dynamics may exhibit similar behaviour to that of a temporally stable system, therefore, to observe temporal transition from one Turing-type spatial steady state to another can take long time. Figure 4.15 shows a visualisation of the transitional temporal instability, which is a transitional period from one type of spatial pattern to another. As stated in Theorem 4.3.1, that when ρ satisfies condition (4.57) with respect to d and γ then, given that the parameters (α, β) are chosen from the curves t_i for $i = 1, ..., 8$ indicated in Figure 4.7 (b), one may expect the dynamics of system (4.13)-(4.15) to exhibit spatio-temporally periodic pattern referred to as the transcritical bifurcation. This kind of behaviour in the dynamics is also known as the limit cycles (Perko, 2013). Figure 4.16 shows this spatio-temporally periodic behaviour in the evolution of the numerical solution of system (4.13)-(4.15). This is the case corresponding to parameters that ensures the

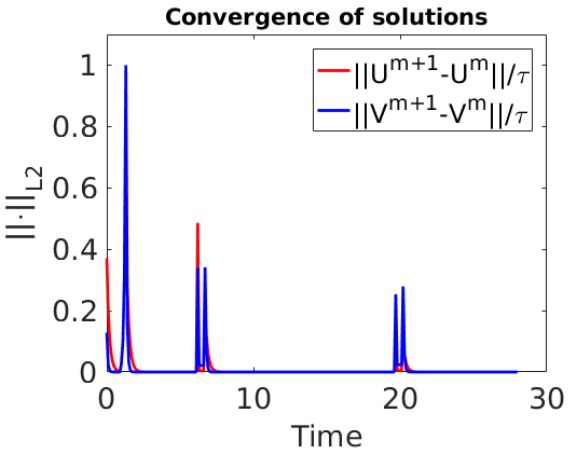

FIGURE 4.15: Spatio-temporal periodicity in the dynamics measured in discrete L_2 norm of the successive time-step difference of the solutions u and v.

eigenvalues to be pure imaginary, therefore, it can be observed that the temporal instability occurs with approximately constant periods along the time axis, which verifies the theoretical prediction of the limit-cycle behaviour. It is also observed that during the transitional instability from spots in Figure 4.16 (a) to the angular stripes in Figure 4.16 (b) the peak of the discrete L_2 norm of the successive time-step difference of the activator u is bigger than that of the inhibitor v. However, when the transitional temporal instability occurs to turn the angular stripes in Figure 4.16 (b) into spots in Figure 4.16 (c), then the L_2 norm of the successive time-step difference of the inhibitor v exceeds in magnitude than that of the activator u. This alternating behaviour can be clearly observed in Figure 4.15, where in the annotated legend U and V denote the discrete solutions of the activator u and that of the inhibitor v. However if (α, β) are chosen from the curves of transcritical bifurcation given in Figure 4.7 (b), then the frequency of temporal periods is predicted to remain constant for all times, emerging a constant interchanging behaviour between different spatial patterns.

Plot index	Figure 4.11	Figure 4.12	Figure 4.13	Figure 4.14	Figure 4.16
Instability / Parameters	No instability No pattern	Turing type instability Spatial pattern	Turing type instability Spatial pattern	Hopf bifurcation Spatial and temporal pattern	Transcritical bifurcation Spatial and temporal pattern
(α, β)	$(2, 2)$	$(0.1, 0.5)$	$(0.13, 0.3)$	$(0.15, 0.4)$	$(0.05, 0.7)$
(n, d, γ)	$(2.7, 10, 210)$	$(2.7, 10, 210)$	$(1.7, 6, 450)$	$(1.7, 6, 480)$	$(1.7, 6, 500)$
Condition on Ω	(4.68)	(4.68)	(4.57)	(4.57)	(4.57)
Simulation time	6	6	6	28	9
CPU time (sec)	784.24	784.56	784.91	4151.48	1197.66

TABLE 4.2: Showing the choice of parameters (α, β) for each simulation and the choice of (n, d, γ) subject to the relevant condition referred to in third row. Each simulation was run with time-step of 1×10^{-3}.

4.6 Conclusion

Linear stability theory was applied to a reaction-diffusion system with activator *activator-depleted* reaction kinetics on a two dimensional disc-shape domain. Analytical method was applied to derive explicit expressions for eigenfunctions and the corresponding eigenvalues of the diffusion operator in polar coordinates satisfying the homogeneous Neumann boundary conditions. Non-periodic chebyshev grid and periodic Fourier grid was used to discretise a unit disc on which the analytical solutions of

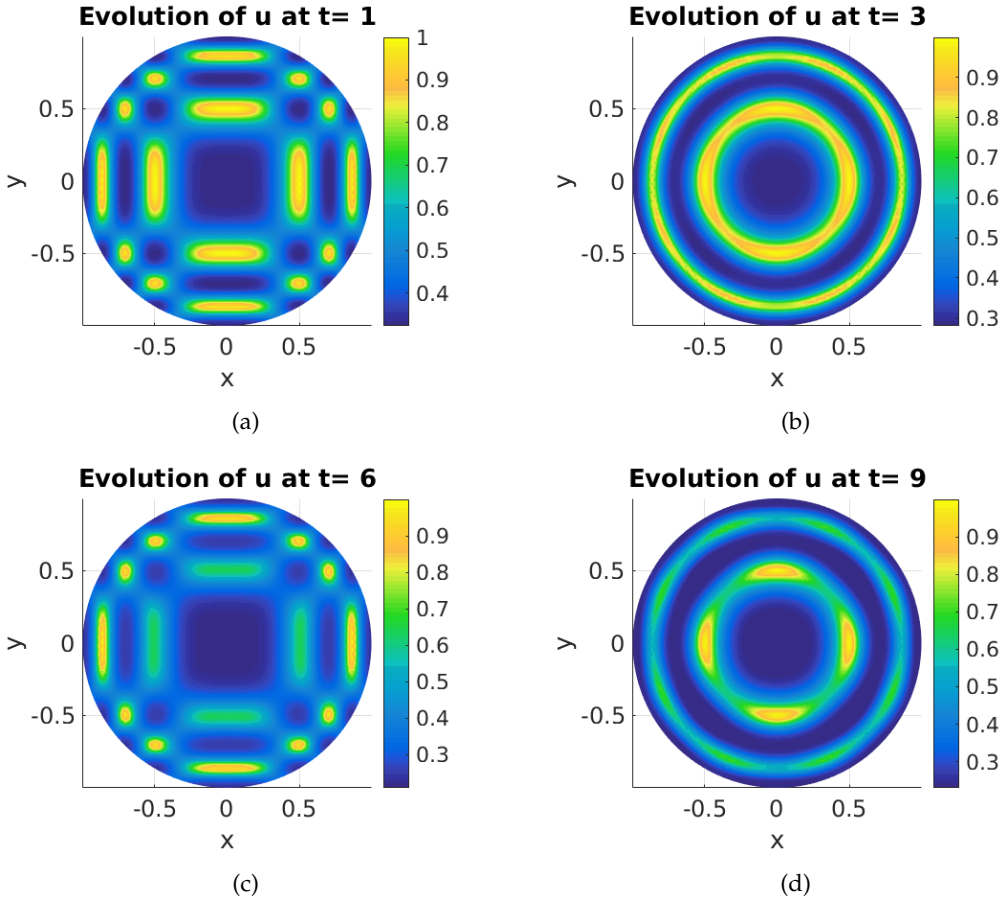

FIGURE 4.16: In (a) the initial spatially periodic pattern (spots) obtained at $t = 1$ is shown when, α and β are chosen from the region of Hopf bifurcation under condition (4.57) on the radius ρ. In (b) it is shown that the spatially periodic pattern evolves to become a different pattern (angular stripes) at $t = 3$ for the same choice of parameters. In (c) at $t = 6$ the angular stripes undergo another period of temporal instability and become spotty as the initial pattern. In (d) at $t = 9$ the pattern of the second temporal period emerges again, indicating that temporally the dynamics behave in alternating (periodic) way between the spots and angular stripes.

the eigenvalue problem were simulated. A colour encoded scheme (HSV) was applied to present the phase plots of the complex valued eigenfunctions. The solution of the eigenvalue problem was used to linearise the reaction-diffusion system for linear stability analysis. The partitioning curves on the admissible parameter spaces were found and simulated. Analytical methods were used to derive conditions (4.57) and (4.68) on the radius of a disc-shape domain in the context of bifurcation analysis. Relationship between reaction-diffusion rates and the radius of a disc-shape domain was established and analytically proven in Theorem 4.3.1 and 4.3.2. The full parameter space was classified with respect to the stability and types of the uniform steady state. Parameter values from all of the regions were tested and the predicted bifurcation in the dynamics was verified using finite element method. Due to the curved boundary of the domain *distmesh* was used to obtain the triangulation for simulating the numerical solutions of the system. Spatio-temporal periodicity of Hopf and transcritical types were shown and the corresponding error plots for the difference of the solutions in the successive time-steps were obtained to demonstrate the temporal periods of limit cycles and Hopf bifurcation. It was further verified that under certain condition on the radius of a disc with respect to the reaction-diffusion rates, the instability in the dynamics is restricted to Turing-type only forbidding the existence of a region for temporal bifurcation. A distinction between the transcritical bifurcation and Hopf bifurcation was numerically established by analysing the temporal periods between transitional instabilities in the dynamics from one spatial pattern to another. In Chapters 3 and 4, we have conducted the study on convex geometries. Next chapter presents the application of the same methodology of the previous chapter but this time on a non-convex circular geometry that consists of annular region. It is interesting to reveal the role played by the size and the non-convexity of the domain on the bifurcation behaviour of the RDS.

Chapter 5

Analysis on annular geometries

This chapter explores the influence of domain-size (thickness) of a non-convex two dimensional annular domain on the evolution of pattern formation modelled by the *activator-depleted* RDS. A closed form expression is derived for the spectrum of Laplace operator on the domain satisfying a set of homogeneous conditions of Neumann type both at inner and outer boundaries. The closed form solution of the diffusion spectrum is numerically verified using the spectral method on polar coordinates. The bifurcation analysis of *activator-depleted* reaction-diffusion system is conducted on the admissible parameter space under the influence of two bounds on the parameter denoting the thickness of the annular region. The admissibility of Hopf bifurcation and limit-cycle behaviour is proven conditional on the domain-size satisfying a lower bound in terms of reaction-diffusion parameters. The admissible parameter space is partitioned under the proposed conditions corresponding to each case, and in turn such conditions are numerically verified by applying the numerical method of polynomials on a quadrilateral mesh that was used in Chapters 3 and 4. Finally, the full system is numerically simulated on a two dimensional annular region using the standard Galerkin finite element method to verify the influence of the analytically derived conditions on the domain-size for all types of admissible bifurcations.

5.1 Domain and model equations

A reaction-diffusion system of *activator-depleted* class is used to model the evolution of two chemical species u and v that react and diffuse on a non-convex two dimensional circular domain Ω, which consists of a region bounded between two concentric circles of different radii a and b respectively. The reaction-diffusion system is considered on Ω with annular geometry consisting of points on the Cartesian plane defined by

$$\Omega = \{(x,y) \in \mathbb{R}^2 : a^2 < x^2 + y^2 < b^2\},$$

with $\partial\Omega$ denoting the boundary of Ω, which consists of all the points forming the two concentric circles given by

$$\partial\Omega = \{(x,y) \in \mathbb{R}^2 : x^2 + y^2 = a^2\} \cup \{(x,y) \in \mathbb{R}^2 : x^2 + y^2 = b^2\}.$$

A schematic of Ω is shown both in cartesian and polar coordinates in Figure 5.1 along with the boundaries and their respective definitions. The boundary of Ω is subject to homogeneous Neumann condition, which places a restriction of zero flux on u and v through $\partial\Omega$. Initial conditions for the *activator-depleted* model are positive bounded and continuous functions (Murray, 2001; Edelstein-Keshet, 1988) with pure spatial dependence. With this set-up in mind, the RDS in its non-dimensional form reads as

$$\begin{cases} \begin{cases} \frac{\partial u}{\partial t} = \Delta u + \gamma(\alpha - u + u^2 v), & (x,y) \in \Omega, \quad t > 0, \\ \frac{\partial v}{\partial t} = d\Delta v + \gamma(\beta - u^2 v), \end{cases} \\ \frac{\partial u}{\partial \boldsymbol{n}} = \frac{\partial v}{\partial \boldsymbol{n}} = 0, \qquad \text{on} \quad (x,y) \in \partial\Omega, \quad t \geq 0, \\ u(x,y,0) = u_0(x,y), \qquad v(x,y,0) = v_0(x,y), \qquad (x,y) \in \Omega, \quad t = 0, \end{cases} \tag{5.1}$$

where $\boldsymbol{n}$ denotes the outward normal to $\partial\Omega$. Parameters α, β, γ and d are defined the same way as in Chapters 3, 4. Due to the geometrical nature of Ω, it is essential to

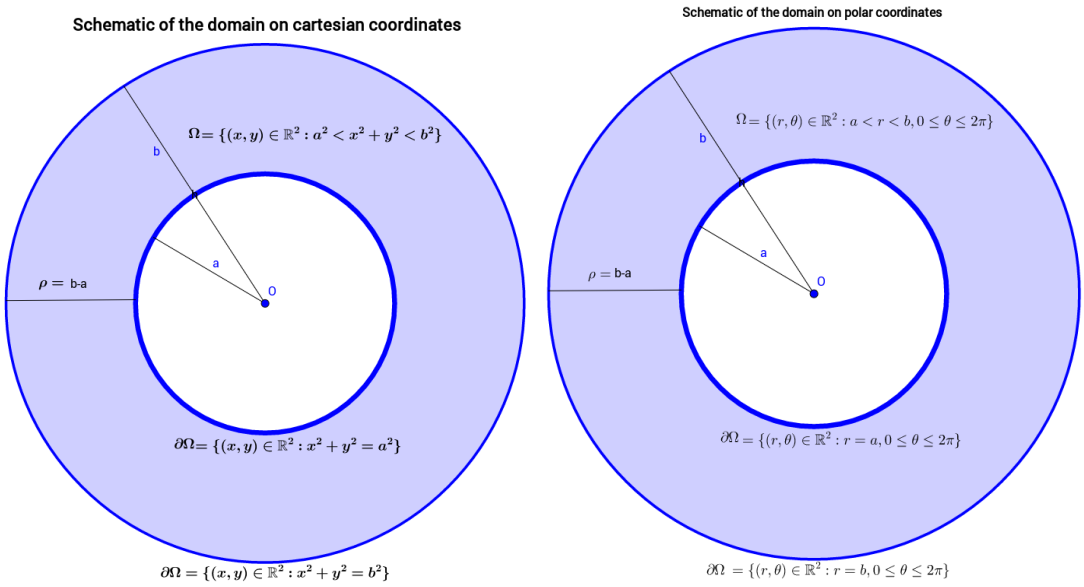

(a) (b)

FIGURE 5.1: Schematics of the domain in cartesian and polar coordinates.

conduct the analysis of (5.1) on polar coordinates. Standard coordinate transformation are applied in the form $r = \sqrt{x^2 + y^2}$ and $\theta = \tan^{-1}(\frac{y}{x})$ to transform every point $(x, y) \in \Omega$ to its counterpart $(r, \theta) \in \Omega$. The transformation is time-independent therefore, any operator with respect to the variable t remains unchanged. The diffusion operator Δ is purely spatial, therefore, as a consequence of coordinate transformation the diffusion operator Δ, in polar coordinates is denoted by Δ_p and given in the form (Arfken and Weber, 1999; Spanier and Oldham, 1987; Benedetto, 1996)

$$\Delta_p = \frac{1}{r}\frac{\partial}{\partial r}\left(r\frac{\partial}{\partial r}\right) + \frac{1}{r^2}\frac{\partial^2}{\partial \theta^2}. \tag{5.2}$$

A further advantage of using polar coordinates for system (5.1) is related to the application of homogeneous Neumann boundary conditions, in the sense that the zero-flux through $\partial\Omega$ has no angular relevance, therefore it can be expressed as spatial variation with respect to radial variable r only, thus offering a relative simplicity compared to expressing the outward normal in cartesian coordinates. Using the notation given by (5.2) and applying the coordinate transformation we can write system (5.1) in (r, θ)

coordinates in the form

$$\begin{cases} \begin{cases} \frac{\partial u}{\partial t} = \Delta_p u + \gamma f(u,v), & (r,\theta) \in \Omega, \quad t > 0, \\ \frac{\partial v}{\partial t} = d\Delta_p v + \gamma g(u,v), \\ \frac{\partial u}{\partial r}\big|_{r=a} = \frac{\partial v}{\partial r}\big|_{r=a} = 0, & (r,\theta) \in \partial\Omega, \quad t \geq 0, \\ \frac{\partial u}{\partial r}\big|_{r=b} = \frac{\partial v}{\partial r}\big|_{r=b} = 0 \end{cases} \\ u(r,\theta,0) = u_0(r,\theta), \qquad v(r,\theta,0) = v_0(r,\theta), \qquad (r,\theta) \in \Omega, \quad t = 0, \end{cases} \tag{5.3}$$

where functions f and g are given by $f(u,v) = \alpha - u + u^2 v$ and $g(u,v) = \beta - u^2 v$.

5.2 Linearisation and the eigenfunctions

5.2.1 Linearisation of the reaction terms

Let u_s and v_s denote the steady state solutions of system (5.3), then through a straightforward algebraic manipulation it can be verified that there exists a pair of constants (Murray, 2001) in the form $(u_s, v_s) = (\alpha + \beta, \frac{\beta}{(\alpha+\beta)^2})$ satisfying the steady state solutions for the non-linear reaction terms in (5.3). It is worth noting that the pair (u_s, v_s) is a unique set of positive real constants satisfying $f(u_s, v_s) = g(u_s, v_s) = 0$ and hence, it automatically satisfies the zero-flux boundary conditions prescribed for (5.3). The standard practice of linear stability theory is applied, which requires to perturb system (5.3) in the neighbourhood of the uniform steady state solution in the form $(u,v) = (u_s + \bar{u}, v_s + \bar{v})$, where $\bar{u}$ and $\bar{v}$ are assumed small. System (5.3) is expanded using Taylor expansion for functions of two variables up to and including the linear terms, with u and v replaced by their corresponding expressions in terms of u_s, $\bar{u}$, v_s and $\bar{v}$. It leads us to write system (5.3) in a matrix form as

$$\frac{\partial}{\partial t}\begin{bmatrix} \bar{u} \\ \bar{v} \end{bmatrix} = \begin{bmatrix} 1 & 0 \\ 0 & d \end{bmatrix}\begin{bmatrix} \Delta_p \bar{u} \\ \Delta_p \bar{v} \end{bmatrix} + \begin{bmatrix} \frac{\partial f}{\partial u}(u_s, v_s) & \frac{\partial f}{\partial v}(u_s, v_s) \\ \frac{\partial g}{\partial u}(u_s, v_s) & \frac{\partial g}{\partial u}(u_s, v_s) \end{bmatrix}\begin{bmatrix} \bar{u} \\ \bar{v} \end{bmatrix}. \tag{5.4}$$

System (5.4) is so far linearised only in the reaction kinetics, however the crucial step to complete the linearisation of the full system given in (5.3) is to find explicitly the set of eigenfunctions of the Laplace operator Δ_p satisfying the zero-flux boundary conditions on the geometry of the domain Ω.

5.2.2 Derivation of the eigenfunctions

The spectrum of the Laplace operator is a vast area of study in pure and applied mathematics (Casten and Holland, 1977; Arfken and Weber, 1999; Spanier and Oldham, 1987; Benedetto, 1996) depending on the area of its application. In particular the study of the eigenvalues and eigenfunctions of the Laplace operator on spherical geometry is a well-explored area of mathematics with generalised abstractions to higher dimensional spaces (Arfken and Weber, 1999). However, for the purpose of the current study a theoretical solution of the Laplace operator on a general spherical geometry offers impractical contribution in the sense that the majority of the existing solutions (Arfken and Weber, 1999; Spanier and Oldham, 1987; Benedetto, 1996) to such eigenvalue problems are derived either on boundary-free and/or convex manifolds. It is due to the non-convex nature of the prescribed domain Ω being a two-dimensional annular region and the analytical application of the zero-flux boundary conditions that creates the necessity for a step-by-step derivation of the spectral solutions for the corresponding eigenvalue problem with an explicit treatment to find the particular solution that satisfies the zero-flux boundary conditions prescribed in (5.3). The derivation of general solution to the eigenvalue problem (5.5) is presented in Chapter 4, therefore, we directly start with enforcing the homogeneous Neumann boundary conditions to the general solution. The eigenvalue problem we wish to solve is

$$\begin{cases} \Delta_p w = -\eta^2 w, & \eta \in \mathbb{R}, \qquad (r,\theta) \in \Omega, \\ \frac{\partial w}{\partial r}\big|_{r=a} = \frac{\partial w}{\partial r}\big|_{r=b} = 0, & a, b \in \mathbb{R}_+ \backslash \{0\} \quad \text{and } a < b, \end{cases} \tag{5.5}$$

where Δ_p is defined by (5.2) and Ω prescribed in Section 3.1.2. General solution of the eigenvalue problem (5.5) can be written in the form of a product $R\Theta$, with $R = R_1 + R_2$, which is given by

$$w(r,\theta) = \big[R_1(x(r)) + R_2(x(r))\big]\Theta(\theta), \tag{5.6}$$

where $R_{1,2}(x(r))$ are expressed by (4.28) and $\Theta(\theta) = \exp(il\theta)$. In order to obtain the particular set of solutions satisfying the eigenvalue problem (5.5), it is necessary to impose the prescribed homogenous Neumann boundary conditions. The outward flux through $\partial\Omega$ is independent of the variable θ, therefore, $w(r,\theta)$ is required to satisfy the zero flux boundary conditions at $r = a$ and at $r = b$, which means that the conditions $\frac{\partial w}{\partial r}\big|_{r=a} = 0$ and $\frac{\partial w}{\partial r}\big|_{r=b} = 0$ are equivalent to imposing conditions $\frac{dR}{dr}\big|_{r=a} = \frac{dR}{dr}\big|_{r=b} = 0$. It is important to realise that R now implicitly depends on the variable r through the relation $x = \eta r$, therefore, application of chain rule yields

$$\frac{dR}{dr}\big|_{r=a} = \frac{dx}{dr}\frac{dR}{dx}\big|_{x=\eta a} = \eta\frac{dR}{dx}\big|_{x=\eta a} = 0, \tag{5.7}$$

$$\frac{dR}{dr}\big|_{r=b} = \frac{dx}{dr}\frac{dR}{dx}\big|_{x=\eta b} = \eta\frac{dR}{dx}\big|_{x=\eta b} = 0. \tag{5.8}$$

Adding equations (5.7) and (5.8) we note that R is required to simultaneously satisfy the equation

$$\eta\Big(\frac{dR}{dx}\big|_{x=\eta a} + \frac{dR}{dx}\big|_{x=\eta b}\Big) = 0. \tag{5.9}$$

Using the linear property of differentiation we note that $\frac{dR}{dx}\big|_{x=\eta a} = \frac{dR_1}{dx}\big|_{x=\eta a} + \frac{dR_2}{dx}\big|_{x=\eta a}$, where upon cancellation of η, given that η is non-zero, from equation (5.9) we obtain

$$\frac{dR_1}{dx}\big|_{x=\eta a} + \frac{dR_2}{dx}\big|_{x=\eta a} + \frac{dR_1}{dx}\big|_{x=\eta b} + \frac{dR_2}{dx}\big|_{x=\eta b} = 0. \tag{5.10}$$

Differentiating with respect to x the infinite series expressing R_1 and R_2 in (4.28) and evaluating each summation at $x = \eta a$ and $x = \eta b$ respectively, we find the following

equations, which are presented completely independent of the variable x in the form

$$\sum_{j=0}^{\infty} u_j(l+2j)(\eta a)^{l+2j-1} + \sum_{j=0}^{\infty} v_j(-l+2j)(\eta a)^{-l+2j-1} + \sum_{j=0}^{\infty} u_j(l+2j)(\eta b)^{l+2j-1} + \sum_{j=0}^{\infty} v_j(-l+2j)(\eta b)^{-l+2j-1} = 0, \tag{5.11}$$

where u_j and v_j respectively express the jth coefficient of the series solutions for R_1 and R_2. These are given by $u_j = \frac{(-1)^j C_0}{4^j \times j! \times (l+j) \times (l+j-1) \times \cdots \times (l+1)}$ and $v_j = \frac{(-1)^j C_0}{4^j \times j! \times (-l+j) \times (-l+j-1) \times \cdots \times (-l+1)}$. Equation (5.11) can be grouped into a set of two equations each of which containing two independent summations, which are written as

$$\sum_{j=0}^{\infty} u_j(l+2j)(\eta a)^{l+2j-1} + \sum_{j=0}^{\infty} u_j(l+2j)(\eta b)^{l+2j-1} = \sum_{j=0}^{\infty} u_j(l+2j)\left[(\eta a)^{l+2j-1} + (\eta b)^{l+2j-1}\right] = 0, \tag{5.12}$$

$$\sum_{j=0}^{\infty} v_j(-l+2j)(\eta a)^{-l+2j-1} + \sum_{j=0}^{\infty} v_j(-l+2j)(\eta b)^{-l+2j-1} = \sum_{j=0}^{\infty} v_j(-l+2j)\left[(\eta a)^{-l+2j-1} + (\eta b)^{-l+2j-1}\right] = 0. \tag{5.13}$$

The set of equations given by (5.12) and (5.13) can only satisfy a simultaneous relation if they are independently equal to zero and the only way it can happen is through the application of telescoping argument (Thomson, Bruckner, and Bruckner, 2008) of real analysis. Applying the telescoping argument to (5.12) and (5.13) and noting that each of the series carry alternating signs from term to term (due to $(-1)^j$ in the expression for u_j and v_j), therefore, the only way equation (5.12) can be true is if the subsequent terms within the summation cancel each other pairwise. Let F_j and F_{j+1} denote in equation (5.12) the terms corresponding to indices j and $j+1$ respectively, then (5.12) is true if and only if $F_j + F_{j+1} = 0$ for all $j \in \mathbb{N}_0$. Writing the full expressions for u_j and

u_{j+1}, the terms corresponding to index j and $j+1$ respectively take the form

$$\begin{aligned} F_j =& \frac{(-1)^j C_0(l+2j)\left[(\eta a)^{l+2j-1}+(\eta b)^{l+2j-1}\right]}{4^j \times j! \times (l+j) \times (l+j-1) \times \cdots \times (l+1)}, \\ F_{j+1} =& \frac{(-1)^{j+1} C_0(l+2j+2)\left[(\eta a)^{l+2j+1}+(\eta b)^{l+2j+1}\right]}{4^{j+1} \times (j+1)! \times (l+j+1) \times (l+j) \times \cdots \times (l+1)}. \end{aligned} \tag{5.14}$$

Through a similar approach let S_j and S_{j+1} denote the subsequent terms in the second equation in (5.13), which are given by

$$\begin{aligned} S_j =& \frac{(-1)^j C_0(-l+2j)\left[(\eta a)^{-l+2j-1}+(\eta b)^{-l+2j-1}\right]}{4^j \times j! \times (-l+j) \times (-l+j-1) \times \cdots \times (-l+1)}, \\ S_{j+1} =& \frac{(-1)^{j+1} C_0(-l+2j+2)\left[(\eta a)^{-l+2j+1}+(\eta b)^{-l+2j+1}\right]}{4^{j+1} \times (j+1)! \times (-l+j+1) \times (-l+j) \times \cdots \times (-l+1)}. \end{aligned} \tag{5.15}$$

We add the pairwise terms corresponding to indices j and $j+1$ for equations (5.12) and (5.13) and equate their respective sums to zero. Furthermore, we rearrange for η^2 the resulting equations for both cases namely $F_{j+1}+F_j=0$ and $S_{j+1}+S_j=0$ and evaluate them at few successive indices namely $j=0,...,8$, which reveals a pattern that for every pair of $(j, j+1)$ such that $k=2j, j \in \mathbb{N}_0$, there exists $\eta^2_{k,l}$ that can be written in terms of inner radius a, outer radius b, the corresponding order of the associated Bessel's equation l and a positive integer k as

$$F_{j+1}+F_j=0 \quad \Longrightarrow \quad \eta^2_{1,k,l} = \frac{4(2k+1)(l+2k+1)(l+4k)}{a^{1-l}(a^{l+1}+b^{l+1})(l+4k+2)}, \tag{5.16}$$

$$S_{j+1}+S_j=0 \quad \Longrightarrow \quad \eta^2_{2,k,l} = \frac{4(2k+1)(l+2k+1)(l+4k)}{b^{1-l}(a^{l+1}+b^{l+1})(l+4k+2)}. \tag{5.17}$$

The prescribed boundary conditions in (5.5) require that the corresponding eigenfunctions $w(r,\theta)$ of the Laplace operator Δ_p satisfy a simultaneous relation on the zero-flux condition both through inner (circle with radius a) and outer boundaries (circle with radius b), which in turn suggests that the behaviour of $w(r,\theta)$ given by (5.6) at the two boundaries namely $r=a$ and $r=b$ is related through combining the expressions given by (5.16) and (5.17) and constructing from their combination the eigenvalues

that correspond to those eigenstates that exist in the form of a perfect superposition of those independently given by (5.16) and (5.17) respectively. Such a combination can be constructed if the eigenmode that corresponds to the condition $\frac{dR}{dr}\big|_{r=a}$ is found in perfect superposition with an eigenmode that corresponds to the condition $\frac{dR}{dr}\big|_{r=b}$. We can further observe from the expressions given in (5.16) and (5.17), that the patterns corresponding to index k do not differ from one another, except that they are different in the coefficients that depend on a, b and l. Noting that (5.16) and (5.17) each has a radial dependence on a and b, in addition each one of them satisfies the zero flux boundary conditions at the inner and outer boundaries i.e. through the aforementioned telescoping argument (Thomson, Bruckner, and Bruckner, 2008), therefore using the linear property of differentiation one can write the infinite set of eigenvalues of the Laplace operator Δ_p with the prescribed boundary conditions given in (5.5) as

$$\eta^2_{k,l} = \frac{4(a^l b + a b^l)(2k+1)(l+2k+1)(l+4k)}{ab(a^{l+1}+b^{l+1})(l+4k+2)}, \tag{5.18}$$

where $\eta^2_{k,l}$ in (5.18) is constructed from a perfect superposition of the eigenmodes corresponding to eigenvalues $\eta^2_{1,k,l}$ and $\eta^2_{2,k,l}$. At the points of superposition, due to the linearity of the operator Δ_p, the set of eigenfunctions (5.18) is obtained from the arithmetic sum in the form $\eta^2_{k,l} = \eta^2_{1,k,l} + \eta^2_{2,k,l}$. The summary of these findings is presented in the following theorem.

Theorem 5.2.1 *Let $w(r,\theta)$ satisfy the eigenvalue problem on a non-convex domain Ω defined in (5.5). Given that the associated order of Bessel's equation is chosen such that $l \in \mathbb{R}\backslash\frac{1}{2}\mathbb{Z}$, then the full set of eigenfunctions for the Laplace operator $\triangle_p$ defined by (5.2), satisfying the corresponding homogeneous Neumann boundary conditions are given by*

$$w_{k,l}(r,\theta) = \big[R_1(r) + R_2(r)\big]_{k,l}\Theta_l(\theta), \tag{5.19}$$

where $R_1(r)$, $R_2(r)$ *and* $\Theta(\theta)$ *are explicitly expressed by*

$$[R_1]_{k,l}(r) = \sum_{j=0}^{\infty} \frac{(-1)^j C_0 (\eta_{k,l} r)^{2j+l}}{4^j j!(l+j)(l+j-1)\cdots(l+1)},$$

$$[R_2]_{k,l}(r) = \sum_{j=0}^{\infty} \frac{(-1)^j C_0 (\eta_{k,l} r)^{2j-l}}{4^j j!(-l+j)(-l+j-1)\cdots(-l+1)}$$

and $\Theta_l(\theta) = \exp(il\theta)$. *Furthermore, for every* $w_{k,l}(r,\theta)$ *corresponding to integer* k *and the associated order of Bessel's equation* l, *there exists a real non-negative eigenvalue* $\eta_{k,l}$ *satisfying*

$$\eta_{k,l}^2 = \frac{4(a^l b + a b^l)(2k+1)(l+2k+1)(l+4k)}{ab(a^{l+1}+b^{l+1})(l+4k+2)}. \tag{5.20}$$

Proof

The proof of Theorem 5.2.1 consists of all steps from (5.6) to (5.18).□

5.2.3 Numerical experiments using spectral methods

The spectral method (Trefethen, 2000) is applied to validate Theorem 5.2.1. Let $R_{k,l}(r) = [R_1]_{k,l}(r) + [R_2]_{k,l}(r)$ then the full set of eigenfunctions given by (5.19) can be written as $w(r,\theta) = \sum_{k=0}^{\infty} R_{k,l}(r)\Theta_l(\theta)$. For the numerical simulation a polar mesh is generated through a combination of non-uniform Chebyshev discritisation (Trefethen, 2000) in the direction of radial variable r and uniform Fourier discretisation on the periodic variable θ. The domain is considered annular region centred at $(r,\theta) = (0,0)$ with parameters $a = \frac{1}{2}$ and $b = 1$. A spectral mesh in polar coordinates is constructed on the region $\Omega = \{(r,\theta) \in \mathbb{R}^2 : \frac{1}{2} < r < 1, \theta \in [0, 2\pi)\}$, where a periodic Fourier grid is used to obtain a uniform angular mesh of step size $\frac{2\pi}{M}$, where M is an even positive integer of the form $M = 2n, n \in \mathbb{N}$. The jth mesh point on the angular axis is obtained through $\theta_j = \frac{2\pi j}{M}$ for every index $j = 0, ..., M$. The non-uniform mesh on the radial variable r is obtained by using the Chebyshev discretisation formula $r_j = \cos(\frac{2\pi j}{N})$ on the interval $r \in (\frac{1}{2}, 1)$, where N a positive integer and $j = 0, ..., N$. A combination of the uniform Fourier grid and the non-uniform Chebyshev grid in this particular case

offers the advantage that the non-uniformity of Chebyshev grid contributes to cover for the coarse parts of the Fourier periodic grid. The non-uniform Chebyshev grid clusters more points on the radial direction near the outer boundary $r = 1$, which is precisely the region, where the uniform Fourier grid on θ becomes relatively coarse due to the geometric nature of polar coordinates. On the other hand, regions on Ω that are closer to inner boundary $r = \frac{1}{2}$, the uniform Fourier grid on the variable θ provides a relatively refined mesh in the angular direction, which covers for the fact that the non-uniform Chebyshev grid gradually becomes coarser towards the inner boundary $r = \frac{1}{2}$. It is a strategy that balances out the overall refinement and coarsening in a way so that, the drawbacks associated with the natural and unavoidable non-uniformity due to the radial direction from the uniform Fourier grid applied to θ, is compensated with the non-uniformity that is obtained from the Chebyshev gird formula in the radial direction r. Figure 5.2 (a) shows a coarse structure of a combination of a uniform Fourier grid applied to the angular variable θ with $M = 30$, which makes the angular step-size of 12° and a non-uniform Chebyshev grid applied to $r \in (\frac{1}{2}, 1)$ with $N = 25$. In Figure 5.2 (a), it can be observed that the regions near the outer boundary are refined in the direction of r but coarse in the direction of θ, whereas regions closer to the inner boundary are refined in the direction of angular mesh but coarse in the direction of the radial mesh. Figure 5.2 (b) is constructed in similar way with $M = 90$ resulting in angular step-size 4° and $N = 95$, which is used to depict few of the eigenmodes proposed by Theorem 5.2.1 with their respective approximation of the eigenvalues $\eta_{k,l}$ proposed by formula (5.20). The eigenstates $w_{k,l}(r, \theta)$ given by (5.19) corresponding to $k = 1, ..., 12$ are visualised using HSV (Hue, Saturation Value) colour encoded scheme, which is a method presented in (Qian and Wegert, 2013; Steele, 2001) specifically for depicting functions of complex output. Direct methods of plotting functions of two variables do not provide a meaningful representation of the formula (5.19). It can be noted that only the angular part in the formula (5.19), namely $\Theta(\theta)$ contains imaginary parts, therefore, the variable θ is colour encoded through the application of HSV scheme and the resulting output is depicted directly on Ω. This means in each case the

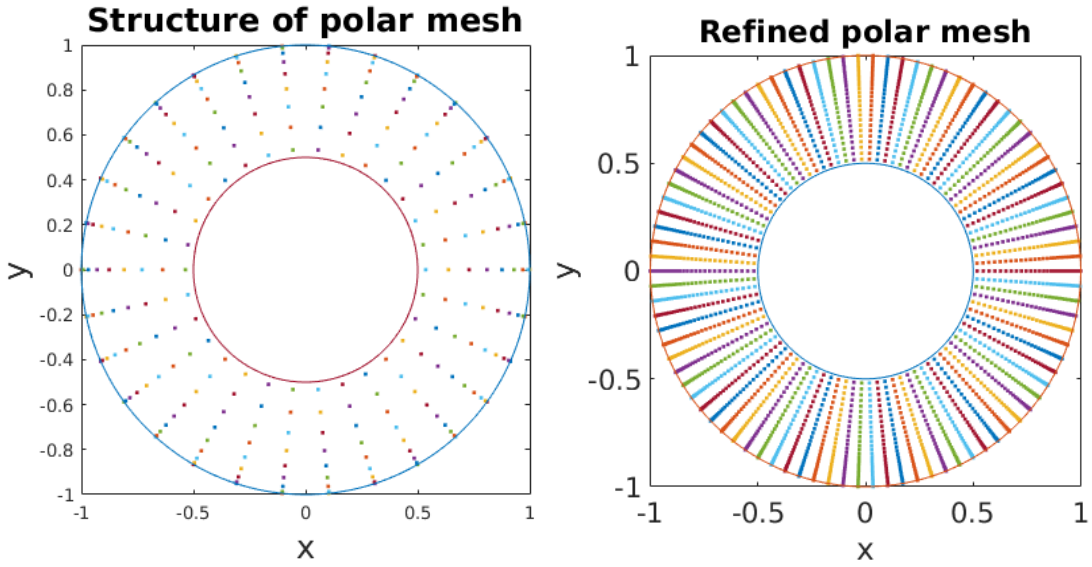

(a) (b)

FIGURE 5.2: In (a) the polar grid with $N = 25$ and using the periodic Fourier grid with $M = 30$, leading to an angular step-size of 12°. In (b) the fully refined polar mesh with $N = 95$ Chebyshev grid-points and $M = 90$ Fourier periodic grid-points, with angular step-size of 4° is shown.

radial solution is rotated as a consequence of the complex effect by an angle θ and the resulting solution is presented through HSV colour map. For full details on depicting complex valued functions, the interested reader is referred to (Qian and Wegert, 2013; Steele, 2001). The eigenvalues corresponding to each index k for a fixed value of $l = \frac{2\pi}{20} \approx 0.3$ are computed and presented in the respective captions in Figure 5.2.2. The values of $\eta_{k,l}$ are also computed for combinations of positive integer $k = 1, ..., 12$ with a variety of values for the associated order of Bessel's equation l. Table 5.1 shows the computed values of $\eta_{k,l}$ for different combinations of k and l, which offers an insight into the variations of the eigenvalues of the diffusion operator Δ_p, with respect to k for a fixed choice of l and how $\eta_{k,l}$ varies with respect to l for a fixed choice of k. In order to obtain a pictorial representation of the variation of $\eta_{k,l}$ with respect to both k and l to observe how this variation is influenced by the thickness $\rho = b - a$ of the domain-size Ω, a finitely truncated spectrum matrix that corresponds to negative and positive values of l is simulated and presented in Figure 5.4. It can be observed

from Figure 5.4 (a) that as the discrete finite spectrum approaches $l = 0$ for a particular value of k, it is subject to a steep decline in the magnitude of $\eta_{k,l}$. As the thickness $\rho = b - a$ is decreased i.e. the value of $a = 0.3, 0.5, 0.7$ in Figure 5.4 (b), (c) (d) and (e) are chosen for fixed value of $b = 1$, then one can observe from these Figures that the steep decline in the magnitude of $\eta_{k,l}$ around $l = 0$ becomes gradually smoother. Figure 5.4 (c) in particular is simulated for the choice of $\rho = b - a$ with $a = \frac{1}{2}$ and $b = 1$ to encapsulate the eigenvalues that are associated to eigenmodes shown in Figure 5.3. In particular, since the value of l in Figure 5.3 is kept fixed at $l = 0.3$, therefore, the corresponding eigenvalues can be captured from the intersection of a vertical line at $l = \frac{2\pi}{20} \approx 0.3$ and the spectrum lines for $k = 1, ..., 12$ in Figure 5.4 (c). The intersection points extract the eigenvalues given on the first column of those given in Table 5.1, which are precisely the values presented in each of the sub-captions in Figure 5.3.

k \ l	0.3	1.3	2.3	3.3	4.3	5.3	6.3	7.3	8.3	9.3	10.3	11.3
1	7.1027	7.5122	7.8501	8.2427	8.7082	9.2225	9.7582	10.2961	10.8254	11.3407	11.8399	12.3228
2	12.6266	12.4983	12.4927	12.7075	13.1098	13.6310	14.2134	14.8198	15.4290	16.0304	16.6187	17.1920
3	18.1149	17.4447	17.0769	17.0888	17.3997	17.8974	18.4949	19.1376	19.7947	20.4503	21.0965	21.7296
4	23.5924	22.3758	21.6362	21.4330	21.6385	22.0976	22.6942	23.3568	24.0452	24.7384	25.4257	26.1021
5	29.0652	27.2996	26.1827	25.7575	25.8495	26.2611	26.8475	27.5201	28.2297	28.9502	29.6684	30.3779
6	34.5354	32.2191	30.7217	30.0701	30.0436	30.4021	30.9720	31.6483	32.3724	33.1135	33.8557	34.5913
7	40.0041	37.1361	35.2559	34.3750	34.2266	34.5281	35.0775	35.7529	36.4869	37.2437	38.0050	38.7618
8	45.4719	42.0513	39.7869	38.6747	38.4020	38.6438	39.1696	39.8409	40.5813	41.3503	42.1272	42.9014
9	50.9391	46.9654	44.3157	42.9706	42.5719	42.7519	43.2519	43.9168	44.6610	45.4396	46.2291	47.0180
10	56.4057	51.8786	48.8427	47.2638	46.7376	46.8544	47.3268	47.9834	48.7296	49.5155	50.3156	51.1170
11	61.8721	56.7912	53.3685	51.5549	50.9003	50.9526	51.3961	52.0428	52.7894	53.5811	54.3901	55.2021
12	67.3382	61.7032	57.8933	55.8444	55.0605	55.0474	55.4610	56.0967	56.8423	57.6385	58.4549	59.2761

TABLE 5.1: Numerical values of $\eta_{k,l}$ for a variety of choices of positive integer k and the associated order of the Bessel's equation l.

5.2.4 Stability matrix and the characteristic polynomial

We employ the solution proposed by Theorem 5.2.1 of the eigenvalue problem (5.5) and adopt an application of separation of variables to write the analytical solutions to the linearised approximation of problem (5.3) as an infinite sum that consists of the product of the eigenfunctions of Δ_p, namely $w(r, \theta) = R_{k,l}(r)\Theta_l(\theta)$ and $T(t) = \exp(\sigma_{k,l})$. With bars omitted from the variables $\bar{u}$ and $\bar{v}$, one may write the solution to

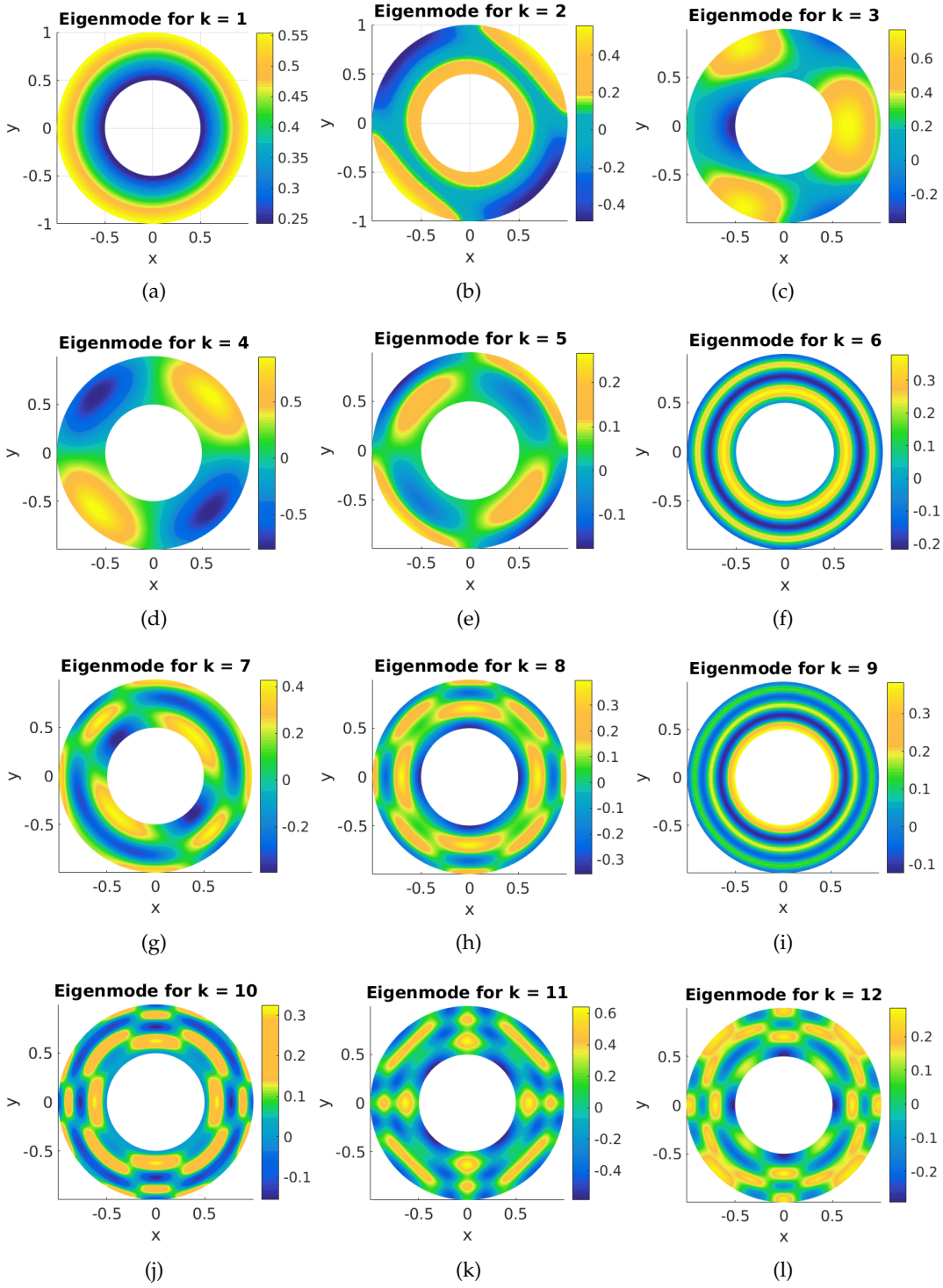

FIGURE 5.3: Colour encoded phase plots of $w(r,\theta)$ for different values of k indicated in each subtitle.

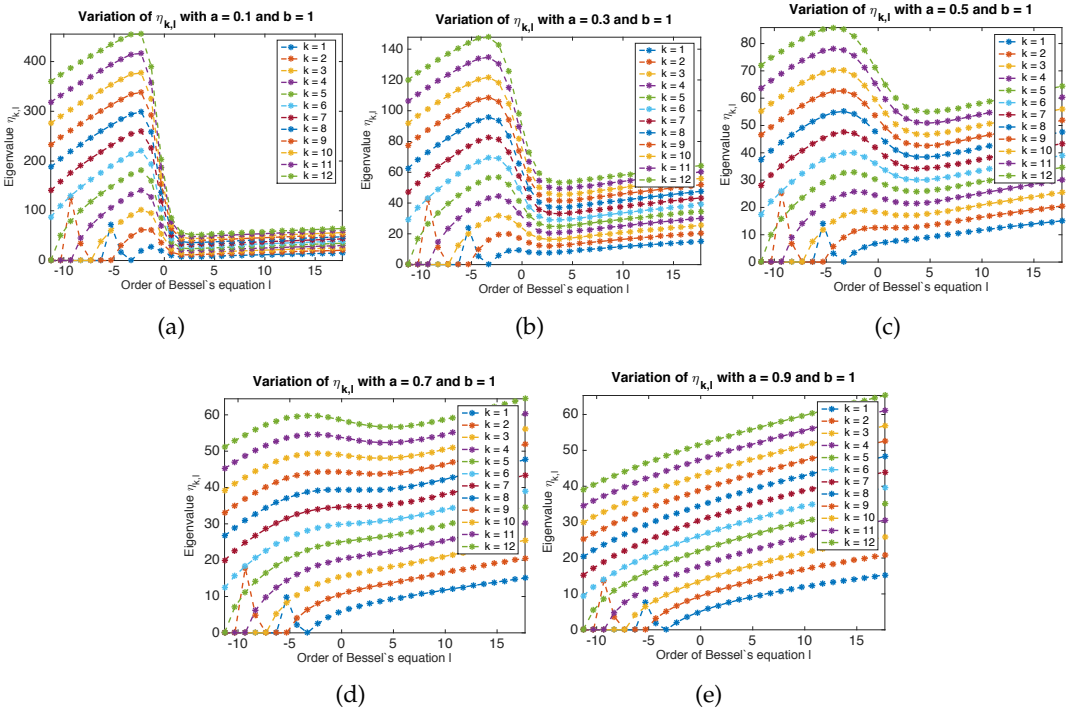

FIGURE 5.4: Variation of the discrete spectrum with respect to the order of the associated Bessel's equation.

the linearised system (5.4) in the form

$$u(r,\theta,t) = \sum_{k=0}^{\infty} U_{k,l} \exp(\sigma_{k,l} t) R_{k,l}(r)\Theta_l(\theta) \text{ and } v(r,\theta,t) = \sum_{k=0}^{\infty} V_{k,l} \exp(\sigma_{k,l} t) R_{k,l}(r)\Theta_l(\theta),$$

where $U_{k,l}$ and $V_{k,l}$ denote the coefficients of the terms that correspond to the eigenmodes of superposition. We substitute this form of solutions and the expressions of the uniform steady state namely $(u_s, v_s) = (\alpha + \beta, \frac{\beta}{(\alpha+\beta)^2})$ in system (5.4), which leads to a fully linearised version of (5.4), which is written as

$$\sigma \begin{bmatrix} u \\ v \end{bmatrix} = \begin{bmatrix} -\eta_{k,l}^2 & 0 \\ 0 & -d\eta_{k,l} \end{bmatrix} \begin{bmatrix} u \\ v \end{bmatrix} + \gamma \begin{bmatrix} \frac{\beta-\alpha}{\beta+\alpha} & (\beta+\alpha)^2 \\ -\frac{2\beta}{\beta+\alpha} & -(\beta+\alpha)^2 \end{bmatrix} \begin{bmatrix} u \\ v \end{bmatrix}, \tag{5.21}$$

where $\sigma_{k,l}$ is replaced by σ, since it denotes the discrete pair of eigenvalues corresponding to a two dimensional algebraic system of equations of the form

$$\begin{bmatrix} \gamma\frac{\beta-\alpha}{\beta+\alpha} - \eta_{k,l}^2 & \gamma(\beta+\alpha)^2 \\ -\gamma\frac{2\beta}{\beta+\alpha} & -\gamma(\beta+\alpha)^2 - d\eta_{k,l}^2 \end{bmatrix} \begin{bmatrix} u \\ v \end{bmatrix} = \sigma \begin{bmatrix} u \\ v \end{bmatrix}. \tag{5.22}$$

The left hand-side matrix in (5.22) is known as the stability matrix (Murray, 2001; Edelstein-Keshet, 1988; Perko, 2013), whose eigenvalues $\sigma_{1,2}$ provide insight on the evolution of the dynamical behaviour exhibited by system (5.3). These eigenvalues are computed through solving the relevant characteristic polynomial which is written as

$$\begin{vmatrix} \gamma\frac{\beta-\alpha}{\beta+\alpha} - \eta_{k,l}^2 - \sigma & \gamma(\beta+\alpha)^2 \\ -\gamma\frac{2\beta}{\beta+\alpha} & -\gamma(\beta+\alpha)^2 - d\eta_{k,l}^2 - \sigma \end{vmatrix} = 0, \tag{5.23}$$

and it can further be written in terms of the trace $\mathcal{T}(\alpha,\beta)$ and the determinant $\mathcal{D}(\alpha,\beta)$ of the stability matrix (5.22) in the form of a quadratic equation as

$$\sigma^2 - \mathcal{T}(\alpha,\beta)\sigma + \mathcal{D}(\alpha,\beta) = 0, \tag{5.24}$$

where $\mathcal{T}(\alpha,\beta)$ and $\mathcal{D}(\alpha,\beta)$ are given by

$$\begin{cases} \mathcal{T}(\alpha,\beta) = & \gamma\big(\frac{\beta-\alpha-(\beta+\alpha)^3}{\beta+\alpha}\big) - (d+1)\eta_{k,l}^2, \\ \mathcal{D}(\alpha,\beta) = & \big(\gamma\frac{\beta-\alpha}{\beta+\alpha} - \eta_{k,l}^2\big)\big(-\gamma(\beta+\alpha)^2 - (d+1)\eta_{k,l}^2\big) + 2\gamma^2\beta(\beta+\alpha). \end{cases} \tag{5.25}$$

The formula for the roots of equation (5.24) is given as $\sigma_{1,2} = \frac{\mathcal{T}\pm\sqrt{\mathcal{T}^2-4\mathcal{D}}}{2}$ in terms of $\mathcal{T}$ and $\mathcal{D}$. If $\sigma_{1,2} \in \mathbb{R}$ then the stability of the uniform steady state (u_s, v_s) is determined by the signs of $\sigma_{1,2}$. If $\sigma_{1,2}$ turns out to be a pair of complex conjugate values i.e. $\sigma_{1,2} \in \mathbb{C}\backslash\mathbb{R}$, then it is the sign of the real part $\mathrm{Re}(\sigma)$ that determines the stability of the uniform steady state (u_s, v_s). If $\sigma_{1,2}$ is real, then the uniform steady state undergoes unstable behaviour if at least σ_1 or σ_2 has positive sign. Therefore, when the roots of the characteristic polynomial (5.24) are purely real, then the existence of one positive

root suffices to decide that the corresponding uniform steady state is unstable. The uniform steady state (u_s, v_s) under this circumstance is stable if and only if both $\sigma_{1,2}$ possess negative signs. Therefore, in order to encapsulate all the possibilities for the stability and types of the uniform steady state (u_s, v_s) in light of parameters α and β, it is necessary to consider the cases when $\sigma_{1,2} \in \mathbb{C}\backslash\mathbb{R}$ and $\sigma_{1,2} \in \mathbb{R}$. The parameter space is rigorously analysed and fully classified under both cases to determine regions on the plane $(\alpha, \beta) \in \mathbb{R}^2_+$ that correspond to different types of dynamical predictions of system (5.3). Furthermore, it is investigated to find how the classification of the parameter spaces is influenced by the variation of the diffusion parameter d. In light of such classification, the analysis is further extended to explore the effects of domain-size in particular the thickness $\rho = b - a$ corresponding to the annular domain Ω on the spatial and temporal bifurcation of the dynamical system (5.3).

5.3 Partitioning curves and bifurcation analysis

Regions on the admissible parameter space i.e. $(\alpha, \beta) \in \mathbb{R}^2_+$ that correspond to the stability and types of the uniform steady state is extensively explored and the equations that determine the partition of such classification within the admissible parameter space are obtained and an analytical study is performed on them to find how the domain-size (thickness $\rho = b - a$) influences the bifurcation predictions of the dynamics corresponding to system (5.3). The admissible parameter space is partitioned with respect to a discrete variation of the diffusion parameter d and under the conditions that are derived in consequence of exploring the influence of the domain-size $\rho = b - a$ on the bifurcation behaviour of the dynamical evolution.

5.3.1 Equations of the partitioning curves

Considering the roots of the quadratic polynomial (5.24), which is given by $\sigma_{1,2} = \frac{\mathcal{T} \pm \sqrt{\mathcal{T}^2 - 4\mathcal{D}}}{2}$, we note that the partitioning of the admissible parameter space namely $(\alpha, \beta) \in \mathbb{R}^2_+$ is determined by two curves, one of which satisfies the equation $\mathcal{T}^2(\alpha, \beta) -$

$4\mathcal{D}(\alpha,\beta) = 0$ and the other one satisfying $\mathcal{T}(\alpha,\beta) = 0$ given that $\mathcal{T}^2(\alpha,\beta) < \mathcal{D}(\alpha,\beta)$. We start with the curve satisfying $\mathcal{T}^2(\alpha,\beta) - 4\mathcal{D}(\alpha,\beta) = 0$ on the parameter plane $(\alpha,\beta) \in \mathbb{R}^2_+$ that forms a boundary for the region that corresponds to eigenvalues $\sigma_{1,2}$ containing non-zero imaginary part from that which corresponds to a pair of purely real $\sigma_{1,2}$. It must be noted that the only possibility through which $\sigma_{1,2}$ can have a non-zero imaginary part is if the inequality $\mathcal{T}^2 - 4\mathcal{D} < 0$ is true. It is worth noting that the partitioning curve satisfying $\mathcal{T}^2(\alpha,\beta) - 4\mathcal{D}(\alpha,\beta) = 0$, is an equation that can be written as an implicit polynomial in β, whose coefficients are functions of the parameter α. We proceed with this set up in mind and write the equation of the curve that forms the boundary between regions corresponding to $\sigma \in \mathbb{R}$ and that which corresponds to $\sigma_{1,2} \in \mathbb{C}\backslash\mathbb{R}$. Such as equation is of the form

$$\begin{aligned}\Big(\gamma\frac{\beta-\alpha-(\beta+\alpha)^3}{\beta+\alpha} - (d+1)\eta_{k,l}^2\Big)^2 =& 4\Big(\big(\gamma\frac{\beta-\alpha}{\beta+\alpha} - \eta_{k,l}^2\big)\big(-\gamma(\beta+\alpha)^2 \\ & - (d+1)\eta_{k,l}^2\big) + 2\gamma^2\beta(\beta+\alpha)\Big),\end{aligned} \tag{5.26}$$

where $\eta_{k,l}^2$ satisfies (5.20). Equation (5.26) is numerically solved in Section 5.4, where a numerical method using polynomials (Sarfaraz and Madzvamuse, 2017) is employed to find combinations of $\alpha,\beta \in \mathbb{R}_+$ on the plane $(\alpha,\beta) \in \mathbb{R}^2_+$, that lie on the curve satisfying (5.26). At the points (α,β), which satisfies (5.26), entails that $\sigma_{1,2}$ is a repeated real root of the form $\sigma_1 = \sigma_2 = \frac{1}{2}\mathcal{T}(\alpha,\beta)$, whose sign is further explored in Section 5.4 for real eigenvalues. Note that the curve satisfying (5.26) also forms the boundary on the parameter space for regions of spatial and temporal bifurcations. The side of the curve (5.26), that corresponds to real eigenvalues $\sigma_{1,2} \in \mathbb{R}$, contains a sub-region that corresponds to the spatial bifurcation. However, it completely excludes any region that corresponds to temporal bifurcation, because for temporal bifurcation to take place, the eigenvalues must be a pair of complex conjugate i.e. $\sigma_{1,2} \in \mathbb{C}\backslash\mathbb{R}$. Similarly the unstable sub-region on the side of the curve satisfying (5.26), that corresponds to $\sigma_{1,2} \in \mathbb{C}\backslash\mathbb{R}$ only triggers temporal bifurcation with no influence on the spatial patterning, because any choice of (α,β) from this part of the admissible parameter space

results in a $\sigma_{1,2}$ to be a complex conjugate pair with non-zero imaginary parts. Any instability occurring from choosing the parameters from the side of the partitioning curve where $\sigma_{1,2}$ are a pair of real values, it is predicted to evolve to a steady state of spatial variation of Turing type, hence the obtained pattern from system (5.3) evolves with a globally stable and invariant behaviour in time. It is contradictory to claim the existence of such regions, since a fixed choice of the admissible (α, β) cannot simultaneously excite spatial and temporal instability. It is impossible for a fixed choice of (α, β) to yield a real σ_1 and a complex σ_2 or vice versa. However, the current study reveals that this counter-intuitive behaviour is possible for system (5.3) to exhibit, which is related to the existence and shift in the location of a partitioning curve on which the real part of $\sigma_{1,2} \in \mathbb{C}\backslash\mathbb{R}$ becomes zero during the course of the temporal evolution. It means that the curve on which this counter intuitive behaviour in the dynamic is expected to occur is that on which the real part of a complex conjugate pair of eigenvalues become zero. This entails that it must be the solution of the equations $\mathcal{T}(\alpha, \beta) = 0$, given that $\mathcal{T}^2 - 4\mathcal{D} < 0$, and can be written as

$$\gamma\big(\beta - \alpha - (\beta + \alpha)^3\big) = (\alpha + \beta)(d + 1)\eta_{k,l}^2, \tag{5.27}$$

which forms the second equation of the partitioning curves. Note that the solutions to (5.26) and (5.27) offer a full classification of the admissible parameter space in the sense that it predicts the dynamical behaviour exhibited by system (5.3) for every possible choice of $(\alpha, \beta) \in \mathbb{R}_+^2$. It is intuitive to expect the number of partitions subject to the types and stability of the uniform steady state (u_s, v_s), corresponding to the parameter plane $(\alpha, \beta) \in \mathbb{R}_+^2$ to consist of four regions separated by three distinct curves. These regions are obtained by the sub partition of the region corresponding to a pair of real $\sigma_{1,2}$, into two sub-regions where $\sigma_{1,2}$ is a pair of real negative values and another where at least σ_1 or σ_2 is positive. Similarly the region that corresponds to complex eigenvalues on the parameter plane $(\alpha, \beta) \in \mathbb{R}_+^2$, can also be sub-partitioned into two regions, one of which provides a pair of complex conjugate $\sigma_{1,2}$ with negative real part, and

the other corresponds to a pair of complex conjugate $\sigma_{1,2}$, but with a positive real part. The numerical solution of equation (5.26) reveals that the region associated with complex eigenvalues is in fact bounded by two curves in the parameter plane $(\alpha, \beta) \in \mathbb{R}^2_+$, each of which satisfies (5.26). Therefore, (5.26) implicitly provides two partitioning curves instead of one, which upon including the solution of (5.27) makes a total of three partitioning curves dividing the admissible parameter space into four different regions. Subject to the types and stability of the uniform steady state, one obtains at most four regions separated by three curves, with the possibility that parameters such as γ, d and $\eta^2_{k,l}$ may induce equations (5.26) and (5.27) in such a way that the number of partitioning curves may become less than three in total. Consequently this entails that a region corresponding to a certain type of bifurcation could completely vanish from the admissible parameter space. This kind of influence on the location and existence of the partitioning curves is quantitatively explored, in particular, the effect of $\rho = b - a$ embedded in the expression for $\eta^2_{k,l}$ in (5.20) is studied to analyse its influence on the bifurcation and stability of the uniform steady state.

5.3.2 Analysis for the case of complex eigenvalues

We analyse the real part of $\sigma_{1,2}$, when $\sigma_{1,2}$ is a complex conjugate pair, which occurs if and only if (α, β) satisfies the inequality

$$\mathcal{T}^2(\alpha, \beta) - 4\mathcal{D}(\alpha, \beta) < 0. \tag{5.28}$$

Given that (α, β) satisfies (5.28), then the sign of $\mathrm{Re}(\sigma_{1,2})$ determines the stability of the uniform steady steady state (u_s, v_s), which is the expression

$$\mathrm{Re}(\sigma_{1,2}) = \frac{1}{2}\Big(\gamma\frac{\beta - \alpha - (\beta + \alpha)^3}{\beta + \alpha} - (d+1)\eta^2_{k,l}\Big). \tag{5.29}$$

If the sign of the right hand-side of (5.29) is negative, under the restriction (5.28), then the dynamics of system (5.3) are forbidden from temporal instability for all choices of $(\alpha, \beta) \in \mathbb{R}^2_+$. Therefore, with (5.28) satisfied and the RHS of (5.29) positive, if the

dynamics of system (5.3) do exhibit diffusion-driven instability, it must be restricted to a spatially periodic behaviour only, which uniformly converges to a temporal steady state, consequently one obtains spatial pattern that is invariant in time. The sign of the expression given in (5.29) is further investigated to derive from it, relations between the parameter $\rho = b - a$, which controls the domain-size and the reaction-diffusion rates denoted by γ and d respectively. Given that assumption (5.28) is satisfied then the sign of expression (5.29) is negative if parameters α, β, γ and d satisfy the inequality

$$\frac{\beta - \alpha - (\beta + \alpha)^3}{\beta + \alpha} < \frac{(d+1)\eta_{k,l}^2}{\gamma}, \tag{5.30}$$

with $\eta_{n,k}^2$ defined by (5.20). Note that the expression on the left hand-side of (5.30) is a bounded quantity by the constant value of 1 (Sarfaraz and Madzvamuse, 2017), for all the admissible choices of $(\alpha, \beta) \in \mathbb{R}_+^2$. We aim to investigate inequality (5.30), so that we can establish a restriction on the parameter $\rho = b - a$ in terms of everything else that ensures the real part of $\sigma_{1,2}$ to be negative, which is equivalent to imposing a condition that guarantees global temporal stability in the dynamics. For this to hold we need to incorporate the parameter ρ defining the quantity $b - a$ into the expression for $\eta_{k,l}^2$. This expression can be written in terms of parameter ρ and a, where we replace parameter b by $\rho + a$, and using $\rho = b - a$, then (5.20) takes the form

$$\eta_{k,l}^2 = f(\rho)\frac{4(2k+1)(l+2k+1)(l+4k)}{(l+4k+2)}, \tag{5.31}$$

. The weighting function $f(\rho)$ in (5.31) is given by

$$f(\rho) = \frac{a^{l-1} + (\rho + a)^{l-1}}{a^{l+1} + (\rho + a)^{l+1}}. \tag{5.32}$$

The boundedness of the expression on the left hand-side of (5.30) by the constant value of 1 (Sarfaraz and Madzvamuse, 2017), entails that the inequality given by (5.30) can be written as

$$\gamma < f(\rho)\frac{4(d+1)(2k+1)(l+2k+1)(l+4k)}{(l+4k+2)}. \tag{5.33}$$

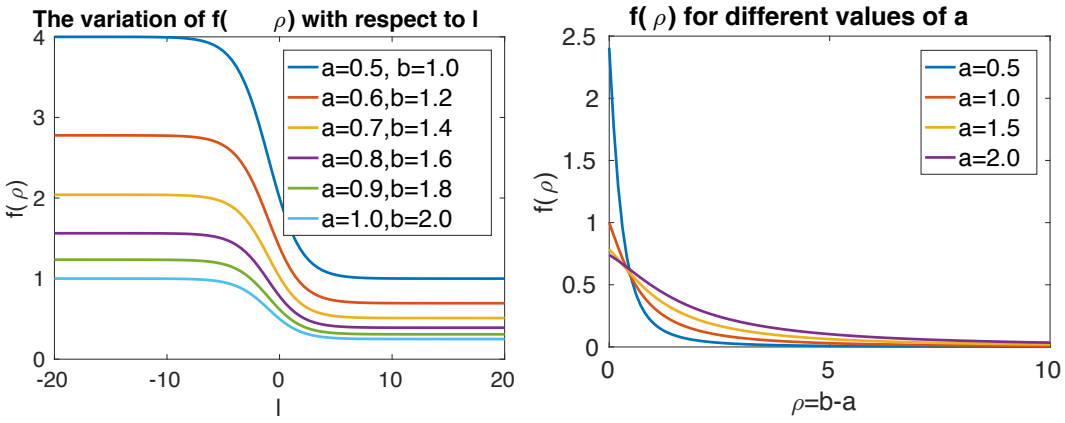

(a) (b)

FIGURE 5.5: The variation of the weighting function $f(\rho)$ with respect to the order of Bessel's equation l in (a) and with respect to ρ in (b).

This can further be studied by investigating the behaviour of $f(\rho)$ in (5.32), since $f(\rho)$ has a weighting effect on the magnitude of $\eta_{k,l}^2$. In order to encapsulate all the possibilities for $f(\rho)$, we first assert that $f(\rho)$ is a monotonically decreasing function, irrespective of the choice of a and b, given that $0 < a < b$. The behaviour of $f(\rho)$ is similar to that of $\frac{1}{\rho^2}$ with the limiting case as $a \to 0$, which follows from the fact that $(\rho + a)^{l+1}$ resides in the denominator and $(\rho + a)^{l-1}$ resides in the numerator, therefore asymptotically one may write that $f(\rho) < f(\rho + \epsilon), \forall \epsilon > 0$, and hence $\eta_{k,l}^2 \to 0$, as $\rho \to \infty$. This claim is verified numerically and shown in Figure 5.5 (b) where, $f(\rho)$ is simulated for various values of a shown in the respective legend. The point where all the plots intersect in Figure 5.5 (b), determines the value of $\rho = \frac{a}{b}$, which entails that at this point a and b must satisfy the equation $b - a = \frac{a}{b}$, implying that b can be obtained in terms of a using the formula $b = \frac{a+\sqrt{a^2-4a}}{2}$. It suggests that $f(\rho)$ at the intersection point remains independent of the values of a, given that the ratio $\frac{a}{b}$ is equal to their difference. The analysis of $f(\rho)$ and the variation of the spectrum of Δ_p with respect to the associated order of Bessel's equation l (shown in Figure 5.4) on the non-convex domain Ω suggests that two asymptotic cases require independent focus for the validity of inequality (5.33). Two cases correspond to the two local supremums attained by $f(\rho)$ with respect to $l < 0$ and $l > 0$ respectively.

From numerical investigation of $f(\rho)$ and its dependence on l the associated order of Bessel's equation, it is shown in Figure 5.5 (a) that two local suprema are attained by $f(\rho)$ for $l \in \mathbb{R}$ and are respectively given by

$$\sup_{0>l\in\mathbb{R}\setminus\frac{1}{2}\mathbb{Z}} f(\rho) = \lim_{l\to-\infty} f(\rho) = \frac{2}{a(\rho+a)} \text{ and } \sup_{0<l\in\mathbb{R}\setminus\frac{1}{2}\mathbb{Z}} f(\rho) = \lim_{l\to 0} f(\rho) = \frac{1}{a(\rho+a)}.$$

We proceed to employ these asymptotic upper bounds on the weighting function $f(\rho)$ to obtain the necessary conditions in each of the limiting cases for l, that ensures the validity of inequality (5.33). We note that requiring (5.33) to be valid for each one of the two cases corresponding to $l \to -\infty$ and $l \to 0^+$, give rise to a different condition on ρ. Starting with the case $\lim_{l\to-\infty} f(\rho) = \frac{2}{a(\rho+a)}$ by substituting in (5.33) and rearranging, we obtain that for (5.33) to be valid with $0 > l \in \mathbb{R}\setminus\frac{1}{2}\mathbb{Z}$, the parameter $\rho = b - a$ must satisfy

$$\rho < \frac{8(d+1)(2k+1)(l+2k+1)(l+4k) - \gamma a^2(l+4k+2)}{\gamma a(l+4k+2)}. \tag{5.34}$$

Using similar approach by substituting $\lim_{l\to 0^+} f(\rho) = \frac{1}{a(\rho+a)}$ in (5.33), we can find for positive values of $l \in \mathbb{R}\setminus\frac{1}{2}\mathbb{Z}$ the associated condition on the parameter ρ in the form given by

$$\rho < \frac{4(d+1)(2k+1)(l+2k+1)(l+4k) - \gamma a^2(l+4k+2)}{\gamma a(l+4k+2)}. \tag{5.35}$$

It is worth noting that (5.34) and (5.35) are sharp conditions on the parameter ρ controlling the area of Ω for positive and negative order of the associated Bessel's equation given by $0 > l \in \mathbb{R}\setminus\frac{1}{2}\mathbb{Z}$ and $0 < l \in \mathbb{R}\setminus\frac{1}{2}\mathbb{Z}$ respectively. However, since condition (5.34) corresponds to the global supremum for the weighting function $f(\rho)$, therefore, without loss of generality, condition (5.34) can be represented to ensure the validity of (5.33) for all the admissible choices of $l \in \mathbb{R}\setminus\frac{1}{2}\mathbb{Z}$. Condition (5.34) conversely implies that when $\sigma_{1,2} \in \mathbb{C}\setminus\mathbb{R}$ then $\mathrm{Re}(\sigma_{1,2}) > 0$ if parameter ρ satisfies

$$\rho \geq \frac{8(d+1)(2k+1)(l+2k+1)(l+4k) - \gamma a^2(l+4k+2)}{\gamma a(l+4k+2)}, \tag{5.36}$$

which consequently means that if (5.36) is satisfied then the steady state (u_s, v_s) undergoes temporal diffusion-driven instability leading to a spatial pattern bifurcating in time. This statement is formally proven in Theorem 5.3.1. Conditions (5.34) and (5.36) both influence the topology of the partitioning curves obtained from the numerical solutions of (5.26) and (5.27) in the admissible parameter plane, namely $(\alpha, \beta) \in \mathbb{R}^2_+$. System (5.3) is restricted from any type of temporal bifurcation if parameter $\rho = b - a$ of Ω is related to the reaction-diffusion parameters γ and d, through inequality (5.34). It also means that the non-convex domain Ω with thickness ρ satisfying (5.34), the dynamics of system (5.3), either exhibit spatially periodic pattern or no pattern at all, both of which are globally stable in time. If the dynamics of a system become unstable along the time axis and exhibits temporal periodicity, then the system is said to undergo *Hopf bifurcation* (Xu and Wei, 2012; Yi, Wei, and Shi, 2009; Gaffney, Yi, and Lee, 2016). If the real part of a pair of complex eigenvalues become zero, then the system is expected to exhibit oscillations with orbital periodicity. This is known as the limit-cycle behaviour (Murray, 2001; Perko, 2013). The consequences of the restriction on ρ in the sense of bifurcation analysis means that, whenever the thickness $\rho = b - a$ of a two dimensional shell is bounded by (5.34) in terms of γ and d, then the dynamics of system (5.3) is guaranteed to forbid *Hopf* and *transcritical bifurcations*, only allowing for *Turing instability* to occur. If system (5.3) allows only Turing type instability to occur under condition (5.34), it indicates that the eigenvalues $\sigma_{1,2}$ only become positive, when they are a pair of real values with zero imaginary parts. Therefore, it is also an indication that diffusion-driven instability is still possible, but it just becomes strictly spatial with (5.34) satisfied. If the values of parameters γ and d are chosen such that inequality (5.36) is satisfied, then the possibility of all three types of diffusion-driven instabilities exist on the admissible parameter plane $(\alpha, \beta) \in \mathbb{R}^2_+$, namely Turing, Hopf and transcritical types of bifurcations.

5.3.3 Remark

It must be noted that the domain-dependent weighting function (5.32) corresponding to each eigenvalue $\eta_{k,l}^2$ can be shown to be in agreement with that proposed for a disc-shape domain in (Sarfaraz and Madzvamuse, 2018) upon substituting $a = 0$ in $f(\rho)$. Note that $\lim_{a\to 0} f(\rho) = \frac{1}{\rho^2}$, which is exactly the same weighting function for $\eta_{k,l}^2$ in the case when Ω is a convex two-dimensional disk-shape domain presented in (Sarfaraz and Madzvamuse, 2018). Furthermore, $a = 0$ implies that Ω regains convexity, upon which $\rho = b$, hence $\frac{1}{\rho^2} = \frac{1}{b^2}$, due to the definition of parameter $\rho = b - a$.

Theorem 5.3.1 (Hopf or transcritical bifurcation) *Let u and v satisfy the non-dimensional reaction-diffusion system with activator-depleted reaction kinetics (5.3) on a non-convex two dimensional (shell) domain $\Omega \subset \mathbb{R}^2$ with thickness ρ and positive real parameters γ, d, α and β. For the system to exhibit Hopf or transcritical bifurcation in the neighbourhood of the unique steady state $(u_s, v_s) = \left(\alpha + \beta, \frac{\beta}{(\alpha+\beta)^2}\right)$, the necessary condition on the thickness ρ of $\Omega \subset \mathbb{R}^2$ is that it must be sufficiently large satisfying*

$$\rho \geq \frac{8(d+1)(2k+1)(l+2k+1)(l+4k) - \gamma a^2(l+4k+2)}{\gamma a(l+4k+2)}, \tag{5.37}$$

where $l \in \mathbb{R}\backslash\frac{1}{2}\mathbb{Z}$ is the associated order of the Bessel's equations and k is any positive integer. In (5.37) the parameter a denotes the radius of the inner boundary of Ω.

Proof

The proof of this theorem takes a similar approach to that given in (Sarfaraz and Madzvamuse, 2017; Sarfaraz and Madzvamuse, 2018). The numerical verification of Theorem 5.3.1 is presented in Section 5.4 to show that regions corresponding to Hopf and transcritical bifurcations exist under condition (5.37) on the controlling parameter for the domain-size, which is ρ. It is also numerically demonstrated that no choice of parameters $(\alpha, \beta) \in \mathbb{R}_+^2$ exist that would lead to Hopf or transcritical bifurcation, when condition (5.37) is violated.□

5.3.4 Analysis for the case with real eigenvalues

The necessary and sufficient condition on the discriminant $\mathcal{T}^2(\alpha,\beta) - 4\mathcal{D}(\alpha,\beta)$ for $\sigma_{1,2}$ to be a pair of real values is that

$$\mathcal{T}^2(\alpha,\beta) \geq 4\mathcal{D}(\alpha,\beta). \tag{5.38}$$

We first analyse the equal case of (5.38) and consider

$$\mathcal{T}^2(\alpha,\beta) = 4\mathcal{D}(\alpha,\beta), \tag{5.39}$$

which vanishes the discriminant, therefore, $\sigma_{1,2}$ become a pair of repeated real values given by

$$\sigma_1 = \sigma_2 = \frac{1}{2}\Big(\gamma\frac{\beta-\alpha-(\beta+\alpha)^3}{\beta+\alpha} - (d+1)\eta_{k,l}^2\Big). \tag{5.40}$$

where we substitute in (5.40) for $\eta_{k,l}^2$ the expression given in (5.31) with both the local suprema of the weighting function $f(\rho)$ for $l < 0$ and $l > 0$, which are respectively given by

$$\sup_{0>l\in\mathbb{R}\setminus\frac{1}{2}\mathbb{Z}} f(\rho) = \frac{2}{a(\rho+a)}, \qquad \sup_{0<l\in\mathbb{R}\setminus\frac{1}{2}\mathbb{Z}} f(\rho) = \frac{1}{a(\rho+a)}.$$

When α and β satisfy condition (5.39), the stability of the steady state is determined by the sign of the root itself. The supremum of the weighting function $f(\rho)$ for $l < 0$ is substituted in (5.40), which can be easily shown to be negative if parameter ρ satisfies the inequality

$$\rho < \frac{8(d+1)(\beta+\alpha)(2k+1)(l+2k+1)(l+4k) - \gamma a^2(\beta-\alpha-(\alpha+\beta)^3)(l+4k+2)}{\gamma a(\beta-\alpha-(\alpha+\beta)^3)(l+4k+2)}. \tag{5.41}$$

Otherwise, the repeated root is positive provided that ρ satisfies

$$\rho > \frac{8(d+1)(\beta+\alpha)(2k+1)(l+2k+1)(l+4k) - \gamma a^2(\beta-\alpha-(\alpha+\beta)^3)(l+4k+2)}{\gamma a(\beta-\alpha-(\alpha+\beta)^3)(l+4k+2)}. \tag{5.42}$$

Similarly with (5.39) satisfied and $l > 0$, upon substituting $\sup_{0<l\in\mathbb{R}\setminus\frac{1}{2}\mathbb{Z}} f(\rho) = \frac{1}{a(\rho+a)}$ in (5.40) and rearranging one can easily show that the sign of the expression given by (5.40) is negative if ρ satisfies

$$\rho < \frac{4(d+1)(\beta+\alpha)(2k+1)(l+2k+1)(l+4k) - \gamma a^2(\beta-\alpha-(\alpha+\beta)^3)(l+4k+2)}{\gamma a(\beta-\alpha-(\alpha+\beta)^3)(l+4k+2)}. \tag{5.43}$$

Otherwise, the repeated root $\sigma_{1,2}$ given by (5.40) is positive with $l > 0$ if ρ satisfies

$$\rho > \frac{4(d+1)(\beta+\alpha)(2k+1)(l+2k+1)(l+4k) - \gamma a^2(\beta-\alpha-(\alpha+\beta)^3)(l+4k+2)}{\gamma a(\beta-\alpha-(\alpha+\beta)^3)(l+4k+2)}. \tag{5.44}$$

Further analysis of conditions (5.41) and (5.42) is required to ensure that parameter ρ is not compared against a negative quantity. First we note that the only terms that can possibly invalidate inequalities (5.41), (5.42),(5.43) and (5.44) are in the denominator of the right hand-side, namely the expression $\beta - \alpha - (\beta+\alpha)^3$. Therefore, a restriction is required to be stated on this term to ensure that the radius ρ of Ω is not compared against a negative or imaginary number, such a restriction is

$$\beta > \alpha + (\beta+\alpha)^3. \tag{5.45}$$

Furthermore, given that restriction (5.45) is satisfied then we note that the right hand-sides of inequalities (5.41), (5.42),(5.43) and (5.44) are ensured to be positive if parameter a satisfies

$$\frac{4(d+1)(\beta+\alpha)(2k+1)(l+2k+1)(l+4k)}{\gamma a(\beta-\alpha-(\alpha+\beta)^3)(l+4k+2)} > a.$$

It must be noted that (5.45) is an identical restriction on the parameter choice obtained for the case of repeated real eigenvalues in the absence of diffusion (Sarfaraz and Madzvamuse, 2017). By further comparison of inequalities (5.42) and (5.44), they are similar to condition (5.37) of Theorem 5.3.1, except that (5.37) does not depend on the parameters α and β. This makes (5.37) a sharper version of (5.42) in the sense, that

the curve satisfying (5.39) subject to conditions (5.42) and (5.44) must be the one forming the boundary of the region on the admissible parameter plane, that corresponds to complex eigenvalues $\sigma_{1,2} \in \mathbb{C}\backslash\mathbb{R}$ with positive real parts. This is also known as the region for Hopf bifurcation (Xu and Wei, 2012; Yi, Wei, and Shi, 2009; Gaffney, Yi, and Lee, 2016). Therefore, the region of the admissible parameter plane that corresponds to Hopf bifurcation is on one side bounded by curve (5.39) and on the other side it is bounded by the curve satisfying (5.27) under their respective assumptions. In Section 5.4 it is verified to be the case by the numerical computation of the partitioning curve (5.26), which is the same curve (5.39). This analysis motivates to explore the possibility of similar comparison between the conditions (5.41) and (5.31). A reasonable intuition behind this comparison is that the sub-region on the admissible parameter plane that corresponds to complex eigenvalues with negative real parts must be bounded by curve (5.39) subject to conditions (5.41) and (5.43), outside of which every possible choice of parameters α and β will guarantee the eigenvalues $\sigma_{1,2}$ to be a pair of distinct real values, which promotes the necessity to state and prove Theorem 5.3.2.

Theorem 5.3.2 (Turing type diffusion-driven instability) *Let u and v satisfy the non-dimensional reaction-diffusion system with activator-depleted reaction kinetics (5.3) on a non-convex (shell) domain $\Omega \subset \mathbb{R}^2$ with inner radius a, thickness ρ and positive real parameters γ, d, α and β. Given that the thickness ρ of domain $\Omega \subset \mathbb{R}^2$ satisfies the inequality*

$$\rho < \frac{4(d+1)(2k+1)(l+2k+1)(l+4k) - \gamma a^2(l+4k+2)}{\gamma a(l+4k+2)}, \tag{5.46}$$

where $l \in \mathbb{R}_+\backslash\frac{1}{2}\mathbb{Z}$ is the associated order of the Bessel's equations and k is any positive integer, then for all $\alpha, \beta \in \mathbb{R}_+$ in the neighbourhood of the unique steady state $(u_s, v_s) = \left(\alpha+\beta, \frac{\beta}{(\alpha+\beta)^2}\right)$ the diffusion-driven instability is restricted to Turing type only, forbidding the existence of Hopf and transcritical bifurcations.

Proof

The strategy of this proof is mostly identical to those given in (Sarfaraz and Madzvamuse, 2017; Sarfaraz and Madzvamuse, 2018), therefore to avoid repetition the details of the proof is omitted and the interested reader may consult the corresponding papers. The only difference in the proof of the current theorem is in the final stage where an explicit representation of eigenvalues given in (5.31) is substituted, which contains the domain controlling parameter ρ, where in the last step by rearranging for ρ the desired inequality namely (5.46) can be obtained.□

5.4 Numerical simulation of parameter spaces and partitioning curves

Equation (5.26) can be algebraically manipulated and rearranged as a six degree polynomial in β whose coefficients depend on α, d, γ and $\eta_{k,l}^2$. Let $\mathcal{P}_1$ denote the six degree polynomial in β, which can be written in the form $\mathcal{P}_1(\beta) = \sum_{n=0}^{6} C_n(\alpha)\beta^n$ with C_n denoting the coefficient of the term β^n. The region on the admissible parameter space $(\alpha, \beta) \in \mathbb{R}_+^2$ satisfying equation (5.26) is equivalent to finding the pair of $(\alpha, \beta) \in \mathbb{R}_+^2$ satisfying $\mathcal{P}_1(\beta) = 0$, which can also be written as

$$\mathcal{P}_1(\beta) = C_0(\alpha) + C_1(\alpha)\beta + C_2(\alpha)\beta^2 + C_3(\alpha)\beta^3 + C_4(\alpha)\beta^4 + C_5(\alpha)\beta^5 + C_6(\alpha)\beta^6. \quad (5.47)$$

Solutions satisfying the implicit curve given by (5.26) is obtained through solving $\mathcal{P}_1(\beta) = 0$ by constructing a two-dimensional quadrilateral mesh on a rectangular domain $D = [0, \alpha_{max}] \times [0, \beta_{max}]$, where α_{max} and β_{max} are the maximum positive real values in the respective directions of α and β. The values of α_{max} and β_{max} are chosen large enough to ensure that beyond the boundaries of the rectangle $[0, \alpha_{max}] \times [0, \beta_{max}]$ the pair of eigenvalues $\sigma_{1,2}$ corresponding to the uniform steady state (u_s, v_s) neither change sign nor its type. Note that for a fixed value of α by the fundamental theorem of algebra (Milewski, 2001) equation $\mathcal{P}_1(\beta) = 0$ has at most six distinct roots namely

β_j for $j = 1, ..., 6$ on the complex plane $\mathbb{C}$, some of which maybe real positive others negative real or those with non-zero imaginary parts. Due to the defined nature of parameters $\alpha, \beta \in \mathbb{R}_+$ in system (5.3), only those combinations of (α, β) that lie on the admissible two dimensional positive real plane $\mathbb{R}^2_+$, represent the curves that provide the partitioning boundaries for region corresponding to $\sigma_{1,2} \in \mathbb{C}\backslash\mathbb{R}$ to that which corresponds to a pair of real $\sigma_{1,2} \in \mathbb{R}$. Domain D is discretised by a quadrilateral mesh consisting of N points in both directions of α and β, where N is a positive integer. Such discretisation leads to a rectangular mesh of $(N-1) \times (N-1)$ cells, each of size $\frac{\alpha_{max}}{N} \times \frac{\beta_{max}}{N}$, with N^2 points in D. To compute $(\alpha, \beta) \in \mathbb{R}^2_+$ satisfying (5.26), at every mesh point α_i for $i = 1, ..., N$ the six roots of equation $\mathcal{P}_1(\alpha_i, \beta) = 0$ are computed from which only the combinations $(\alpha_i, \beta_j) \in \mathbb{R}^2_+$ are returned and the remaining combinations are discarded at each iteration. The coefficients C_0,...,C_6 of (5.47) for each mesh point α_i in the direction of α are respectively given by

$$\begin{aligned} C_0(\alpha_i) =& \alpha_i^2\gamma - 2\alpha_i^2\gamma\eta_{k,l}^2 + 2\alpha_i^4\gamma + \alpha_i^2\eta_{k,l}^4 - 2\alpha_i^2 d\gamma\eta_{k,l}^2 - 4\alpha_i^4\gamma^2 + 2\alpha_i^2 d\eta_{k,l}^4 - 4\alpha_i^3\eta_{k,l}^4 \\ &+ 2\alpha_i^4\gamma\eta_{k,l}^2 + \alpha_i^6\gamma + \alpha_i^2 d^2\eta_{k,l}^4 + 2\alpha_i^4 d\eta_{k,l}^2 - 4\alpha_i^5\gamma\eta_{k,l}^2, \end{aligned}$$

$$\begin{aligned} C_1(\alpha_i) =& 8\alpha_i^3\gamma d\eta_{k,l}^2 - 20\alpha_i^4\gamma\eta_{k,l}^2 - 12\alpha_i^2 d\eta_{k,l}^4 + 2\alpha_i^2 d\eta_{k,l}^4 + 6\alpha_i^5\gamma + 8\alpha_i^3\gamma\eta_{k,l}^2 - 12\alpha_i^2\eta_{k,l}^4 \\ &+ 4\alpha_i d\eta_{k,l}^4 + 2\alpha_i\eta_{k,l}^4 + 4\alpha_i^3\gamma - 2\alpha\gamma, \end{aligned}$$

$$\begin{aligned} C_2(\alpha_i) =& \gamma + 2\gamma\eta_{k,l}^2 + \gamma\eta_{k,l}^2 + \eta_{k,l}^4 + 2d\gamma\eta_{k,l}^2 + 24\alpha_i^2\gamma^2 + 2d\eta_{k,l}^4 - 12\alpha_i\eta_{k,l}^4 + 12\alpha_i^2\gamma\eta_{k,l}^2 \\ &+ 15\alpha_i^4\gamma + d^2\eta_{k,l}^4 - 12\alpha_i d\eta_{k,l}^4 + 12\alpha_i^2 d\gamma\eta_{k,l}^2 - 40\alpha_i^3\gamma\eta_{k,l}^2, \end{aligned}$$

$$C_3(\alpha_i) = 32\alpha_i\gamma^2 - 4\alpha_i\gamma - 4\eta_{k,l}^4 + 8\alpha_i\gamma\eta_{k,l}^2 + 20\alpha_i^3\gamma - 4d\eta_{k,l}^4 + 8\alpha_i d\gamma\eta_{k,l}^2 - 40\alpha_i^2\gamma\eta_{k,l}^2,$$

$$C_4(\alpha_i) = 12\alpha_i^2 - 2\gamma + 2\gamma\eta_{k,l}^2 + 15\gamma\alpha_i^2 + 2d\gamma\eta_{k,l}^2 - 20\alpha_i\gamma\eta_{k,l}^2,$$

$$C_5(\alpha_i) = 6\alpha_i\gamma - 4\gamma\eta_{k,l}^2, \quad \text{and} \quad C_6(\alpha_i) = \gamma.$$

In the expressions for the coefficients of (5.47), the values of $\eta_{k,l}$ are used as given by (5.20), with $a = \frac{1}{2}$, $\rho = \frac{1}{2}$, which implies $b = 1$ due to the definition of parameter

$\rho = b - a$. Note that the point (α_i, β_j) satisfying $\mathcal{P}_1(\alpha_i, \beta_j) = 0$ is obtained by pairing each index $i = 1, 2, 3, ..., N$ of α with each root β_j, which is conditionally filtered through to output if $(\alpha_i, \beta_j) \in \mathbb{R}^2_+$, otherwise the algorithm is instructed to discard the pair in order to achieve optimised consumption of memory. A similar procedure is applied to obtain the solutions of the second partitioning curve satisfying (5.27), that corresponds to a curve in the admissible parameter space on which the real part of $\sigma_{1,2} \in \mathbb{C}\backslash\mathbb{R}$ is zero and it corresponds to the uniform steady state (u_s, v_s) undergoing a transcritical bifurcation. Using $\mathcal{P}_2(\beta)$ to denote the cubic polynomial obtained from algebraic manipulation and rearranging the equation (5.27). Solving equation (5.27) is equivalent to finding all the roots of an implicit cubic polynomial in β of the form $\mathcal{P}_2(\beta) = 0$. For every fixed value α_i in the direction of coordinate α on the quadrilateral mesh, equation $\mathcal{P}_2(\beta) = 0$ can be written as

$$\mathcal{P}_2(\beta) = C_0(\alpha_i) + C_1(\alpha_i)\beta + C_2(\alpha_i)\beta^2 + C_3(\alpha_i)\beta^3. \tag{5.48}$$

The coefficients of (5.48), take the form $C_0(\alpha_i) = -\alpha_i^3\gamma - \alpha_i d\eta_{k,l}^2 - \alpha_i\eta_{k,l}^2 - \alpha_i\gamma$, $C_1(\alpha_i) = \gamma - \eta_{k,l}^2 - d\eta_{k,l}^2 - 3\alpha_i^2\gamma$, $C_2(\alpha_i) = -3\alpha_i\gamma$, $C_3(\alpha_i) = -\gamma$ and $\eta_{k,l}$ as given by (5.20). As previously mentioned that parameters α and β resemble strictly positive real values in system (5.3), therefore, upon computing all the roots of polynomials (5.48), the algorithm is instructed to return only the roots satisfying $\beta_j \in \mathbb{R}_+$, and any roots that are either negative real or have non-zero imaginary part, are discarded. In Figures the number of intersections of a vertical straight line in the direction of β for a fixed value of α, indicates the number of positive real roots of polynomial (5.47) and (5.48) respectively. In Figure 5.6 the number of intersections of a vertical straight line in the direction of β for a fixed value of α, indicates the number of positive real roots of polynomial (5.47).

This algorithm is executed for five different values of d to obtain the solutions of (5.26) and (5.27) under conditions (5.37) and (5.46) on the parameter that controls the size of Ω, namely ρ. The shift and existence of the partitioning curves satisfying (5.26) and

(5.27) are analysed subject to the variation of parameter d. It is worth noting that under the current analysis the variation of d suffices to disclose every desirable insight one wishes to obtain about the variation of the parameter γ. This is due to their reciprocal locations in the expression on the right hand-sides of conditions (5.37) and (5.46). In other words, increasing parameter d is equivalent to decreasing the parameter γ and vice versa. Therefore, for fixed value of γ it suffices to study the variation of d. Using condition (5.37) of Theorem 5.3.1, the variation of the diffusion coefficient is analysed for five different values of d and Figure 5.6 (a) shows the shift of the solutions of (5.26). It is shown that solution of (5.26) determines a partition of the region in the parameter space that corresponds to $\sigma_{1,2}$ to be a pair of complex values and it can be seen that under condition (5.37), as the value of the parameter d increases the region that corresponds to complex eigenvalues gradually decrease, however so long as condition (5.37) remains satisfied, the vertical axis β continues to have at least two distinct intercepts of the curves satisfying (5.26) for the same value of d. It is this behaviour of the real-complex eigenvalues partitioning curve that either preserves or vanishes the existence of a sub-partition for positive and negative real parts of a complex pair of roots. The five values of parameter d are clearly indicated on the curves in Figure 5.6. It would be reasonable to use exactly the same range for the variational values of d under both conditions (5.37) and (5.46), however, it was noted that, when the domain-size ρ is restricted by (5.46) then the same values used for varying d in Figure 5.6 (a) invalidate inequality (5.46), therefore, the range of variational values for parameter d under condition (5.46) is significantly smaller. Using such a range despite that a significant observable shift is emerged in the location of the solution curves, it does not invalidate inequality (5.46) for ρ. Figure 5.6 (b) shows the variation of parameter d using the values indicated in the respective legend of. It can be noted that as d increases significantly, the number of intercepts on β axis reduces from two to one and eventually to zero. The fact that condition (5.46) on the domain-size forbids the existence of a region in the admissible parameter space that corresponds to complex conjugate pair of $\sigma_{1,2}$ with positive real part, is related to the behaviour of the curve satisfying (5.47).

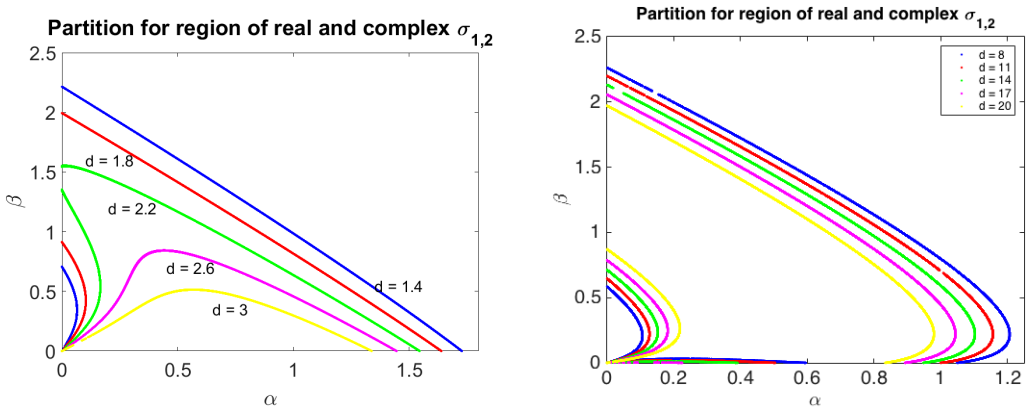

(a) (b)

FIGURE 5.6: In (a) the partitioning curves satisfying (5.26) and condition (5.37) of Theorem 5.3.1 are shown, that partition the region corresponding to real $\sigma_{1,2}$ from that, which corresponds to complex conjugate pair of $\sigma_{1,2}$. In (b) the partitioning curves satisfying (5.26) and condition (5.46) of Theorem 5.3.2 are shown, that partition the region corresponding to real pair of $\sigma_{1,2}$ from that, which corresponds to complex conjugate pair of $\sigma_{1,2}$.

It is the location of the curve associated to the solution of (5.47), that either admits or restricts the curve satisfying (5.48) on the admissible parameter space. This relation is in agreement and is a numerical demonstration of the conditions for diffusion-driven instability presented in (Murray, 2001; Liu et al., 2013). Using the method of trial and error proposed in (Sarfaraz and Madzvamuse, 2017) it is determined that the sides shown in Figures 5.7 (a) and (b) are the regions corresponding to $\sigma_{1,2} \in \mathbb{C}\backslash\mathbb{R}$. Each stripe corresponding to a distinct value of d is colour coded and denoted by capital alphabets in the form of a set containing all the points corresponding to a specific colour. These sets of points are referred to from Table 5.2 to present and summarise the quantitative analysis of the current numerical simulations of the admissible parameter spaces. Through further study of regions corresponding to complex values for $\sigma_{1,2}$ in Figure 5.7, using the solution of (5.48), it is numerically verified that a sub-partition only exists if the value of ρ satisfies condition (5.37), with respect to the values of d and γ. This is a numerical demonstration of the claim proposed by Theorem 5.3.1. If the values of d and/or γ are changed such that ρ no longer satisfies condition (5.37), it causes to vanish the existence of a sub-partition, within the region corresponding

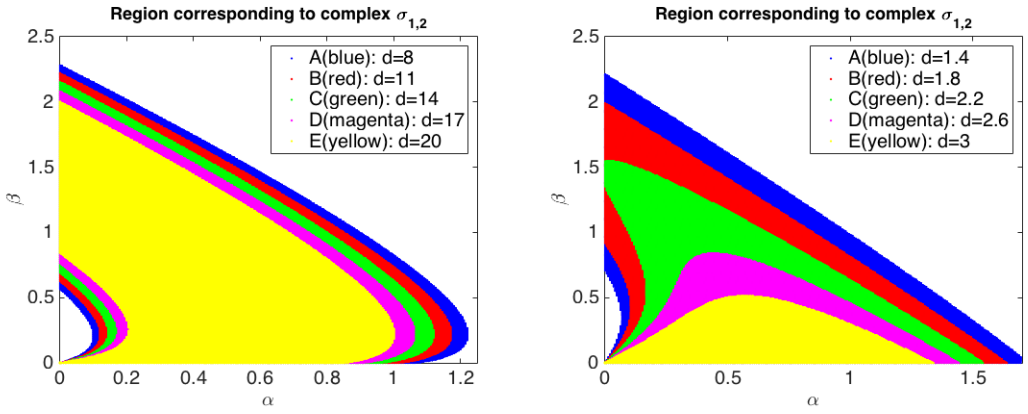

(a) (b)

FIGURE 5.7: In (a) the shift of regions corresponding to complex $\sigma_{1,2}$ and subject to condition (5.37) of Theorem 5.3.1. In (b) the shift of regions corresponding to complex $\sigma_{1,2}$ and subject to condition (5.46) of Theorem 5.3.2.

to complex eigenvalues $\sigma_{1,2}$, which is in agreement with Theorem 5.3.2. Under such choices of d and γ, the region of the parameter space corresponding to complex $\sigma_{1,2}$ has no stability partition, therefore, everywhere on this region the real part of $\sigma_{1,2}$ is negative. If parameters α and β are fed into system (5.3), then the dynamics are expected to exhibit global temporal stability. Figure 5.8 shows the regions on the admissible parameter spaces corresponding to complex $\sigma_{1,2} \in \mathbb{C}\backslash\mathbb{R}$ with negative real part. It can be noted that Figure 5.8 (b) portrays exactly the same spaces as shown in Figure 5.7 (b), which is a further verification of Theorem 5.3.2, namely, when ρ satisfies condition (5.46), then for no choice of $\alpha, \beta \in \mathbb{R}_+$ the complex eigenvalue $\sigma_{1,2}$ can have positive real part. It further means that if ρ is chosen such that it satisfies condition (5.46), then system (5.3) is guaranteed to exhibit global temporal stability in the dynamics, with the only possibility of spatial periodic behaviour. The consequence of this relationship is to state that if the value of ρ is bounded above by the right hand-side of condition (5.46), then the diffusion-driven instability will remain restricted to Turing type only, hence any pattern obtained under condition (5.46) on ρ is expected to be spatially periodic pattern, with a global temporally stable behaviour. In this case we can only obtain a pattern of spots or stripes, with spatial periodicity. If a condition on ρ is set so that

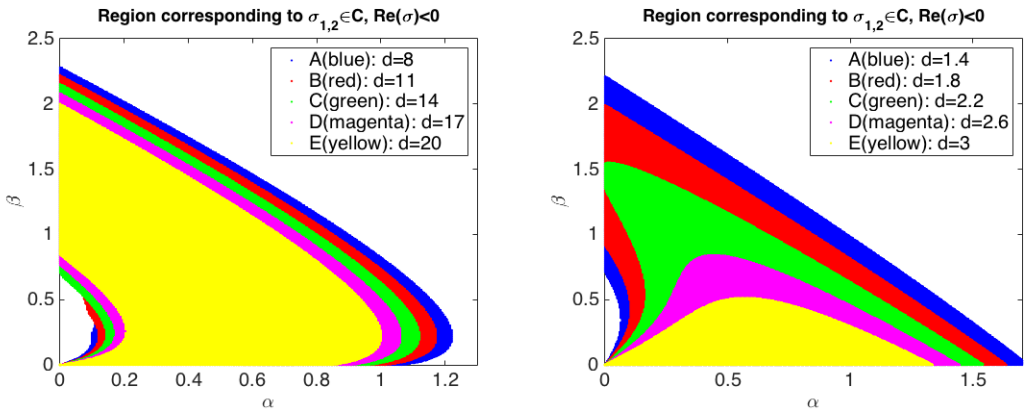

(a) (b)

FIGURE 5.8: In (a) the shift of regions corresponding to complex $\sigma_{1,2}$ are shown with negative real part and subject to condition (5.37) of Theorem 5.3.1. In (b) the shift of regions corresponding to complex $\sigma_{1,2}$ are shown with negative real parts and subject to condition (5.46) of Theorem 5.3.2.

it is large enough to exceed the value on the right hand-side of condition (5.46), i.e. ρ satisfying (5.37), only then a sub-partition can emerge within the admissible parameter space corresponding to $\sigma_{1,2} \in \mathbb{C}\backslash\mathbb{R}$. This can be observed by comparing Figure 5.8 (a) with Figure 5.7 (a), in particular the deficiency of regions is clearly visible on the inner stripes of the shifted spaces near the origin in Figure 5.8 (a). Figure 5.9 (b) shows the emergence of these curves that partition the region corresponding to $\sigma_{1,2} \in \mathbb{C}\backslash\mathbb{R}$. Recalling that if a sub-partition in the regions indicated by Figure 5.7 exist, then the corresponding partitioning curves must satisfy (5.27), which resembles the values of the parameter space that causes the real part of $\sigma_{1,2}$ to become zero when it is a pair of complex conjugate values. Therefore, on these curves the uniform steady state (u_s, v_s) undergoes limit-cycle behaviour. These are also the curves on which the real part of $\sigma_{1,2} \in \mathbb{C}\backslash\mathbb{R}$ changes sign, which means to one side of these curves a region in the admissible parameter space exist that corresponds to $\sigma_{1,2}$ to be complex conjugate pair but with positive real part. Parameter values of such kind result in the uniform steady state (u_s, v_s) to become periodic in time. This entails that the values of α and β from this region causes system (5.3) to exhibit Hopf bifurcation. Figure 5.9 (a) shows a shift in the region of the parameter spaces that corresponds to Hopf bifurcation for the

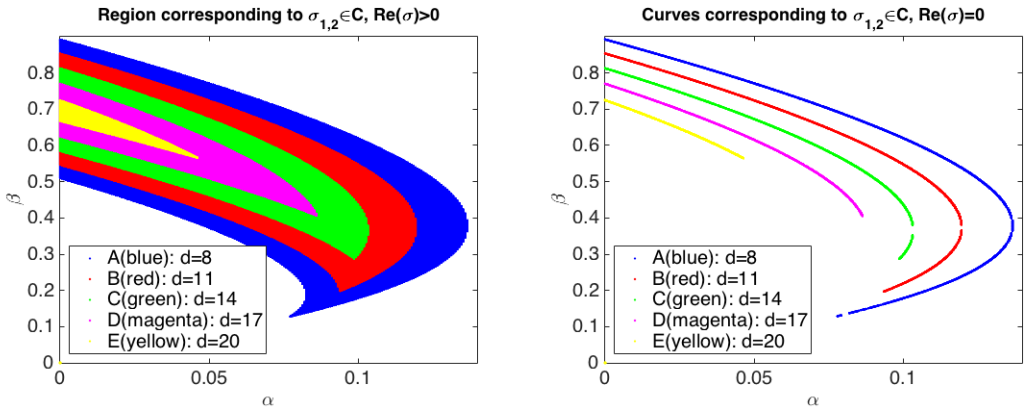

(a) (b)

FIGURE 5.9: In (a) the shift of regions corresponding to complex $\sigma_{1,2}$ is shown with positive real part and ρ restricted to condition (5.37) of Theorem 5.3.1. With condition (5.46) no region exists for Hopf bifurcation. In (b) the shift in the location of curves for five different values of d, on which the values of $\sigma_{1,2}$ are pure imaginary, and ρ is restricted to condition (5.37) of Theorem 5.3.1.

same variation in the value of d as used in Figure 5.7. It is also worth noting that with increasing values of d, the parameter spaces corresponding to Hopf bifurcation gradually decrease. This is in agreement with the mathematical reasoning behind Theorem 5.3.1, because as the value of d is increased, one gets closer to the violation of the necessary condition (5.37) for the existence of regions for Hopf bifurcation. Figure 5.9 (b) shows a more gradual extinction of the sub-partitioning curves within the region corresponding to $\sigma_{1,2} \in \mathbb{C}\backslash\mathbb{R}$. For different values of d, with ρ still satisfying (5.37), the solution of (5.47) and (5.48) is plotted near the origin to closely observe the interaction and a shift of the location. It is found that for small values of d, the intersection between the curves (5.47) and (5.48) occurs at the tip of curves in Figure 5.9 (b), such that a significant part of the curve satisfying (5.48) forms a sub-partition within the region of the admissible parameter space that corresponds to complex eigenvalues. However, as the value of d is gradually increased, so did the location of the intersection moved, reducing the sub-partition formed by the solution of (5.48). The whole of the admissible parameter space consisting of the top right quadrant of $\mathbb{R}^2_+$ plane is partitioned by the union of the spaces presented in Figure 5.7 and those corresponding to

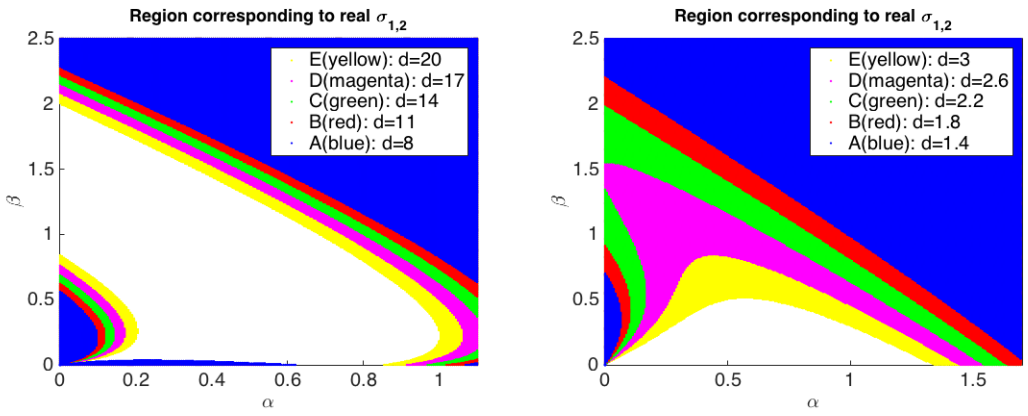

(a) (b)

FIGURE 5.10: In (a) the shift of regions corresponding to real $\sigma_{1,2}$ and subject to condition (5.37) of Theorem 5.3.1 is shown. In (b) the shift of regions corresponding to real $\sigma_{1,2}$ and subject to condition (5.46) of Theorem 5.3.2.

eigenvalues that are real. Figure 5.10 shows, under both conditions (5.37) and (5.46) on ρ, the shift of parameter spaces that correspond to real eigenvalues for different values of d. The longer partitioning curves presented in Figure 5.6, indicate the choice of α and β for which the eigenvalues $\sigma_{1,2}$ is a pair of real repeated negative values, therefore, parameter spaces bounded by these curves corresponds to a pair of distinct negative real values. A choice of (α, β) from these regions corresponds to a global spatio-temporally stable behaviour of the dynamic of system (5.3). Figure 5.11 shows the shift of these spatio-temporal stable regions on the admissible parameter space. Any choice of α and β from these regions will result in the dynamics of system (5.3) to exhibit global stability in space as well as in time, which means that if system (5.3) is perturbed in the neighbourhood of the uniform steady state (u_s, v_s) using parameters from these regions, the dynamics will guarantee to return back to the uniform steady state (u_s, v_s). It can be clearly observed that under both conditions (5.37) and (5.46) on ρ, regions corresponding to a pair of real negative eigenvalues form a proper subset of those spaces that corresponds to a pair of real values irrespective of sign. Figure 5.11 shows under both conditions (5.37) and (5.46) on ρ the shift in the spaces that correspond to global spatio-temporally stable behaviour of the dynamics of system (5.3).

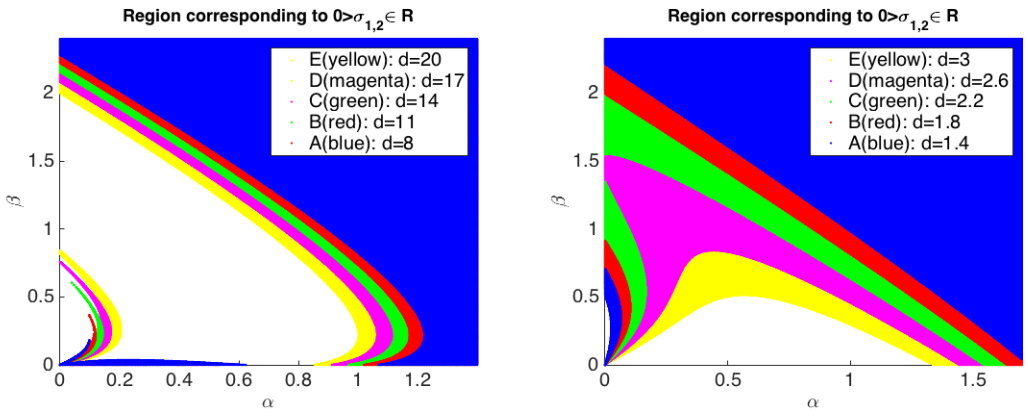

(a) (b)

FIGURE 5.11: In (a) the shift of regions corresponding to a pair of negative distinct real $\sigma_{1,2}$ and subject to condition (5.37) of Theorem 5.3.1. In (b) Shift of regions corresponding to a pair of negative distinct real $\sigma_{1,2}$ and subject to condition (5.46) of Theorem 5.3.2.

Comparing Figure 5.10 and 5.11 it can be clearly observed that under both conditions on ρ the regions of spaces corresponding to negative real values are deformed versions of those that corresponds to arbitrary real values. The remaining spaces to analyse are those corresponding to diffusion-driven instability of Turing type under conditions (5.37) and (5.46) on ρ. This region corresponds to Turing type instability and under both conditions on ρ these regions exist. It can be noted that near the origin of the admissible parameter space in Figure 5.6, for each value of d the small curves starting at the origin $(\alpha, \beta) = (0, 0)$ and curving back to intercept the β axis, are the curves on which the eigenvalues $\sigma_{1,2}$ are repeated positive real roots, therefore these curves correspond to diffusion-driven instability of Turing type. We know that the diffusion-driven instability can also happen, when either σ_1 or σ_2 are positive real. Figure 5.12 shows the shift of those regions corresponding to Turing type instability and it can be observed that as d increases, the region in the parameter space enlarges. In Figures 5.8 and 5.12, all the points specific to a certain colour on the parameter plane are denoted by an alphabetic letter. This is for the purpose to be able to cross reference using set notation to a specific region when summarising the results in Table 5.2.

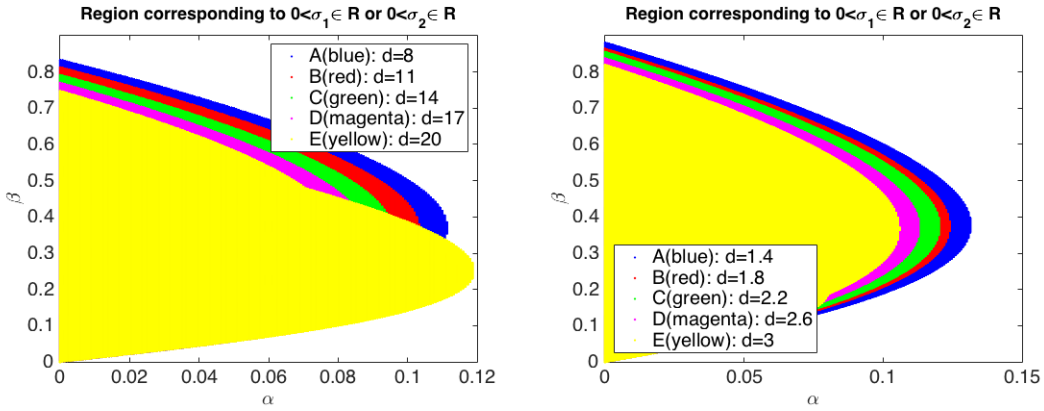

(a) (b)

FIGURE 5.12: In (a) the shift of regions are shown corresponding to Turing instability where at least one eigenvalue $\sigma_{1,2}$ is real positive and subject to condition (5.37) of Theorem 5.3.1. In (b) the shift of regions corresponding to Turing instability are shown where at least one eigenvalue $\sigma_{1,2}$ is real positive and subject to condition (5.46) of Theorem 5.3.2.

Stability of USS (u_s, v_s)			Stable regions		Unstable regions		
Types of USS (u_s, v_s)			Node	Spiral	Turing-instability	Hopf bifurcation	Transcritical bifurcation
Figure index			Figure 5.11 (a)	Figure 5.8 (a)	Figure 5.12 (a)	Figure 5.9 (a)	Figure 5.9 (b)
Theorem 5.3.1	ρ satisfying (5.37)	$\sigma_{1,2}$ / (d,γ,ρ,l)	$0 > \sigma_{1,2} \in \mathbb{R}$	$\sigma_{1,2} \in \mathbb{C}\backslash\mathbb{R}, \mathrm{Re}(\sigma) < 0$	$0 < \sigma_1 \in \mathbb{R}$ or $0 < \sigma_2 \in \mathbb{R}$	$\sigma_{1,2} \in \mathbb{C}\backslash\mathbb{R}, \mathrm{Re}(\sigma_{1,2}) > 0$	$\sigma_{1,2} \in \mathbb{C}\backslash\mathbb{R},\ \mathrm{Re}(\sigma_{1,2}) = 0$
		$(8.0, 21, \frac{1}{2}, 0.27)$	A	$A\cup B\cup C\cup D\cup E$	A	$A\cup B\cup C\cup D\cup E$	curve A
		$(11, 21, \frac{1}{2}, 0.27)$	$A\cup B$	$B\cup C\cup D\cup E$	$A\cup B$	$B\cup C\cup D\cup E$	curve B
		$(14, 21, \frac{1}{2}, 0.27)$	$A\cup B\cup C$	$C\cup D\cup E$	$A\cup B\cup C$	$C\cup D\cup E$	curve C
		$(17, 21, \frac{1}{2}, 0.27)$	$A\cup B\cup C\cup D$	$D\cup E$	$A\cup B\cup C\cup D$	$D\cup E$	curve D
		$(20, 21, \frac{1}{2}, 0.27)$	$A\cup B\cup C\cup D\cup E$	E	$A\cup B\cup C\cup D\cup E$	E	curve E
Figure index			Figure 5.11 (b)	Figure 5.8 (b)	Figure 5.12 (b)	Figure 5.9 (b)	Figure 5.8 (b)
Theorem 5.3.2	ρ satisfying (5.46)	$\sigma_{1,2}$ / (d,γ,ρ,l)	$0 > \sigma_{1,2} \in \mathbb{R}$	$\sigma_{1,2} \in \mathbb{C}\backslash\mathbb{R}, \mathrm{Re}(\sigma) < 0$	$0 < \sigma_1 \in \mathbb{R}$ or $0 < \sigma_2 \in \mathbb{R}$	$\sigma_{1,2} \in \mathbb{C}\backslash\mathbb{R}, \mathrm{Re}(\sigma_{1,2}) > 0$	$\sigma_{1,2} \in \mathbb{C}\backslash\mathbb{R},\ \mathrm{Re}(\sigma_{1,2}) = 0$
		$(1.4, 1, \frac{1}{2}, 0.27)$	E	$A\cup B\cup C\cup D\cup E$	A	$\emptyset$	$\emptyset$
		$(1.8, 1, \frac{1}{2}, 0.27)$	$E\cup D$	$A\cup B\cup C\cup D$	$A\cup B$	$\emptyset$	$\emptyset$
		$(2.2, 1, \frac{1}{2}, 0.27)$	$E\cup D\cup C$	$A\cup B\cup C$	$A\cup B\cup C$	$\emptyset$	$\emptyset$
		$(2.6, 1, \frac{1}{2}, 0.27)$	$E\cup D\cup C\cup B$	$A\cup B$	$A\cup B\cup C\cup D$	$\emptyset$	$\emptyset$
		$(3.0, 1, \frac{1}{2}, 0.27)$	$E\cup D\cup C\cup B\cup A$	A	$A\cup B\cup C\cup D\cup E$	$\emptyset$	$\emptyset$

TABLE 5.2: The summary of the full classification of parameter spaces for system (5.3) is presented with the associated numerical verification of the predictions made by Theorems 5.3.1 and 5.3.2. Furthermore, it is shown how a certain type of bifurcation space shifts according to the variation of parameter d.

5.4.1 Remark

It must be observed that the first non-trivial mode $k = 0$ corresponding to the pair $(j = 0, j = 1)$ in the infinite series of the eigenfunctions is used for all the computations of the partitioning curves and the corresponding parameter spaces. It is worth noting that higher modes such as $k = 1, 2, 3, ...$ for the expressions of the eigenvalues $\eta_{k,l}$ will only cause a scaled shift in the location of the partitioning curves, whilst keeping the validity of conditions (5.37) and (5.46) intact. This is because the choice of higher modes k enforces a corresponding change in the value of parameter ρ in order for inequalities corresponding to conditions (5.37) and (5.46) to hold. In other words, given that conditions (5.37) and (5.46) are satisfied the dynamics are guaranteed to exhibit the proposed behaviour independent of the choice of the mode k and the order of the corresponding Bessel's equation $l \in \mathbb{R}\backslash\frac{1}{2}\mathbb{Z}$.

5.5 Finite element solutions of RDS

For numerical verifications of the proposed classification of the parameter spaces in particular to visualise the influence of domain-size conditions given by Theorems 5.3.1 and 5.3.2, the reaction-diffusion system (5.3) is simulated using the finite element method (Smith, Griffiths, and Margetts, 2013; Becker, 1998) on Ω that consists of all the points obtained from a planar projection of a torus with inner radius $a = \frac{1}{2}$ and outer radius $b = 1$. This leads to $\rho = b - a = \frac{1}{2}$, which is kept constant throughout the finite element simulations in this section. Conditions (5.37) and (5.46) are in turn satisfied by varying the values of d and γ accordingly. The advantage of such strategy is that it reduces the computational cost significantly in the sense that an efficient degree of freedom on the finite element triangulation can be consistently used to obtain results under both of the proposed conditions in Theorems 5.3.1 and 5.3.2 respectively. Therefore, to avoid such unnecessary computational cost by varying ρ we proceed with a fixed $\rho = \frac{1}{2}$ and vary the constants d and γ to meet the relevant restriction required on the size of ρ. Due to the curved boundary of Ω, the triangulation

is obtained through an application of an iterative algorithm using a technique called *distmesh* The algorithm for *distmesh* was originally developed in MATLAB by Persson and Strang (Persson and Strang, 2004; Lee and Schachter, 1980) for generating uniform and non-uniform refined meshes on two and three dimensional geometries. *Distmesh* utilises signed-distance function $d(x, y)$, which is negative inside the discretised domain Ω and is positive outside $\partial\Omega$. The construction of distmesh triangulation is an iterative process using a set of two interactive algorithms, one of which controls the displacement of nodes within the domain and the other ensures that the consequences of node displacement does not violate the properties of the Delaunay triangulation (Lee and Schachter, 1980). For details on how to generate meshes using *distmesh* we refer the interested reader to the joint work by Persson and Strang presented in (Persson and Strang, 2004). An annular region Ω of thickness $\rho = \frac{1}{2}$ is descritised through the application of *distmesh* (Persson and Strang, 2004) to generate a triangular mesh for simulating the finite element solution of (5.3). The two circles forming the inner and out boundaries of Ω are concentrically centred at the origin of cartesian plane as shown in Figure 5.1. The annular region is discretised by 6340 triangles consisting of 3333 vertices. In each simulations in this section the initial conditions are continuous bounded functions with pure spatial dependence in the form of a small perturbations in the neighbourhood of the uniform steady state $(u_s, v_s) = (\alpha + \beta, \frac{\beta}{(\alpha+\beta)^2})$ (Murray, 2001; Edelstein-Keshet, 1988; Madzvamuse and Chung, 2014) in the form

$$\begin{cases} u_0(x,y) = \alpha + \beta + 0.0016\cos(2\pi(x+y)) + 0.01\sum_{i=1}^{8}\cos(i\pi x), \\ v_0(x,y) = \frac{\beta}{(\alpha+\beta)^2} + 0.0016\cos(2\pi(x+y)) + 0.01\sum_{i=1}^{8}\cos(i\pi x). \end{cases} \tag{5.49}$$

The values of parameters α and β are verified from all of those regions that correspond to some type of diffusion-driven instability. The numerical values of the parameters corresponding to each of the simulations in this section are presented in Table 5.3.

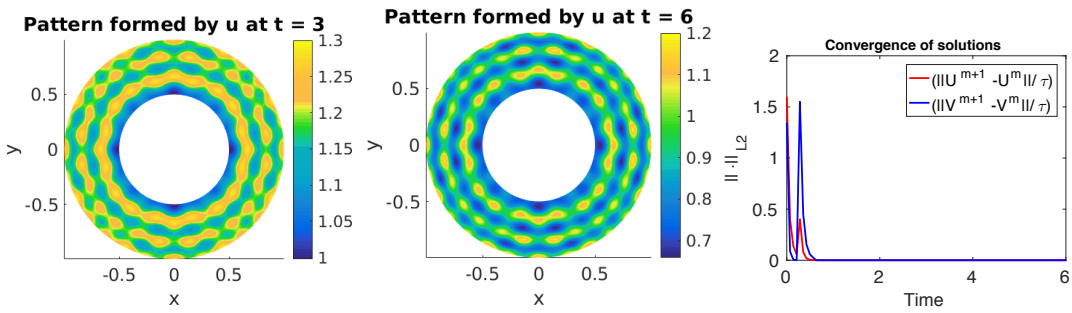

(a) (b) (c)

FIGURE 5.13: In (a) the pattern evolution is restricted to spatial periodicity for α and β in the Turing space under condition (5.46) on the domain-size controlling parameter ρ. In (b) the pattern evolution is restricted to spatial periodicity for α and β in the Turing space under condition (5.46) on the domain-size controlling parameter ρ. bIn (c) the instability is shown through the evolution of the discrete L_2 norm of the discrete time derivatives of the solutions u and v.

Figure 5.13 (a) shows the evolution of a spatial pattern as a consequence of choosing (α, β) from Turing region under condition (5.46) indicated in Figure 5.12 (b). Depending on the initial conditions and the mode of the eigenfunctions, the spatially periodic pattern provided by parameter spaces in Figure 5.12 (b) is expected to be a combination of radial and angular stripes or spots. Once the initial pattern is formed by the evolution of the dynamics, then the system is expected to uniformly converge to a Turing-type steady state, which means the initially evolved spatial pattern becomes temporally invariant as time grows. The simulation of Figure 5.13 was executed for long enough time such that the discrete time derivative of solutions u and v decaying to a threshold of 5×10^{-4} in the discrete L_2 norm. Figure 5.13 (b) demonstrates the behaviour of the discrete time derivatives of both species for the entire period of simulation time until the threshold was reached. It is observed that after the initial Turing-type instability, the evolution of the system uniformly converges to a spatially patterned steady state. Figure 5.14 presents two snapshots to show how the spatially periodic pattern is evolved to a Turing type steady state, when parameters α and β are chosen from Turing region and ρ satisfying condition (5.37), with respect to d and γ. For simulations in Figure 5.14, parameters α and β are chosen from regions presented

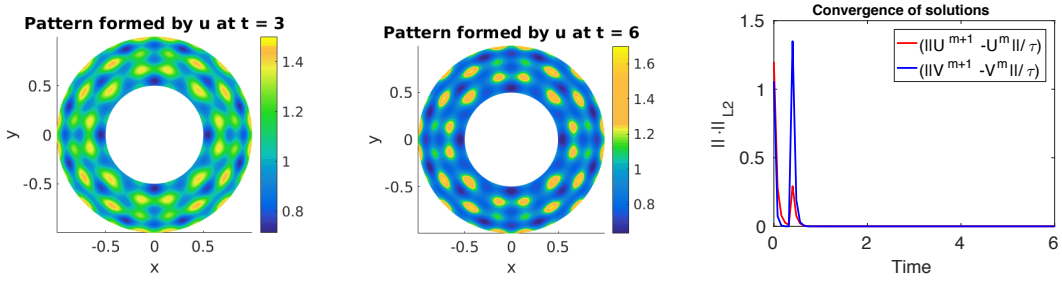

(a) In (a) (b) (c)

FIGURE 5.14: In (a) the stage of evolving spatially periodic pattern at $t = 3$ is shown when, α and β are chosen from Turing space under condition (5.37) on the radius ρ. In (b) the spatially periodic pattern at $t = 6$ is as expected converging to the Turing type steady state without allowing the initial pattern to be deformed. In (c) the instability and convergence is shown through the behaviour of the discrete time derivatives of the solutions u and v.

in Figure 5.12 (a); the dynamics within these regions evolve to a spatial pattern with global temporal stability. It can be noted from Figure 5.14 (d), that after the initial pattern is formed, the system is uniformly converging to the spatially periodic steady state. Turing instability is a domain independent phenomena, and only depends on the choice of parameters and the initial conditions. At $t = 6$ the required threshold of 5×10^{-4} on the discrete L_2 norm of the discrete time derivatives of the solutions u and v is reached, which can be observed in Figure 5.14 (d). The remaining two unstable regions in the admissible parameter space presented in Figure 5.9 correspond to spatio-temporal periodicity. Regions presented in Figure 5.9 (a) are those corresponding to a complex conjugate pair of eigenvalues with non-zero positive real part. These regions emerge in the admissible parameter space under condition (5.37) on ρ. Choosing parameters from regions in Figure 5.9 (a) admits temporal periodic behaviour in the dynamics of system (5.3) as shown in Figure 5.15. The initial pattern in Figure 5.15 (a) is in fact achieved earlier than at $t = 1$, therefore, the temporal gap between the initial and second pattern in Figure 5.15 (b) is relatively smaller than the temporal gaps that exist between the second, third and fourth temporal periods. It is worth noting that the temporal period between the successive transitional temporal instabilities from one type of spatial pattern to another grows larger with time. The initial pattern

is obtained at around $t \approx 1$, which becomes unstable during the transition to the second temporal period at $t \approx 5$ in Figure 5.15 (b). At $t \approx 8$ the system undergoes a third period of instability and reaches a different spatial pattern at $t \approx 12$ shown in Figure 5.15 (c). The fourth period of temporal instability is reached at $t \approx 20$, which converges to the fourth temporally-local but spatially periodic steady state at $t \approx 28$ presented in Figure 5.15 (d). It follows that when parameters are chosen from the Hopf bifurcation region then the temporal gaps in the dynamics of system (5.3) between successive transitional instabilities from one spatial pattern to another is approximately doubled as time grows. It is speculated that the temporal period-doubling behaviour is connected to the analogy of unstable spiral behaviour in the theory of ordinary differential equations (Perko, 2013). If the eigenvalues of a dynamical system modelled by a set of ordinary differential equations is a complex number with positive real part, then the cycles of the corresponding unstable spiral grow larger as time grows. The long-term evolution of temporal instability depends on the magnitude of the real part of $\sigma_{1,2}$. If parameters (α, β) are chosen such that the trace of the stability matrix (5.22) is large and yet the discriminant is negative, then the dynamics exhibit long-term temporal periodicity, which means that the frequency of temporal cycles will become smaller. A decaying frequency in temporal cycles means that locally on the time axis, the dynamics may exhibit similar behaviour to that of a temporally stable system, therefore, to observe temporal transition from one spatial pattern to another, the model requires to be simulated for much longer periods of time. Figure 5.15 (e) shows a visualisation of the transition of such temporal periodicity with a decaying frequency. Theorem 5.3.1 states that, if the thickness ρ of the annular region Ω is chosen according to condition (5.37) with respect to d and γ, and the parameters (α, β) are chosen from the curves corresponding to transcritical bifurcation indicated in Figure 5.9 (b), then the dynamics of system (5.3) are expected to exhibit spatio-temporal periodic behaviour. This kind of behaviour in the dynamics is referred to as the limit cycles (Perko, 2013; Schnakenberg, 1979). Figure 5.16 shows this spatio-temporal periodic behaviour in the evolution of the numerical solution of system (5.3). This is the case corresponding to

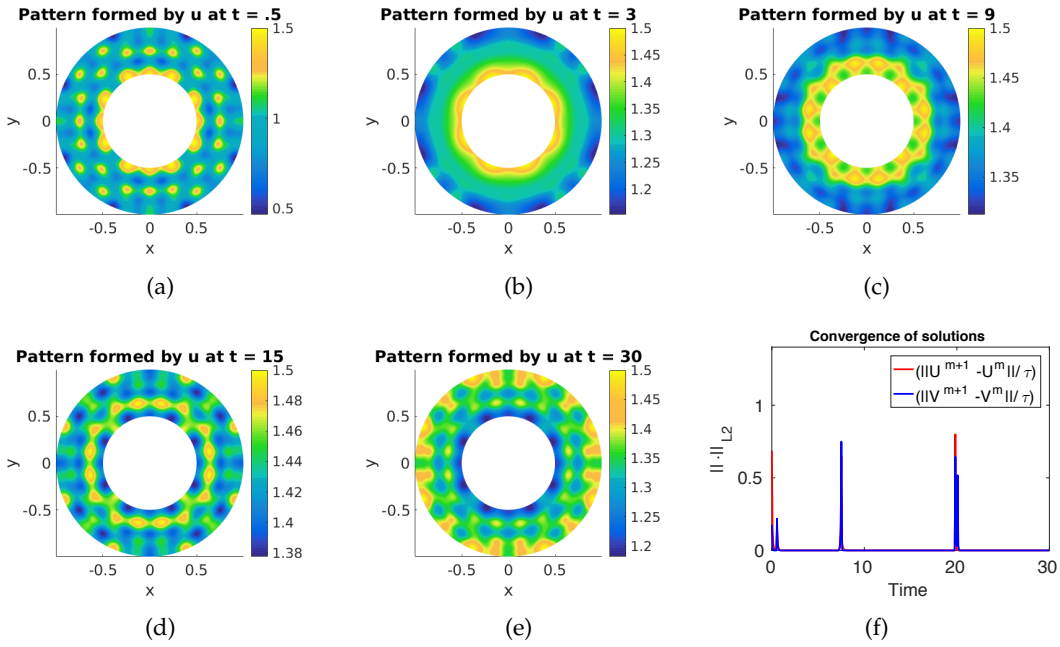

(a) (b) (c)

(d) (e) (f)

FIGURE 5.15: In (a) the first temporal period evolving the initial spatially periodic pattern at $t = 0.5$. In (b) the spatial pattern is evolved after the first transitional instability and during the second temporal period at $t = 3$. In (c) the spatial pattern is evolved after the second transition of the temporal instability and during the third temporal period at $t = 9$. In (d) the spatial pattern after the third transition of temporal instability and during the fourth temporal period obtained at $t = 15$. In (e) the spatial pattern after the fourth transition of the temporal instability and during the fifth temporal period obtained at $t = 30$. In (f) the spatio-temporal periodicity in the dynamics measured in discrete L_2 norm of the successive discrete time derivative of the solutions u and v.

Plot index	Figure 5.13	Figure 5.14	Figure 5.15	Figure 5.16
Instability / Parameters	Turing type instability Spatial pattern	Turing type instability Spatial pattern	Hopf bifurcation Spatial and temporal pattern	Transcritical bifurcation Spatial and temporal pattern
(α, β)	$(0.09, 0.45)$	$(0.08, 0.40)$	$(0.05, 0.55)$	$(0.05, 0.625)$
(l, d, γ)	$(1.3, 10, 250)$	$(1.3, 5, 630)$	$(1.3, 5, 730)$	$(1.3, 5, 730)$
Condition on Ω	(5.46)	(5.37)	(5.37)	(5.37)
Simulation time	6	6	30	9
CPU time (sec)	648.21	631.63	4230.55	1097.32

TABLE 5.3: The choice of parameters (α, β) for each simulation and the choice of (l, d, γ) subject to the relevant condition referred to in third row. Each simulation is run with time-step of 1×10^{-3}.

parameters that ensure the eigenvalues to be purely imaginary, therefore, it can be observed that the temporal instability occurs unlike the Hopf bifurcation, with constant periods along the time axis, which verifies the theoretical prediction of the transcritical bifurcation. It is worth noting that the transitional instability from angular stripes in Figure 5.16 (a) to the spots in Figure 5.16 (b), the discrete L_2 norm of the discrete time-derivative of the activator u exceeds compared to that of the inhibitor v. However, during the second temporal period when the spots in Figure 5.16 (b) turn back into angular stripes in Figure 5.16 (c), then the discrete L_2 norm of the time-derivative of the inhibitor v exceeds in magnitude than that of the activator u. This alternating behaviour can be clearly observed in Figure 5.16 (d), where in the annotated legend U and V denote the discrete solutions of the activator u and that of the inhibitor v. It can further be understood from Figure 5.16 (d), that if (α, β) are chosen from the curves of the transcritical bifurcation given in Figure 5.9 (b), then the frequency of temporal periods is predicted to remain constant for all times, resulting in a constant interchanging behaviour between different spatial patterns.

5.6 Conclusion

A reaction-diffusion model of *activator-depleted* class was analysed on polar coordinates on a closed bounded but non-convex domain that consists of an annular region. The model was subject to homogeneous boundary conditions of Neumann type. For linearisation purpose the spectrum of Laplace operator on the annular domain was

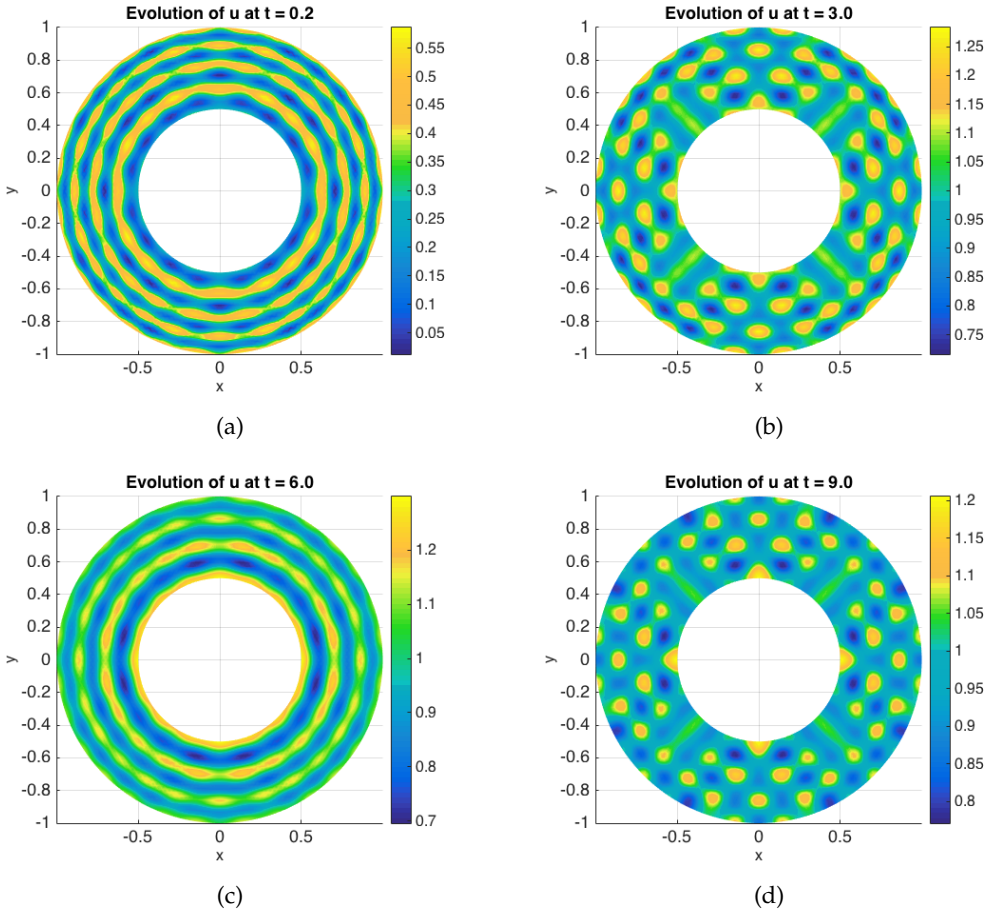

FIGURE 5.16: In (a) the initial spatially periodic pattern (angular stripes) at $t = 0.2$ is shown when, α and β are chosen from the region of the transcritical bifurcation under condition (5.37) on the thickness ρ. In (b) the spatially periodic pattern evolves to change structure to (spots) at $t = 3$. In (c) at $t = 6$ the spots undergo another period of temporal instability to return to angular stripes same as the initial pattern. In (d) at $t = 9$ the pattern of the second temporal period emerges again, indicating the temporally the dynamics behaviour in an alternating way between the spots and angular stripes.

analysed and closed form power series solutions were obtained for the relevant eigenvalue problem.

It was further shown that the spectrum of the Laplace is semi-discrete set of complex valued functions with real eigenvalues. The solutions of the relevant eigenvalue problem were simulated using the spectral method on a two dimensional annular geometry, which was conducted through the application of a particular depicting technique, since the solutions are complex valued. The eigen-functions and the corresponding eigenvalues are incorporated through the application of linear stability theory to derive analytical results relating the thickness of the annular domain to the reaction and diffusion parameters. It was found that a lower bound exists on the thickness of a two dimensional shell with respect to the reaction and diffusion rates that can admit the three types of bifurcations namely Turing, Hopf and transcritical bifurcation. Furthermore, it was found that an upper bound also exists on the thickness of the two dimensional annular domain that forbids temporal periodicity such as Hopf and transcritical bifurcations, and still admitting a Turing type behaviour in the evolution of the dynamics. In order to verify the analytical findings on the predicted behaviour of the system, a numerical technique was applied to solve the implicit non-linear partitioning curves for the parameter plane. The numerical solutions of these partitioning curves and the parameter classification was obtained under the analytically proven conditions on the thickness of the annular domain. It was shown that with the upper bound satisfied on the thickness of the annular domain, the numerical solutions of the partitioning curves reveal no region in the parameter plane

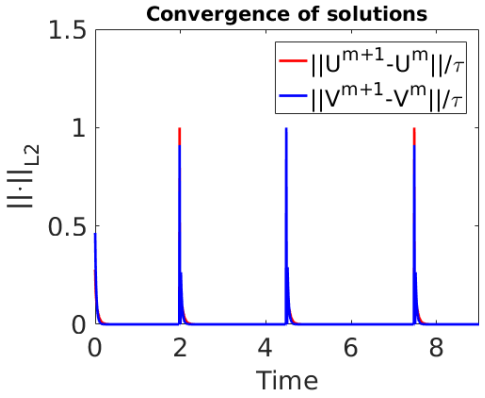

FIGURE 5.17: Plot of the discrete L_2 norm of the time-derivative of u and v showing the spatio-temporal behaviour of the solutions for successive time-steps.

that corresponds to Hopf and transcritical bifurcations. Furthermore, if the thickness of the annular region satisfies the lower bound with respect to the reaction and diffusion rates, then the numerical solutions of the partitioning curves indeed reveal regions that correspond to all the three types of predicted behaviours such as Turing, Hopf and limit-cycle behaviour. Finite element simulations were used to verify the analytically proven results through numerical solutions of *activator-depleted* class reaction-diffusion model on an annular region. Parameter values for the finite element simulations were chosen from the proposed regions by the solutions of the non-linear partitioning curves and it was shown that when the thickness of the annular domain satisfies the upper bound with respect to reaction and diffusion parameters then the finite element simulations do portray only a single type of unstable behaviour leading to the evolution of Turing type pattern. However, when the thickness of annular domain satisfies the lower bound condition with respect to reaction and diffusion parameters, then finite element simulations reveal that upon choosing parameter values from regions corresponding to Hopf and transcritical bifurcations, the system undergoes a temporal bifurcation of a spatial pattern. It means that the dynamics exhibit a spatio-temporal periodic behaviour. Furthermore, under the same condition, when parameters are chosen from Turing region, then the finite element solutions do reveal a Turing type pattern that is a spatially periodic behaviour with global temporal invariance in structure.

Chapter 6

Conclusions

Despite that at the end of each chapter a detailed conclusion is presented summarising the contents therein, this chapter is therefore, devoted to present in a bullet-point form a brief and qualitative overview expressing the overall novelty, contribution and the impact associated to the results and methodology of this thesis. Furthermore, a number of possible research extensions initiated by the contents of this thesis are also presented in this chapter.

6.1 Concluding points

- Reaction-diffusion system was derived on time-dependent domain from first principle using conservation of mass and Fick's law of diffusion.
- ALE formulation of RDS was derived both in *conservative* and *non-conservative* forms on reference and evolving frames. This is to serve as a computational framework for solving RDSs on time-dependent domains, when the material velocity obeys a law that is different from the one driving domain deformation.
- The contribution and novelty associated to the contents of this thesis lies in the application of a complete and transferable methodology to explore RDSs, examples of such methodology are applied to three types of domains namely rectangular, circular and annular geometries.

- A reaction-diffusion system of *activator-depleted* class is analysed on rectangular stationary domains to establish the relationship between domain-size and reaction-diffusion parameters. Subject to this relationship the bifurcation analysis and parameter classification is computationally obtained through a novel numerical technique of polynomials exclusive to this thesis. Finite element method is used to verify the proposed bifurcation results and parameter classification.

- The methodology is extended to investigate the model on a two dimensional compact circular domain of disc-shape. The semi-discrete spectrum of Laplace operator was analytically derived subject to homogeneous Neumann boundary conditions and spectral method is applied to numerically demonstrate the analytical results on the spectrum of the diffusion operator. The influence of the radius of a circular compact domain is studied in the context of bifurcation admissibility, which is further verified through standard Galerkin finite element method.

- The framework is extended to carry out a similar study on a two dimensional annular geometry in which both the inner and the outer boundaries are subject to homogeneous Neumann type conditions, which makes the analytical techniques for spectral solutions non-trivial. A relationship between domain-size controlling parameter (thickness of annulus) and reaction-diffusion parameters is established and verified through standard finite element method.

- One of the novelties associated with the current work is the application of a numerical technique of polynomials to solve the partitioning curves for parameter classification for all types of geometries that are studied in the scope of this thesis.

- Instead of obtaining just Turing spaces, the admissible parameter spaces are fully classified through this numerical technique for all types of geometries. The capability to fully classify the parameter spaces is crucial if we wish to completely reveal the bifurcation properties of an RDS on a given domain.

- Rigorous analytical results expressing the influence of domain-size on the admissibility of different types of diffusion-driven instabilities are obtained. All of these results are numerically supported by finite element simulations.

- An analytical technique of telescoping argument from real analysis is employed to acquire closed-form spectral solutions on circular domains with Neumann boundary conditions.

- Application of *distmesh* technique to obtain a non-uniform spatial discretisation of circular compact and non-compact domains for the finite element approximate solutions.

- The methodology used in the current paper proposes an exclusive framework to investigate general reaction-diffusion systems on arbitrary geometries. The current work brings together the applications of stability theory, harmonic analysis, finite element method to obtain a robust and complete insight on the parameter spaces and the influence of domain-size on the predicted dynamics governed by RDSs.

- Conditions on the side length of a rectangular geometry are analytically proven that can be used for quantitative analysis of the choice of reaction-diffusion constants with respect to the domain-size in consideration.

- The derivation of these conditions is extended to conduct similar study on a flat disc-shape domain, where the radius of a disc-shape domain is conditioned with respect to the choice of reaction-diffusion constants to quantify the influence of domain size on the dynamical behaviour of RDSs.

- Identical framework was also applied to annular geometry to analytically derive similar conditions on the thickness of a flat-ring, and it is found where such conditions are influential on the dynamics governed by RDSs on an annulus.

- The contents of third, fourth and fifth chapter serve to demonstrate the robustness and novelty of the proposed methodology that successfully analyses the influence of domain-size/s on the pattern formation properties.

- The results for different geometries can be compared from an empirical perspective in the sense, that in all cases the formation of spatial pattern is admissible regardless of the relative values chosen for reaction-diffusion constants with respect to domain-size. It means that so long as the diffusion-driven instability conditions are satisfied, spatial pattern can be formed. This is in agreement with the current state of mathematical knowledge on the emergence of spatial pattern. However, for a spatial pattern to undergo a temporal transition in structure due to the periodic occurrence of diffusion-driven instability, the current thesis finds that domain-size must be sufficiently large with respect to the values of the reaction-diffusion constants. These conditions are quantitatively derived and numerically demonstrated.

6.2 Possible research extensions

The theoretical set-up proposed by the current thesis can be applied to reaction-diffusion systems with linear cross-diffusion. In Madzvamuse, Ndakwo, and Barreira, 2016 it is shown that the known condition of $d > 1$ is no longer necessary for pattern formation in the presence of linear cross-diffusion, which also provides a possible platform for the extension of the current work, to see, whether the invalidation of the condition $d > 1$ in the presence of linear cross-diffusion is influenced by the relationship between reaction-diffusion parameters and the domain-size. Furthermore, it can be investigated, whether the existence of a linear cross-diffusion has any influence on the conditions derived for the domain-size in the context of bifurcation analysis with independent diffusion rates. The parameter spaces are expected to significantly change as the diffusion matrix is no longer diagonal in the presence of linear cross diffusion.

Using the methodology of this work, on arbitrary geometries for domain may be investigates to obtain full insight on the parameter spaces and possible relationship between reaction-diffusion rates with the domain-size in the context of stability theory.

In particular a biological application of the current study is to model the reaction and diffusion of chemo-taxis with the immune cells of a tumour after reaching the hypoxic stage, an example of this is shown in Figure 1.1 (b). Cancer tumours evolve to grow in size by attracting local capillaries for oxygen and nutrition. As the process continues and the tumour grows larger in size. It reaches a point when the attracting capillaries can no longer supply the interior of the tumour due to its size and the extensive consumption of nutrition contributing to its growth on the surface. When the interior of the tumour lacks oxygen and nutrition, the tumour enters a stage called *hypoxia*, during which the cells in the interior of the tumour starve to death and with long enough time, the activities of uncontrolled growth concentrates on a hollow sphere. At this stage of the tumour the hollow sphere can be modelled by a two dimensional shell using the rotation symmetry with respect to the zenith angle, which leads to a two dimensional annular region.

The current work can also be extended to the analysis of bulk-surface reaction-diffusion systems. It is possible to apply the idea of the present work to the problems of pattern formation on bulk-surface geometries, where the relationship of surface area with reaction-diffusion parameters can be explored to find the relevant influence of such relationship on the formation of spatial and/or temporal patterns. The evolution of pattern in a coupled bulk-surface reaction-diffusion system can be investigated to find the influence of the area of the surface and the volume of the bulk on the evolution of dynamics. Bulk-surface reaction-diffusion systems are used to model various coupled biological processes such as the interaction of Receptor-ligand in the process of cellular signalling and cell motility.

A further extension of this work is to apply the framework to reaction-diffusion systems on evolving domains. Conditions that are found in the scope of this study can further be explored, whether, with the growth of the domain, these conditions still

hold to influence the evolution of pattern formation, or is there a threshold for the domain-size, beyond which these conditions no longer hold?

Bibliography

Acheson, DJ (1990). *Elementary fluid dynamics: Oxford applied mathematics and computing science series*. Oxford: Oxford University Press.

Arfken, George B and Hans J Weber (1999). *Mathematical methods for physicists*. AAPT.

Avnir, David and Michael Kagan (1984). "Spatial structures generated by chemical reactions at interfaces". In: *Nature* 307.5953, p. 717.

Baines, Michael John (1994). *Moving finite elements*. Oxford University Press, Inc.

Barreira, R, Charles M Elliott, and A Madzvamuse (2011). "The surface finite element method for pattern formation on evolving biological surfaces". In: *Journal of mathematical biology* 63.6, pp. 1095–1119.

Barrio, Rafael A et al. (2009). "Modeling the skin pattern of fishes". In: *Physical Review E* 79.3, p. 031908.

Becker, AA (1998). *Programming The Finite Element Method*. Vol. 212. 4. SAGE PUBLICATIONS, INC., p. 330.

Benedetto, John J (1996). *Harmonic analysis and applications*. Vol. 23. CRC Press.

Boas, Mary L (2006). *Mathematical methods in the physical sciences*. Wiley.

Bonito, Andrea, Irene Kyza, and Ricardo H Nochetto (2013). "Time-discrete higher-order ALE formulations: stability". In: *SIAM Journal on Numerical Analysis* 51.1, pp. 577–604.

Casten, Richard G and Charles J Holland (1977). "Stability properties of solutions to systems of reaction-diffusion equations". In: *SIAM Journal on Applied Mathematics* 33.2, pp. 353–364.

Chaplain, Mark AJ, Mahadevan Ganesh, and Ivan G Graham (2001). "Spatio-temporal pattern formation on spherical surfaces: numerical simulation and application to solid tumour growth". In: *Journal of mathematical biology* 42.5, pp. 387–423.

De Kepper, P, J Boissonade, and I Szalai (2009). "From sustained oscillations to stationary reaction-diffusion patterns". In: *Chemomechanical Instabilities in Responsive Materials*. Springer, pp. 1–37.

Doelman, Arjen, Tasso J Kaper, and Paul A Zegeling (1997). "Pattern formation in the one-dimensional Gray-Scott model". In: *Nonlinearity* 10.2, p. 523.

Edelstein-Keshet, Leah (1988). *Mathematical models in biology*. Vol. 46. Siam.

Estep, Donald J, Mats G Larson, and Roy D Williams (2000). *Estimating the error of numerical solutions of systems of reaction-diffusion equations*. Vol. 696. American Mathematical Soc.

Gaffney, EA, F Yi, and Sungrim Seirin Lee (2016). "The bifurcation analysis of turing pattern formation induced by delay and diffusion in the Schnakenberg system". In: *Discrete and Continuous Dynamical System-Series B* 22.2, pp. 647–668.

Ghorai, Santu and Swarup Poria (2016). "Turing patterns induced by cross-diffusion in a predator-prey system in presence of habitat complexity". In: *Chaos, Solitons & Fractals* 91, pp. 421–429.

Gierer, Alfred and Hans Meinhardt (1972). "A theory of biological pattern formation". In: *Kybernetik* 12.1, pp. 30–39.

Grimes, David Robert et al. (2014). "A method for estimating the oxygen consumption rate in multicellular tumour spheroids". In: *Journal of The Royal Society Interface* 11.92, p. 20131124.

Hobson, Ernst William (1944). *The Theory of spherical and ellipsoidal harmonics: 1. 2*. CUP Archive.

Horváth, Judit, István Szalai, and Patrick De Kepper (2009). "An experimental design method leading to chemical Turing patterns". In: *Science* 324.5928, pp. 772–775.

Hoveyda, Amir H, David A Evans, and Gregory C Fu (1993). "Substrate-directable chemical reactions". In: *Chemical reviews* 93.4, pp. 1307–1370.

Hsia, Justin et al. (2012). "A feedback quenched oscillator produces turing patterning with one diffuser". In: *PLoS computational biology* 8.1, e1002331.

Huang, Weizhang and Robert D Russell (2010). *Adaptive moving mesh methods*. Vol. 174. Springer Science & Business Media.

Iron, David, Juncheng Wei, and Matthias Winter (2004). "Stability analysis of Turing patterns generated by the Schnakenberg model". In: *Journal of mathematical biology* 49.4, pp. 358–390.

Kondo, Shigeru and Takashi Miura (2010). "Reaction-diffusion model as a framework for understanding biological pattern formation". In: *science* 329.5999, pp. 1616–1620.

Korvasová, K et al. (2015). "Investigating the Turing conditions for diffusion-driven instability in the presence of a binding immobile substrate". In: *Journal of theoretical biology* 367, pp. 286–295.

Lakkis, Omar, Anotida Madzvamuse, and Chandrasekhar Venkataraman (2013). "Implicit–explicit timestepping with finite element approximation of reaction–diffusion systems on evolving domains". In: *SIAM Journal on Numerical Analysis* 51.4, pp. 2309–2330.

Larson, Mats G and Fredrik Bengzon (2013). *The finite element method: Theory, implementation, and applications*. Vol. 10. Springer Science & Business Media.

Lebedev, NN (1965). *Special Functions and Their Applications, English edition translated and revised by RA Silverman*. Prentice-Hall.

Lee, Der-Tsai and Bruce J Schachter (1980). "Two algorithms for constructing a Delaunay triangulation". In: *International Journal of Computer & Information Sciences* 9.3, pp. 219–242.

Lee, Kyoung-Jin et al. (1994). "Experimental observation of self-replicating spots in a reaction–diffusion system". In: *Nature* 369.6477, p. 215.

Lengyel, Istvan and Irving R Epstein (1992). "A chemical approach to designing Turing patterns in reaction-diffusion systems." In: *Proceedings of the National Academy of Sciences* 89.9, pp. 3977–3979.

Li, Liangpan et al. (2007). "On the second eigenvalue of the Laplacian in an annulus". In: *Illinois Journal of Mathematics* 51.3, pp. 913–925.

Liu, Ping et al. (2013). "Bifurcation analysis of reaction–diffusion Schnakenberg model". In: *Journal of Mathematical Chemistry* 51.8, pp. 2001–2019.

Mackenzie, JA and A Madzvamuse (2009). "Analysis of stability and convergence of finite-difference methods for a reaction–diffusion problem on a one-dimensional growing domain". In: *IMA journal of numerical analysis* 31.1, pp. 212–232.

Madzvamuse, A. (2000). "A numerical approach to the study of spatial pattern formation,"

Madzvamuse, Anotida (2006). "Time-stepping schemes for moving grid finite elements applied to reaction–diffusion systems on fixed and growing domains". In: *Journal of computational physics* 214.1, pp. 239–263.

— (2008). "Stability analysis of reaction-diffusion systems with constant coefficients on growing domains". In: *International Journal of Dynamical Systems and Differential Equations* 1.4, pp. 250–262.

Madzvamuse, Anotida and Andy HW Chung (2014). "Fully implicit time-stepping schemes and non-linear solvers for systems of reaction–diffusion equations". In: *Applied Mathematics and Computation* 244, pp. 361–374.

— (2016). "The bulk-surface finite element method for reaction–diffusion systems on stationary volumes". In: *Finite Elements in Analysis and Design* 108, pp. 9–21.

Madzvamuse, Anotida, Andy HW Chung, and Chandrasekhar Venkataraman (2015). "Stability analysis and simulations of coupled bulk-surface reaction–diffusion systems". In: *Proc. R. Soc. A* 471.2175, p. 20140546.

Madzvamuse, Anotida, Eamonn A Gaffney, and Philip K Maini (2010). "Stability analysis of non-autonomous reaction-diffusion systems: the effects of growing domains". In: *Journal of mathematical biology* 61.1, pp. 133–164.

Madzvamuse, Anotida and Philip K Maini (2007). "Velocity-induced numerical solutions of reaction-diffusion systems on continuously growing domains". In: *Journal of computational physics* 225.1, pp. 100–119.

Madzvamuse, Anotida, Philip K Maini, and Andrew J Wathen (2005). "A moving grid finite element method for the simulation of pattern generation by Turing models on growing domains". In: *Journal of Scientific Computing* 24.2, pp. 247–262.

Madzvamuse, Anotida, Hussaini S Ndakwo, and Raquel Barreira (2016). "Stability analysis of reaction-diffusion models on evolving domains: the effects of cross-diffusion". In: *Discrete and Continuous Dynamical Systems-Series A* 36.4, pp. 2133–2170.

Madzvamuse, Anotida, Andrew J Wathen, and Philip K Maini (2003). "A moving grid finite element method applied to a model biological pattern generator". In: *Journal of computational physics* 190.2, pp. 478–500.

Marsden, Jerrold E (1978). "Qualitative methods in bifurcation theory". In: *Bulletin of the American Mathematical Society* 84.6, pp. 1125–1148.

Meier, Peter (1990). "On the critical exponent for reaction-diffusion equations". In: *Archive for Rational Mechanics and Analysis* 109.1, pp. 63–71.

Milewski, Robert (2001). "Fundamental theorem of algebra". In: *Formalized Mathematics* 9.3, pp. 461–470.

Muir, CE, BJ Lowry, and BJ Balcom (2011). "Measuring diffusion using the differential form of Fick's law and magnetic resonance imaging". In: *New Journal of Physics* 13.1, p. 015005.

Mullins, Mary C et al. (1996). "Genes establishing dorsoventral pattern formation in the zebrafish embryo: the ventral specifying genes". In: *Development* 123.1, pp. 81–93.

Muratov, Cyrill B and VV Osipov (2002). "Stability of the Static Spike Autosolitons in the Gray–Scott Model". In: *SIAM Journal on Applied Mathematics* 62.5, pp. 1463–1487.

Murray, James D (2001). *Mathematical biology. II spatial models and biomedical applications {Interdisciplinary Applied Mathematics V. 18}*. Springer-Verlag New York Incorporated.

Nobile, Fabio and Luca Formaggia (1999). "A stability analysis for the arbitrary lagrangian: Eulerian formulation with finite elements". In: *East-West Journal of Numerical Mathematics* 7.EPFL-ARTICLE-176278, pp. 105–132.

Oldham, Keith and Jerome Spanier (1974). *The fractional calculus theory and applications of differentiation and integration to arbitrary order*. Vol. 111. Elsevier.

Perko, Lawrence (2013). *Differential equations and dynamical systems*. Vol. 7. Springer Science & Business Media.

Perraud, JJ et al. (1992). "Stationary Turing patterns versus time-dependent structures in the chlorite-iodide-malonic acid reaction". In: *Physica A: Statistical Mechanics and its Applications* 188.1-3, pp. 1–16.

Persson, Per-Olof and Gilbert Strang (2004). "A simple mesh generator in MATLAB". In: *SIAM review* 46.2, pp. 329–345.

Pfeffer, WF (1986). "The divergence theorem". In: *Transactions of the American Mathematical Society* 295.2, pp. 665–685.

Qian, Tao and Elias Wegert (2013). "Optimal approximation by Blaschke forms". In: *Complex Variables and Elliptic Equations* 58.1, pp. 123–133.

Sarfaraz, Wakil and Anotida Madzvamuse (2017). "Classification of parameter spaces for a reaction-diffusion model on stationary domains". In: *Chaos, Solitons & Fractals* 103, pp. 33–51.

— (2018). "Domain-dependent stability analysis and parameter classification of a reaction-diffusion model on compact geometries". In: *International Journal of Bifurcation and Chaos (Accepted)*.

Sarrate, Josep, Antonio Huerta, and Jean Donea (2001). "Arbitrary Lagrangian–Eulerian formulation for fluid–rigid body interaction". In: *Computer Methods in Applied Mechanics and Engineering* 190.24-25, pp. 3171–3188.

Schmitz, Y et al. (2007). "Pattern Formation of Competing Microorganisms in Sediments". In: *Mathematical Modelling of Natural Phenomena* 2.4, pp. 74–104.

Schnakenberg, J (1979). "Simple chemical reaction systems with limit cycle behaviour". In: *Journal of theoretical biology* 81.3, pp. 389–400.

Schnepf, Andrea and Daniel Leitner (2009). "FEM simulation of below ground processes on a 3-dimensional root system geometry using distmesh and comsol multiphysics". In: 18, pp. 321–330.

Smith, Ian Moffat, Denwood Vaughan Griffiths, and Lee Margetts (2013). *Programming the finite element method*. John Wiley & Sons.

Spanier, Jerome and Keith B Oldham (1987). *An atlas of functions*. Hemisphere.

Steele, Fintan R (2001). *Depicting Complex Beauty*. Elsevier.

Thomas, Daniel, Georges Broun, and Eric Sélégny (1972). "Monoenzymatic model membranes: diffusion-reaction kinetics and phenomena". In: *Biochimie* 54.2, pp. 229–244.

Thomée, Vidar and Lars Wahlbin (1975). "On Galerkin methods in semilinear parabolic problems". In: *SIAM Journal on Numerical Analysis* 12.3, pp. 378–389.

Thomson, Brian S, Judith B Bruckner, and Andrew M Bruckner (2008). *Elementary real analysis*. ClassicalRealAnalysis. com.

Trefethen, Lloyd N (2000). *Spectral methods in MATLAB*. Vol. 10. Siam.

Turing, Alan Mathison (1952). "The chemical basis of morphogenesis". In: *Philosophical Transactions of the Royal Society of London. Series B, Biological Sciences* 237.641, pp. 37–72.

Venkataraman, C. (2011). "Reaction-diffusion systems on evolving domains with applications to the theory of biological pattern formation."

Venkataraman, Chandrasekhar, Omar Lakkis, and Anotida Madzvamuse (2012). "Global existence for semilinear reaction–diffusion systems on evolving domains". In: *Journal of mathematical biology* 64.1-2, pp. 41–67.

Wang, Xu-cheng et al. (2003). *Finite element method*. Tsinghua University Press, Beijing.

Xu, Chuang and Junjie Wei (2012). "Hopf bifurcation analysis in a one-dimensional Schnakenberg reaction–diffusion model". In: *Nonlinear Analysis: Real World Applications* 13.4, pp. 1961–1977.

Yan, Shuling et al. (2013). "Spatiotemporal dynamics in a delayed diffusive predator model". In: *Applied Mathematics and Computation* 224, pp. 524–534.

Yi, Fengqi, Junjie Wei, and Junping Shi (2009). "Bifurcation and spatiotemporal patterns in a homogeneous diffusive predator–prey system". In: *Journal of Differential Equations* 246.5, pp. 1944–1977.

Zhang, Rongpei et al. (2014). "Direct discontinuous Galerkin method for nonlinear reaction–diffusion systems in pattern formation". In: *Applied Mathematical Modelling* 38.5-6, pp. 1612–1621.